



THE UNIVERSITY OF  
**WAIKATO**  
*Te Whare Wānanga o Waikato*

Research Commons

<http://researchcommons.waikato.ac.nz/>

## Research Commons at the University of Waikato

### Copyright Statement:

The digital copy of this thesis is protected by the Copyright Act 1994 (New Zealand).

The thesis may be consulted by you, provided you comply with the provisions of the Act and the following conditions of use:

- Any use you make of these documents or images must be for research or private study purposes only, and you may not make them available to any other person.
- Authors control the copyright of their thesis. You will recognise the author's right to be identified as the author of the thesis, and due acknowledgement will be made to the author where appropriate.
- You will obtain the author's permission before publishing any material from the thesis.

**A study on the use of indigenous New Zealand  
plant fibres for producing biomorphic  
hydroxyapatite fibres and chars used in  
reinforcing biomedical hydroxyapatite sourced  
from cattle bone**

A thesis  
submitted in fulfilment  
of the requirements for the degree  
of  
**Doctor of Philosophy in Engineering**  
at  
**The University of Waikato**  
by  
**Humair Ahmed Siddiqui**



THE UNIVERSITY OF  
**WAIKATO**  
*Te Whare Wānanga o Waikato*

2022

# Abstract

---

This research describes studies on the use of animal derived hydroxyapatite (HAp) with natural plant fibres. The study was divided into two sections, a major section and a minor section. The major section describes animal derived hydroxyapatite (HAp)-char composites containing low weight percent additions of two different types of plant chars (0.1, 0.5, 1, 1.5 and 2 wt%) derived from harakeke and cabbage tree leaf fibres.

The work on hydroxyapatite (HAp)-char composites was conducted in three parts, where the initial two parts dealt with the development of precursors for the composite i.e., HAp and char while the third part detailed the composite made from these precursors. The other section of the thesis deals with development of biomorphic biomaterials-based fibres via treatments involving animal derived hydroxyapatite (HAp) and natural plant fibres. Initially waste bovine bone was processed to produce hydroxyapatite via re-precipitation. In this process, the bovine bone was initially converted into crystalline HAp, which was then further processed through acid digestion and alkali neutralisation at varying reaction temperatures, to produce re-precipitated HAp. Further to this, the as-precipitated HAp powders were subsequently subjected to a high temperature calcination process to develop its morphology. Various characterisation methods confirmed the development of pure HAp via re-precipitation and based on their morphological development and crystallinity, HAp that was re-precipitated at 80°C and calcined at 800°C (H<sub>80-800</sub>), was subsequently chosen as the optimal matrix to be used in the composites. The second part of this study dealt with the development of the reinforcing material for the composites i.e., the char. Harakeke plant leaf fibres and cabbage tree leaf fibres were used to obtain char via pyrolysis followed by acid washing and a “piranha solution” treatment. The harakeke fibrous char was found to have developed carbon nanoscrolls attached to the surface of the char fibres. In contrast, cabbage tree leaf char did not show any form of nano carbon structure with some of the cabbage tree leaf char fibres found to be hollow. Composites were made using re-precipitated hydroxyapatite (H<sub>80-800</sub>) and natural fibre char. The control samples (made up of H<sub>80-800</sub>) displayed porous structure (61% porosity and 36% apparent porosity) having compressive strength, diametral tensile strength, Vickers hardness, brittleness index and indentation fracture toughness values of ca. 26 ± 0.8 MPa, 5 ± 0.1MPa, 190 ± 30 HV, 4 ± 0.2 and 0.5 ± 0.1 Mpa.m<sup>1/2</sup> respectively. Both types of composites showed an increase in mechanical properties up to certain maximum values of incorporated char before dropping to values either equal to or less than the control sample. The 0.5 wt% harakeke leaf fibre char increased the values of (relative to the control

sample) hardness by approx. 118%, diametral tensile strength by 158%, and indentation fracture toughness by 334%. In contrast, 0.5 wt% cabbage tree leaf fibre char addition increased the values of (as compared to the control sample) of compressive strength and hardness by approx. 40% each, diametral tensile strength by 66%, and indentation fracture toughness by 148.5 %.

The minor section of this thesis reports the successful development of calcium deficient biomorphic HAp fibres using a simple aqueous soaking technique. A harakeke fibre biotemplate was soaked in a bovine digest solution (biogenic source of  $\text{Ca}^{2+}$  and  $\text{PO}_4^{3-}$  ions), dried and calcined to obtain HAp fibres. Extensive characterisation was carried out at all stages of the biomorphic fibres.

# Acknowledgements

---

Winston Churchill once said, “Success is not final; failure is not fatal: It is the courage to continue that counts”. My journey toward this thesis has been circuitous but it was that “people induced courage” that propelled me all the way through. The completion of thesis is the credit to all those special personalities, who became the source of courage for me. First, I must express my gratitude to the University of Waikato Doctoral Scholarship that helped me in removing financial concerns to embark on this journey, sustained me for three years and also for their generosity to extend it an additional three months during the challenging times of Covid-19. I consider myself tremendously fortunate to have Associate Professor Michael Mucalo (Associate Dean Postgraduate (Division of Health, Engineering, Computing, & Science)) as my chief supervisor and Professor Kim Pickering (Associate Dean Research (Division of Health, Engineering, Computing, & Science)) as my co supervisor. Michael’s proficiency with the chemistry of hydroxyapatite and Kim’s expertise with natural fibres, have brought a depth of knowledge that only few could match. Michael was a tremendous anchor of support throughout this time and his investment of time and energy into my work, kept me motivated. I am one of those students, who was deeply influenced by his research work on the “re-precipitating of hydroxyapatite” and consider myself lucky to complete this work under his guidance. I am extremely grateful to him for all his time, support, guidance, countless hours of reading my thesis and most importantly for believing in me. His expressive support made the difference in some of the crucial turning points in my candidacy. Kim, a thought stimulating interlocutor, was of great help to me at critical points in my research, especially her idea of harvesting char from natural fibres made me understand, more about pyrolysis, which eventually helped me secure a very good job in a research company which is working on developing graphite from renewable feedstocks. I am highly indebted to Kim for all her support and guidance.

I am extremely thankful to Dr. John McDonald-Wharry, who was always there to help me. John’s expertise with the char material (especially with its Raman spectroscopic characterisation) and his incisive questions proved formative. His thoughtful feedback (especially about nanoscrolls) offered me great guidance and were aimed at moving me forward. I would also like to thank Dr. Amanda French for all her help in analysing samples via ICP-MS and Dr. Christian Gauss for his help in X-ray diffraction. This is also a great opportunity to acknowledge and provide thanks to all our learned and skilful technicians, office staff and laboratory managers. This includes Helen Turner, Duncan

Barnard, Annie Barker, Jenny Stockdill, Jonathan van Harselaar, Stella Raynova, Mary Dalbeth, Natalie Shaw, Chungfu Wang (Chris) and Yuanji Zhang. This brings forward the acknowledgement for all those, who didn't know anything about my research but remained worried for me and helped me live a balanced life.

It's my fortune to gratefully acknowledge all the support and motivation of my friends, Irfan Habib, Tariq Ashraf, Amir Mukhtar, Zubair Moughal, Ejaz Janjua, Tom Sunny, Yousef Alshammari, Ashok Kumar, Hassan Zaki, Wasi Ur Rehman and the remaining 103 friends. My heartfelt thanks to all of them for their support and generous care throughout my studies. Finally, I acknowledge all those people who mean a lot to me. I am still unsure, how to acknowledge my parents, Anjum Fatima and Sohail Ahmed. I am highly indebted to them for showing faith in me and the way they selflessly encouraged me to explore new directions in life and to seek my own destiny. I know, it was a very hard decision for them to initially let me and then my son (their grandchild) go abroad but it was this care, pain and sacrifice that shaped my life. Thank you, Ammi and Papa, for making this possible. In addition, I express gratitude to my brothers Araib Ahmed and Faraz Ahmed for their valuable support and prayers. I cannot forget, how they have taken care of our parents despite being so much younger than me. My special thanks go to my aunt (she is like my mother), Nighat Parveen, and her family, which includes, Habib Ur Rehman, Wahaib Habib, Talha Habib and Hamza Habib. I will forever remain indebted to their selfless love, care and dedicated efforts which contributed a lot to making this possible. I would also like to express gratitude to my uncle, Kamil Siddiqui and aunt-in-law, Tanveer Sultana and their family for keeping me in prayers and motivating me. I owe thanks to a very extraordinary individual, my wife, Rida Humair for her persistent and enduring love, encouragement and understanding during my research that made the completion of this thesis possible. She is the only person, beside me, who went through the same roller coaster ride of a Ph.D. life. She was always there at low moments, when I felt confused about the future, she helped me in keeping things in perspective. I admire her not only for her strength as a great housewife, but also for the fact that she knew how a bowl of pizza fries can bring me back on the track of Ph.D. I greatly value her contribution and deeply appreciate her belief in me. I appreciate my son, Izhan Ahmed Siddiqui for his energetic presence around me, which made me forget all those failed experiments. Although he is only five-years-old, at the moment, he had already contributed positively to my Ph.D. studies. My heartfelt regards go to my father-in-law, Shakeel Ahmed Siddiqui and mother-in-law, Saba Shakeel, for their love, unconditional support and prayers. Words could never express; how thankful I am to both of them.

## Related Publications

---

- 1) Siddiqui, H. A., Pickering, K. L., & Mucalo, M. R. (2018). **A review on the use of Hydroxyapatite-carbonaceous structure composites in bone replacement materials for strengthening purposes.** *Materials*, 11(10). <https://doi.org/10.3390/ma11101813>
  
- 2) Siddiqui, H. A., Pickering, K. L., & Mucalo, M. R. (2020). **Study of biomorphic calcium deficient hydroxyapatite fibres derived from a natural Harakeke (Phormium Tenax) leaf fibre template.** *Bioinspiration & Biomimetics*. <https://doi.org/10.1088/1748-3190/abbc64>

*The review paper mentioned at 1) is related to the earliest literature review done for this study (front page of this paper is attached as Appendix A), while the research paper mentioned at 2) is included as chapter 6 of this thesis (front page of this paper is attached as Appendix B).*

# Table of Contents

---

Abstract.....	i
Acknowledgements.....	iii
Related Publications.....	v
Table of Contents.....	vi
List of Figures.....	xi
List of Tables.....	xvii
List of Abbreviations.....	xviii
1. CHAPTER ONE: INTRODUCTION.....	1
1.1. Introduction.....	1
1.1.1. Current goals and trajectory of the biomaterials field.....	3
1.1.1.1. Tissue Engineering: The way forward.....	3
1.1.2. Properties of Biomaterials.....	3
1.1.3. Modern requirements from Biomaterials.....	5
1.1.4. Hydroxyapatite Carbon composites.....	5
1.1.5. Research Rationale.....	6
1.1.5.1. Research Objectives.....	7
1.1.6. Thesis outlines.....	8
2. CHAPTER TWO : LITERATURE REVIEW.....	9
2.1. Literature review.....	9
2.1.1. Bone and its physiological structures:.....	9
2.1.1.1. Physical Structure of Bone:.....	9
2.1.1.2. Chemical Structure of Bone:.....	9
2.1.1.2.2. Inorganic phase:.....	10
2.1.1.3. Bone remodelling.....	11
2.1.1.4. Bone-tissue repair and regeneration.....	12



2.1.1.5. Historical Perspective .....	13
2.1.2. Hydroxyapatite.....	15
2.1.2.1. Strengthening of Hydroxyapatite – and its importance.....	19
2.1.2.1.1. Indentation Fracture Toughness.....	22
2.1.3. Carbon and its Structures .....	24
2.1.3.1. Pyrolytic Carbon .....	28
2.1.3.2. Carbon Fibres.....	28
2.1.3.3. Nano Carbonaceous Materials .....	29
2.1.3.3.1. Carbon Nanotubes.....	29
2.1.3.3.2. Graphene .....	31
2.1.3.3.3. Graphene Oxide .....	31
2.1.3.3.4. Reduced Graphene Oxide .....	33
2.1.3.3.5. Nanodiamonds .....	33
2.1.3.3.6. Fullerenes.....	34
2.1.3.3.7. Carbon Nanofibres .....	34
2.1.3.3.8. Other systems involving Carbon Structures and Hydroxyapatite .....	35
2.1.4. Carbon from renewable source: Char .....	35
2.1.4.1. Properties of Biochar .....	36
2.1.4.2. Harakeke Plant Fibres .....	40
2.1.4.3. Cabbage Tree Fibres .....	42
2.1.5. Conclusion .....	43
3. CHAPTER THREE : REPRECIPITATION OF HYDROXYAPATITE FROM BOVINE BONE.....	44
3.1. Introduction.....	44
3.2. Materials and Methods.....	45
3.2.1. Materials .....	45
3.2.2. Precipitation of HAp to make digest solution.....	45
3.2.3. Digestion and Re-precipitation of HAp .....	46

3.2.4. Characterisation .....	48
3.3. Results & Discussion .....	48
3.3.1. Fourier transform infrared spectroscopy (FTIR) Analysis.....	48
3.3.2. X-ray diffraction analysis.....	55
3.3.3. Raman Spectroscopy Analysis.....	62
3.3.4. Thermal Analysis .....	65
3.3.5. Imaging .....	67
3.4. Conclusions.....	71
4. CHAPTER FOUR : SYNTHESIS OF CHARS FROM NEW ZEALAND PLANT FIBRES .....	72
4.1. Introduction.....	72
4.2. Materials and Methods.....	72
4.2.1. Materials .....	72
4.2.2. Fibre treatment .....	73
4.2.3. Preparation, modification, and dispersion of Biochar.....	74
4.2.4. Characterisation .....	75
4.3. Results and Discussion .....	76
4.3.1. Fourier transform infrared spectroscopy (FTIR) Analysis.....	76
4.3.2. X-ray diffraction analysis.....	80
4.3.3. Raman Spectroscopy Analysis.....	83
4.3.4. Proximate Analysis via TGA .....	87
4.3.5. Imaging .....	88
4.4. Conclusions.....	95
5. CHAPTER FIVE : BOVINE BONE DERIVED HYDROXYAPATITE COMPOSITES REINFORCED WITH PLANT FIBRE CHARS.....	96
5.1. Introduction.....	96
5.2. Materials and Methods.....	97

5.2.1. Materials .....	97
5.2.2. Composite Powder synthesis .....	98
5.2.3. Composite body synthesis.....	99
5.2.4. Characterisation .....	101
5.3. Results & Discussion .....	102
5.3.1. Fourier transform infrared (FTIR) spectroscopic Analysis.....	102
5.3.2. X-ray diffraction analysis.....	104
5.3.3. Inductively coupled plasma-mass spectrometry (ICP-MS) .....	106
5.3.4. Imaging .....	107
5.3.5. Vickers Hardness Measurements: .....	112
5.3.6. Apparent Porosity and Relative Density Measurement: .....	115
5.3.7. Indentation Fracture Toughness and Brittleness Index .....	117
5.3.8. Compressive Strength: .....	119
5.3.9. Diametral tensile strength (DTS) .....	121
5.4. Conclusions.....	124
<b>6. CHAPTER SIX : BIOMORPHIC CALCIUM DEFICIENT HYDROXYAPATITE FIBRES DERIVED FROM A NATURAL HARAKEKE (PHORMIUM TENAX) LEAF FIBRE TEMPLATE .....</b>	<b>126</b>
6.1. Introduction.....	126
6.2. Materials and Methods.....	127
6.2.1. Materials .....	127
6.2.2. Solution preparation.....	128
6.2.3. Harakeke leaf fibre formation and initial treatments .....	128
6.2.4. Characterisation .....	129
6.3. Results & Discussion .....	130
6.3.1. FTIR Analysis.....	130
6.3.2. Raman Spectroscopy Analysis.....	134

6.3.3. Thermal Analysis .....	135
6.3.4. X-ray diffraction analysis.....	138
6.3.5. Imaging .....	143
6.3.6. Inductively coupled plasma-mass spectrometry (ICP-MS) .....	146
6.4. Conclusions.....	147
7. CHAPTER SEVEN : SYNOPSIS & FUTURE RECOMMENDATIONS .....	148
7.1. Synopsis .....	148
7.2. Re-purposing waste Bovine Bones .....	148
7.2.1. Effect of reprecipitation temperature on HAp crystallinity and morphology	148
7.2.2. Effect of reprecipitation temperature on the development of disordered/amorphous calcium phosphate .....	150
7.3. Natural plant fibres as a source of carbonaceous micro and nano structures..	151
7.3.1. Harakeke char-HAp composites .....	151
7.3.2. Cabbage tree leaf fibre char-HAp Composites .....	152
7.4. Calcium deficient biomorphic HAp fibres.....	153
7.5. Future Recommendations .....	153
Reference .....	155
APPENDIX A.....	176
APPENDIX B .....	177
APPENDIX C .....	178
APPENDIX D.....	179
APPENDIX E .....	180
APPENDIX F.....	181
APPENDIX G.....	182

# List of Figures

---

Figure 2.1: A microstructural representation of bone with size scales[17].	10
Figure 2.2: A typical bone remodelling process. Illustrations drawn by author and are based on the paper “Bone Remodelling” [36].	11
Figure 2.3: A typical representation of strengthening and toughening by fibres; (a and c) represent two views of crack in a body being perturbed by fibres, (b and d) represents the see-through image of the body presented in “a” and “c , for a better understanding.	22
Figure 2.4: A series of SEM images of differing magnifications showing the surface morphology of high temperature sintered bovine rib bone; (a-c, appears from left to right, d-f appears from right to left) (a) shows a particle of bovine bone-derived HAp, (b & c) presents one of the interconnected pores, (c, d & e) presents surface imaging of a HAp particle & (f) depicts surface sub-micron cracks on the surface of HAp [17].	22
Figure 2.5: A pictorial view of indentation made in a ceramic body by a Vickers indentation point.	23
Figure 2.6: Types of cracks that can be generated in a ceramic body due to indentation.	24
Figure 2.7: A broad classification of carbon and its structures (0D, 1D and 2D means zero dimensional, one dimensional and two dimensional respectively) [17].	25
Figure 2.8: Some important carbonaceous structures, (a) graphene, (b) fullerene C <sub>60</sub> , (c) diamond, (d) nanocone, (e) graphite, (f) single-wall carbon nanotube and (g) multiwall carbon nanotube [17].	26
Figure 2.9: Scheme for making graphene oxide and reduced graphene oxide from graphite [17].	32
Figure 2.10: Cell wall structure of harakeke fibre [222].	41
Figure 2.11: Top view of cabbage tree leaf.	42
Figure 3.1: Raw sectioned bovine bone pieces.	46
Figure 3.2: A pictorial representation of processing steps, which summarises production of reprecipitated HAp from bovine bone at different reaction temperatures.	47
Figure 3.3: FTIR spectra of a) defatted Cow bone (R <sub>DCB</sub> ) and b) crystallised (via sintering of bone) HAp (H <sub>P</sub> )	49
Figure 3.4: FTIR spectra of a) H <sub>20</sub> , b) H <sub>40</sub> , c) H <sub>60</sub> and d) H <sub>80</sub> , depicting characteristic features of hydroxyapatite.	50
Figure 3.5: FTIR spectra of sintered reprecipitated HAp (that had been originally reprecipitated at different temperatures): a) H <sub>20-800</sub> , b) H <sub>40-800</sub> , c) H <sub>60-800</sub> and d) H <sub>80-800</sub> .	51
Figure 3.6: FTIR spectra of a) H <sub>20-1000</sub> , b) H <sub>40-1000</sub> , c) H <sub>60-1000</sub> and d) H <sub>80-1000</sub> , depicting characteristic features of hydroxyapatite.	52

Figure 3.7: FTIR spectra of the observed $\nu_4$ PO <sub>4</sub> domain from all reprecipitated and calcined HAp samples.....	53
Figure 3.8: Deconvolution of the $\nu_4$ PO <sub>4</sub> domain in FTIR spectra of all reprecipitated samples, where a) H <sub>20</sub> , b) H <sub>40</sub> , c) H <sub>60</sub> and d) H <sub>80</sub> .....	54
Figure 3.9: XRD diffractograms of a) H <sub>20</sub> , b) H <sub>40</sub> , c) H <sub>60</sub> , d) H <sub>80</sub> , e) H <sub>20-800</sub> , f) H <sub>40-800</sub> , g) H <sub>60-800</sub> , h) H <sub>80-800</sub> , i) H <sub>20-1000</sub> , j) H <sub>40-1000</sub> , k) H <sub>60-1000</sub> and l) H <sub>80-1000</sub> , all depicting the characteristic features of hydroxyapatite. ....	56
Figure 3.10: Portion of an XRD diffractogram of a) H <sub>20</sub> , b) H <sub>40</sub> , c) H <sub>60</sub> & d) H <sub>80</sub> .....	57
Figure 3.11: Lattice strain and crystallite size, a) H <sub>20</sub> , b) H <sub>40</sub> , c) H <sub>60</sub> & d) H <sub>80</sub> .....	61
Figure 3.12: Lattice strain and crystallite size, a) H <sub>20-800</sub> , b) H <sub>40-800</sub> , c) H <sub>60-800</sub> , d) H <sub>80-800</sub> .	61
Figure 3.13: Lattice strain and crystallite size, a) H <sub>20-1000</sub> , b) H <sub>40-1000</sub> , c) H <sub>60-1000</sub> , d) H <sub>80-1000</sub> .....	62
Figure 3.14: This figure represents the Raman spectra a) H <sub>20</sub> , H <sub>20-800</sub> & H <sub>20-1000</sub> b) H <sub>40</sub> , H <sub>40-800</sub> & H <sub>40-1000</sub> c) H <sub>60</sub> , H <sub>60-800</sub> & H <sub>60-1000</sub> d) H <sub>80</sub> , H <sub>80-800</sub> & H <sub>80-1000</sub> .....	63
Figure 3.15: This figure represents deconvoluted PO <sub>4</sub> $\nu_1$ peak of a) H <sub>20</sub> , b) H <sub>40</sub> , c) H <sub>60</sub> , and d) H <sub>80</sub> .....	64
Figure 3.16: Ratio of ACP and HAp bands in Raman spectra, obtained after deconvolution of the PO <sub>4</sub> $\nu_1$ peak observed in Raman spectra of H <sub>20</sub> , H <sub>40</sub> , H <sub>60</sub> & H <sub>80</sub> . ....	64
Figure 3.17: Thermal analysis (heating and cooling) of re-precipitated HAp samples a) H <sub>20</sub> , b) H <sub>40</sub> , c) H <sub>60</sub> & d) H <sub>80</sub> , with numbers (1) to (4) depicting important thermal events which are described fully in a).....	66
Figure 3.18: Derivative weight loss of a) H <sub>20</sub> , b) H <sub>40</sub> , c) H <sub>60</sub> and d) H <sub>80</sub> .....	66
Figure 3.19: Derivative heat flow of a) H <sub>20</sub> , b) H <sub>40</sub> , c) H <sub>60</sub> and d) H <sub>80</sub> .....	67
Figure 3.20: SEM images of HAp powders at different magnifications: a and b) H <sub>20</sub> , c and d) H <sub>40</sub> , e and f) H <sub>60</sub> and g and h) H <sub>80</sub> .....	68
Figure 3.21: SEM images of HAp powders at different magnifications a & b) H <sub>20-800</sub> , c & d) H <sub>40-800</sub> , e & f) H <sub>60-800</sub> and g & h) H <sub>80-800</sub> .....	69
Figure 3.22: SEM images of HAp powders at different magnifications a & b) H <sub>20-1000</sub> , c & d) H <sub>40-1000</sub> , e & f) H <sub>60-1000</sub> and g & h) H <sub>80-1000</sub> .....	71
Figure 4.1: (a) Lab scale granulator and (b) schematic of a pulp digester. ....	73
Figure 4.2: A pictorial representation of the processing steps summarizing the harvesting of char from New Zealand natural fibres. ....	75
Figure 4.3: IR spectra of a) H <sub>bundle</sub> and b) H <sub>Def</sub> , representing decrease of lignin and hemicellulose due to the mild alkali treatment. ....	77
Figure 4.4: IR spectra of a) HC <sub>AF</sub> (harakeke char as formed), b) HC <sub>AW</sub> (harakeke char acid washed) and c) HC <sub>PT</sub> (harakeke char piranha solution treated).....	78

Figure 4.5: IR spectra of a) $C_{\text{bundle}}$ and b) $C_{\text{Def}}$ , representing key changes due to defibrillation.....	79
Figure 4.6: IR spectra of a) $CC_{\text{AF}}$ (cabbage tree leaf char as formed), b) $CC_{\text{AW}}$ (cabbage tree leaf char acid washed) and c) $CC_{\text{PT}}$ (cabbage tree leaf char piranha solution treated). ....	79
Figure 4.7: X-ray diffractogram of, a) raw harakeke fibres bundles ( $H_{\text{Bundle}}$ ) and, b) its defibrillated form made using alkali treatment ( $H_{\text{Def}}$ ).....	81
Figure 4.8: X-ray diffractogram of, a) char made from delignified harakeke leaf fibres ( $HC_{\text{AF}}$ ), b) Acid washed harakeke leaf fibre char ( $HC_{\text{AW}}$ ) and c) piranha solution treated harakeke leaf fibre char (previously acid washed) ( $HC_{\text{PT}}$ ). ....	81
Figure 4.9: X-ray diffractogram of, a) raw cabbage tree leaf bundles ( $C_{\text{Bundle}}$ ) and, b) its defibrillated form made using alkali treatment ( $C_{\text{Def}}$ ).....	82
Figure 4.10: X-ray diffractogram of, a) char made from delignified cabbage tree leaf fibres ( $CC_{\text{AF}}$ ), b) Acid washed cabbage tree leaf fibre char ( $CC_{\text{AW}}$ ) and c) piranha solution treated cabbage tree leaf fibre char (previously acid washed) ( $CC_{\text{PT}}$ ). ....	83
Figure 4.11: Raman spectra of a) $HC_{\text{AF}}$ , b) $HC_{\text{AW}}$ and c) $HC_{\text{PT}}$ .....	85
Figure 4.12: Raman spectra of a) $CC_{\text{AF}}$ , b) $CC_{\text{AW}}$ and c) $CC_{\text{PT}}$ .....	85
Figure 4.13: (ID/IG) ratios of $HC_{\text{AF}}$ , $HC_{\text{AW}}$ , $HC_{\text{PT}}$ , $CC_{\text{AF}}$ , $CC_{\text{AW}}$ and $CC_{\text{PT}}$ .....	86
Figure 4.14: D and G band peak positions of $HC_{\text{AF}}$ , $HC_{\text{AW}}$ and $HC_{\text{PT}}$ .....	86
Figure 4.15: D and G band peak positions of $CC_{\text{AF}}$ , $CC_{\text{AW}}$ and $CC_{\text{PT}}$ .....	87
Figure 4.16: Stereo microscopy images of a, b) $H_{\text{bundle}}$ and c, d) $H_{\text{sep}}$ .....	89
Figure 4.17: Stereo microscopy images of a, b) $C_{\text{bundle}}$ and c, d) $C_{\text{sep}}$ . ....	89
Figure 4.18: SEM images of as formed harakeke char ( $HC_{\text{AF}}$ ).....	90
Figure 4.19: SEM images of harakeke char after acid washing ( $HC_{\text{AW}}$ ) .....	90
Figure 4.20: SEM images of piranha treated harakeke char ( $HC_{\text{PT}}$ ).....	91
Figure 4.21: SEM images depicting the nanotube like structure present on the surface of piranha treated harakeke char .....	92
Figure 4.22: a-d) Close up view of nanotube like structures, where d) is showing the EDS analysis(as an inset) of one of the tube-like structures. ....	92
Figure 4.23: SEM images of nanoscrolls as developed in $HC_{\text{PT}}$ , where different scan rates revealed its un-scrolling structure. ....	93
Figure 4.24: SEM images of as formed cabbage tree leaf char ( $CC_{\text{AF}}$ ), where b) is also showing EDS analysis of mushroom like structures developed by a calcite impurity. ....	93
Figure 4.25: SEM images of acid washed cabbage tree leaf char ( $CC_{\text{AW}}$ ).....	94
Figure 4.26: SEM images of piranha treated cabbage tree leaf char ( $CC_{\text{PT}}$ ).....	94
Figure 4.27: SEM image of a hollow fibre of cabbage tree leaf char. ....	94

Figure 5.1: A pictorial representation of the processing steps, which summarises the production of the harakeke char and cabbage tree leaf char composites. ....	98
Figure 5.2: TGA thermograms of PVA powder, which was pre-tested to analyse its burnout behaviour in a) argon and b) air atmosphere.....	100
Figure 5.3: Heating profile of composites, depicting binder/PVA burnout (till soaking/isothermal hold at 650 °C) and sintering (till soaking/isothermal hold at 1050 °C) profiles. ....	100
Figure 5.4: Tools/devices used to make cylindrical compacts, a) and b) represent a hydraulic floor press, c) is a 10 mm die (graphite used for lubrication), d) illustrates a sintered cylindrical composite sample and e) tube furnace. ....	101
Figure 5.5: FTIR spectra of a) H <sub>80-800</sub> b) HH <sub>0.1</sub> , c) HH <sub>0.5</sub> , d) HH <sub>1</sub> , e) HH <sub>1.5</sub> and f) HH <sub>2</sub> ..	103
Figure 5.6: FTIR spectra of a) H <sub>80-800</sub> b) HC <sub>0.1</sub> , c) HC <sub>0.5</sub> , d) HC <sub>1</sub> , e) HC <sub>1.5</sub> and f) HC <sub>2</sub> ....	104
Figure 5.7: XRD diffractograms of a) H <sub>80-800</sub> b) HH <sub>0.1</sub> , b)HH <sub>0.5</sub> , c) HH <sub>1</sub> , d) HH <sub>1.5</sub> and e) HH <sub>2</sub> , which show the characteristic features of hydroxyapatite. ....	105
Figure 5.8: XRD diffractograms of a) H <sub>80-800</sub> b) HC <sub>0.1</sub> , c) HC <sub>0.5</sub> , d) HC <sub>1</sub> , e) HC <sub>1.5</sub> and f) HC <sub>2</sub> , which show the characteristic features of hydroxyapatite.....	106
Figure 5.9: SEM micrograph of H <sub>80-800</sub> , a) unfractured sample, b) fractured sample (compression tested/broken specimen) and c) low magnification image of sintered sample. ....	108
Figure 5.10: Topological microscopy of HH <sub>0.1</sub> , a) matrix and b) area near char fibre....	109
Figure 5.11: Topological microscopy of HH <sub>1</sub> , representing needle like structure near the char fibre. ....	109
Figure 5.12: Topological microscopy of HH <sub>2</sub> , representing the growth of needle like structure throughout the sintered body.....	110
Figure 5.13: Fracture microscopy of a) HH <sub>0.1</sub> and b) HH <sub>0.5</sub> , where the latter is showing a bridging effect that provided resistance to a growing crack. ....	110
Figure 5.14: Development of microstructure in a) HC <sub>0.1</sub> matrix and area near char fibres in b) HC <sub>0.1</sub> , c) HC <sub>0.5</sub> and d) HC <sub>1</sub> . ....	111
Figure 5.15: Structural development and bonding of HAp with the cabbage tree leaf char fibre in HC <sub>1</sub> . (the solid region represents the structure of the char fibre). ....	111
5.16: Structure and fracture pattern of HAp in a) HC <sub>0.5</sub> and b) HC <sub>1</sub> .....	112
Figure 5.17: Structure of HAp in a) HC <sub>1.5</sub> and b) HC <sub>2</sub> .....	112
Figure 5.18: a) Harakeke composites for Vickers hardness b & c) Vickers hardness tester and d) SEM image of an indent. ....	113
Figure 5.19: Micro Vickers hardness measurements performed on harakeke char composite samples. ....	114



Figure 5.20: Micro Vickers hardness measurements carried out on cabbage tree leaf char composite.....	114
Figure 5.21: a) Archimedes setup for porosity measurement and b) evolving bubbles from the sintered sample when immersed in water .....	115
Figure 5.22: Relative density and apparent porosity measurements conducted on harakeke char composites relative to $H_{80-800}$ .....	116
Figure 5.23: Relative density and apparent porosity measurements conducted on cabbage tree leaf char composites relative to $H_{80-800}$ .....	117
Figure 5.24: $K_{IC}$ and Brittleness index in harakeke leaf char-containing HAp composites.....	118
Figure 5.25: $K_{ic}$ and Brittleness index in cabbage tree leaf char composites.....	119
Figure 5.26: Composite sample ready to be compression tested on the universal testing machine (UTM). .....	119
Figure 5.27: Compressive strength measurements conducted on harakeke char composite as a function of char loading. ....	120
Figure 5.28: Compressive strength measurements of cabbage tree leaf char composite specimens as a function of char loading. ....	121
Figure 5.29: a) Compression testing machine, b) sample undergoing DTS test and c) schematic of DTS test. ....	122
Figure 5.30: DTS measurements conducted on harakeke leaf char composite samples. ....	123
Figure 5.31: a) Diametral tensile strength test fractured $H_{80-800}$ , b) diametral tensile strength test fractured $HH_1$ and c) lateral view of both fractured samples. ....	123
Figure 5.32: DTS measurements conducted on cabbage tree leaf char composite samples.....	124
Figure 6.1: A pictorial representation of the processing steps, which summarises production of the digest solution containing calcium and phosphate ions and the soaking and calcination of the NaOH treated <i>harakeke</i> fibres in the solution, resulting in the production of the biomorphic fibres.....	129
Figure 6.2: FTIR spectra of (a) raw harakeke fibres, and (b) mild alkaline treated harakeke fibres. Spectra were recorded as pressed KBr discs.....	130
Figure 6.3: FTIR spectrum of (a) sintered cow bone (b) Biomorphic fibres (as formed) (c) Biomorphic fibres (final product) .....	132
Figure 6.4: Portion of the IR spectrum of biomorphic fibres (final product) used to calculate CI. ....	134
Figure 6.5: This figure represents the Raman spectrum of biomorphic Fibres (final product). ....	135

Figure 6.6: Thermogram (TGA-DSC) of raw harakeke fibres, representing the degradation of its constituents. ....	136
Figure 6.7: Thermogram (TGA-DSC) of solution-treated harakeke fibres, representing the formation of HAp.....	137
Figure 6.8: Derivative weight loss of raw and solution-treated harakeke fibres.....	138
Figure 6.9: XRD diffractograms of (a) biomorphic fibres (final product) compared with the XRD from (b) standard “hydroxyapatite” (reference number 04-010-6315), (c) standard $\beta$ -tri calcium phosphate (reference number 04-008-8714) and (d) standard calcium carbonate (reference number 01-078-4614). ....	139
Figure 6.10: XRD diffractograms of raw and digest treated fibres representing evolving changes due to heating in the range from 120-220 °C .....	141
Figure 6.11: XRD diffractograms of raw and digest treated fibres representing the evolving phase changes occurring due to heating in the range of 300-1000 °C .....	142
Figure 6.12: A portion of the XRD diffractogram of biomorphic fibres, revealing the important peaks used for the calculations of the crystallite size and degree of crystallinity. ....	142
Figure 6.13: SEM images of as received harakeke fibres, with (a) showing bundles of fibres and b) representing a cross-sectional view of the fibre bundle in the as-received fibres.	143
Figure 6.14: SEM images of the NaOH-treated harakeke fibres with (a) representing defibrillation in the fibres and, (b) representing surface roughness/ruggedness in the fibre. ....	143
Figure 6.15: Electron microscopic images of biomorphic fibres (final product) images (a, b) represent surface features, while images (c, d) depict internal structures and porosity. ....	144
Figure 6.16: Optical images of digest solution treated fibres at different heating temperatures.....	145
Figure 7.1: Crystallinity Index (calculated using IR and XRD) and crystallite size of reprecipitated HAp used in the composites in this study. ....	149
Figure 7.2: Calculated shape factor of all reprecipitated samples of HAp as used in the current study.....	150

# List of Tables

---

Table 1.1: Class of materials used in the body.....	2
Table 2.1: Sample coding and their brief descriptions.....	18
Table 2.2: Comparison of fracture toughness of HAp composite with the addition of nano carbonaceous structures. ....	33
Table 3.1: Sample coding and their brief descriptions.....	48
Table 3.2: Assignment of the FTIR spectra of the deconvoluted $\nu_4$ PO <sub>4</sub> domain in reprecipitated HAp samples.....	55
Table 3.3: Calculated lattice parameter and crystallinity of all samples.....	57
Table 3.4: Crystallite size and lattice strain values of all reprecipitated and calcined HAp samples.....	60
Table 3.5: Breakdown of mass loss during heating of H <sub>20</sub> , H <sub>40</sub> , H <sub>60</sub> & H <sub>80</sub> . ....	65
Table 4.1: Sample coding and their brief descriptions.....	76
Table 4.2: Possible IR assignments of char made from natural plant fibres.....	80
Table 4.3: TGA method for proximate analysis.....	87
Table 4.4: Results of proximate analysis carried out on biomass (both defibrillated harakeke fibres (H <sub>sep</sub> ) and cabbage tree leaf fibre (C <sub>sep</sub> )) and biochar samples (both piranha treated harakeke fibres char (HC <sub>PT</sub> ) and cabbage tree leaf fibre (CC <sub>PT</sub> )).....	88
Table 5.1: Sample coding and their brief description. ....	102
Table 5.2: Elemental composition of all harakeke leaf char composites as determined by ICP-MS and comparison with (uncomposited) H <sub>80-800</sub> .....	107
Table 5.3: Elemental composition of all cabbage tree leaf char-based composites found using ICP-MS as compared to H <sub>80-800</sub> ....	107
Table 6.1: Assignment of the FTIR spectra of the calcium phosphate samples acquired in this study.....	133
Table 6.2: The elemental composition obtained using ICP-MS .....	146
Table 7.1: Percent change in mechanical properties of composites with respect to control sample.....	153

# List of Abbreviations

---

ACP	Disordered/Amorphous Calcium Phosphate
AFM	Atomic Force Microscopy
ASTM	American Society for Testing and Materials
BSE	Bovine Spongiform Encephalitis
CAC	Carbon Atomic Chains
CEC	Cation Exchange Capacity
CI	Crystallinity Index
CNF	Carbon Nanofibre
CNT	Carbon Nanotube
DSC	Differential Scanning Calorimetry
DTS	Diametral Tensile Strength
FTIR	Fourier-Transform Infrared
FWHM	Full Width at Half Maximum
GNS	Graphene Nanosheets
GO	Graphene Oxide
HAp	Hydroxyapatite
ICDD	The International Centre for Diffraction Data
ICP-MS	Inductively Coupled Plasma-Mass Spectrometry
$K_I$	Stress Intensity Factor
$K_{IC}$	Critical Stress Intensity Factor or Fracture Toughness

MWCNT or MWNT	Multi-Walled Carbon Nanotubes
NMR	Nuclear Magnetic Resonance
NP	Nanoparticles
OCP	Octacalcium Phosphate
PBS	Phosphate Buffered Saline
PDF	Powder Diffraction File
PLA	Polylactic Acid
PVA	Polyvinyl Alcohol
RGO	Reduced Graphene Oxide
SBF	Simulated Body Fluid
SEM	Scanning Electron Microscope
SPS	Spark Plasma Sintering
SRM	Standard Reference Material
STA	Simultaneous Thermal Analysis
SWCNT or SWNT	Single-Walled Carbon Nanotubes
TCP	Tricalcium Phosphate
TEM	Transmission Electron Microscopy
TGA	Thermogravimetric Analyzer
UTM	Universal Testing Machine
XRD	X-Ray Powder Diffraction
YAG	Yttrium Aluminium Garnet

# CHAPTER ONE: INTRODUCTION

---

## 1.1. Introduction

Historically, the use of materials to treat, repair, replace or augment tissues in the human body dates to antiquity, however, historically mostly natural materials like wood were used for such purposes[1]. One of the classic examples is the discovery of a 3000-year-old artificial wooden big toe of ancient Egyptian origin from a burial site in upper Egypt[2]. Material selection at that time, for such applications, was based on the skills of the person applying the prosthetic (devices/materials used to replace the missing body part.), and partly on the availability of materials. The prosthetic/material was needed for performing the mechanical function and also to remain “inert” i.e., not interact with the biological system it was being placed in. The advancement in materials selection came with the discoveries of new materials and/or discovery of new properties of existing materials, for example as in the use of gold and silver in dental applications[3-5]. The beginning of the twentieth century brought about a revolution in the field of prosthetics mainly because new materials like synthetic polymers, ceramics and metallic alloys were found to be highly effective and to deliver high functional performance (Table 1.1). Artificial hip joints, dental restoratives and cardiac stents are a few examples of implants (devices/materials that are put inside the body) to come out of this revolution in materials. This also led to the coining of a new word for all such materials used in these applications which is “biomaterials”. However, a comprehensive definition of a *biomaterial* states that it describes a material that can be directly applied or can be used to replace, augment and/or repair a specific body part (or to restore its function) in a safe, economic, and physiologically acceptable manner[6]. Materials that are only put in place for a specific function like, hearing aids for instance are not considered as true biomaterials, because they are not intimately incorporated into the biological system. Here, a possible clarification is required with respect to the definition of “biological materials”. In this thesis, materials that are sourced from or produced by biological systems such as flesh, bone, and wood, will be termed “biological materials”[7].

The advancement in the field of biomaterials has kept pace with the general advances in that of materials science in general. Very interestingly, early trial and error-based research, was often found to lead to fortuitous accidents related to biological response which had formed the rational basis of approaches to present-day research being conducted for biomaterials. Biological response remains the key factor still in deciding the most suitable biomaterial, however with the revolutionary advances presently in the field of molecular biology, “bioactive” materials are also being developed, which have the

capability to interact with biological systems without creating any adverse reaction. Among the several examples existing of such bioactive materials, is MEDPOR® PLUS™ which is a composite of glass and polymer that has the capability to not only interact with the biological system but to also allow tissue ingrowth into its porous network for better integration into the body[3, 4, 8].

This new field of biomaterials has successfully grown into a full-fledged academic discipline, which forms part of core scientific research and has also led to a lucrative and vibrant industry. Globally, for 2019 the size of the biomaterials market was estimated at USD 106.5 billion which is expected to reach USD 348.4 billion by 2027. The most important factor of this steady growth has been the ability of researchers and workers in the field to design engineered biomaterials that are more biologically interactive and multifunctional. For designing a biomaterial or even for selecting one, it is very important to understand the choice of materials available, i.e., biological materials/systems as well as their interaction with the biological systems they are placed in.

The successful integration of an implant or the use of a biomaterial in the body depends on the following three factors:

- 1) the properties especially the biocompatibility of the implant/biomaterial,
- 2) the health condition/status of the recipient/patient, and
- 3) the skill and competency of the surgeon who implants and monitors its performance in the body[9].

Table 1.1: Class of materials used in the body.

<b>Material Type</b>	<b>Examples of materials</b>	<b>Pros</b>	<b>Cons</b>	<b>Examples as biomaterials/devices</b>
Metals	Ti and Ti alloys (Ti4Al6V), Stainless steel, Silver	High strength to weight ratio, high ductility, high toughness	Liabile to corrosion, some metals/alloys can be dense	Joint replacements, dental implants, screws, bone plates.
Ceramics	Calcium phosphates, Carbon, Alumina	High biocompatibility, high compression strength	Brittle, weak in tension.	Orthopaedic implants, dental implants.
Polymers	Poly lactic acid, Nylon, Silicone	High toughness, easy to fabricate	Liabile to degradation, low strength	Sutures, soft tissues, hip socket
Composites	Carbon-Carbon composites, Fibre reinforced bone cements	High strength, high toughness, High biocompatibility	Can be difficult to fabricate	Bone cement, Dental resin.

### **1.1.1. Current goals and trajectory of the biomaterials field**

Currently, the field of biomaterials is going through a revolutionary phase mainly due to advancement in the field of nanotechnology which allows the design of biomaterials to perform complex functions. Nanotechnology has also led to the design of biomimetic materials, which have better biological compatibility[10].

#### **1.1.1.1. Tissue Engineering: The way forward**

The biological interaction in the body with the prosthetic or more generally with biomaterial implants, starts when a layer of serum protein is laid down via adsorption on the implant surface. This adsorption of protein is highly dependent on the surface chemistry and topology of the implant[9, 11]. As mentioned earlier, the rapid growth in the field of nanotechnology has also revolutionised biomaterials by producing customised products like micro sized probes, encapsulated drug delivery devices and cancer targeting drugs/devices. In some cases, biomaterials still have limitations i.e., doctors prefer transplantation of autologous or human-donation-sourced implants over synthetically produced biomaterials. For example, in the case of kidney failure, biomaterials or artificial kidneys have not been able to sufficiently restore normal renal function, hence transplantation of an actual kidney sourced from a compatible donor is the only viable option for the patient to extend their life.

To better cater for this inability of biomaterials to deliver in the case of certain bodily functions, an advanced strand of this field has developed over time called *Tissue engineering* which investigates the development/growth of new tissue using living cells on biomaterials-based templates, so that it is a synergistic combination of both the biomaterial and the biological materials that are interacted with. This biomaterial-based template is referred to in the tissue engineering field as a *scaffold*. The requirements for scaffold materials are as strict as that of any biomaterial, however most of them are biodegradable or bioresorbable to allow for the growth of cells and tissues on or into them. In an ideal case, tissues are grown in vitro and implanted in vivo[10, 12, 13].

### **1.1.2. Properties of Biomaterials**

The different properties of biomaterials have been shown to have an important influence in their dynamic interactions with the biological surroundings when used as medical implants and organ or tissue replacements. The performance and success of each one of these implants depend upon the properties and biocompatibility of the biomaterial used to construct it. Thus, when designing any medical device or implant, it is critical to



evaluate the material properties within the context of its future biomedical application. In general, the most important properties associated with biomaterials are classified into chemical, physical, mechanical, and biological in relation to the bulk and surface parts of the material.

The chemistry of biomaterials i.e., the atomic structure and the molecular arrangement is the one of the most important factors as it defines thermal, electrical and biological properties. Apart from strong bonds (metallic, covalent, and ionic bonds), weak or secondary interactions (like van der Waals and hydrogen bonding) also influence the properties of biomaterials like heat capacity. The atomic structure defines whether the biomaterial is crystalline or amorphous. The effect of atomic structure is more pronounced in bioceramics such as calcium phosphate as both amorphous and crystalline calcium phosphate cause different biological responses in the physiological environment[7, 14-16].

The internal microstructure, level and distribution of porosity, defects and impurity level are some of the crucial deciding factors for designing the biomaterial. For load bearing applications, biomaterials are selected and designed to have suitable mechanical properties which usually include elastic modulus, yield strength, yield strain, ductility, fracture strength, resilience, hardness and toughness. The concept of appropriate mechanical properties in biomaterials, is related to their ability to bear static as well as dynamic load. Different types of materials (i.e., metal, ceramic, polymer or composite) exhibit different mechanical properties, which can sometimes lead to a trade-off between the biological and mechanical properties. For example, calcium phosphate-based ceramics have exceptional biological properties however they classically lack in mechanical properties, which has resulted in a limitation of their use either to non-load bearing applications or to forming composites[17].

Advancements in the field of surface engineering have enabled biomedical scientists to specifically create more biologically compatible surfaces to promote protein adsorption, cell adhesion and growth. This is usually controlled by modifying the surface wettability, surface energy, texture and roughness of a material.

The most crucial property of biomaterials is their behaviour in a biological environment, as they are required to perform certain functions within the biological system without compromising it or causing further harm. The ability of the biomaterial to carry out its desired functions by displaying favourable host responses in a specific living system is commonly termed its biocompatibility. The outcomes of biocompatibility testing can be

classified as toxic, bioinert, biotolerant, bioactive, or bioresorbable. Toxic materials are those which cause death and decay of the host tissue and hence they are out of scope as biomaterials. The important understanding in considering the bioinert, bioactive and bioresorbable materials is that they are all non-toxic in nature. Bioinert biomaterials like titanium alloys are biologically inactive, however microscopic biologically favourable responses (mostly fibrous encapsulation) can be produced by such materials. Biotolerant materials are not necessarily rejected by the host but are separated from the host tissue due to the development of a fibrous tissue [18]. Almost all synthetic polymers and most metals fall into this category. Bioactive materials like bioglass are biologically active i.e., they participate in a favourable response in the form of host tissue interaction to form direct interfacial bonds without intervening fibrous tissue layers. A bioresorbable material like hydroxyapatite is a substance that can get completely reabsorbed and replaced by the host tissue over time [1, 4, 9, 19], however its resorption is highly dependent on the crystallinity as low crystallinity hydroxyapatite displays higher resorbability than highly crystalline HAp [20, 21].

### **1.1.3. Modern requirements from Biomaterials**

Modern medical practice holds that an ideal material is one that can perfectly mimic the living tissue and avoid any kind of rejection. The most researched and reliable material in this respect is hydroxyapatite (HAp). HAp is found naturally in human bones and teeth, and due to this fact, synthetic HAp easily interacts with biological tissue. HAp possesses exceptional bioactivity and osteoconductivity, which promotes bone growth and integration, however it lacks adequate mechanical strength and is hence not suitable for load bearing applications. Considering modern medicine requirements, composites based on HAp matrices are being actively researched to overcome the classical inability of this exceptional biological material when materials based on it alone are developed as implants. Reinforcement materials for implants based on biologically favourable materials like carbon are preferred as there would be no compromising of the biological properties of HAp [14, 17, 22].

### **1.1.4. Hydroxyapatite Carbon composites**

The current demand on bone tissue engineering is to produce a scaffold or coating that should in itself be strong enough to bear loads, and also possess favourable biocompatibility and bioactivity properties. This objective can be analysed in two parts as the first one deals with the mechanical properties, while the other deals with the biomedical/biocompatibility properties and out of the two, the maintenance of good

biomedical properties is of the utmost importance i.e., it is crucial to select a material having exceptional biomedical properties and then it is necessary to evaluate its overall strength and toughness. To produce such a robust material, scientists mostly rely on apatites/hydroxyapatite because of the highly favourable biomedical properties of these ceramics and then need to take steps to enhance its strength and toughness. However, reinforcement to enhance mechanical properties must be done without any compromise to the biological properties. Out of the many different materials, that can enhance the mechanical properties of an HAp matrix, i.e. carbonaceous structures, these particular materials are always preferred in the biomedical science community because of their strength and biocompatibility. The biocompatibility of carbonaceous structures with native tissues of the body invites opportunities for medical applications (creation of artificial heart valves, the remedying of bone fractures, burns and diabetic ulcers, the creation of sorbing elements, air filters). The creation of composites based on HAp and carbonaceous structures is a promising strategy for improving the mechanical characteristics of HAp-based implants. The reinforcing effects of different carbonaceous structures in an HAp matrix (as scaffolds or coatings for orthopaedic applications) highlight those different structures, quantities and modifications of carbon which can be useful in increasing the strength and toughness of the HAp matrix.

#### **1.1.5. Research Rationale**

This research uses technology and processes developed in previous research work done at the University of Waikato. This was mainly based on the harvesting of HAp from waste cow bone and developing fibrous char from natural plant fibres. For HAp, the work carried out in this research is actually an expansion of previous work done by Mucalo, Johnson, Foster and Laird[23-26]. All of the previous work was based on upcycling of waste animal bones, particularly bovine bones and can be categorised into two major domains, the first deals with utilisation of animal bone by minor modifications like defatting and deproteinization, while the other domain deals with the more major modifications like complete acid dissolution and reprecipitation (using base) of animal bone. The New Zealand meat industry generates a large quantity of waste animal bones from its everyday operations. At present these waste bones are largely used to produce lower value products like blood and bone fertiliser for instance [27]. Considering the significant amount of waste bone and also the fact that New Zealand like Australia enjoys a BSE (Bovine Spongiform Encephalopathy) free status which has affected strongly overseas beef operations such as in the UK, the waste bone by-products can become a potential source of biomaterials.

The other important part of this research deals with the potential utilisation of fibrous char in or as biomaterials, which is derived from natural plant fibres. This study further divides into two parts, where the first part is an expansion of work done in the University of Waikato by John McDonald Wharry, Kim Pickering, and Marilyn Manley-Harris. In previous work by these co-workers, Raman spectroscopy was used to identify the presence of crystalline graphitic structure embedded in the amorphous structure of fibrous char. Carbon present in the char is mostly amorphous, however previous molecular vibrational studies have revealed, the presence of segregated crystalline, graphitic zones, hence fibrous char can be considered as a composite of amorphous and crystalline char, which can become suitable reinforcement material. In the present study, fibrous char harvested from natural plant fibres was considered as a strengthening agent for HAp. The char was however chemically purified and modified before addition to the matrix. The second part of the study deals with designing of biomorphic materials utilising natural plant fibres. The idea of this work is based on utilising the complex structure of natural plant fibre (bio-organic matter) as templates to design "biomorphic materials", which can maintain the complicated architecture of the plant fibre, while working as a useful bioactive material.

#### **1.1.5.1. Research Objectives**

The aim of the project was to study the potential conversion of waste material/by-products/natural fibres into useful biomaterials. The objective of the current study includes the examination of the possibilities and limitations of incorporating fibrous char from indigenous NZ plant sources into reprecipitated HAp matrix to develop a composite having improved mechanical properties over that of HAp alone and also to develop bio inspired HAp structures.

The following constitutes the main tasks of the project which has led to the above overarching goal.

- To harvest HAp from waste bovine bones after defatting and deprotenisation.
- To dissolve, reprecipitate (at different temperatures) and heat treat (at different temperatures), the harvested HAp and to study their evolving morphologies.
- To harvest elementary fibres from *harakeke* and cabbage tree leaf (*ti kōka*) fibres using chemical treatment.
- To convert the above-named elementary plant fibres into char fibres and their characterisation. This thesis represents the first time that cabbage tree leaf fibre has been considered and studied as a char source for this purpose.

- To devise and carry out a process for generating sintered composite samples (made using reprecipitated HAp and fibrous char) of consistent physical dimensions for mechanical testing.
- To design and develop a process to use HAp (harvested from waste animal bones) and natural plant fibres to generate biomorphic hydroxyapatite-based fibres.

#### **1.1.6. Thesis outline**

This thesis is divided into seven chapters. Chapter 1 introduces the study, with an introduction to the research rationale and the thesis objectives. Chapter 2 covers the relevant literature review, including previous research related to HAp - carbon composites. Chapter 3 investigates the effect of re-precipitation and calcination on the morphology of the HAp derived from bovine bone. The most suitable morphology of HAp was selected from these experiments to make the composites under investigation. Chapter 4 presents the work related to the development of fibrous char from harakeke leaf fibres and cabbage tree leaf fibres. Those chars were used to investigate their reinforcement effect in an HAp matrix. Chapter 5 investigates the properties of the actual composites made for this study using HAp and fibrous char. Chemical and mechanical properties were mainly investigated. Chapter 6 presents the work related to the development of biomorphic hydroxyapatite-based fibres using harakeke leaf fibre as a template, and a natural source of calcium and phosphate ions (from bovine bone). Chapter 7 provides the main conclusions of the research and suggests some future work that could be considered based on the findings of the study.

# CHAPTER TWO : LITERATURE REVIEW

---

## 2.1. Literature review

### 2.1.1. Bone and its physiological structures:

Bone forms the human skeleton, which provides structural stability, strength, and shape to the body. The bone is a hierarchical composite which is heterogeneous, and anisotropic in nature, having different building blocks at different scales. Each of the hierarchical scales has distinctive structural components and chemical composition. The overall hierarchical arrangement in bone provides the desired mechanical properties along with several biological functions[28, 29].

#### 2.1.1.1. Physical Structure of Bone:

A bone structure can be described in terms of five length scales: macrostructure, microstructure, sub-microstructure, nanostructure, and sub-nanostructure. Figure 2.1 depicts the highly hierarchical structures of bone at different scales. The overall structure of bone is supported and affected by the particular units and arrangements at each scale. At the macroscopic scale (over a length of 10–500  $\mu\text{m}$ ), bone can be categorized into cortical (denser, outer structure) and cancellous (spongy, inner structure) bone. Osteons form the building units of the outer denser bone, similarly trabeculae comprise the building units of inner spongy bone. Osteonal structure is cylindrical in nature with concentric lamellae and a canal in the middle of the lamellae (which is known as a Haversian canal) through which different vessels and nerves pass. Trabeculae are usually plate and rod-shaped tissues that comprise all the spongy/porous structure of cancellous bone. At a submicroscopic scale (1–10  $\mu\text{m}$ ) in mature bone, both cortical and cancellous structures are made of lamellae in a twisted “plywood-type” arrangement. At a nanoscopic scale (over 100–1000 nm) and a sub-nanoscopic scale (< 100 nm), those lamellae are found to be made out of collagen fibres with minerals that are randomly/discontinuously attached[28-31].

#### 2.1.1.2. Chemical Structure of Bone:

The chemical composition of bone is an important aspect apart from its physical structure. As discussed earlier, bone is a biological nanostructured composite composed of organic (mainly collagen) and inorganic (nanostructured HAp) phases, however, its composition varies due to several different factors, mainly health status and age. By

weight, bone is composed of approx. 60% inorganic constituents, 30% organic components and 10% water. By volume, in contrast, bone is composed of approx. 40% inorganic component, 35% organic component and a 25% water component[31, 32].

**2.1.1.2.1. Organic phase:** The organic phase of the bone, which forms the matrix is primarily, approx. 90%, composed of type I collagen (with more than 30 proteins) with the remaining 10% being non-collagenous proteins[32].

**2.1.1.2.2. Inorganic phase:** The inorganic composition of the bone is mainly made of hydroxyapatite (HAp), which when possessing a stoichiometric composition has the formula  $\text{Ca}_{10}(\text{PO}_4)_6(\text{OH})_2$  and a Ca/P mole ratio of approx. 1.67, however, in the bone, impurities such as sodium, carbonate and other ions are often substituted into the crystal lattice of HAp[32].

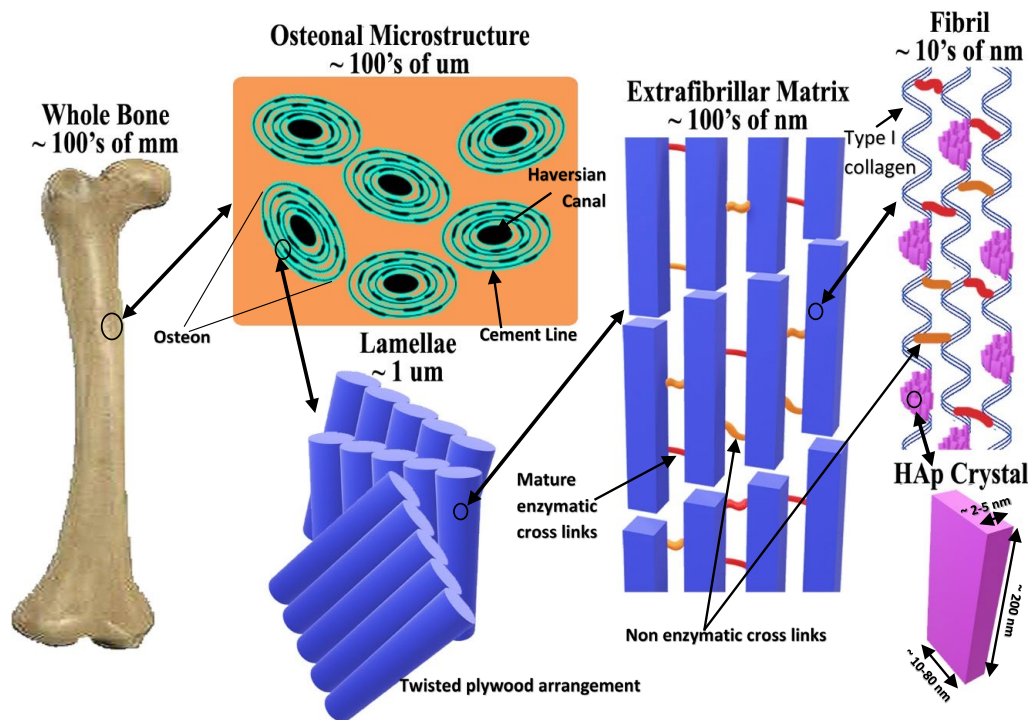


Figure 2.1: A microstructural representation of bone with size scales[17].

The hydroxyapatite structure accommodates many cationic and anionic substitutions. The classic example of natural substituted HAp is bone, which is composed of nanocrystals of carbonated HAp (i.e. incorporation of carbonate ion in the HAp lattice). The ionic substitutions of  $\text{Ca}^{2+}$ ,  $\text{PO}_4^{3-}$  or  $\text{OH}^-$  groups generally lead to changes in the morphology and lattice parameters but without much alteration to the hexagonal symmetry. Researchers in the past have carried out various substitutions for applications like bone/tissue regenerations, antibacterial coating, and drug delivery systems, however

incorporation of therapeutic ions for antibacterial applications have also been reported. The scientific motivation behind this substitution is to enhance osteoconductivity to promote osteogenesis. The general formula of substituted HAp is  $M_{10}(XO_4)_6Y_2m$  where M represents cations which can be  $Ca^{2+}$ ,  $Na^+$ ,  $Mg^{2+}$ ,  $Zn^{2+}$ ,  $Sr^{2+}$ ,  $Cu^{2+}$ ,  $Fe^{2/3+}$ ;  $XO_4$  can be  $PO_4^{3-}$ ,  $CO_3^{2-}$ ,  $SiO_4^{4-}$ , and Y can be  $OH^-$ ,  $CO_3^{2-}$ ,  $F^-$ ,  $Cl^-$ . Recent studies have shown that multi-ionic co-substituted HAp can also be synthesised which make this a multifunctional material[33-35].

### 2.1.1.3. Bone remodelling

Bone remains in a constant state of remodelling, which plays a very important role in the maintenance of overall skeletal structure and function. Any imbalance in this state of remodelling can result in bone metabolism diseases, mainly osteoporosis. In simple terms, bone constantly goes through a process of bone formation and resorption, which should remain in balance under physiological conditions, however if the balance is disturbed it means the resulting structure of the bone will be abnormal. This process of remodelling in the bone happens due to a number of different factors and many types of cells make it possible. The two main cells responsible for this remodelling are: osteoblasts and osteoclasts. Osteoblasts cause bone formation while osteoclasts cause bone resorption. Osteoclasts constantly resorb bone and osteoblasts then deposit it, which, in general, is known as bone remodelling. Figure 2.2 depicts a typical bone remodelling process. Studies in the past have shown that both osteoclast and osteoblast cells affect/interact with each other and that understanding of this interaction can help in drug development.

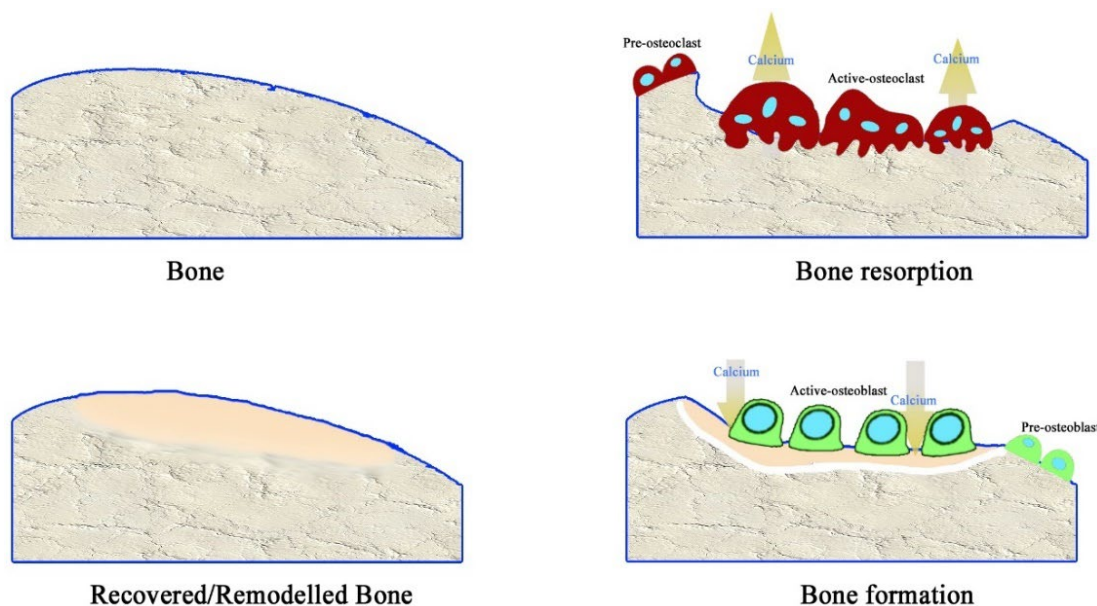


Figure 2.2: A typical bone remodelling process. Illustrations drawn by author and are based on the paper “Bone Remodelling” [36]



#### **2.1.1.4. Bone-tissue repair and regeneration**

People suffer from different bone defect issues mainly because of bone metabolism diseases, age-related bone loss, sports mishaps or other types of serious accidents. This requires medical treatment, and such treatment avenues include transplantation (both bone-tissue and artificial prosthesis) and tissue-engineering processes. Bone-tissue transplantation includes both autograft (i.e., graft tissue from the same individual) and allograft (i.e. graft tissue from other individual of the same species), however autografting is considered to be the gold standard. At present, both autografts and allografts have some limitations, which bring about challenges to their use. Shortage of material and donor site morbidity (rarely) are two important limitations related to autografts, while risks related to transmission of disease are the main limitations related to allografts. These limitations have triggered much effort in the development of alternative approaches, which include the use of artificial prosthesis and bone-tissue engineering treatments. Artificial prostheses proved to be a viable alternative for damaged bone, however its major challenges include failure (mechanical failure and/or loss of integration into natural bone tissue) of prostheses, insufficient biocompatibility (for an extended time) and chronic inflammation. On the other hand, rapidly growing research in the field of tissue-engineering promises to address the aforementioned issues. Tissue engineering focuses on the regeneration of bone (damaged bone) rather than its transplantation (both bone-tissue and artificial prosthesis), eventually this treatment does not require donors and does not attract any unwanted chronic foreign body reaction. Tissue-engineering currently focuses on the stimulation of local bone-tissue regeneration (and growth) after the implantation of suitable biodegradable materials/scaffolds, which happens when material starts to degrade, and growth factors are released to promote new bone formation.

In a typical bone tissue engineering protocol, a three-dimensional (3D) porous scaffold is initially made and then loaded with specific living cells and/or tissue-inducing growth factors to initiate and promote tissue regeneration or replacement [37, 38]. The initiative of bone tissue engineering has escalated research in the field of biomedical sciences, i.e., it has resulted in a more biologically focused and coherent way of designing and developing 3D scaffolds with an appropriate/desired porosity so that they can serve as reinforcement, support, and in some special cases, firmly establish tissue regeneration and replacement. A perfect scaffold is one that has an interconnected porous structure to guide new tissue in-growth and regeneration [37]. Large numbers of people, every year find themselves in need of different kinds of implants, like that needed for dental filling material and for hip joint replacements. Relative to blood transfusion processes, bone

grafting has turned out to be the second most recurrently performed clinical procedure each year. However, the harsh reality is that many patients still accept amputation of diseased/damaged bone/organ as an ultimate treatment because of the unavailability of suitable bone graft substitute materials [39, 40].

At present, various biomaterials are designed and fabricated using polymers, metals, ceramics, or their composites. Bioceramics and their composites have increasingly become an established class of materials applied as human body implants in the form of 3D scaffolds, as they have the necessary properties for biological activity regarding cell adhesion, migration, and proliferation [37, 38, 41]. Amongst the different types of bioceramics available, those having a similar chemical identity to that of bone (i.e. calcium phosphate-based ceramics like hydroxyapatite) have been found to be the most successful, however, their inherently low fracture toughness and strength have historically hampered their use in load-bearing applications [42-46].

In this chapter, the ways in which the historically poor strength of pure hydroxyapatite implants has been improved using different carbonaceous structures are reviewed in terms of their potential to greatly enhance the strength of hydroxyapatite-based composites, manufactured either in the form of a bulk scaffold or as a coating. The literature represents the state of the art in efforts that have been put together to present the abilities of different carbonaceous structures, especially those in nanof orm, to favour crack bridging and deflection in relation to strengthening and toughening effects in a HAp matrix.

#### **2.1.1.5. Historical Perspective**

In past decades, scientists have focused their research efforts on designing and developing artificial bone, with the objective of creating functional bone regeneration candidates. The historical development of the various stages (“generations”) of biomaterials that resulted can be analysed through a consideration of their relative biomedical and mechanical properties. The first generation of biomaterials was mostly related with the development of high strength bioinert materials, which included the development of metallic materials (such as stainless steel and titanium alloys), ceramic materials (like alumina, zirconia), and polymeric materials (like polyethylene and silicone rubber). These biomaterials were used to make devices, commonly known as prostheses. At that time, scientists were only focused on an objective to achieve an appropriate combination of physical properties to match those of the substituted tissue (i.e. the

defective site) with a minimal toxic response in the host [47]. Almost all of the biomaterials of the first generation had a common attribute, i.e. they were bioinert, and hence not able to develop a biological bond to bone or promote repair of bone. Moreover, they were non-degradable in vivo, which meant that secondary surgery was required if the implant failed and/or needed revision[40, 41]. By the end of the 1980's, approximately 50 types of implanted prostheses were in clinical use, which were made from 40 different biomaterials[48]. Many people at that time had had successful surgeries which saw their lives enhanced due to the use of implants made from 'bioinert' biomaterials. However, it was found (specifically in hip and knee implants) that over time there was a tendency for bone to become slowly resorbed at the prosthesis-bone interface, owing to a phenomenon known as "bulk modulus mismatch". This is also known commonly as stress shielding, i.e. almost all the mechanical load is carried by the higher modulus implant device, which initiates the localised osteoporosis-like symptoms leading to gradual bone resorption, deterioration of bone strength at the implant-bone interface hence leading to ultimate failure via loosening. At that time, prominent materials scientists of the 1980s such as Bonfield began working on the concept of designing biomaterials that would diminish bone resorption due to stress shielding at the prosthesis-bone interface [48].

Later stages of research into biomaterials development were largely associated with advances in the field of artificial bone materials, which moved towards the use of bioactive or biodegradable materials. This era came to be known as that of the second-generation biomaterials. Bioactive ceramic materials (e.g. hydroxyapatite) and biodegradable polymeric materials (e.g. polylactic acid and polyglycolic acid) are important materials comprising the second-generation biomaterials group. Unlike the previous generation of materials, second-generation biomaterials possessed the property to develop strong bonds to surrounding bone tissue and were biodegradable/bioresorbable. However, both generations of materials were clinically found to be merely functional/structural substitutes i.e., could only bear the load (in the case of the bioinert materials) or (in the case of the osteoconductive materials) provide a scaffold or "structure" in which bone formation had to be induced by natural bodily processes rather than by the implant itself. Some were also found to be insensitive to physiological changes in vivo such as in the case of stress shielding by bioinert implants [39, 44, 48-50]. With the inception of multidisciplinary developments in the fields of molecular biology, materials science & manufacturing engineering, many innovative and advanced artificial substitutes having unique functionalities were developed, which are capable of bone repair/regeneration, this has led up to the stage where an important area of research known as tissue engineering was created [51-54].

Tissue Engineering develops scaffolds for placement in defect sites, which not only provide mechanical integrity but also encourage/actively induce stem cell proliferation. A typical procedure of tissue engineering consists of manufacturing a scaffold using suitable biomaterials and subsequently subjecting them to seeding/culturing of stem cells (already harvested from the patient) after which the scaffold is implanted. It can be applied in situations where a temporary functional repair is required or for permanent repair/regeneration. For a successful scaffold material, it is necessary to have an appropriate degradation rate, as very slow rates of degradation retard bone growth, while overly fast rates will result in loss of mechanical integrity. Therefore, it is necessary for a bone scaffold to possess the desired biological, mechanical, and topological properties, as well as favourable osteoconductive properties, thereby facilitating bone remodelling from artificial bone into natural bone[39-41, 47, 49, 50, 55].

In general calcium hydroxyapatite (HAp) based bioceramics show excellent biocompatibility, corrosion resistance and excellent compressive strength, which have made them a suitable candidate for implants. However, among the list of different calcium phosphates used biomedically, HAp has attracted the most interest from the scientific community mainly due to its features of promoting osseointegration & new bone formation processes, as well as its low toxicity, and resemblance to mineral bone. Research studies so far suggest that among the list of calcium phosphate compounds, HAp-based materials have been the most successful in bone grafting applications.

### **2.1.2. Hydroxyapatite**

The enhancement of advanced materials for biomedical applications is a critical issue challenging modern-day materials science and engineering, especially when it comes to the development of materials to be used *in vivo*. Historically, hydroxyapatite (HAp),  $\text{Ca}_{10}(\text{PO}_4)_6(\text{OH})_2$  has been the best bone substitute because it can achieve a sound, firm bond with bone tissue, and furthermore can demonstrate osteoconductive behaviour and have no undesirable effects on the human body[35, 49, 56-59]. The term “hydroxyapatite” implies the presence of hydroxyl (OH) groups while “apatite” (derived from the Greek word “apatōs”) meaning “to deceive” was historically used to identify mineral apatites, as they were often mistaken for precious gems like topaz)[60]. Apatites, in general, are known by the chemical formula  $\text{M}_{10}(\text{XO}_4)_6\text{Z}_2$ , in which  $\text{M}^{2+}$  is a metal, and  $\text{XO}_4^{3-}$  and  $\text{Z}^-$  are anions. In the unit cell of HAp, the  $\text{M}^{2+}$  is  $\text{Ca}^{2+}$ ,  $\text{XO}_4^{3-}$  is  $\text{PO}_4^{3-}$  and  $\text{Z}^-$  is  $\text{OH}^-$ . The Ca:P mole ratio in HAp is 1.67. HAp crystallises in a hexagonal system with crystallographic parameters:  $a = 9.418 \text{ \AA}$ ,  $c = 6.881 \text{ \AA}$ , and  $\beta = 120^\circ$ . The crystalline network of HAp is a compact assembly of tetrahedral  $\text{PO}_4$  groups, in which phosphorus atoms are found in the

centre of tetrahedra having 4 oxygen atoms at the top. Each PO<sub>4</sub> tetrahedron delineates two types of distinct channels. The first channel is surrounded by Ca<sup>2+</sup> ions, denoted as Ca(I) (4 per unit cell). The second type of channel contains six other Ca<sup>2+</sup> ions, denoted as Ca(II). These channels host OH<sup>-</sup> groups along the c axis to balance out the positive charge [61].

As long ago as 1926, diffraction and chemical studies of teeth and bone revealed that their inorganic phases were basically calcium hydroxyapatite [62]. In bone, the mineral phase consists broadly of hydroxyapatite but there is also a variety of impurity ions present in the HAp lattice such as carbonate, magnesium, and sodium ions. Carbonate is one of the most abundant impurity ions with its content being about 4-8 wt%. This is the reason that bone/hard tissue can be regarded as carbonate-substituted HAp (CHAp)[63, 64]. Figure 2.1 represents the micron and sub-micron features of bone tissue, in which hydroxyapatite platelets can be seen. The biological behaviour of HAp-based ceramics relies on many factors, such as chemical and phase transformation, microstructure, pore size, and pore volume. In surgery, usage of both porous, as well as dense bioceramics, is common, as it depends upon the function and level of implantation required by the patient. It is most commonly dealt with on a case-to-case basis rather than in general. Experimentally porous ceramics have a low strength (although strength is found to be dependent upon the level of porosity) and hence such ceramics are found clinically to be more appropriate for drug delivery or for implantation into low load-bearing tissues (like maxillofacial applications) [56, 65, 66]. Osteointegration depends heavily on the pores in implants, more specifically the pore size, volume, and their interconnectivity. It was observed that for bone ingrowth into an implant (successful osseointegration) the minimum pore size should be around 100–135 μm, and there is also found to be a direct relation between porosity/pore interconnectivity with the process of bony ingrowth into the implant, as the porosity/pore interconnectivity increases bone ingrowth, especially fixation processes, which become more operative. Moreover, protein adsorption favours separation of osteogenic cells. Subsequently, the presence of small, submicron pores, specifically those about the size of blood plasma proteins, favours biointegration. Thus, it is preferred to have a bimodal distribution of pore-sizes in bioceramics[54, 57, 66, 67].

Small HAp granules are also of interest biomedically as they find wide application in maxillofacial surgery and implantable drug delivery systems. There are numerous ways to produce HAp granules, like hydrothermal synthesis and pelletising. It was observed through scientific study that spherical HAp particles tend to promote osteointegration and diminish inflammatory processes[54, 68]. Ceramics can also serve as a basis for producing composite materials, that can be used for load bearing implant applications. Cortical bone

usually demonstrates in the way of mechanical properties compressive strength of 130-200 MPa tensile strength of 50-151 MPa and fracture toughness values of 2-12 MPam<sup>1/2</sup>, which outline the desired values of potential ceramic composites. There is considerable research effort focused on synthesising HAp-matrix composites which achieve reinforcement of the ceramic materials through the use of fine particles, micro lamellae, or fibres, These can raise the strength and toughness of such materials to the level necessary for hard tissue (bone) replacement implants in more load bearing areas[35, 69].

Researchers have synthesised hydroxyapatite using different techniques such as hydrothermal synthesis, precipitation, and hydrolysis, as well as employing natural resources like bovine bones [24, 70-72], fish bones [73-75], marine shells [76-79], eggshells [80-84]). Historically the usage of xenogeneic bone like Kiel bone (actual bone harvested from calf or ox) and Boplant (actual bone harvested from a calf) in biomedical applications were thought to be the alternate to auto- or homografts mainly due to limited supply of grafts, site morbidity and the difficulty/expense of multiple surgical processes[56]. A study by Callan and Rohrer [71] has also reported patient fears about human tissue transfer, due to the advent of AIDS, especially in dental surgery. They reported that clinicians were actively looking for alternative allograft materials and proposed a naturally derived xenogeneic hydroxyapatite (HAp). The xenogeneic bone grafting material used was a fully crystalline naturally porous bovine-derived hydroxyapatite (with all collagenous protein removed), having a pore size in the range from 250 – 450  $\mu\text{m}$ . Although the organic matter had been previously removed, the bone microstructure was retained. Hydroxyapatite, either synthetic or naturally produced, has been used in wide variety of biomedical applications mainly due to its property of being able to form a bone-like apatite layer at the bone tissue interface [51, 85, 86]. As mentioned previously despite these favourable bioactive characteristics of HAp, its poor mechanical properties like low fracture strength and toughness, preclude its usage for high load bearing applications such as an implant for the hip or knee. Therefore, to make HAp more suitable for such applications, it needs to be reinforced with various biocompatible materials for improving its strength and toughness. This hence necessitates HAp being prepared as a biocomposite material.

Extraction of HAp from natural sources, such as bovine and fish bones is an ingenious way of getting HAp for biomedical use. The bone obtained from such biogenic sources has already been created by nature so not only mimics/replicates bone in terms of chemistry but also provides it via an environmentally friendly and economical process. In the past, studies related to apatite and bovine bone were conducted in abundance, which

were mostly focussed on obtaining pure hydroxyapatite, after calcining defatted bovine bone. This includes studies that have varied calcination temperatures to evaluate the chemistry and quality of hydroxyapatite, Table 2.1 below, summarises a breakdown of such studies. A few studies have modified that bovine harvested HAp into more useful material. The modifications carried out have included lattice substitution, reprecipitation of HAp and creation composites.

Table 2.1: Sample coding and their brief descriptions.

Source	Main Processing	Product	Post Processing
<b>Bovine Bone</b>	Defatting & Calcination at a specific Temperature	Hydroxyapatite [87-91]	Acid Digestion and Re-precipitation[23, 26, 92]
			Composites [93-95]
			Lattice Substitution [96]
	Defatting & Bleaching	Hydroxyapatite (xenograft product) [70, 97]	
	Defatting & Calcination at different temperatures	Hydroxyapatite[98]	
		Hydroxyapatite & Carbonated Hydroxyapatite [99-102]	
Hydroxyapatite & Tri Calcium phosphate [103]			

The process of harvesting HAp from bovine bone, in general involves an initial defatting of the raw bones, and then a suitable heat treatment process to thermally decompose & drive out all the organic matter and a suitable calcination treatment to precipitate HAp. The process is relatively straightforward, but during the process of precipitation there is almost no control over developing particle size and morphology, which is important as current biomedical demands which include patient specific design of implants, require bio-compatible powders with suitable particle shape and size. This issue can be tackled using an approach of re-precipitation, which means digesting precipitated HAp using a suitable acid and then reprecipitation by adjustment of pH. Moreover, researchers in the past have investigated effects of different parameters related to the precipitation method on HAp formation and found that parameters like reaction temperature, pH (initial and final) and solution addition rate have had a strong influence on the purity, particle morphology and size of the resultant HAp particles. Precipitation based synthesis of HAp was studied in depth in the early 1960's mainly by Eanes et. al. [104]. It is important to highlight that if the re-precipitated HAp powders are subjected to high temperatures, it will change the morphology, size and surface properties of the particles.

### **2.1.2.1. Strengthening of Hydroxyapatite – and its importance**

The understanding and the application of strengthening and toughening mechanisms is very crucial for designing new and optimised materials. A common engineering goal for a structural material is to be both strong and tough, yet often, an increase in strength is coupled with a reduction in toughness and vice versa. Strength is simply the material's ability to withstand stress without being subjected to non-recoverable deformation or fracturing, whereas toughness can be regarded as the resistance to crack propagation [105, 106]. Every material contains some form of defects (e.g. pores and cracks) and material design when using inherently brittle materials such as alumina (defect-tolerant design philosophy) is challenging as they are influenced by such defects. Fracture mechanics is a valuable tool for design engineers as it helps in identifying and evaluating conditions under which a crack/defect will propagate and cause a failure, usually by relating three important parameters i.e. the size of the largest/critical flaw, the applied stress, and the fracture toughness.

Ceramic materials are known for their brittleness (lack of ability to plastically deform) [105, 107-109]. In fracture mechanics theory (known as Griffith's theory) fractures inside ceramic materials originate from micro-cracks rather than from atomic bond breaking [110]. Most importantly, these micro-flaws are omnipresent (microscopic flaws, including micro-cracks and internal pores, result from the cooling of the melt or during diffusion-based processes) in the body of a ceramic, and upon loading/stressing, these microcracks tend to extend. Similarly in the case of bioactive ceramics, despite the excellent biological properties, they lack slip systems in their crystals, so whenever they are subjected to an external load, stress relaxing phenomena like plastic deformation and grain boundary sliding that often occur in metals, do not occur in ceramics resulting in poor load-bearing properties for such bioactive ceramics [40]. Hence, general failure mechanisms of ceramic materials are based on the unstable propagation of flaws (pores, cracks or inclusions), as they are unable to relieve the stress build up at the tip of flaws (through plastic deformation as for example a ductile metal would) and consequently, a ceramic body's strength is dependent upon the combination of the size of the flaw and the applied stress. This explains why they are commonly referred to as notch-sensitive. The flaws in ceramics tend to act as stress concentrating points, i.e. they amplify the stress at the crack tip, which eventually leads to material failure at an applied stress point which is much lower than the theoretical stress [110] i.e. a significant decrease in the values of actual strength when being compared with theoretical values [110]. The theoretical strength of pristine glasses is about 7000 [MPa], but practically its strength is merely 1% of the



theoretical value (35-70 [MPa])[111]. The dimensions (in micrometres or nanometres), geometry (penny-like round) and orientation (parallel to applied load) of cracks regulate the magnitude of this amplification of stress. This concentration of stress at the crack tip is commonly denoted by a stress concentration factor, which is the ratio between the maximum stress developed at the microstructural defect to the nominal stress in the body. The threshold value of the stress intensity factor is known as fracture toughness or critical stress intensity factor. In brittle materials, for the fracture to occur, the stress developed at the crack tip must be greater than the fracture toughness values[107, 108, 112]. For bioceramics, where fracture events can be catastrophic, the approach based on utilising fracture toughness values, is the only method that can predict ceramic fracture.

When the stress developed at the crack tip exceeds the fracture toughness value of the material, the crack will fracture. It is important here to discuss the fracture process of this crack first, as the complete fracture is just coalescence of the propagating crack with other ones. Fracture mechanics defines this process as a competition between two phenomena i.e. intrinsic (damage) processes and extrinsic crack-tip shielding mechanisms. Intrinsic damage processes such as micro-void coalescence promote the propagation of a crack tip by operating ahead of it and are dependent upon the nature of microstructure (or nanostructure) or any second phase ahead of crack tip (usually by cracking/debonding), while extrinsic crack-tip-shielding mechanisms attempt to inhibit/resist this propagation of the crack tip and operate behind the crack tip. One of the principal methods of increasing fracture toughness is by increasing the microstructural resistance which will enlarge the plastic zone ahead of the crack tip, eventually making initiation as well as propagation of the crack difficult. This is termed intrinsic toughening and is relevant to ductile materials. For ceramics/bioceramics extrinsic toughening is perhaps the primary source of toughening, as intrinsic toughening would involve altering the bond strength, which is not feasible. Extrinsic toughening is generally based on diverse microstructural mechanisms that play their role (behind the crack tip) in reducing the damaging force developed at the crack tip; this is usually known as crack-tip shielding and can also involve processes like crack bridging by fibres and in situ phase transformation. Intrinsic toughening mechanisms affect crack initiation as well as crack propagation. They are an inherent property of the material and are found to be active in the material irrespective of the crack size and its geometry. Extrinsic mechanisms, which are only effective for crack growth, come in to play in the event of the crack wake and are dependent on the size and geometry of the crack [105, 106, 113, 114]. In the domain of biofabrication using bioceramics, designers are constantly challenged with the issue of low strength and toughness, for which extrinsic

toughening is the only solution which is usually done by reinforcing bioceramics using biocompatible and effective materials [40, 51].

Many successful approaches have been undertaken to toughen the ceramic material. Those techniques can be grouped into three basic categories, i.e., strengthening and toughening mechanism based on fibres, particles and microstructural:

1. Strengthening based on fibres:

- a. Modulus/load transfer; i.e. the use of high elastic modulus fibres in a relatively low elastic modulus matrix[115].
- b. Crack bridging; implying addition of some secondary phase, usually fibrous structures, which bridge the flaws in the ceramic resulting in enhanced strength.
- c. Fibre pull out; is associated with fibre debonding and the corresponding frictional sliding which enhances the fracture toughness. Some part of the energy is consumed due to friction as fibre, particle, or grain slides against adjacent microstructural features, resulting in enhanced fracture toughness.

2. Strengthening based on particles:

- a. Crack deflection or impediment; mainly involving modification in the microstructure of ceramic materials, like dispersing foreign particles, which tend to impede or deflect an advancing crack.

3. Strengthening based on microstructure:

- a. Pre-stressing; which involves placing a portion of the ceramic under a residual compressive stress.
- b. Crack shielding; mainly involving transformation toughening, in which reinforcement particles undergo sudden volumetric change due to an applied stress, which in turn compresses the flaws in ceramic materials.

Two schematic representations show different strengthening and toughening mechanisms: Figure 2.3 represents an opaque and see-through image of the body containing fibrous reinforcement, but Figure 2.4 represents a series of progressive SEM imaging of bovine (rib) bone sintered at high temperatures to burn out all the collagen protein and lipid residues to yield crystalline hydroxyapatite.

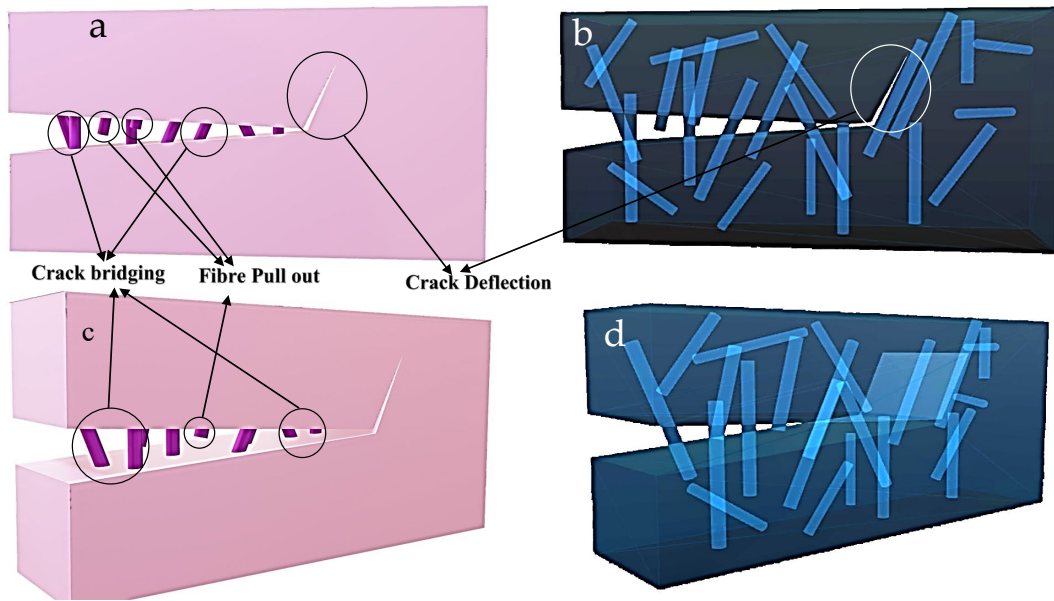


Figure 2.3: A typical representation of strengthening and toughening by fibres; (a and c) represent two views of crack in a body being perturbed by fibres, (b and d) represents the see-through image of the body presented in “a” and “c”, for a better understanding

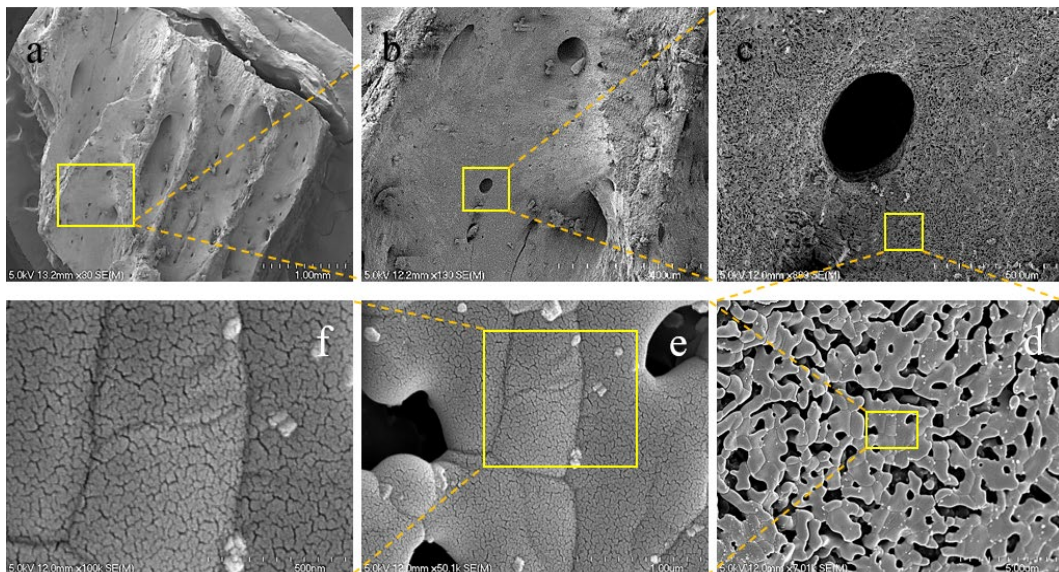


Figure 2.4: A series of SEM images of differing magnifications showing the surface morphology of high temperature sintered bovine rib bone; (a-c, appears from left to right, d-f appears from right to left) (a) shows a particle of bovine bone-derived HAp, (b & c) presents one of the interconnected pores, (c, d & e) presents surface imaging of a HAp particle & (f) depicts surface sub-micron cracks on the surface of HAp [17]

#### 2.1.2.1.1. Indentation Fracture Toughness

For a brittle material, fracture toughness measurements allow assessment of the material’s brittleness or resistance to fracture. Fracture toughness studies in the early 1980’s led to confusion about testing, as results seemed variable and found to be highly dependent upon testing methods. It was because of the different outcomes from different

testing methods, that there was doubt about whether materials have any set value for fracture toughness,  $K_{Ic}$ . However, testing methods became more refined [116] and it is confirmed now that many brittle materials do possess specific fracture toughness values. The analysis of fracture toughness of brittle materials, especially highly porous brittle materials using Vickers indentation is an effective but non-traditional method, as it does not break a pre-cracked specimen (like in a single edge notched beam). The process involved uses a conventional Vickers hardness indenter to create a hardness impression i.e., a plastically deformed region on a polished surface, which generates cracks that originate radially outward and downward from the hardness impression, as shown in Figure 2.5. The lengths of these cracks are precisely measured (using high resolution microscopy like SEM) and by use of values of the crack lengths, as well as the indentation load, the hardness, elastic modulus, indentation diagonal size, and an empirical fitting constant, values of the fracture toughness can then be measured[116-118].

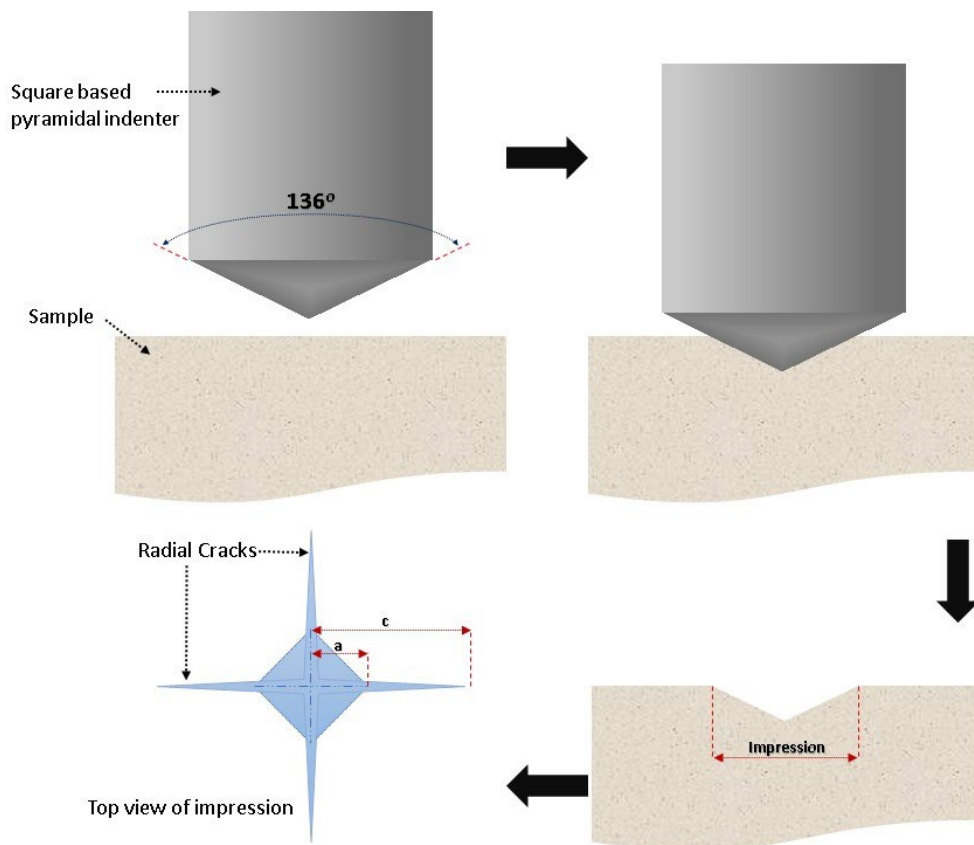


Figure 2.5: A pictorial view of indentation made in a ceramic body by a Vickers indentation point.

Sometimes assessing the fracture toughness ( $K_{Ic}$ ) of brittle materials via conventional methods becomes difficult due to sample limitations, porosity, and limited

resources. To cope with such issues, an alternative method based on measuring crack lengths referred to as the “Indentation Fracture” technique was developed, which was extensively reported in literature [119-121]. Different researchers have developed/derived mathematical equations based on linear mechanical fracture theory to refine the results close to  $K_{IC}$  determination [122].

Researchers have found this method useful for measuring approximate values of  $K_{IC}$ . This technique is based on normalized standard hardness tests (ASTM E1820 - 09e1 Standard Test Method for Measurement of Fracture Toughness, 2008 and ASTM C 1327-99, Standard Test Method for Fracture Toughness at Room Temperature of Advanced Ceramics, 1999). Palmqvist for the first time utilised this technique to identify parameters related to the testing and proposed a relationship between  $K_{IC}$  and the effort to nucleate cracks. He described that when a critical force is reached, crack length ( $c$ ) becomes directly proportional to the applied force ( $P$ ), as shown in figure 2.5. Many later studies also endorsed the relationship between  $P$  and  $c$ . Figure 2.6 depicts some of the most common types of cracks, that can appear in materials due to indentation.

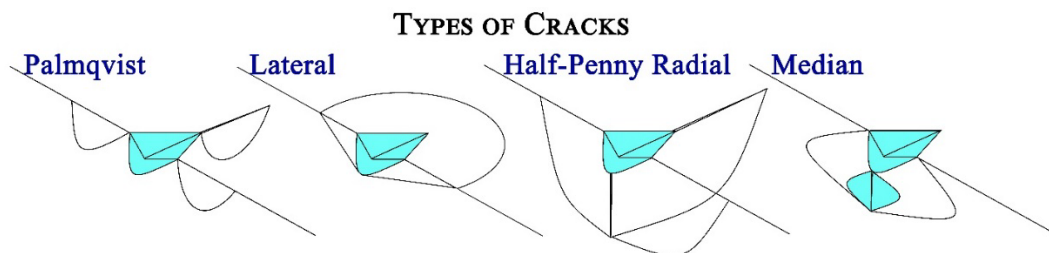


Figure 2.6: Types of cracks that can be generated in a ceramic body due to indentation.

### 2.1.3. Carbon and its Structures

In this study, carbon-based fibres were selected for reinforcing HAp mainly because other carbon-based materials had successfully enhanced mechanical strength without sacrificing the biological properties of HAp. Carbon, which is the sixth element in the periodic table, is one of the most abundant elements on earth having an average atomic mass of 12 amu. Carbon is an important building block of all living organisms and after oxygen, is the most dominant element in the human body (approx. 18% of body weight). Scientists often regard carbon as a unique element since it has extraordinary ability to catenate (bond with one another) resulting in cyclic or acyclic chains. It can also form single, double, or triple bonds as well as straight or branched chains. After hydrogen, carbon is the element which can form the most compounds of any of the elements which

is why it has many different allotropic forms. Some of the main allotropes of carbon are graphite, diamond, glassy carbon, pyrolytic carbon, fullerenes ( $C_{60}$ ,  $C_{70}$ ), hexagonal diamond (lonsdaleite), and carbon nanotubes[123, 124]. Figure 2.7, presents a broad classification of carbon allotropes while Figure 2.8, shows the important carbonaceous structures possible.

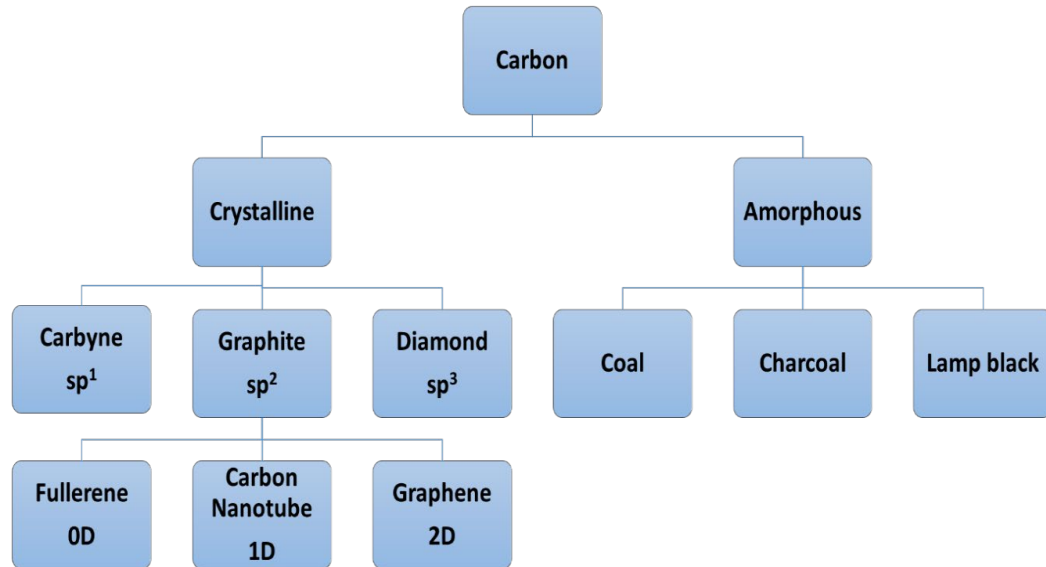


Figure 2.7: A broad classification of carbon and its structures (0D, 1D and 2D means zero dimensional, one dimensional and two dimensional respectively) [17].

Today, carbonaceous materials have been employed in many applications spanning from electronics to medical applications, however novel uses of carbon are continuously being investigated and discovered. At present, there exists a strong world-wide interest in the usage of graphite and its use as an anode material in lithium-ion battery technology[125, 126]. In the field of biomedical materials, the use of carbonaceous structures has been successful, and most importantly, there are innovative applications continually being invented. The biocompatibility of carbonaceous structures with living systems, encourages many uses in medical contexts such as the fixation of bone fractures, artificial heart valves as well as the creation of sorbing elements, air filters etc. Scientists in the biomedical field have found that the development of composites using HAp and carbonaceous structures is an encouraging approach for improving the load bearing capacity of HAp-containing composites without sacrificing their biomedical properties [51, 86, 127-129].

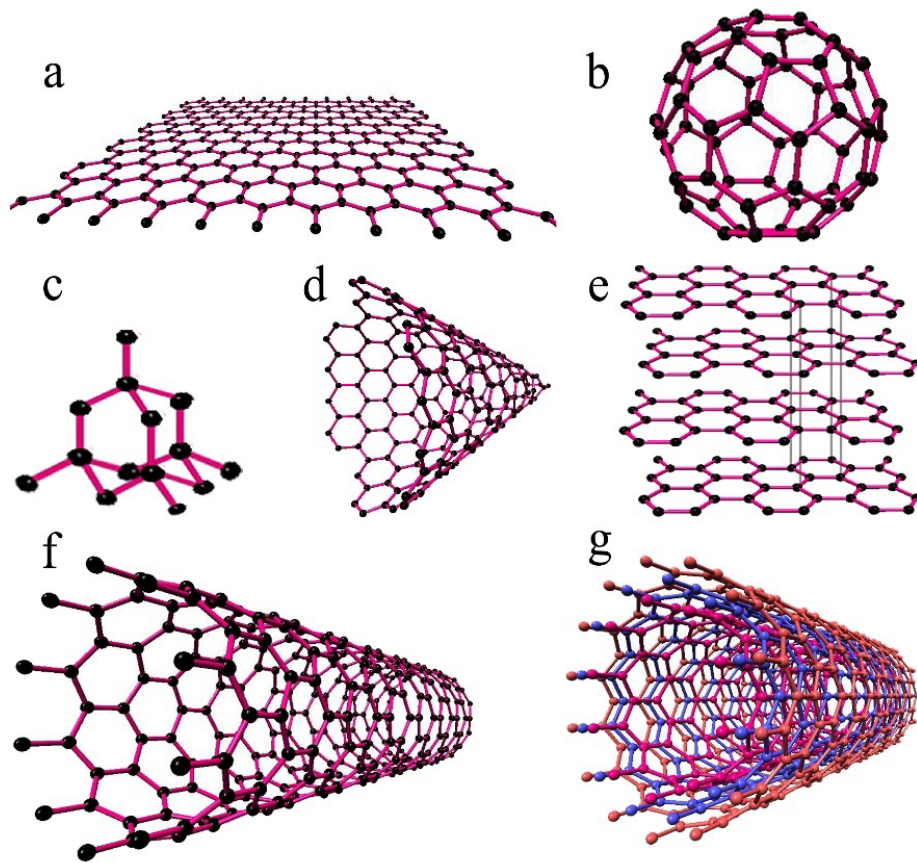


Figure 2.8: Some important carbonaceous structures, (a) graphene, (b) fullerene  $C_{60}$ , (c) diamond, (d) nanocone, (e) graphite, (f) single-wall carbon nanotube and (g) multiwall carbon nanotube [17].

Limited/low quantities of carbonaceous structures when added into the ceramic matrix, tend to disperse more uniformly, and hence develop good interfacial bonding within the ceramic matrix. It was found that carbonaceous structures like graphene and graphene oxide were very effective at enhancing mechanical properties of ceramics because of its two-dimensional structure, large contact area and inherent mechanical properties. Their surface features give rise to creative mechanical interlocking [130]. When a crack propagates in a composite made using carbonaceous reinforcement with a large elastic modulus (900-1000 GPa) and a significantly lower elastic modulus bio-ceramics matrix (40-50 GPa), the stress is effectively transferred from the ceramic matrix to the carbonaceous structures. At this point of crack propagation, there will be stretching and fracturing at their ultimate strain values in the carbonaceous structure, or when the stress exceeds the critical interface bond strength, carbonaceous structures will be pulled out from the matrix. However, in any of these circumstances, a substantial amount of the fracture energy will hence be consumed. Upon further spread of the crack, another mechanism known as crack bridging may appear, due to other carbonaceous structures present in the composite, as they may start to act like “elastic bridges” to hinder the further

spread of the crack [112, 131]. In addition, to the bridging effect, another phenomenon known as crack deflection may also come into play, in which the crack after interacting with the dispersed carbonaceous material, is deflected towards the ceramic/carbonaceous material interface instead of following its normal path. However, there is chance that the crack (crack tip) will become seized if the external energy is insufficient to debond the carbonaceous structure/matrix junction. This condition occurs like a shielding effect which improves fracture toughness by preventing additional fracturing of the matrix. All of the above-mentioned phenomena absorb most of the external energy, leaving behind very little energy for the additional spread of the crack hence, the spread of the crack becomes limited. In an actual composite body, the crack propagates in a step-like pattern by progressive deceleration (or even ceasing), hence resulting in improved fracture toughness. This results in a “strengthened material” that is capable of load-bearing applications. Consequently, introducing carbonaceous structure capable of forming a strong interfacial bond with the ceramic materials, as a secondary phase, can be very useful in hindering crack propagation.

For achieving optimum mechanical properties of ceramic and carbonaceous structure composites, optimisation of the quantity of carbonaceous material and its dispersion are the important requirements. The quantity of carbonaceous material is extremely important for strengthening of the ceramic matrix. Scientists, through optimisation studies, have found that when the content level approaches a certain threshold, the optimum mechanical properties are achieved, however beyond that threshold properties began to deteriorate[132]. This deterioration can be attributed to the undesirable agglomeration of carbonaceous material, when used in excessive quantities, mainly due to strong van der Waals forces,  $\pi$ - $\pi$  stacking, and the deficiency of functional sites in carbonaceous structures. Dispersion of carbonaceous structures in the ceramic matrix, is another challenge, as inhomogeneous dispersion may lead to defects and weak interface bonding eventually leading to a poor reinforcing effect. Good dispersion of carbonaceous structures in the ceramic powder have been achieved either by physical mixing or by colloidal processing. In a typical physical mixing process, carbonaceous structures were primarily ultrasonicated (suitable for disaggregation) and then mixed with the ceramic powder (in a solvent) aided by milling (usually ball milling), while in typical colloidal processing, opposite charges are induced on both the carbonaceous material and ceramic powder particles which helps carbonaceous structures to effectively disperse in the ceramic powder via electrostatic attraction (albeit ultrasonication and stirring are needed to complete the dispersion). Opposite charges are usually achieved by surface functionalisation via acidification and oxidation or by using surfactants[40, 110, 132].



The following section provides details about the use of different carbonaceous structures in reinforcing HAp based materials. The most successful carbonaceous structures are those having their dimensions in nanometre scale like graphene oxide.

### **2.1.3.1. Pyrolytic Carbon**

Pyrolytic carbon has a crystal structure that is loosely like that of graphite. It is highly fatigue resistant having elastic modulus values like that of bone. This material finds use in a wide variety of biomedical applications however, its preferred use is mostly for developing frictionless surfaces on implants by coating. The coating developed via pyrolytic carbon tend to resist blood clotting on its surface, which becomes important for implants that need to have some sort of relative motion with other implants/surfaces [133, 134]. Hetherington et. al. [135] plasma-sprayed HAp on pyrolytic carbon implants to investigate the bone response to HAp-coated pyrolytic carbon. They implanted cylindrical samples of pyrolytic carbon, HAp-coated pyrolytic carbon and HAp-coated titanium in the femurs of beagle dogs. After 8 weeks, samples were taken out and it was revealed that the pyrolytic carbon had almost nil attachment strength ( $\sim 1.59$  MPa) with the adjacent tissues, while the other two had similar interfacial strengths ( $\sim 8.71$  MPa). This study demonstrated that HAp facilitates a sturdy bond with the host tissue. In a different study, Lin and Jiarui [133] have used electrophoretic deposition (EPD) of HAp coating on pyrolytic carbon in glycol and ethanol separately (as the dispersion medium). However, this coating was chemically and biologically studied but not mechanically.

### **2.1.3.2. Carbon Fibres**

Carbon fibres (CF) are made up of thin crystalline filaments of carbon, having a regular hexagonal pattern of carbon sheets. They are typically produced via high-temperature conversions of carbon-rich (mostly polymeric) precursors during the pyrolysis. Carbon fibres are known for their high strength-to-weight ratio, high elasticity modulus, sorption, and thermomechanical properties, that why they have been widely used as a reinforcing material in polymer and ceramic matrices. Carbon fibres are also categorised as an important member of the family of biomaterials due to their inherent biocompatibility (both in vitro and in vivo). Carbon fibres have been used to treat bone fractures/wounds, an to make artificial heart valves [136].

Zakharova et. al. [137] developed composite powders using micrometre-sized carbon fibres (1.0, 2.0, and 5.0 wt. % CFs) and nanocrystalline hydroxyapatite via a co-

precipitation technique. The HAp-carbon fibre along with hydroxyapatite were co-precipitated from a solution of carbon fibres, calcium and orthophosphate ions ( $\text{Ca}(\text{OH})_2\text{-H}_3\text{PO}_4\text{-CF-H}_2\text{O}$ ). It was observed that increasing the amount of carbon fibres led to progressive decreases in HAp sizes (finer sized HAp particles), mainly because more carbon fibres meant more nucleation sites. Slosarczyk et. al. [138] used hot pressing to produce a HAp – carbon fibre composite at a temperature of 1100 °C and a pressure of 25 MPa in an argon atmosphere. The composite had enhanced fracture strength and toughness. Dorner-Reisel et. al. [139] also produced HAp-CF composite using hot pressing (using a pressure of 25 MPa, a temperature of 1000 to 1150 °C and pressing time of 15 min under an argon atmosphere) and compared its abrasion resistance (via ball crater test) with unaltered HAp. It was reported that 20 vol% addition of CF increased abrasion resistance, and most of the cracking develops at the interfaces of carbon fibres and the HAp matrix mainly due to the thermal mismatch. Boehm et. al. [140] tried surface functionalisation of carbon fibres, in an effort to improve their wettability (which helps in precipitation and also helps developing a strong adhesion with the matrix) by activating their surface. Aqua regia was used to modify fibres and then  $\text{CaCl}_2$  was used for calcium ion adhesion to the fibres, which provided nucleation sites for the precipitation of calcium phosphate crystals on the fibre surface.

### **2.1.3.3. Nano Carbonaceous Materials**

Carbon nanomaterials include several different types of materials having diverse appearances and properties. The list of nano carbonaceous materials available is growing with new materials being frequently discovered, however some of the most useful structures are carbon nanotubes, graphene, graphene oxide and buckyballs. Most of these nano carbonaceous materials find their uses in many advanced applications like in sensors and smart materials, because of their extraordinary electrical, mechanical, thermal, and magnetic properties as compared to their bulk form. Quantum effects and large surface-to-volume ratios are some of the reasons for the existence of such unique properties. Nanotubes and sheet like nano carbonaceous structures have been successfully utilised as a secondary phase material for composites, mainly due to their large specific surface areas [130]. Table 2.2 briefly compares few studies displaying enhancement of fracture toughness via nano carbonaceous structures in HAp composites .

#### **2.1.3.3.1. Carbon Nanotubes**

Carbon nanotubes (CNTs) can be visualised as a tubular structure made by rolling single/multi-layer graphite sheets (or a single graphene layer). CNTs, were accidentally

discovered in 1991 by the Japanese physicist, Iijima, and since then, have ignited intense research mainly because of their distinctive structural and physicochemical properties. They are characterised as materials having a high aspect ratio (mainly because their diameters are in nanoscale and their lengths are, by contrast, at the micron-scale), high tensile strength, high resilience, and large specific surface areas ( $50\text{--}1315\text{ m}^2\text{g}^{-1}$ ). The strength to weight ratio of CNTs is extraordinary, for example, their strength is 100 times that of steel while its density is just a fraction of that of steel. The presence of stable chemical bonds CAC (carbon atomic chain) covalent bond that exists in the carbon rings are considered to be the reason for all such extraordinary mechanical properties[141]. CNTs can be categorised into two major types based on their physical structure, i.e., single-walled carbon nanotube (SWCNT or SWNT) which is made up of a single sheet of carbon (which is generally called graphene) rolled into a tubular structure (single tube) or multi-walled carbon nanotubes (MWCNT or MWNT) which is made up of multiple sheets of carbon (it is more appropriate to call it graphite) rolled into a tubular structure [142-145]. In terms of their biomedical applications, their unique property to act as carriers for bone morphogenetic proteins, along with such high mechanical properties, make them stand out as an ideal candidate for reinforcing hydroxyapatite. So far numerous scientific studies on CNT-based biocomposites have been performed to ascertain strengthening, toughening, cell growth and enzyme activity[142, 144].

Chen et al. [146] report the deposition of a strong bio-composite coating on titanium (Ti-6Al-4V) substrate made using a sophisticated technique known as “laser surface alloying”. This coating was based on CNT reinforced hydroxyapatite, where CNT percentages varied from 0 to 20%. A significant increase of hardness was noted, and at an addition of approx. 7 vol% CNTs fracture toughness enhanced by 50% and flexural strength up by 28%. In a separate study, Lahiri et al. [147] developed CNT-HAp composites using spark plasma sintering and reported an enhancement of 92% in fracture toughness and 25% enhancement in elastic modulus values by just addition of 4 wt.% CNTs. Similarly, in another study, 3% CNT addition in hydroxyapatite-nanorods/CNTs composite increased the fracture toughness and flexural strength by 260% and 50% respectively, however the composite was made using vacuum hot-pressing[148]. Meng et al. [149] used needle like nano-sized HAp particles to develop HAp-CNT composite via hot pressing, where CNTs were initially functionalised to introduce -COOH groups onto its surface, for better interaction with HAp. Addition of 7 vol% CNTs, increases the fracture toughness by approx. 50% and flexural strength by 28%. Similarly, Sarkar et al. [150] made composites using modified CNT and HAp nanopowders via spark plasma-sintering. 2.5 vol% of CNTs and sintering at 1100 °C produced the maximum fracture

toughness of  $1.27 \text{ MPa}\cdot\text{m}^{1/2}$ . In another study, Balani et al. [151] performed plasma spraying of composite powder comprising 4% CNTs onto a titanium (Ti-6Al-4V) substrate which resulted in a coating demonstrating a ca. 56% improvement in fracture toughness.

### **2.1.3.3.2. Graphene**

Graphene, a leading material in the category of nano carbonaceous materials and the basic building block of all graphitic materials is comprised of a single layer of  $\text{sp}^2$ -hybridized carbon atoms assembled into a honeycomb lattice-like arrangement. Graphene has a strong successful research history in developing biocomposites because of its two-dimensional structure, large contact area and inherent mechanical properties like its tensile strength of ca. 130 GPa and a Young's modulus of ca. 0.5–1 TPa [152, 153]. It has been observed that even a low concentration level of graphene (reinforcing graphene also called graphene nanosheets (GNS)) can promote a toughening effect in a HAp matrix. GNS normally displays similar mechanical & biological properties like single layer graphene and are normally made up of a few graphene layers having thicknesses around 8-10 nm. Two further materials can be derived from graphene having unique properties i.e., graphene oxide (GO) and reduced graphene oxide (RGO). Many biomaterial scientists have used graphene to develop HAp based composites mainly for orthopaedic applications[154].

Liu et al. [155] synthesised graphene/hydroxyapatite composite powder via precipitation where rod-like HAp nanoparticles were grown on a graphene surface. The spark plasma sintering of composite displayed a 203% increase in the fracture toughness with just 1.0 wt.% graphene. In contrast, Zhang et al. [156] reported a 80% increase in the fracture toughness with the addition of 1 wt.% GNS in HAp based composite made via spark plasma sintering.

### **2.1.3.3.3. Graphene Oxide**

Graphene oxide (GO) can be regarded as an oxygenated counterpart of graphene, as oxygen-based functional groups like hydroxyls cover the planes of graphene sheets, while carboxyl & carboxyl groups cover its edges. Apart from exceptional biostability, biocompatibility and mechanical properties, some of the additional advantages of these materials are their antibacterial properties, ease of chemical functionalisation which favours its dispersion behaviour and interfacial bonding which also favours better load transfer in composites [157-159]. Historically, Schafhaeutl [160] first reported GO in 1840, and then Brodie [161] in 1859 but the controlled synthesis process of GO was

proposed in 1958 by Hummers and Offeman [162]. There is also a modified Hummers method which is more environmentally friendly, but the main synthesis strategy is the same. Scientists carry out reduction of GO in order to achieve graphene but due to limited reduction “reduced graphene oxide” (RGO) is usually formed rather than graphene. Figure 2.9. illustrates how GO and RGO that can be obtained from graphite.

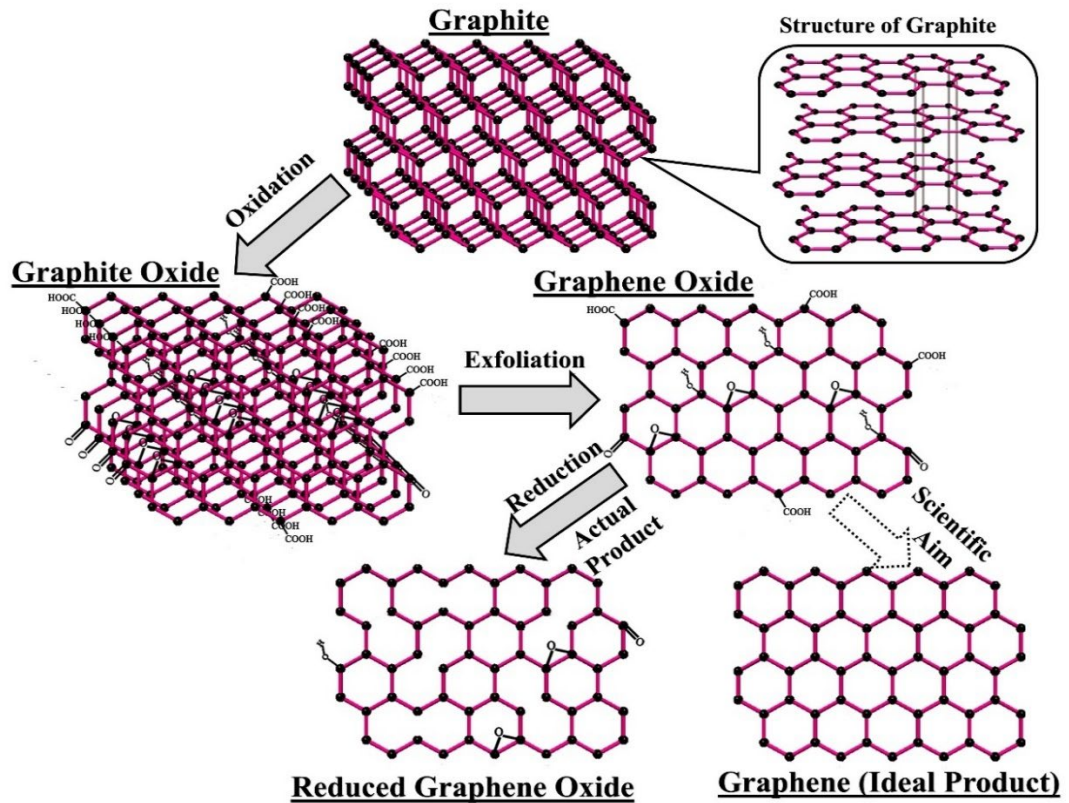


Figure 2.9: Scheme for making graphene oxide and reduced graphene oxide from graphite [17]

Li et al. [163] developed a GO-HAp composite using in situ mineralisation of HAp on GO (made using Hummers method). The composite revealed higher modulus values around 13.6 GPa, which were analogous to those measured for human femur bone (13–15 GPa), and tibia bone (13–16 GPa). Fathyunes and Khalil-Allafi [164] developed GO-HAp coatings on titanium substrates via ultrasound-assisted pulse electrodeposition. Ultrasonication was used for better dispersion of GO. The coating displayed higher hardness (3.08 GPa) and modulus values (41.26 GPa) along with enhanced corrosion resistance. Similarly Li et al. [165] reported superior corrosion resistance and in vitro biocompatibility, along with enhanced coating adhesion properties of HAp-GO coatings developed using electrophoretic deposition. In this research, HAp composites were made with two types of char fibres, where one of the char fibres has rolled graphene oxide (nano scrolls) attached to its surface.

#### 2.1.3.3.4. Reduced Graphene Oxide

Reduced Graphene Oxide is one of the attractive derivatives of GO, which after undergoing (partial) reduction (by removing some of the oxygen-containing groups). RGO is regarded as a type of graphene, and is also known as “functionalized graphene”, “reduced graphene”, or “chemically modified/converted graphene”. This reduction process is usually carried out via chemical, thermal or electrochemical principles, and the aim of this process is to develop pristine graphene, however, this always results in residual defects and functional groups, severely altering the structure of the carbon plane. RGOs having a natural honeycomb crystal lattice, reportedly have unique properties like high surface, electrical & thermal conductivity, biocompatibility, and chemical stability[159, 166].

Liu et al. [155] reported HAp (nanorods)-RGO composite made using spark plasma sintering. It has a maximum fracture toughness value of 3.94 MPa m<sup>1/2</sup>; which is much higher than HAp alone. They reported crack tip shielding, crack deflection and bridging phenomenon positively contributing to superior mechanical properties. Baradaran et al. [167] also developed HAp (nanotubes)-RGO composites which were pelletised using hot isostatic pressing at 160 MPa and 1150 °C. They found promotion of osteoblast and proliferation, along with increased fracture toughness (40%) and elastic modulus (86%). Similarly, Elif et. al. [168] found a 3.2 times increment in compressive strength of HAp-RGO composite with just 1% of RGO and also increased biocompatibility.

Table 2.2: Comparison of fracture toughness of HAp composite with the addition of nano carbonaceous structures.

Materials	Sintering Method	Increase in Fracture toughness
HAp nanorods-3% CNT [145]	vacuum hot-pressing	260%
HAp-1% graphene [155]	spark plasma sintering	203%
HAp-4 wt.% CNTs[147]	spark plasma sintering	92%
HAp-1% GNS[156]	spark plasma sintering	80%
HAp-7 vol% CNTs[149]	hot pressing	50%
HAp nanotubes-1.5 wt.% [167]	hot isostatic pressing	40%

#### 2.1.3.3.5. Nanodiamonds

Nanosized diamond particles (Nanodiamond (ND)) are among some of less renowned forms of carbonaceous structures used for scientific studies. NDs are known for their high hardness, low friction coefficient, chemical stability and biocompatibility. Commercially, they are made by detonation of carbon-based explosives and usually have some impurity species like Fe, Cr and some functional groups like N–H, C–OH present

results in their multi-functionality. Biologically, they have been trialled with HAp to develop composites and also for some drug delivery applications. Nanodiamonds have also been used to produce mechanically strong HAp based coatings for load-bearing biomedical applications. The addition of nanodiamonds in HAp based coatings may also increase coating adhesion and prevent metal ion release from metal surfaces. Nanodiamonds have also been explored for their application in drug delivery applications [169-171]. Chen et. al. [172] developed and deposited HAp – nanodiamond (0.5% and 2%) based coating on a titanium substrate via spark plasma sintering. The coating had a uniform structure, low porosity and enhanced mechanical properties. Similarly, Pecheva et. al. [173] added ND particles into SBF solution to develop and deposit a composite coating on a titanium substrate via an electrodeposition method. The coating had a homogenous structure, no residual stresses and demonstrated high hardness and ductility values. Li et. al. [174] used a novel approach to initially biofunctionalize NDs and then made a composite with HAp.

#### **2.1.3.3.6. Fullerenes**

Fullerenes were discovered in 1986 and are widely used in biomedical applications mostly for drug delivery systems. They have a carbon cage structure in the form of hollow sphere (or can be ellipsoidal in nature) [175]. Fullerenes that are highly symmetrical spherical are known as Buckyballs or  $C_{60}$  [176]. They have superior hydrophobicity and biological properties, however its insolubility and tendency toward aggregation are the issues limiting their use [177]. To tackle such issues, chemical modification converting fullerene into fulleranol (a polyhydroxylated structure  $C_{60}(OH)_x$ ) is mostly preferred, which is done by adding hydroxyl groups to the fullerene. Djordjevic et. al. [178] reported the development of HAp-fullerenol nanocomposites via sonochemical processing, however no mechanical properties were reported for this.

#### **2.1.3.3.7. Carbon Nanofibres**

Carbon nanofibres (CNFs) are made up of linear  $sp^2$  hybridised carbon-based short fibres, having high aspect ratio. They are favoured for biomedical applications because of their superior mechanical properties and non-toxicity. Satoshi et. al. [179] developed HAp-CNF composite via hot-pressing. It was found that the addition of 10 vol.% CNFs displayed bending strengths (i.e., 90 MPa), close to that of cortical bone and an increase of fracture toughness of approx. 1.6 times. Wu et. al. [180] reported an increase of fracture strength of 41% CNF reinforced composites which was around 67.3 MPa.

### **2.1.3.3.8. Other systems involving Carbon Structures and Hydroxyapatite**

Researchers in the past have also trialled adding additional components into the HAp-carbonaceous structure composite to achieve further improved properties. Moreover, addition of trace metallic ions in the composite was also trialled on a regular basis to improve mainly biological properties mostly because the HAp structure is labile to these ions. Scientists have used ions like  $\text{Sr}^{2+}$ ,  $\text{Mg}^{2+}$ ,  $\text{Mn}^{2+}$ ,  $\text{Ag}^+$ ,  $\text{Zn}^{2+}$ , and  $\text{Y}^{3+}$ , which all have different advantages. For instance,  $\text{Mn}^{2+}$  was found to impact the osteoblast differentiation and bone resorption properties, while  $\text{Zn}^{2+}$  was found to inspire new bone formation, inhibit osteoclastic proliferation, and bone resorption [181-183]. Some of the examples of such systems are: Herkendell et. al. [184] who added 10wt% silver nanoparticles into a HAp-CNT composite to increase fracture toughness values up to 244% along with imparting on it good antibacterial properties together with high interfacial strength. Chen et. al. [185] added chitosan (0 to 5%) into the CNT-HAp nanocomposite. The composites reportedly have good biocompatibility and superior mechanical properties (an increase of ca. 110 % in elastic modulus and 210% in compressive strength). Khanal et. al. [132] used 1% nylon in the functionalized CNTS-HAp composite, to enhance fracture toughness up to 3.60 MPa.m<sup>1/2</sup>. It is worth mentioning that, both chitosan and nylon were used for their geometrical shape and size.

### **2.1.4. Carbon from renewable source: Char**

The term “biomass” refers to biologically produced matter containing any mixture of hydrocarbon-based material consisting of carbon, hydrogen, oxygen with minor contents of nitrogen and sulphur. Biomass comprises numerous natural and derived materials, such as woody species, wood wastes, bagasse & herbaceous species, agricultural remains, grass, and aquatic plants [186, 187]. Usually, biomass is converted into a more useful form to get maximum benefit from its existing natural hydrocarbons. Biomass conversion processes can be grouped into two types. The first type is the thermochemical conversion which involves processes like combustion, carbonization/pyrolysis, gasification, & liquefaction, while the second type is the biochemical conversion comprising digestion and fermentation. The resultant products of both groups of techniques are also different, as thermochemical processes yield liquid products (wood tar, tar, oil, pyrolytic oil), gas products (wood gas, pyrolytic gas) and solid products (char, charcoal), while biological conversion processes produce biogas, hydrogen, and ethanol, moreover the retting of natural fibres produces modified solid fibres. Most biomass is composed of three main groups of natural polymeric materials namely, cellulose (which is



supposed to be 50% on a dry basis), hemicellulose (generally approx. 10–30% in woods and 20–40% in herbaceous biomass on a dry basis) and lignin (usually approx. 20–40% in woods and 10–40% in herbaceous biomass on a dry basis). Apart from natural polymeric materials, other typical components found in biomass can be grouped as extractives (which are smaller organic molecules like protein and salts) and minerals (inorganic compounds like potassium, calcium, sodium, silicon). The relevant amounts of these inorganic compounds depend on the type of feedstock. For example, it can be less than 1% in wood to 15% in herbaceous biomass [186, 188].

Char (commonly known as biochar), which is one of the most useful converted products of biomass, is generated by pyrolysis of biomass under anoxic or hypoxic conditions (i.e., low oxygen environments) and it usually results in more than 50% carbon (C) (typically 70%–80%). It can be simply described as a carbon-rich, solid product of thermally stabilised biomass/organic matter. In addition to carbon, biochar is composed of oxygen, nitrogen, and other elements; biochar can be preserved for hundreds of years [28]. Some of the most remarkable properties of biochar are its resistance to degradation, high surface area and considerable negative charge. The negative charge of biochars mainly originated from their oxygen-containing functional groups like carboxylic and phenolic groups [189]. The deprotonation of functional groups causes the negative charge on biochar surfaces to increase. Biochar, itself, can be chemically, physically, or biologically modified using different approaches. The objective of modification is to either, (i) increase the surface area of the biochar, (ii) modify or enhance the surface properties of the biochar, or (iii) use the surface as a platform to embed another material with beneficial surface properties [190].

#### **2.1.4.1. Properties of Biochar**

Most of the properties, especially the elemental composition and spatial structure of biochar can be directly related to that of the raw materials and reaction conditions. As a general rule, the higher the biochar porosity, the larger the specific surface area [191].

##### **2.1.4.1.1. Biochar microstructure**

One of the most useful features of biochar is its microporous structure, which plays an important role in enhancing the specific surface area. Large pores can promote adsorption capability and provide space for nucleation and growth of other desired materials on it. Small pores can improve the adsorption capacity of biochar [186, 192].

#### **2.1.4.1.2. Elemental content**

As a converted form of organic matter, biochar mainly contains carbon, hydrogen, oxygen, nitrogen, sulphur, and other trace elements. The carbon content of wood biochar can be as high, up to 55-70%. For all types of biochar, the nitrogen content is usually less than 3 wt%, the hydrogen content is slightly above that of nitrogen, the oxygen content reaches a maximum value of 50 wt%, while the sulphur content is lower than 1 wt%. The remaining fraction is ash and contains Na, Mg, K, Ca and other mineral elements[191].

#### **2.1.4.1.3. Chemical properties of biochar**

##### **a) pH**

The pH change induced in water when biochar is immersed in it depends on the source material and its preparation conditions. Biochar always induces an alkaline pH change in water and the extent of this induced pH change is related to the ash content with a higher ash content resulting in a higher pH change in water [193].

##### **b) Cation exchange capacity (CEC)**

The pyrolysis of biomass and its exposure to the atmosphere results in oxygenation i.e., formation of oxygen containing functional groups like carboxyl, hydroxyl and carbonyl on biochar surfaces. Biochar CEC is primarily linked with its preparation temperature and also dependent upon these functional groups. In general, Biochar CEC varies with increasing pyrolysis temperatures, because higher pyrolysis temperatures lower the CEC values due to a decrease in the oxygenated (acid) functional groups and a lower oxygen:carbon ratio[194].

#### **2.1.4.1.4. Physical characteristics**

The large specific surface area comes about as a result of the high porosity of biochar. It is found that the specific surface area of biochar, (the total surface area and the volume of the micro-pores), is the main reason for its enhanced adsorption abilities. The pore structure, including the specific surface area and micropore volume of biochar, can be very different based on the type of biomass used for biochar preparation.

The transformation of biomass materials into carbon black has been documented for over 50 years. Baumann [195] in his publication, reported that biochar-based materials had been used for embalming and burial purposes in ancient Egyptian times. He emphasized the dominant role played by plant products in the preparation for burial of mummies similarly Sombroek [196] and Eden et al. [197] in their publications reported the use of biochar aka "*Terra Preta*" in different locations of Amazonian soils, which

according to many researchers were the main reason for such high cultivation occurring in these areas in past times. The earlier use of biochar or similar product has predominantly been for agricultural or archaeological purposes, moreover, little research has been carried out in seeking optimised methods to produce biochar.

It was Pondolfo et al. [198] in 1994, who made a targeted effort at producing activated carbon chars from different varieties of coconuts. Chars were prepared, using a tube furnace under a nitrogen environment, from dried coconut shell. The process was successful and was termed “slow pyrolysis”. Similarly, Gergova et. al. [199] (1996) had reported carbonization of apricot stones in nitrogen at 750~850°C for 2-4 hours to yield biochar, which was eventually converted into activated carbon (a modified charcoal having high adsorptive power due to heat treatment or any other type of treatment). Filiz Karaosmanoğlu et. al. [200] have also utilised a slow pyrolysis technique on the rapeseed plant, to investigate the effects of heating rate and temperature on the yields and characteristics of biochars. All of their experimental work was performed under an inert atmosphere of N<sub>2</sub> gas in a tube furnace. The biochars obtained were carbon-rich and reactive. This research work was considered a landmark in this field as after this publication, the effect of different parameters like time of holding at elevated temperature etc. on biomass became more clearly understood. Moreover, Purevsuren [201, 202] had performed groundbreaking research in the field of casein pyrolysis. His research was mainly focussed on the optimisation of the thermal processing of casein, to yield a porous biochar with suitable functional properties. Marris [203] published an eye-opening news feature “Black is the new green” in which she explained the importance of *Terra Preta* and biochar from an environmental/agricultural aspect and related it to the production of fuels. This “Nature” publication proved to be vital in motivating mostly agricultural-based countries to utilise more effectively their large stocks of waste biomasses. Özçimen [204] performed some carbonization experiments of grapeseed and chestnut shell samples to determine the effect of temperature, gas flow rate and heating rate on the biochar yield. He presented a statistical design to interpret experimental results. The temperature was found to have more influence on biochar yields than gas flow rate and heating rate. It was reported that Biochar yields were decreased with increasing temperature, heating and sweep gas flow rate, which can be attributed to gasification and oxidation reactions. Kim et. al. [57] have utilised cellulose-based natural fibre namely kenaf fibres, to manufacture carbon fibre using pyrolysis. The main objective of the study was to investigate the impacts of carbonization temperature and chemical pre-treatment (of biomass) on morphology and chemical structure of carbon fibre. It was found that notable weight losses and longitudinal shrinkage occurred during the conversion process, however, NaOH pre-treatment of kenaf

fibres was found to reduce the weight loss and shrinkage effects and increase the carbon content of the materials. It was also noted that the micrometre-sized cells fused and restructured with neighbouring cells, which was mainly due to densification/diffusion-based processes.

McDonald-Wharry et. al. [205] in recent research used three different oxygen-rich precursors, *pinus radiata* wood, *phormium tenax* leaf fibres, and sucrose crystals, to produce different chars. These biochars were primarily studied using Raman spectroscopy to observe the nanostructural development corresponding to charring temperature. The thermal reduction of a commercial graphene oxide (GO, a form of carbon, which is non-conductive and hydrophilic) was comparatively examined, as this is considered to develop graphene-like domains (nanometre-sized). As far as its structure is concerned, the aromatic lattice of carbon sheets is interrupted by functional groups like ketones and carboxylic groups. The interruption of the lattice is manifested by an increase in interlayer spacing [158]. It was found that increasing the charring temperature, led to significant changes in many parameters measured via the Raman spectra; most importantly it revealed that chars became precursor independent, when the charring temperatures exceeded 700 °C. The spectra of chars appeared to be same as those obtained from thermally reduced graphene oxides, especially when compared to a wide range of other carbonaceous materials analysed using this particular methodology. Qian et. al. [206] presented a very important and comprehensive review of the production and application of biochar. They provided an overview of advanced applications of biochar such as its use as a catalyst, in fuel cells, and for gas storage. Similarly, Cha et. al. [207] wrote a comprehensive review of the usability of biochar in sophisticated applications like hydrogen storage in which activated biochar is very useful, as it gives materials rich in micropores and a large specific surface area. Choi et al. [208] investigated the hydrogen storage capacity of watermelon flesh char which was produced using a hydrothermal reaction and later modified with KOH at different temperatures. Modified char exhibited high hydrogen storage capacity, apparently due to its large specific surface area and micropore volume. Similarly, Ramesh et al. [209] also reported an improved hydrogen storage capacity of biochar produced from tamarind seed using heat and microwave treatments and activated with KOH. It is also reported that the microwave treatment produced carbon with a larger pore fraction than thermal treatment. Oleszczuka et. al. [210] compared the physicochemical properties of macro and nanoparticles of biochars. The results of this comparative analysis indicate that the properties of biochar-NPs, like pH changes they induce in water upon immersion, cation exchange capacity, the content of elements, and aromaticity/polarity, differ from the properties of their macro-counterparts. The nano-biochars had a predictably larger

surface area and smaller pore sizes than the corresponding macro-biochars and were characterized by a more highly negative zeta potential and a greater diversity of crystalline forms than the macro-biochar. Moreover, the nano-biochar had significantly lower levels of C, H, and N compared to the macro biochars, which might be due to a lower degree of pyrolysis in the nano-biochar.

#### 2.1.4.2. Wood and Harakeke Plant Fibres

Wood is a natural biopolymeric composite composed of hemicellulose, cellulose and lignin. It displays a complex macro/micro/nanostructure with ordered cellular honeycomb-like channels, which resembles the structure of cancellous bone[211, 212]. The basic wood cell types are called tracheid, vessel members, fibres, and parenchyma (packing matter). The main function of tracheid is to transport water and inorganic salts, while fibres are there to provide strength. Tracheid are shorter than fibres[213]. One study reported the successful use of heat-treated birch wood directly as an implant for osteochondral bone defects in a rabbit [214]. Many different types of wood (or wood-derived materials) due to their open trabecular structure, have been used as templates for making porous ceramics providing flexibility for the manufacture of complex shapes, biological properties, and inherent 3D interconnected porous structure.

Harakeke (*Phormium tenax*, New Zealand flax) is a unique and ancient plant species, which is monocotyledonous. This plant usually has long stiff/erect leaves, which can grow up to 3 metres. When exploring the anatomy of the leaf, the aggregates of fibres, referred to as muka (from the Māori language), can be found lying along the leaf, which are extractable sclerenchyma fibres (individual elongated hollow cells). This plant was very popular with European traders due to the extraordinary strength of its muka. They called it ‘flax’ because its fibres were like that of true flax found in other parts of the world. Clothing, mats, plates, baskets, ropes, fishing lines and nets were all made from the flax leaves by Māori. [215, 216]. Like every lignocellulosic fibres, harakeke fibres also consist of three main components: cellulose, lignin, and water. A typical chemical composition of harakeke is presented in Table 2.3. The cellulose and lignin are usually tightly bound together, while the water is adsorbed on the cellulose/lignin structure.

Table 2.3: Chemical composition of harakeke fibre as reported in literature [217]

Composition	Percentage
Cellulose	45.1
Hemicelluloses	30.1

Pectin	0.7
Lignin	11.2
Water soluble components	2.2
Fat and wax	0.7
Moisture	10

Harakeke fibre like other lignocellulosic fibres have multi layered cell wall structures which can be categorised into three major layers, middle lamella (the most outer layer, composed of “pectins” (heterogeneous polysaccharides), which helps in cell binding/adhesion), primary cell wall (composed of polysaccharides cellulose, hemicellulose, and pectin), and secondary cell walls (composed of cellulose and hemicellulose, however sometimes they also contain lignin, which is a complex polymer of aromatic aldehydes). Lumen in fibre is a narrow central channel formed when a plant cell dies at the end of biosynthesis [218, 219]. A typical cell wall structure in natural fibre is presented in figure 2.10. Harakeke fibres are generally regarded as highly porous, due to a large lumen and are hydrophilic in nature. Their surface chemistry is determined by the presence of reactive hydroxyl groups –OH which mainly emanate from cellulose. Carboxyl groups –COOH are also found at the surface due to pectins, hemicelluloses and fatty acids, however their contribution to the surface chemistry is still unknown[220, 221]. Moreover, Harakeke fibres can also potentially have small amounts of aldehydes –CHO and esters –COOR due to lipophilic components (aldehydes, sterol esters and ester waxes), however this has not been confirmed in studies to date.

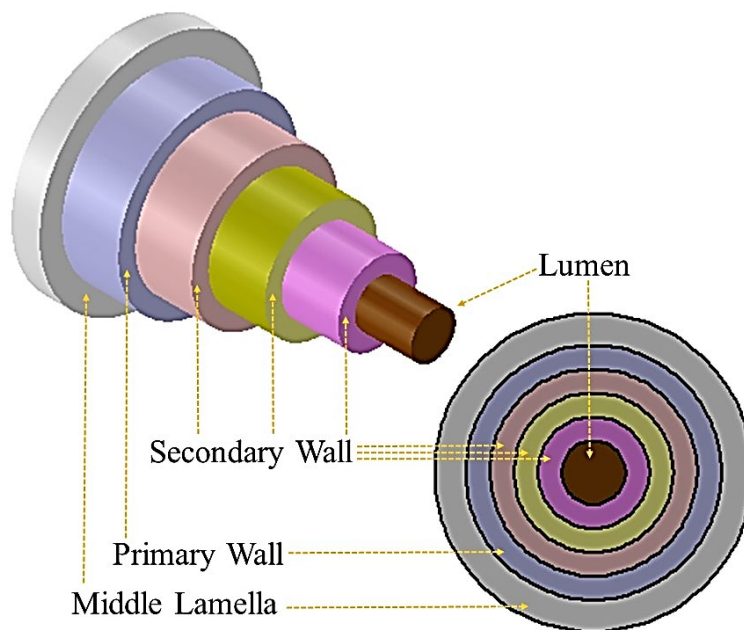


Figure 2.10: Cell wall structure of harakeke fibre [222].

### 2.1.4.3. Cabbage Tree Fibres

*Cordyline australis*, also known as Cabbage tree, is one of New Zealand's native and most distinctive trees found in a variety of habitats. This tree usually carries bushy heads of large, long leaves (sword-like) which are narrow leaves and can be up to a metre long. In late spring and summer, the tree develops large panicles of small, white, fragrant flowers which emerge from the centre of the heads. *Cordyline australis* in its maximum developed form, can reach up to 40 ft in height and is widely cultivated in New Zealand, with this especially being so after 1987, when a "sudden decline" was noted in the population of this plant due to mystery disease. It was found that the disease was due to a parasitic organism called a phytoplasma. This plant is also very popular in Europe, Britain, and the U.S.[223].

Cabbage trees have a very strong root system which can tolerate wet soil, so they are effective in the prevention of soil erosion and land sliding on steep slopes. Early European settlers used to make chimneys for their huts out of *cordyline australis* trunks due to their impressive fire-resistance. *Cordyline australis* has four different species. Traditionally, Māori used to harvest nutritious food from the root of the young *cordyline australis* trees. They also used this tree for developing medicines, harvesting strong fibres and for making baskets, rope, and rain capes from its leaves[223, 224].

A tough and durable fibre can be extracted from the leaves of *cordyline australis*. The fibre was valued for its strength and durability. The fibres were traditionally used to make anchor ropes and fishing lines, which were very strong. This is the reason, Simpson [224] in his book compared the strength of this fibre with that of harakeke flax. A top view of *cordyline australis* leaf is shown in Figure 2.11.



Figure 2.11: Top view of cabbage tree leaf

In common with other plant species, harakeke and *cordyline australis* leaves consist of three main components: cellulose, lignin, and water. The cellulose and lignin are usually tightly bound together, while the water is adsorbed to the cellulose/lignin structure. This adsorbed water must be driven off as vapour before carbonization can take place. To do

this, sun drying is usually preferred, however, forced oven drying also yields good results. During the carbonization/pyrolysis at elevated temperatures, the leaf begins to spontaneously break down to produce charcoal plus water vapour (which, overall, is an exothermic reaction liberating energy), and some complex chemicals, chiefly in the form of tars and a non-condensable gas consisting mainly of hydrogen, carbon monoxide and carbon dioxide. This process of carbonization continues until only the carbonised residue called “charcoal” remains. There is also experimental evidence that the lignin content is directly associated with the charcoal yield. A high lignin content gives a correspondingly high yield of charcoal.

### **2.1.5. Conclusion**

In short, HAp is an exceptional bioactive material, which can be effectively harvested from waste animal waste. HAp, alone, lacks mechanical characteristics that make it suitable for use in implants for load bearing applications. Scientists have for a long time tried to develop composites based on HAp having suitable mechanical properties without compromising its biomedical properties. One way of making such composites is by using a reinforcing material like a carbonaceous structure that will have suitable mechanical and biomedical properties. Various carbonaceous structures have been successfully used to develop HAp based composites having enhanced mechanical properties, however carbonaceous structure derived from natural sources like plant fibres have never been trialled for use as a reinforcement in an HAp matrix. The carbon from natural plants usually known as char, is mostly amorphous, however as per previous molecular vibrational studies, they also have segregated crystalline, graphitic zones, which can prove beneficial in terms of reinforcement material. In this study, it is aimed to trial char derived from natural plant fibres of harakeke leaf and cabbage tree leaf, to reinforce HAp. Natural fibres of both harakeke and cabbage tree leaf have been previously utilised for their strength and toughness, so in this study it was researched to see, if the same strength can be translated into their carbon form. During pyrolysis, shrinking and volatilization of biomass occurs, which leads to the development of some of the characteristic features of biochar.



# CHAPTER THREE : REPRECIPITATION OF HYDROXYAPATITE FROM BOVINE BONE

---

## 3.1. Introduction

Currently, research in the field of “Biomaterials” has had a strong impact on clinical medicine. In general, biomaterials are defined as those materials that are made to interact with the biological system for the purpose of repairing or renewing the damaged or lost tissue/organ. Events such as traffic accidents, orthopaedic disorders, illness etc. make the usage of these materials inevitable for applications like, medical implants (stents, artificial joints, dental implants), healing promoters (sutures), biosensors (blood glucose monitoring) and drug-delivery systems (cancer targeting systems). The research in biomaterials is by necessity “multidisciplinary”, which involves development across several disciplinary fields for the purpose of generating improved synthetic (metals, polymers, ceramics & composites) and biological materials (proteins, cells and tissues).

Bioceramics falls under the category of advanced ceramics which are defined as ceramic components used in medical applications which are mostly in the form of implants. They are well-known for their exceptional biocompatibility with the biological systems they are implanted in. Ceramics and cements based on calcium phosphate (hydroxyapatite, tricalcium phosphate etc.) and silica-based glasses (bioglasses) are well known bioceramics used in orthopaedic and dental applications. For researchers, hydroxyapatite  $[\text{Ca}_{10}(\text{PO}_4)_6(\text{OH})_2]$  has become a natural choice for bone related applications mainly due to its matching chemical composition with the bone, exceptional biocompatibility and osteoconductivity. Similarly, HAp is commonly coated on dental implants so as to enhance osseointegration with the surface of these implants during the healing process. However, HAp is not suitable for load bearing application owing to its poor mechanical properties and brittle nature.

There are numerous methods of synthesising HAp such as from natural sources, hydrothermal, sol-gel reactions etc. however wet chemical precipitation is a preferred method due to its low cost and simplicity. The emergence of a separable solid from a chemical solution is commonly known as a chemical precipitation process, which usually occurs via a sequence of nucleation, aggregation, agglomeration, and growth mechanisms from a supersaturated solution containing calcium and phosphate ions. This supersaturated

solution is usually made using various calcium and phosphate salts. It has been found from many previous studies that the various process parameters, like reaction temperature, reactant addition rate, heat treatment conditions, heavily influence particle shape, particle size, stoichiometry[225-229]. Similarly, re-precipitation of HAp from a digest solution made using acid dissolution of precipitated CaP initially harvested from waste animal bone is an attractive concept in this age of needing to make processes sustainable and economically viable. However, this type of reprecipitation can be different from that of a chemical-based precipitation mainly because of the presence of elements other than calcium and phosphate which may affect reprecipitation, morphology and quality of the HAp generated. For instance, biogenically sourced HAp commonly contains Mg which can influence reprecipitation of HAp[230-232].

In this study, biogenically sourced CaP was used to generate a solution containing calcium and phosphate ions and was also expected to contain extra components like Mg ions for instance. Hence, different processing parameters i.e., incremental reaction temperature (20 °C, 40 °C, 60 °C and 80 °C), rapid alkali addition rate and heat-treatment temperature (800 °C and 1000 °C) were selected to assess the quality and morphology of reprecipitated HAp. This was done to produce a range of morphologies for HAp out of which the most suitable one was selected as the HAp matrix of the HAp-carbon composites which constituted the main aim of the study.

## **3.2. Materials and Methods**

### **3.2.1. Materials**

All chemicals and solvents used in the experimental work were employed as received without further purification. Nitric acid (HNO<sub>3</sub>) (65%, Merck Germany) and sodium hydroxide (NaOH) (Sigma Aldrich) were used as the chemicals to carry out the digestions and in reprecipitation processes respectively. Ultra-pure water (Type 1) was used for all experimental and cleaning purposes. Raw sectioned bovine femur bones (in frozen condition, breed unknown) were used as a source of calcium and phosphate ions and were procured from a supermarket butchery in New Zealand. The pre-sectioned frozen bones were defrosted in water at room temperature for 24 hours before defatting was carried out.

### **3.2.2. Precipitation of HAp to make digest solution**

The process involved initial precipitation of HAp from raw cow bone, its digestion using nitric acid solution and then the reprecipitation of HAp. The idea of digestion of cow bone in nitric acid is to prepare a precursor solution containing Ca<sup>2+</sup> and PO<sub>4</sub><sup>3-</sup> ions, out of

which HAp can be re-precipitated for the matrix of the composite. This digest solution was produced from bovine femur bone, which was pre-processed to remove most of the unwanted, extraneous organic matter. The cleaning (defatting) process involved boiling of the raw bones (as shown in Figure 3.1) in a large beaker for 8 hours with a change of water after every 2 hours followed by drying at 105 °C for 12 hours in an oven. The cleaning (defatting) process parameters were taken from previous studies[26, 97]. Defatted and dried bones were subjected subsequently to heat treatment at 1000 °C for 4 hours. This temperature (1000 °C) was chosen after performing a thermogravimetric analysis of the defatted bone to gauge composition changes with temperature (Appendix C). The heat treatment was designed in a way to ensure that removal of all organic matter, namely collagenous protein and carbonate, occurs and that the resultant hydroxyapatite is achieved in a crystalline state. The bone obtained after such a heat treatment was white in colour and fragile in nature. These bones are referred to as “sintered cow bone(s)” in further descriptions.



Figure 3.1: Raw sectioned bovine bone pieces.

### 3.2.3. Digestion and Re-precipitation of HAp

The sintered cow bones were crushed/powdered, DI water-washed and dried to obtain a powder which was subsequently digested in dilute (20%) nitric acid to achieve a transparent solution of  $\text{Ca}^{2+}$  and  $\text{PO}_4^{3-}$  ions. The powder weight (g) to solution (mL) ratio was 1:5. The digest solution is referred to as “bone digest solution” and was filtered before use. A 5-neck glass flat bottom reactor vessel was used for the reprecipitation of the HAp. A mechanically controlled stirrer bar was used through the central neck of the flask, however during re-precipitation, magnetic stirring (using a magnetic bar) was also employed as this combination of dual stirring helped in homogenising the thick/gel like consistency of the solution. A thermometer and pH probe were used in the side necks of the precipitation vessel, while NaOH addition was carried out from the fourth neck (using a dropping funnel). A combination of a hot plate and a water bath was used to achieve the

required temperatures. The filtered digest solution was introduced into the reaction vessel and was stirred (mechanical stirrer, 240 rpm) at the required reaction temperature (20 °C, 40 °C, 60 °C and 80 °C) for two hours. Fast addition (approx. 10 mL sec<sup>-1</sup>) of saturated NaOH solution (approx. 15 mol L<sup>-1</sup>) was carried out in the digest solution to form HAp. The purpose of using a fast addition rate is to increase nucleation rate relative to growth rate, which may assist in forming nanosized HAp[233, 234]. Nanosized HAp due to its expectedly higher surface area, will have higher reactivity which can form a mechanically sound matrix for the composite. The addition of NaOH was continued until pH 10.5 was reached. After the pH and temperature had stabilised, the mixture had its stirring maintained at the reaction temperature of interest for two hours after which the resulting precipitates were aged for 24 hours at room temperature and without stirring. This step also allowed the settling of the particles with the supernatant being decanted off the sedimented precipitates on completion. Fresh DI water was then added to the white precipitates to wash them, and decantation carried out until nitrate could no longer be detected in the washings. The brown ring test was used to check for nitrate presence[26]. The hydroxyapatite precipitates were subsequently vacuum filtered using glass fibre filter paper and oven dried at 105 °C after which they were manually ground to a fine powder. The dried re-precipitated powder was further calcined at different temperatures (800 °C and 1000 °C) and the obtained powders were finally DI washed and dried for characterisation. A pictorial representation of the process steps is given in Figure 3.2. HAp powders were then subjected to chemical, thermogravimetric and microscopic characterisation.

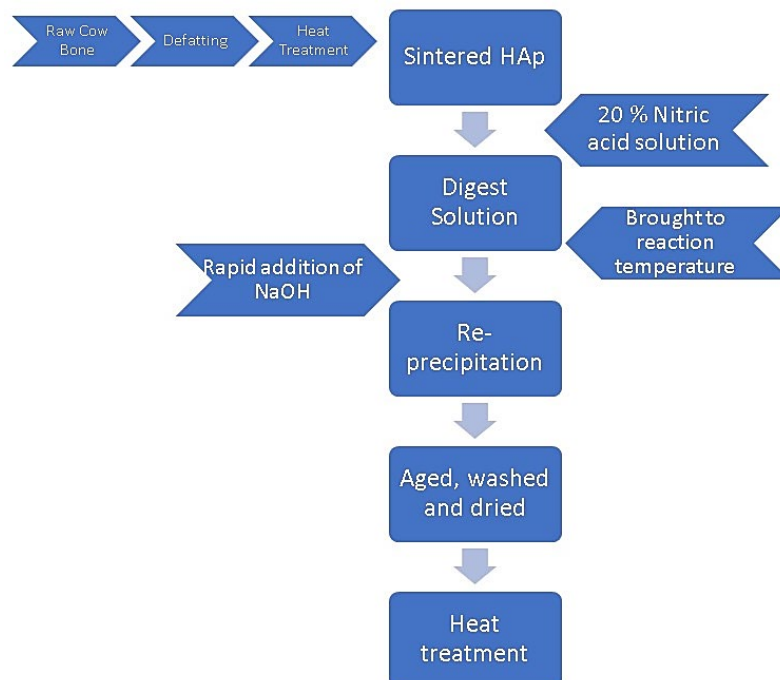


Figure 3.2: A pictorial representation of processing steps, which summarises production of reprecipitated HAp from bovine bone at different reaction temperatures.

### 3.2.4. Characterisation

The phase composition of all calcium phosphate materials was determined by X-ray diffractometry (Panalytical Empyrean Series 2 diffractometer) with Cu K $\alpha$  radiation at 45 kV & 40 mA ( $\lambda = 1.5406 \text{ \AA}$ ) and step size of  $0.0260^\circ$ . A Fourier transform infrared (FTIR) spectrometer (Spectrum 100A, Perkin Elmer) was utilised for recording IR spectra via the KBr disc method (recorded between  $4000 - 450 \text{ cm}^{-1}$ ) (5 samples, with 5 scans per sample). A spectral resolution of  $4 \text{ cm}^{-1}$  was used. Raman spectra of all calcium phosphate materials were recorded with a Raman station 400F (PerkinElmer) spectrometer with a spectral resolution of  $1 \text{ cm}^{-1}$  (using a 785 nm near-infrared laser) (5 samples, with 3 scans per sample). The morphological characteristics of the samples were observed using a scanning electron microscope (SEM) (S-4700, Hitachi) instrument. Thermogravimetric analysis (TGA) (STA 8000, Perkin Elmer) was also carried out to study the loss of weight associated with the different heating events. Heat profiles were recorded from  $35^\circ\text{C}$  to  $1250^\circ\text{C}$  for heating and  $1250^\circ\text{C}$  to  $90^\circ\text{C}$  for cooling, where a cooling profile was used to investigate chemisorption of water by the dehydrated material.

Table 3.1: Sample coding and their brief descriptions.

S. No.	Sample	Description	Code	
1	Raw Cow bone	Defatted cow bone	R <sub>DCB</sub>	
2	Sintered cow bone	R <sub>DCB</sub> sintered at $1000^\circ\text{C}$ and powdered	H <sub>P</sub>	
3	Re-precipitated HAp	Reaction temperature	20 $^\circ\text{C}$	H <sub>20</sub>
			40 $^\circ\text{C}$	H <sub>40</sub>
			60 $^\circ\text{C}$	H <sub>60</sub>
			80 $^\circ\text{C}$	H <sub>80</sub>
4	Re-precipitated HAp	800 $^\circ\text{C}$ calcination	H <sub>20</sub>	H <sub>20-800</sub>
			H <sub>40</sub>	H <sub>40-800</sub>
			H <sub>60</sub>	H <sub>60-800</sub>
			H <sub>80</sub>	H <sub>80-800</sub>
5	Re-precipitated HAp	1000 $^\circ\text{C}$ calcination	H <sub>20</sub>	H <sub>20-1000</sub>
			H <sub>40</sub>	H <sub>40-1000</sub>
			H <sub>60</sub>	H <sub>60-1000</sub>
			H <sub>80</sub>	H <sub>80-1000</sub>

## 3.3. Results & Discussion

### 3.3.1. Fourier transform infrared spectroscopy (FTIR) Analysis

In this research, initially the chemical structure of the defatted cow bone (R<sub>DCB</sub>) and sintered cow bone (H<sub>P</sub>) was evaluated to make sure complete deproteinisation and precipitation of HAp from cow bone had taken place, as incomplete deprotenisation may lead to unwanted orange-yellow colouration from xanthoproteic-associated reactions during nitric acid digestion[26]. The FTIR spectra of both samples are represented in Figure 3.3 (a) and (b). FTIR spectra representing R<sub>DCB</sub> displayed important information about the

cowbone after defatting. A broad band at 3250-3700  $\text{cm}^{-1}$  was assigned to adsorbed  $\text{H}_2\text{O}$  molecules which indicate the presence of micropores that can hold water molecules. The organic matter in the defatted cow bone was shown by the occurrence of characteristic C–H stretching vibration peaks in the range 2700-3100  $\text{cm}^{-1}$  i.e. the shoulder band at around 2959  $\text{cm}^{-1}$  which is due to the asymmetric C–H bonds of the aliphatic hydrocarbon chains of collagen (structural protein in the bone). The additional bands at around 2923  $\text{cm}^{-1}$  and 2853  $\text{cm}^{-1}$  are due the superimposing of  $\text{CH}_2$  asymmetric, CH modes and  $\text{CH}_3$  symmetric vibration modes respectively. The occurrence of C=O stretching vibrations in the range of 1600-1700  $\text{cm}^{-1}$ , N–H deformations in the range of 1500-1555  $\text{cm}^{-1}$  and 1200–1300  $\text{cm}^{-1}$  indicates the presence of three characteristic collagen amide adsorption bands. The O–H  $\nu_2$  bending mode (due to adsorbed water) is around 1639  $\text{cm}^{-1}$ . The intense  $\text{PO}_4^{3-}(\nu_1)$  symmetric stretching and  $\text{PO}_4^{3-}(\nu_3)$  asymmetric stretching mode was found at 961.9  $\text{cm}^{-1}$ . Carbonate peaks (C–O asymmetric stretching ( $\nu_3$ )) were found at 1412 and 1457  $\text{cm}^{-1}$ , while the band at 872.2  $\text{cm}^{-1}$  is thought to be the overlapping of the  $\text{HPO}_4^{2-}$  with the  $\text{CO}_3^{2-}(\nu_2)$  bending mode. In case of incomplete defatting CH stretching peaks and the 1743  $\text{cm}^{-1}$  peak due to carbonyl could be due to residual fats in the bone. Upon comparison with  $\text{H}_\text{P}$ , see Figure 3.3 (b), there were found to be a number of changes observed in the spectrum. The occurrence of stretching modes of lattice hydroxyl groups at 3575  $\text{cm}^{-1}$  proved that the crystallisation of hydroxyapatite through sintering had occurred. Moreover, a marked decrease in the  $\text{CO}_3^{2-}$ , collagen-associated and C-H stretching bands confirms this. The peak at around 632.5  $\text{cm}^{-1}$ , is attributed to the OH librational mode.

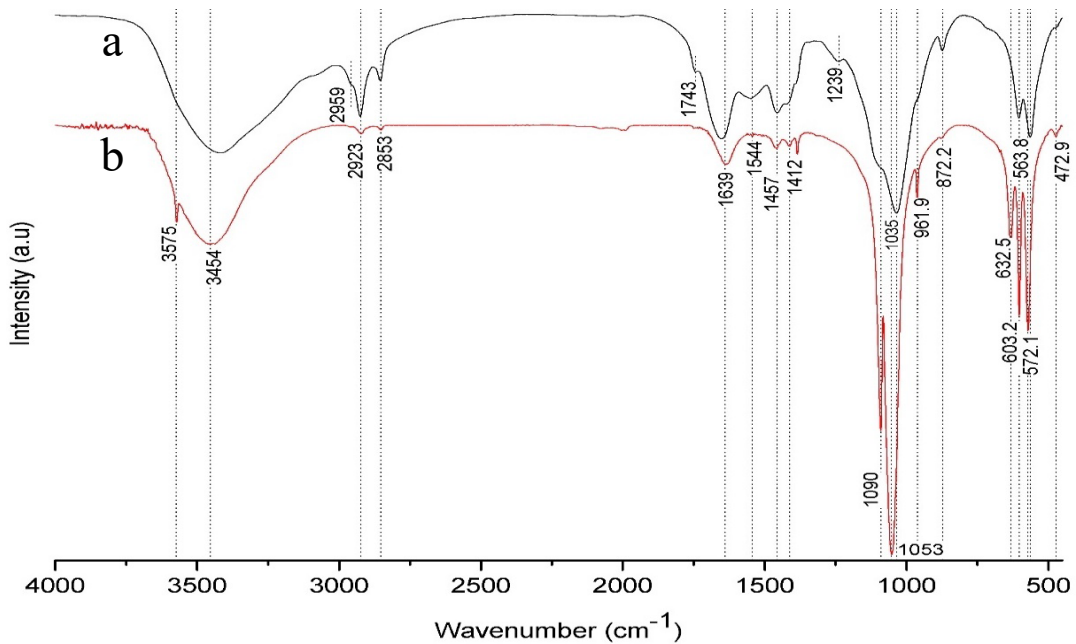


Figure 3.3: FTIR spectra of a) defatted Cow bone ( $\text{R}_{\text{DCB}}$ ) and b) crystallised (via sintering of bone) HAp ( $\text{H}_{\text{P}}$ )

The FTIR spectra of the re-precipitated HAp at the various reaction temperatures (20 °C, 40 °C, 60 °C and 80 °C) are shown in Figure 3.4. All spectra display the characteristic peaks of hydroxyapatite as well as carbonate and moisture-related features though these were observed to be broader than that observed for the sintered HAp. All spectra have the band centred around 1000–1100  $\text{cm}^{-1}$  which is solid evidence of formation of hydroxyapatite, similarly they all show peaks at around 962.7  $\text{cm}^{-1}$  & 603.6  $\text{cm}^{-1}$  which are related to the  $\nu_1$  and  $\nu_4$  fundamental vibrational modes of the phosphate group respectively. The weak bands at around 875.5, 1419 and 1462  $\text{cm}^{-1}$  indicate type-B substituted  $\text{CO}_3^{2-}$  vibrations ( $\text{CO}_3^{2-}$  substituting for  $\text{PO}_4^{3-}$  in the HAp crystal lattice). This substitution is mainly due to atmospheric carbon dioxide ingress into the solution during preparation which converts to carbonate and gets substituted into the lattice during reprecipitation and aging. The band at around 3440  $\text{cm}^{-1}$  is due to adsorbed  $\text{H}_2\text{O}$ /moisture on the HAp and a weak shoulder at 3574  $\text{cm}^{-1}$  is due to stretching modes of lattice hydroxyl groups in the HAp. In general, the appearance of the lattice hydroxyl peaks indicates that HAp has been successfully re-precipitated and is partially crystalline.

In general, peak sharpening of the broad HAp-associated peaks was observed with the increase of reaction temperature for the reprecipitated HAp samples with similar results also being reported previously by Luis Rodriguez-Lorenzo [235]. Interestingly, there was also found to be decreasing  $\text{CO}_3^{2-}$  band intensity with increasing reaction temperature, which signifies that at higher temperatures dissolution of atmospheric carbon dioxide in solution is less due to the lower solubility of  $\text{CO}_2$  at higher temperatures in water [236]. .

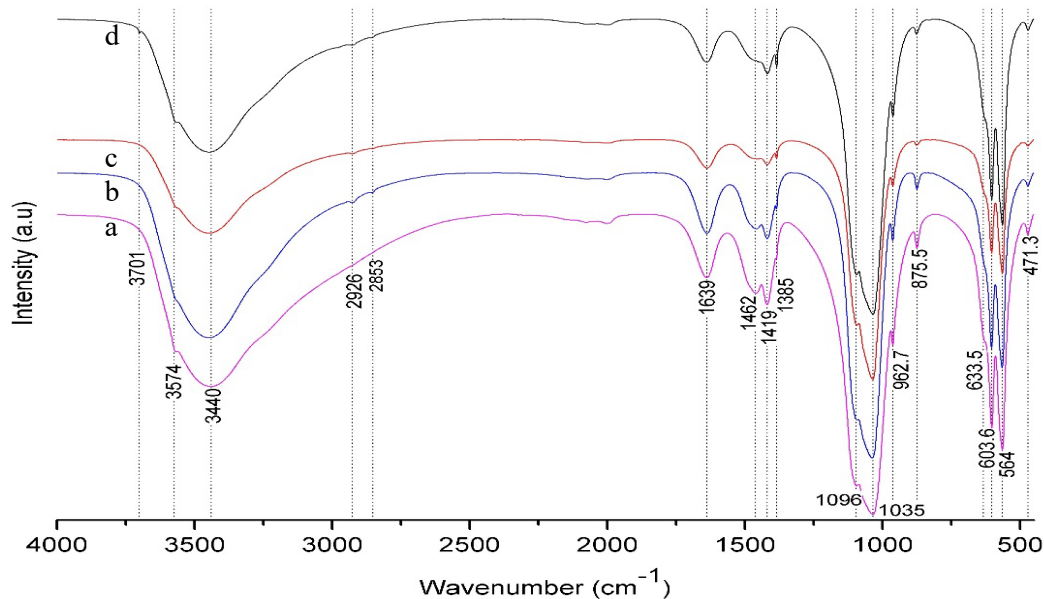


Figure 3.4: FTIR spectra of a)  $\text{H}_{20}$ , b)  $\text{H}_{40}$ , c)  $\text{H}_{60}$  and d)  $\text{H}_{80}$ , depicting characteristic features of hydroxyapatite.

Figure 3.5 represents FTIR spectra of H<sub>20-800</sub>, H<sub>40-800</sub>, H<sub>60-800</sub> and H<sub>80-800</sub>. These are sintered (at 800°C) samples of reprecipitated HAp powder formed at the different temperatures. All samples displayed characteristic features of crystalline hydroxyapatite, however the presence of very weak CO<sub>3</sub><sup>2-</sup> group bands in all samples (except H<sub>20-800</sub>) suggest the presence of surface adsorbed carbonate rather than the expected substituted carbonate, as inferred from a study reported by Ren and Leng [237]. Their research concluded that for substituted carbonate, the presence of signature bands for type-B (CO<sub>3</sub><sup>2-</sup> substituting for PO<sub>4</sub><sup>3-</sup>) at ~1465 cm<sup>-1</sup> and for type A (CO<sub>3</sub><sup>2-</sup> substituting for OH<sup>-</sup>) at ~1546 cm<sup>-1</sup>, is mandatory otherwise the carbonate can be either surface adsorbed or a separate chemical entity.

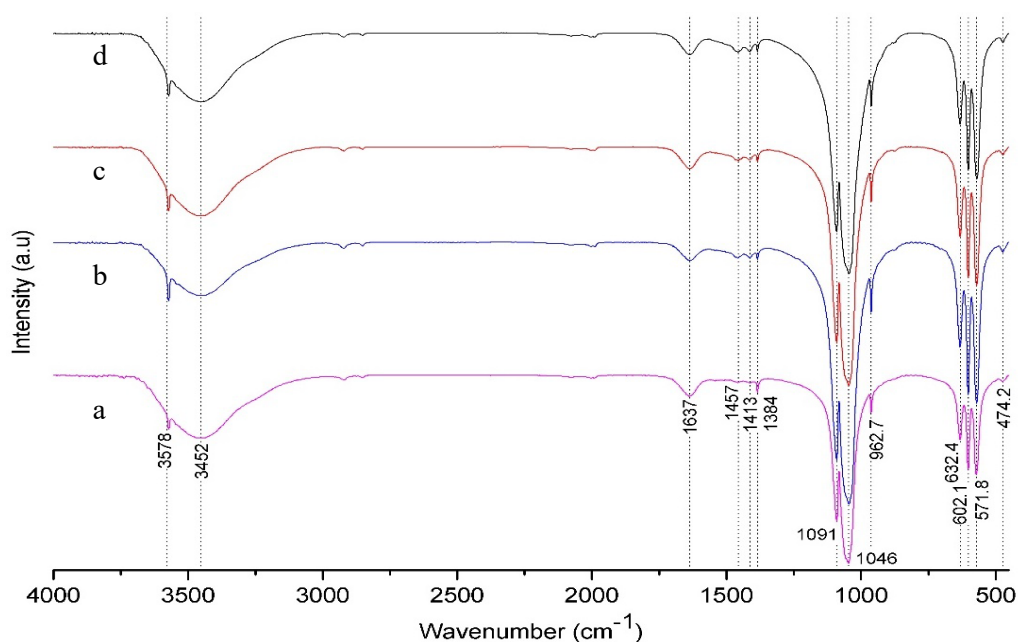


Figure 3.5: FTIR spectra of sintered reprecipitated HAp (that had been originally reprecipitated at different temperatures): a) H<sub>20-800</sub>, b) H<sub>40-800</sub>, c) H<sub>60-800</sub> and d) H<sub>80-800</sub>.

Similarly, Figure 3.6 represents FTIR spectra of H<sub>20-1000</sub>, H<sub>40-1000</sub>, H<sub>60-1000</sub> and H<sub>80-1000</sub>. These are sintered (at 1000°C) samples of reprecipitated HAp powder formed at the different temperatures. All samples displayed the characteristic features of crystalline hydroxyapatite with no other features like carbonate detected. A minor peak at around 1385 cm<sup>-1</sup> was thought to be due to a nitrate impurity present in the sample that had not been removed by washing.



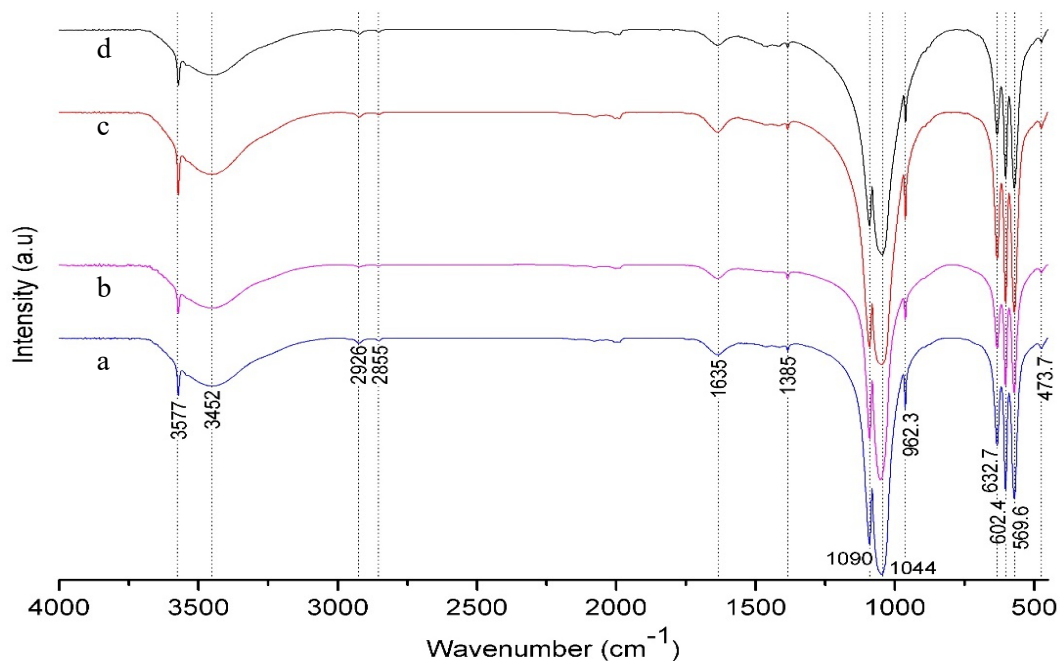


Figure 3.6: FTIR spectra of a) H<sub>20-1000</sub>, b) H<sub>40-1000</sub>, c) H<sub>60-1000</sub> and d) H<sub>80-1000</sub>, depicting characteristic features of hydroxyapatite.

Figure 3.7 represents a magnified portion of the IR spectra showing the  $\nu_4$  PO<sub>4</sub> and (librational) OH peaks of all reprecipitated and calcined HAp samples. This shows on comparison that development of OH peaks with increasing temperatures as well as the sharpening of the  $\nu_4$  PO<sub>4</sub> peaks. Equation 1, as stated below, can be used to calculate the crystallinity index (CI) of the reprecipitated and calcined hydroxyapatite, which is a measure of the fraction of crystallinity of one phase in a given sample and helps to understand the extent of splitting in the  $\nu_4$  PO<sub>4</sub><sup>3-</sup> band [238, 239]:

$$CI = \frac{A_x + A_y}{A_z} \text{ (eq. 1)}$$

where,  $A_x$ ,  $A_y$  and  $A_z$ , is the absorbance at wave number x, y and z, respectively. In the present study, the absorbances of peaks at around 602, 572 and 596 cm<sup>-1</sup> were taken as  $A_x$ ,  $A_y$  and  $A_z$ , respectively, however, the relevant portion of the IR spectrum needed to be baseline corrected before performing these measurements. The heights of the 602 cm<sup>-1</sup> and 571 cm<sup>-1</sup> absorptions were summed and then divided by the height of the valley between them.

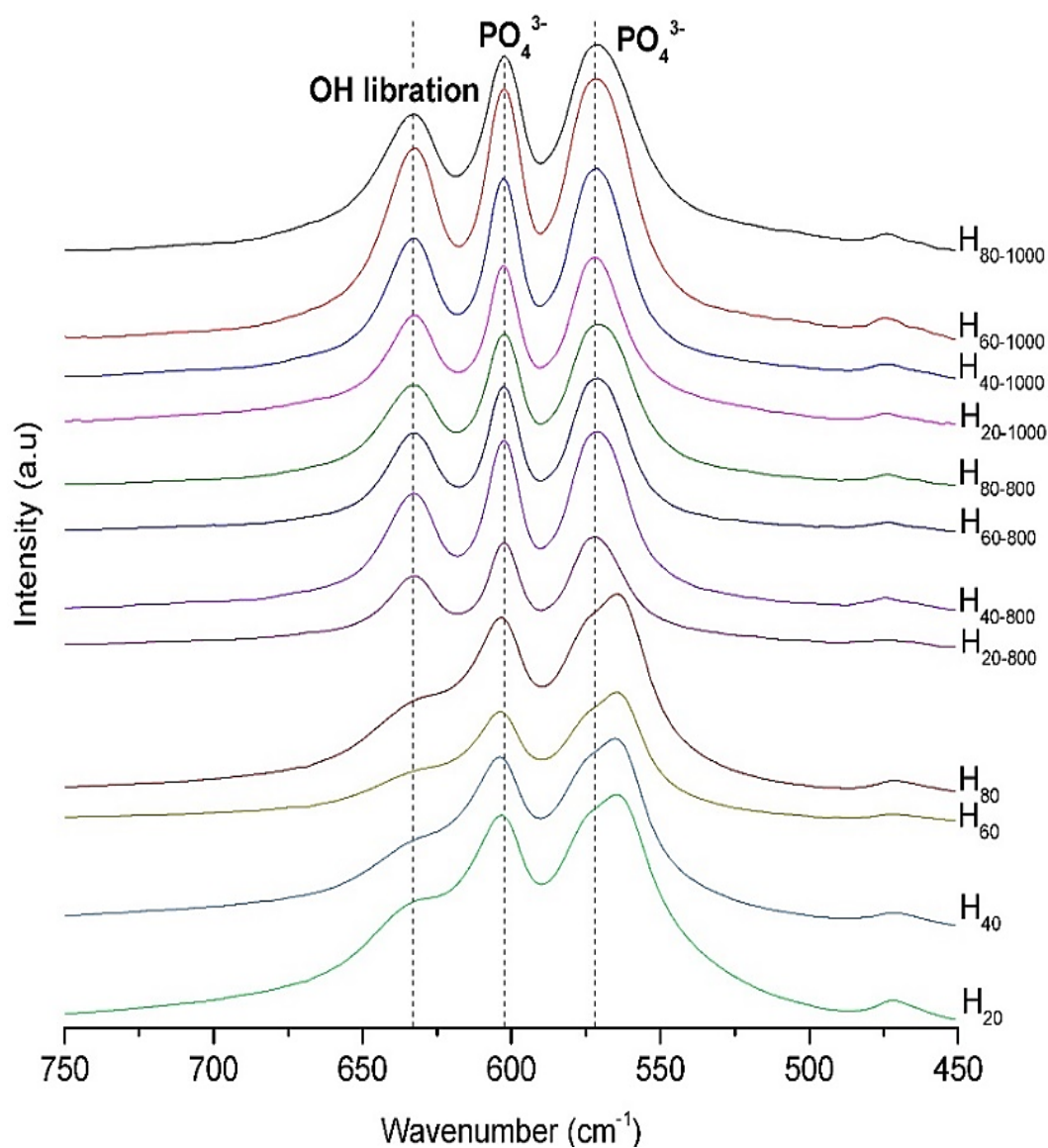


Figure 3.7: FTIR spectra of the observed  $\nu_4$   $\text{PO}_4$  domain from all reprecipitated and calcined HAp samples.

Curve fitting and deconvolution of the observed  $\nu_4$   $\text{PO}_4$  domain (for  $\text{H}_{20}$ ,  $\text{H}_{40}$ ,  $\text{H}_{60}$  and  $\text{H}_{80}$ ) of the FTIR spectra was carried out using the software “FITYK”[240] (see Figure 3.8). The band shape in the curve fitting was considered to be Lorentzian and the baseline taken to be linear in all instances. As seen in Table 3.2, deconvolution revealed “additional” bands that are not usually present for regular apatite environments and most importantly it revealed the difference between crystallographically incorporated (structurally incorporated in the lattice) phosphate and hydroxide groups (i.e., apatitic) with those absorbed in the surface hydration layer[241]. C. Rey[242] referred these additional bands as “non-apatitic”. These species result during the initial nucleation, stabilisation and growth phase of crystal development, causing development of fully non apatitic phosphocalcic clusters (which are hydrated i.e., having residual water in the interstices of the Posner

structure (the structural unit in hydroxyapatite)) and apatitic core. This favours high temperature consolidation, where the apatitic core crystallises and grow along its c axis, while high mobility ionic hydration layers fuses together to form grain boundaries. These non-apatitic ionic species are also found on the hydrated layer of natural bone apatite, which plays a significant role in protein interaction because of their high mobility[243]. In this study, it was revealed that with increasing temperature, the intensities of apatitic  $\text{PO}_4^{3-}$  peaks appeared to increase while the intensities of the non-apatitic  $\text{PO}_4^{3-}$  and  $\text{HPO}_4^{2-}$  peaks decreased. Non-apatitic  $\text{HPO}_4^{2-}$  peaks diminished in  $\text{H}_{60}$  and  $\text{H}_{80}$ , similar behaviour has been reported elsewhere as well [243]. Hence, it is evident that the apatitic domains grew at the expense of non-apatitic species, which were present within the surface hydrated layer on the HAp crystals. Drouet et. al. [244] referred to these changes as the structural variations in the apatite compositions that leads towards stoichiometry.

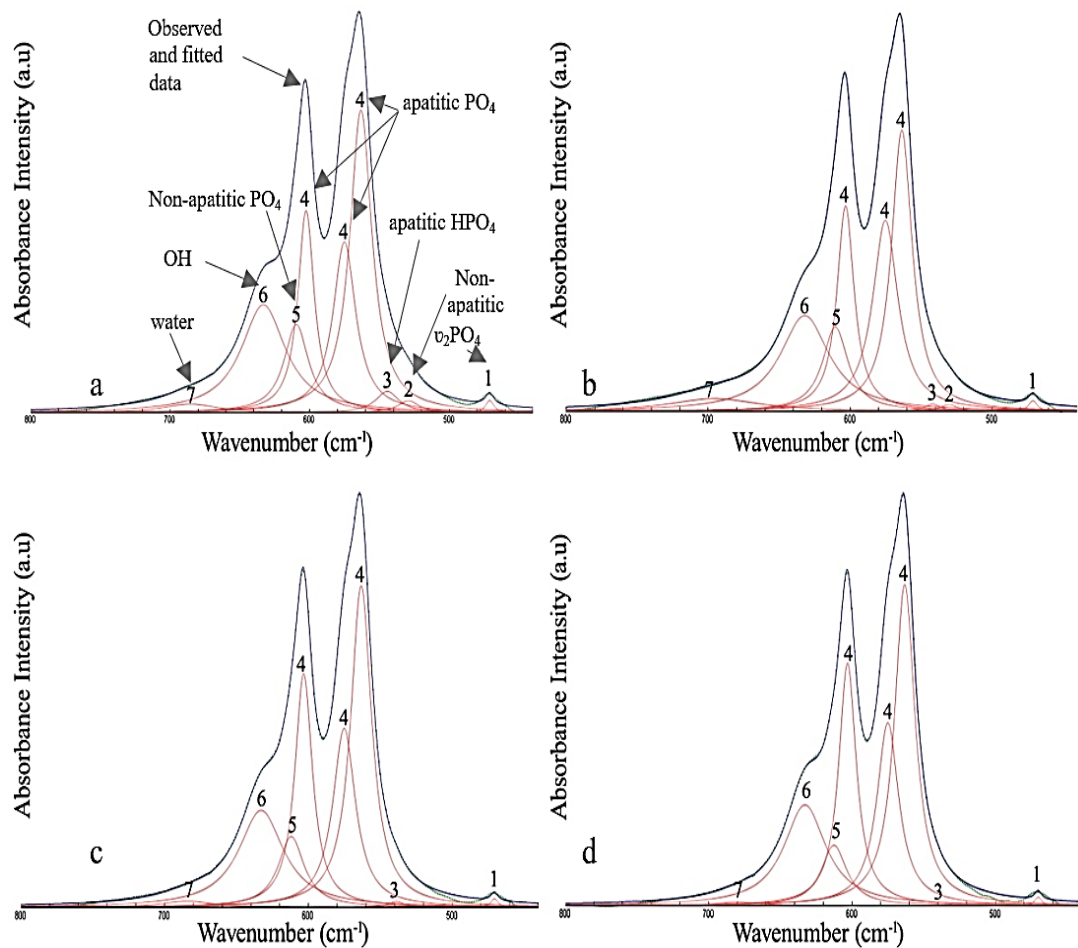


Figure 3.8: Deconvolution of the  $\nu_4$   $\text{PO}_4$  domain in FTIR spectra of all reprecipitated samples, where a)  $\text{H}_{20}$ , b)  $\text{H}_{40}$ , c)  $\text{H}_{60}$  and d)  $\text{H}_{80}$ .

Table 3.2: Assignment of the FTIR spectra of the deconvoluted  $\nu_4$  PO<sub>4</sub> domain in reprecipitated HAp samples.

Peak assignment		Peak Position (and their number as per Figure 3.8)			
		H <sub>20</sub>	H <sub>40</sub>	H <sub>60</sub>	H <sub>80</sub>
Apatitic	Bending mode $\nu_4$ PO <sub>4</sub> <sup>3-</sup>	563, 575, 602 (4)	564, 575, 603 (4)	563, 575, 603 (4)	563, 575, 603 (4)
	HPO <sub>4</sub> <sup>2-</sup>	544 (3)	542 (3)	539 (3)	540 (3)
	OH <sup>-</sup>	633 (6)	632 (6)	633 (6)	633 (6)
Non-apatitic	HPO <sub>4</sub> <sup>2-</sup>	529 (2)	530 (2)	--	--
	PO <sub>4</sub> <sup>3-</sup>	610 (5)	610 (5)	612 (5)	613 (5)
Adsorbed water		685 (7)	695 (7)	684 (7)	681 (7)

\*  $\nu_2$ PO<sub>4</sub><sup>3-</sup> is peak 1 which is  $\sim 475$  cm<sup>-1</sup>

### 3.3.2. X-ray diffraction analysis

X-ray diffraction (XRD) is a valuable structural analysis method for materials, that has been reliably employed to characterize the phase composition, crystallite size and crystallinity index in calcium phosphate-based materials in the past. In this study, XRD was used to observe the evolving changes in the reprecipitated samples with increasing reaction temperatures; moreover, effects of the calcination temperature were also monitored with this technique. Figure 3.9 shows XRD patterns of all reprecipitated (H<sub>20</sub>, H<sub>40</sub>, H<sub>60</sub> and H<sub>80</sub>) and calcined (H<sub>20-800</sub>, H<sub>40-800</sub>, H<sub>60-800</sub>, H<sub>80-800</sub>, H<sub>20-1000</sub>, H<sub>40-1000</sub>, H<sub>60-1000</sub> and H<sub>80-1000</sub>) samples. The obtained diffractograms were imported into Philips ‘‘HighScore Plus’’ software[245] and compared with the reference spectra from the ICDD PDF-4+ database (The International Centre for Diffraction Data, 2020). The identified peaks of all samples matched well with hydroxyapatite (Ca<sub>5</sub>(PO<sub>4</sub>)<sub>3</sub>(OH), reference number 009-0432) and no other phases were found.

The degree of crystallinity which reflects the fraction of the crystalline phase ( $X_c$ ) present in the samples, was calculated using equation 2 [246]:

$$\chi_c = 1 - \frac{v_{112/300}}{I_{300}} \text{ (eq. 2)}$$

where  $I_{300}$  is the intensity of the (300) diffraction peak and  $v_{112/300}$  is the intensity of the hollow between the (1 1 2) and (3 0 0) diffraction peaks (measured by averaging the intensities). The values of degree of crystallinity are provided in Table 3.3. Rietveld refinement was carried out on both samples, using Philips ‘‘HighScore Plus’’ software[245, 247, 248] (based on the Rietveld code from Wiles & Young [249]). All refined lattice

parameters are reported in Table 3.3. The correlation between CI (IR) and  $\chi_c$  (XRD) was found to be 0.914.

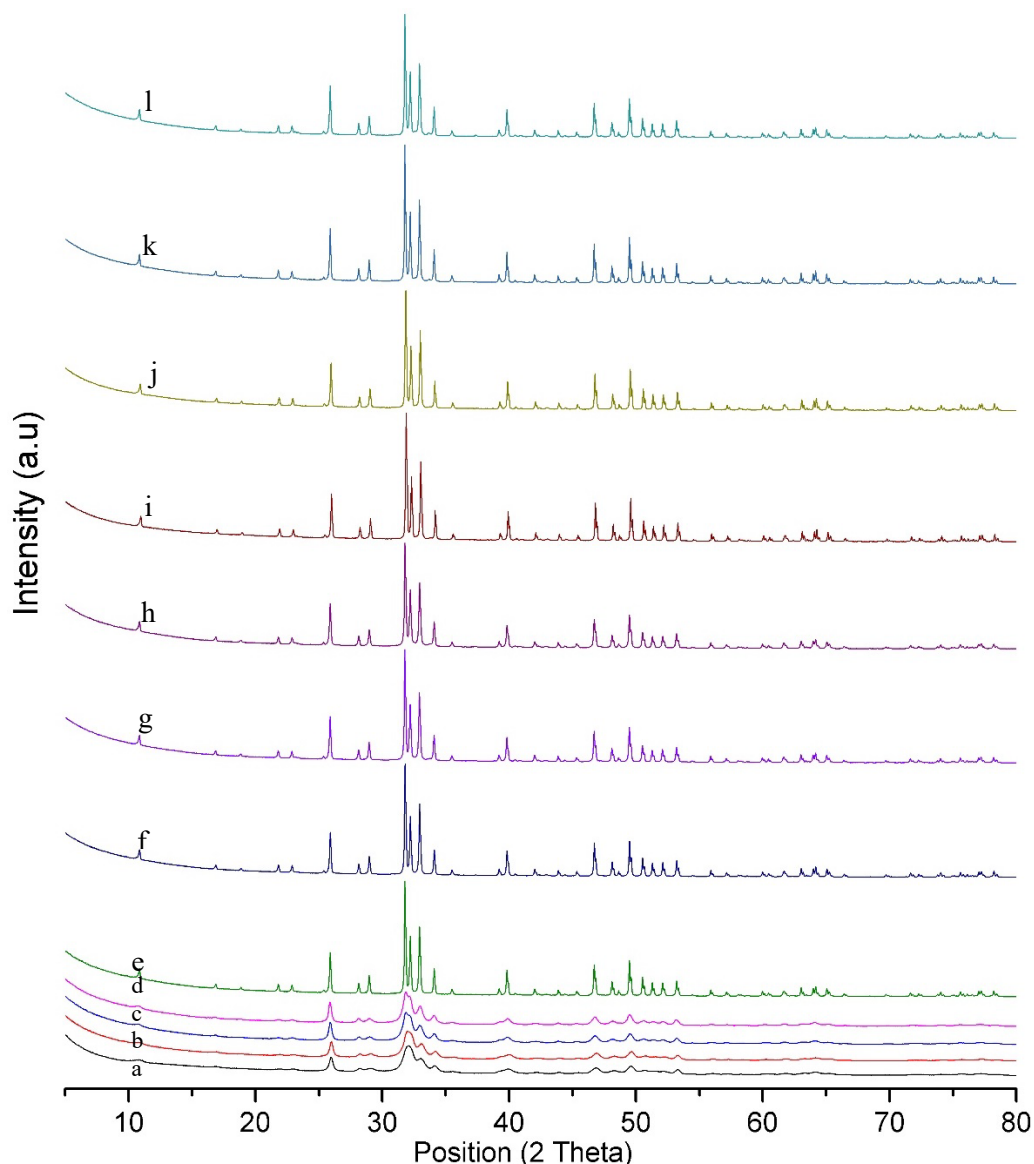


Figure 3.9: XRD diffractograms of a) H<sub>20</sub>, b) H<sub>40</sub>, c) H<sub>60</sub>, d) H<sub>80</sub>, e) H<sub>20-800</sub>, f) H<sub>40-800</sub>, g) H<sub>60-800</sub>, h) H<sub>80-800</sub>, i) H<sub>20-1000</sub>, j) H<sub>40-1000</sub>, k) H<sub>60-1000</sub> and l) H<sub>80-1000</sub>, all depicting the characteristic features of hydroxyapatite.

Figure 3.10 displays the portion of the diffractogram of reprecipitated HAp, where the effect of increasing reaction temperature can easily be observed. Peak sharpening at (0 0 2) and evolution of sharp peaks from broad and low intensity peaks between 2 theta = 31-35°, clearly demonstrate the increasing of crystallinity in the samples. The amorphous/disordered apatite surface layer (ACP) (on the ordered/crystalline HAp) halo is also highlighted in each diagram, similar halos were reported in other studies as well[250, 251].

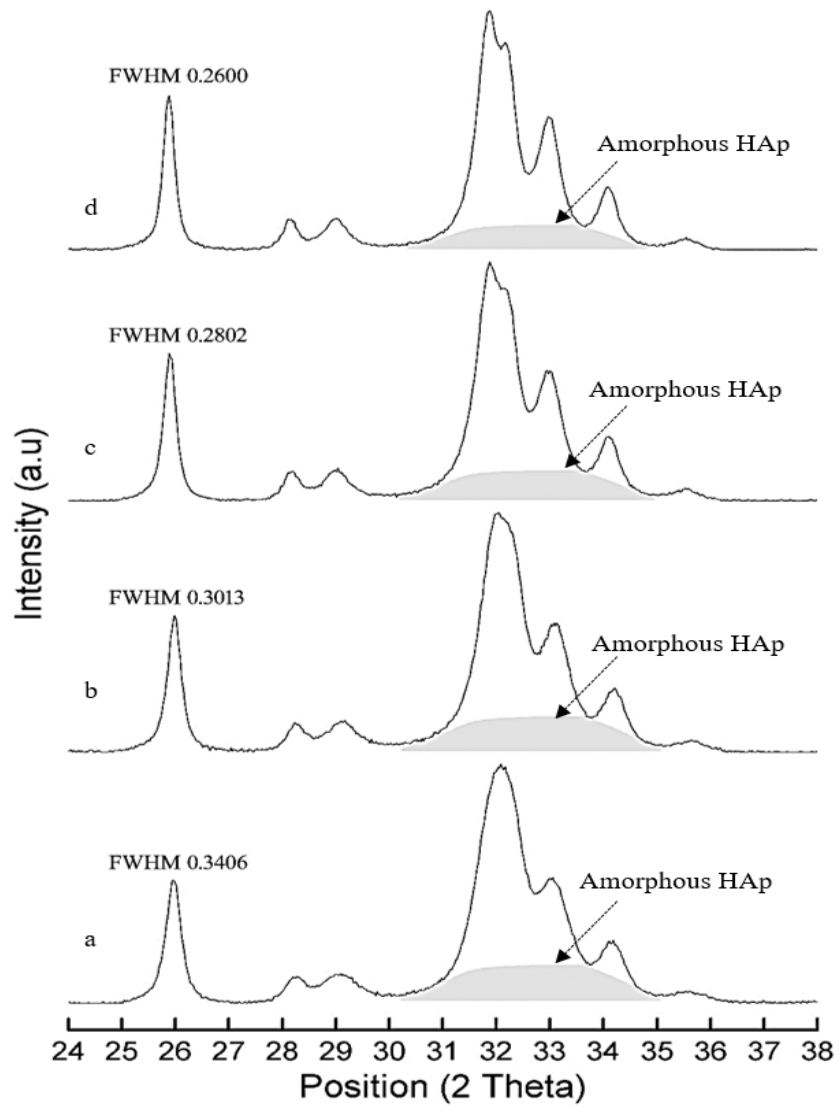


Figure 3.10: Portion of an XRD diffractogram of a) H<sub>20</sub>, b) H<sub>40</sub>, c) H<sub>60</sub> & d) H<sub>80</sub>

Table 3.3: Calculated lattice parameter and crystallinity of all samples

	Lattice Parameters				CI (IR)	$\chi_c$ (XRD)
	a (Å)	b (Å)	c (Å)	Cell volume (Å <sup>3</sup> )		
H <sub>20</sub>	9.40817	9.40817	6.88465	527.73	3.263	0.1046
H <sub>40</sub>	9.40546	9.40546	6.88723	527.62	3.429	0.125
H <sub>60</sub>	9.41411	9.41411	6.88707	528.58	3.631	0.291
H <sub>80</sub>	9.41036	9.41036	6.8882	528.25	3.774	0.4924
H <sub>20-800</sub>	9.41879	9.41879	6.88239	528.75	6.166	0.9741
H <sub>40-800</sub>	9.41856	9.41856	6.88295	528.76	5.707	0.9511
H <sub>60-800</sub>	9.41904	9.41904	6.88305	528.83	5.939	0.9649
H <sub>80-800</sub>	9.41801	9.41801	6.88419	528.80	5.218	0.9476
H <sub>20-1000</sub>	9.42258	9.42258	6.88513	529.38	6.076	0.9818
H <sub>40-1000</sub>	9.42124	9.42124	6.88415	529.16	5.731	0.9615
H <sub>60-1000</sub>	9.41965	9.41965	6.88294	528.89	4.656	0.9652
H <sub>80-1000</sub>	9.41977	9.41977	6.88427	529.00	5.017	0.9506

The existence of disordered/amorphous apatite (ACP) in reprecipitated samples, as a surface layer over ordered/crystalline HAp, indicates the stabilisation of this surface layer may be due to presence of carbonate or may be due to presence of metallic ions in the solution like magnesium. The amorphous calcium phosphate (ACP) is a precursor phase of crystalline hydroxyapatite i.e. it is the initial solid that emerges from super-saturated solution calcium phosphate solution, however due to its unstable nature it readily converts in the presence of water into stable crystalline apatitic phases. Studies have showed that ACP has a chemical composition of  $\text{Ca}_9(\text{PO}_4)_6$  with a Ca/P mole ratio of approx. 1.5 and is a random assembly of ion clusters. ACP particles usually have a size in the range of 300-1000 Å, but the exact size depends on the preparation conditions employed. It is understood that there is 15–20% of water in the interstices between, and not within, the individual clusters of ACP. ACP is a highly unstable phase mainly due to its disordered structure. It is believed HAp embryos form from ACP forms, when the rearrangement of calcium and phosphate ions in ACP takes place with an exchange of ions with the surrounding solution[251-253]. Once such embryos reach a critical size, their crystallinity slowly and steadily increases. However, a few studies report formation of intermediate phases (like octacalcium phosphate (OCP)) during the conversion. However, there is still a lack of precise information about the exact crystallisation of irregular amorphous components into platelet-like HAp crystals.

It is important to highlight theories related to formation of ACP. One such theory proposed by Posner and Betts, details the formation of a pre-nucleation “Posner’s cluster”, which is approx. 1 nm size clusters of  $\text{Ca}_9(\text{PO}_4)_6$ . As per this theory, these clusters can be the building blocks for ACP formation[254, 255]. It was also suggested that ACP dissociates into these clusters rather than undergoing full ionic dissolution and that these dissociated clusters slowly and steadily rearrange themselves into HAp crystals by taking up additional  $\text{OH}^-$  and  $\text{Ca}^{2+}$  ions. Similarly, pre-nucleation clusters of calcium triphosphate  $[\text{Ca}(\text{HPO}_4)_3]_4^-$ -ion-associated complexes of similar sizes were also proposed to be building blocks of ACP[256-260]. ACP is known for its effective role in biomineralisation and found to possess good bioactivity with better in vivo osteoconductivity than HAp and better biodegradability than TCP, with no cytotoxicity. Therefore, researchers have studied the possible kinetic stabilisation of ACP for which different metal ions (like  $\text{Mg}^{2+}$ ), carbonate, hydrogels and citrate adsorption were found to be effective[251, 252]. Now, it is generally understood that during ACP to HAp conversion if no intermediate phase (like OCP) is formed then the HAp formed is said to be stoichiometric[104].

The Scherrer equation was used to find the mean crystallite size (D) from the XRD line-broadening measurement [238]:

$$D=0.89\lambda/\beta_{hkl}\cos\theta \text{ (eq. 3)}$$

where  $\lambda$  is the wavelength (CuK $\alpha$ ),  $\beta_{hkl}$  is the full width at half-maximum of the chosen diffraction line and  $\theta$  the diffraction angle. The diffraction peak at approx.  $2\theta = 25.9^\circ$  (corresponding to the (0 0 2) Miller plane) was chosen for calculating crystallite size (D), as this was found to be sufficiently isolated from the other peaks to allow measurement and was sharper and more representative of the crystal growth along the c-axis. The measurement of  $\beta_{hkl}$  was made after automatic instrumental broadening correction via HighScore Plus software. For the correction of instrumental broadening, A silicon (Si) sample was analysed (and Rietveld refined) as a standard[261, 262] because it has large crystallites and is free from any defect. The automatic correction followed below mentioned equation:

$$\beta_{hkl}=[(\beta_{hkl})^2_{\text{Measured}}-(\beta_{hkl})^2_{\text{Instrumental}}]^{1/2} \text{ (eq. 4)}$$

The contribution of lattice strain in the peak broadening cannot be underestimated as nanomaterials are vastly affected by lattice strain (like crystallite size) mainly because of the presence of a large volume of grain boundaries. X-ray diffraction peak profile analysis is an efficient method to estimate crystallite size, because unlike Scherrer's method, it considers the contribution of inhomogeneous strain in peak broadening. It can also be used to estimate lattice distortion, twinning and stacking fault probabilities in nanocrystalline materials. In order to measure strain and its effects on crystallite size, a method known as the Williamson–Hall method is widely used, which differentiates between size and strain induced contributions to the peak broadening by considering the peak width as a function of  $2\theta$ . The Williamson–Hall equation for lattice strain is given by:

$$\varepsilon = \beta_{hkl}/4 \tan\theta \text{ (eq. 5)}$$

and the Williamson–Hall equation for crystallite size is given by:

$$\beta_{hkl} \cos\theta = K\lambda/D + 4\varepsilon \sin\theta \text{ (eq. 6)}$$

where  $\varepsilon$  is micro-strain, D is the crystallite size, K is the shape coefficient (value between 0.9 and 1.0),  $\lambda$  is the wavelength ( $\sim 1.54 \text{ \AA}$ ),  $\beta_{hkl}$  is the full width at half maximum



of each phase and  $\theta$  is the diffraction angle. A plot is drawn with “ $4\sin\theta$ ” along the x-axis and “ $\beta_{hkl} \cos\theta$ ” along the y-axis for reprecipitated (figure 3.11) and heat-treated HAp powders (figure 3.12 & 3.13), which was then fitted to a linear trendline to get the y-intercept and the slope. The crystalline size was estimated from the y-intercept, and the strain, from the slope of the fit. Table 3.4 presents crystallite size and strain values of those HAp samples.

Table 3.4: Crystallite size and lattice strain values of all reprecipitated and calcined HAp samples.

Sample Name	Crystallite Size (nm)		Strain
	W-H method	Scherrer Equation	
H <sub>20</sub>	16 ± 0.13	14 ± 0.09	0.001048 ± 4 E-5
H <sub>40</sub>	22 ± 0.37	17 ± 0.10	0.001944 ± 5 E-5
H <sub>60</sub>	22 ± 0.37	17 ± 0.10	0.002039 ± 5 E-5
H <sub>80</sub>	25 ± 0.32	21 ± 0.13	0.001090 ± 4 E-5
H <sub>20-800</sub>	78 ± 0.60	81 ± 0.50	-0.000102 ± 7 E-6
H <sub>40-800</sub>	79 ± 0.63	82 ± 0.50	-0.000106 ± 7 E-6
H <sub>60-800</sub>	76 ± 0.60	78 ± 0.48	-0.000082 ± 7 E-6
H <sub>80-800</sub>	72 ± 0.53	74 ± 0.46	-0.000078 ± 7 E-6
H <sub>20-1000</sub>	86 ± 0.80	91 ± 0.56	-0.000121 ± 7 E-6
H <sub>40-1000</sub>	84 ± 0.76	89 ± 0.54	-0.000111 ± 8 E-6
H <sub>60-1000</sub>	87 ± 0.87	92 ± 0.57	-0.000122 ± 8 E-6
H <sub>80-1000</sub>	83 ± 0.76	86 ± 0.53	-0.000099 ± 8 E-6

The crystallite size values of all the samples obtained using both W-H method and Scherrer equation, were found to be quite close, moreover the trend of increasing crystallite size with increasing the reaction temperature and calcination was also same. The reprecipitated HAp samples displayed a positive slope for the Williamson-Hall plot (Figure 3.11), which signifies the influence of the microstrains on the peak broadening, but the 800 °C and 1000 °C treated HAp sample (Figure 3.12 & 3.13) displayed negative slope for the plot which indicates that micro strains were not a dominant source of broadening[263]. Negative slope/negative strain also indicates lattice shrinkage i.e., compressive strain on the lattice. Hence, crystallite sizes of reprecipitated samples found using the W-H method were considered accurate because the values represent the contribution of the microstrain to the crystallite size.

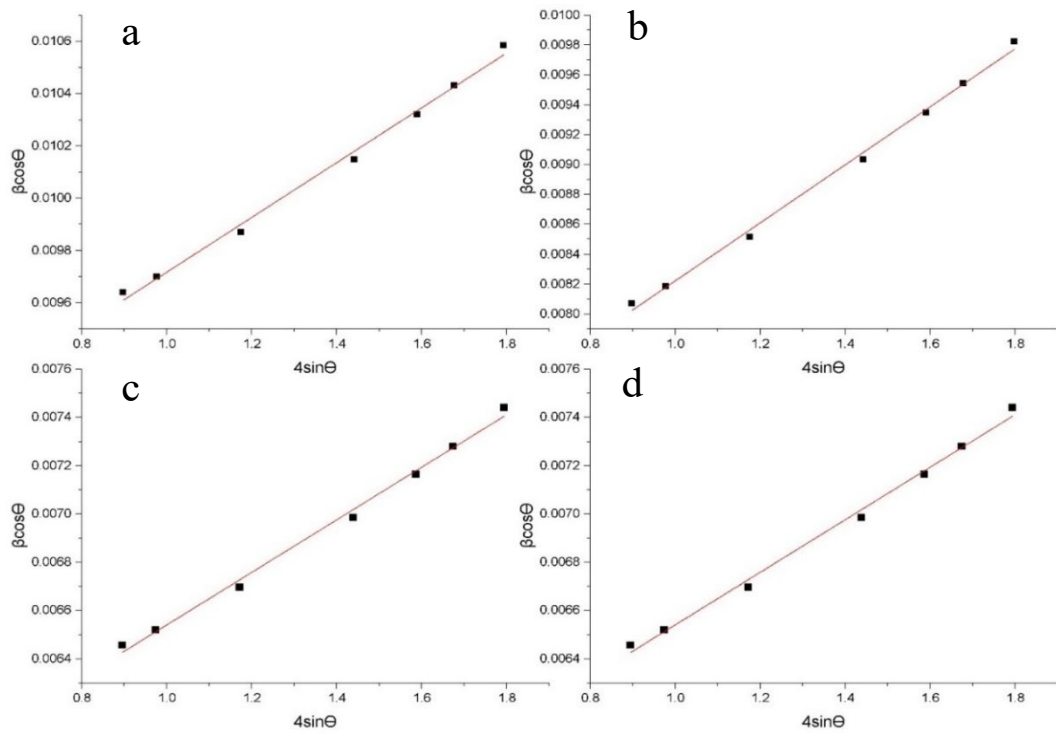


Figure 3.11: Lattice strain and crystallite size, a)  $H_{20}$ , b)  $H_{40}$ , c)  $H_{60}$  & d)  $H_{80}$

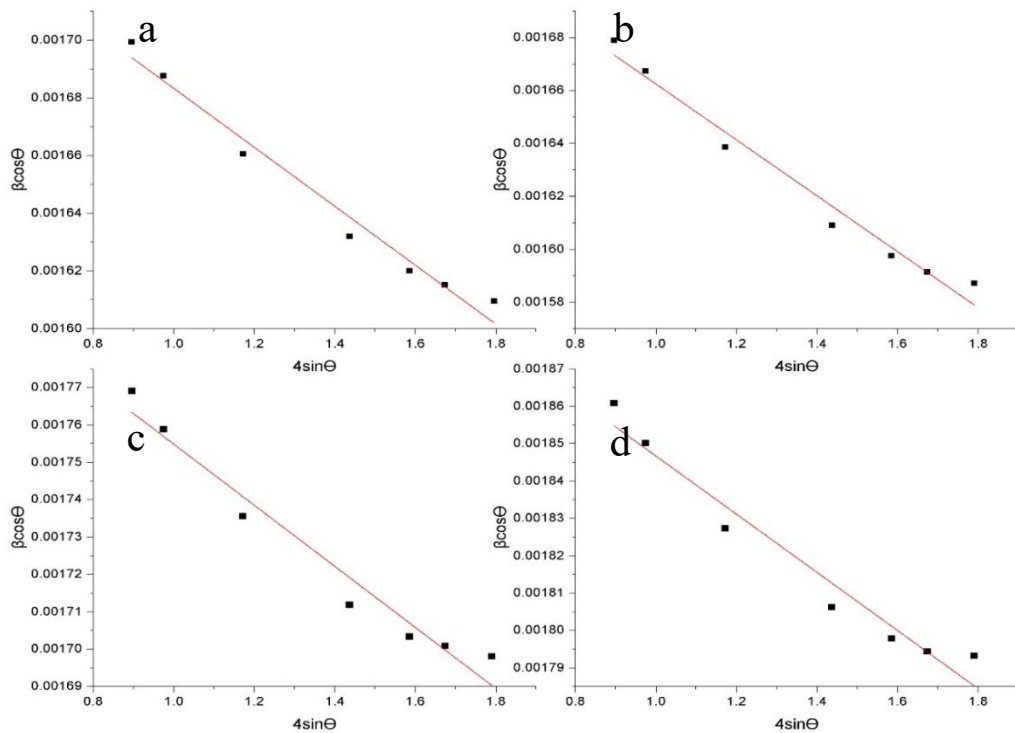


Figure 3.12: Lattice strain and crystallite size, a)  $H_{20-800}$ , b)  $H_{40-800}$ , c)  $H_{60-800}$ , d)  $H_{80-800}$

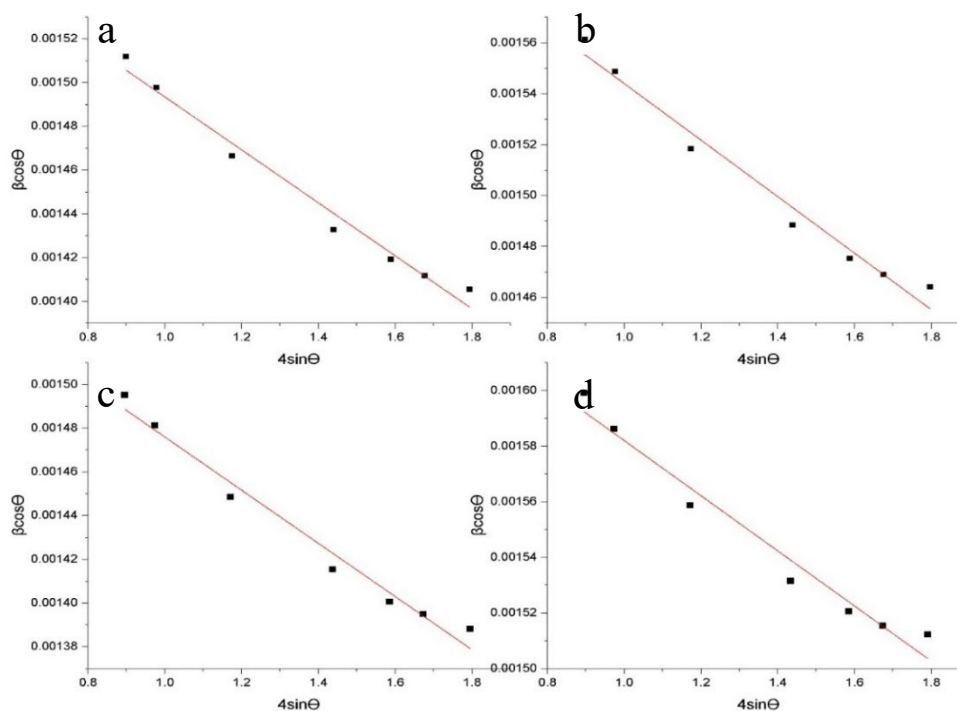


Figure 3.13: Lattice strain and crystallite size, a) H<sub>20-1000</sub>, b) H<sub>40-1000</sub>, c) H<sub>60-1000</sub>, d) H<sub>80-1000</sub>

### 3.3.3. Raman Spectroscopy Analysis

Raman spectroscopic studies for apatites generated in this study were mostly used to complement IR results, however researchers have also used it to study the crystallinity index (CI), the carbonate-to-phosphate ratio and the mineral maturity of bone[264-268]. Similarly, in this study Raman spectroscopy provided valuable insight into evolving changes in the crystallinity indices, which represent the degree of atomic ordering. All reprecipitated (H<sub>20</sub>, H<sub>40</sub>, H<sub>60</sub> and H<sub>80</sub>) and calcined (H<sub>20-800</sub>, H<sub>40-800</sub>, H<sub>60-800</sub>, H<sub>80-800</sub>, H<sub>20-1000</sub>, H<sub>40-1000</sub>, H<sub>60-1000</sub> and H<sub>80-1000</sub>) samples displayed strong signature PO<sub>4</sub> ν<sub>1</sub> peaks at around 962 cm<sup>-1</sup> along with vibrational modes of phosphate groups, i.e. ν<sub>2</sub>(PO<sub>4</sub>) at around 432 cm<sup>-1</sup>, ν<sub>3</sub>(PO<sub>4</sub>) at around 1028–1076 cm<sup>-1</sup> and ν<sub>4</sub>(PO<sub>4</sub>) at around 447, 579-607 cm<sup>-1</sup>, which indicate the formation of hydroxyapatite, however, the (solely) reprecipitated samples expectedly showed broader features typical of amorphous hydroxyapatite (Figure 3.14).

Figure 3.15 illustrates the Gaussian fitting and deconvolution of all reprecipitated (H<sub>20</sub>, H<sub>40</sub>, H<sub>60</sub> and H<sub>80</sub>) samples, using FITYK, which revealed an additional band at around 950 cm<sup>-1</sup>, believed to be representative of disordered/amorphous apatite (ACP). For disordered/amorphous apatite (ACP), previous researchers also documented an approx. 10 cm<sup>-1</sup> shift of the PO<sub>4</sub> ν<sub>1</sub> stretching towards 950 cm<sup>-1</sup>. Thus, the occurrence of a broad peak at ca. 950 cm<sup>-1</sup> along with the narrow 962 cm<sup>-1</sup> peak describes the presence of a disordered/amorphous apatite (ACP) surface layer on top of ordered/crystalline HAp. It

is noted that with increasing reaction temperature, both intensity and FWHM of the ACP band decreased. The band area ratio of ACP and HAp was calculated and reported in figure 3.16, which clearly demonstrates the decreasing ACP content with increasing reaction temperature.

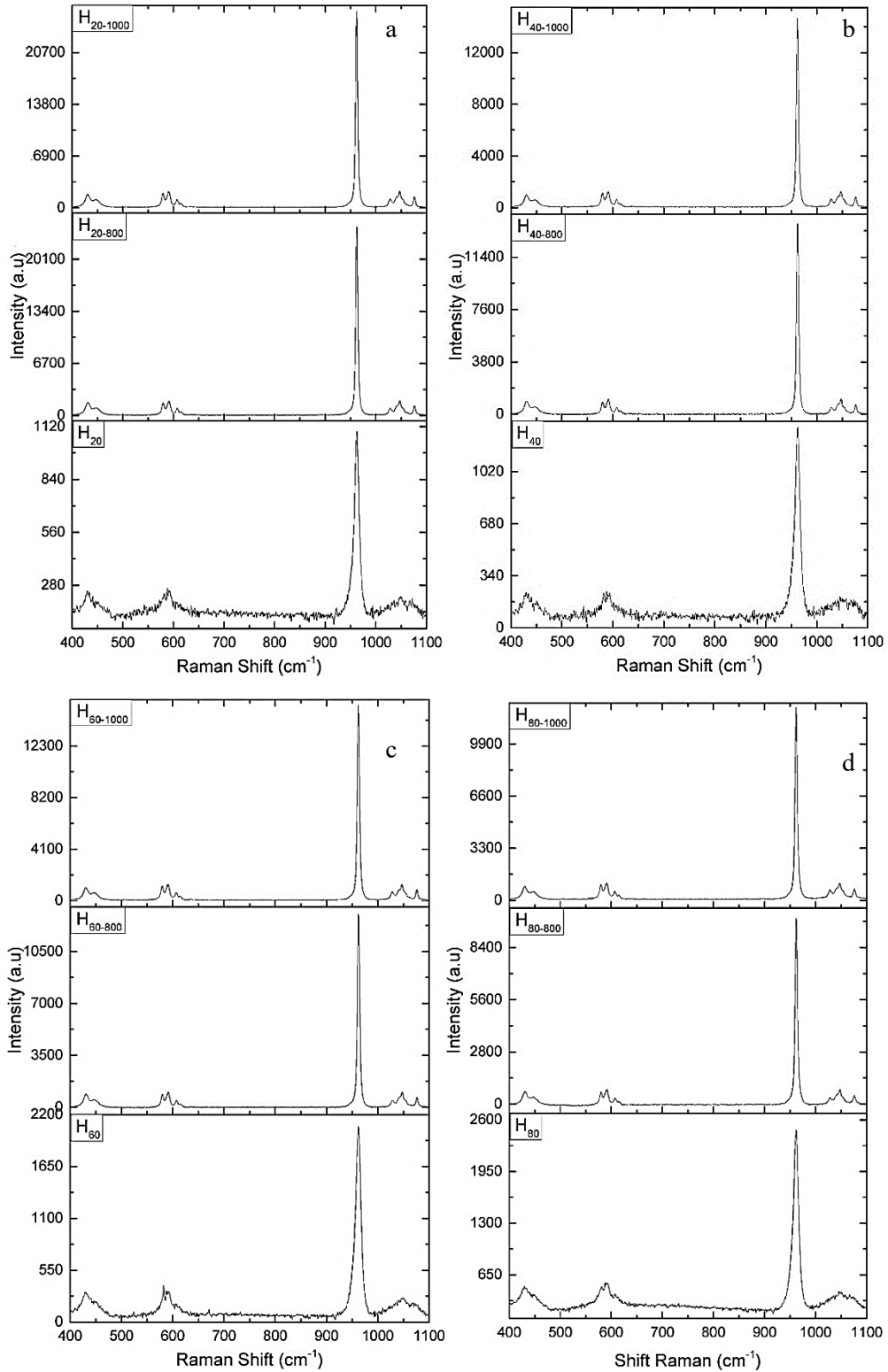


Figure 3.14: This figure represents the Raman spectra a) H<sub>20</sub>, H<sub>20-800</sub> & H<sub>20-1000</sub> b) H<sub>40</sub>, H<sub>40-800</sub> & H<sub>40-1000</sub> c) H<sub>60</sub>, H<sub>60-800</sub> & H<sub>60-1000</sub> d) H<sub>80</sub>, H<sub>80-800</sub> & H<sub>80-1000</sub>

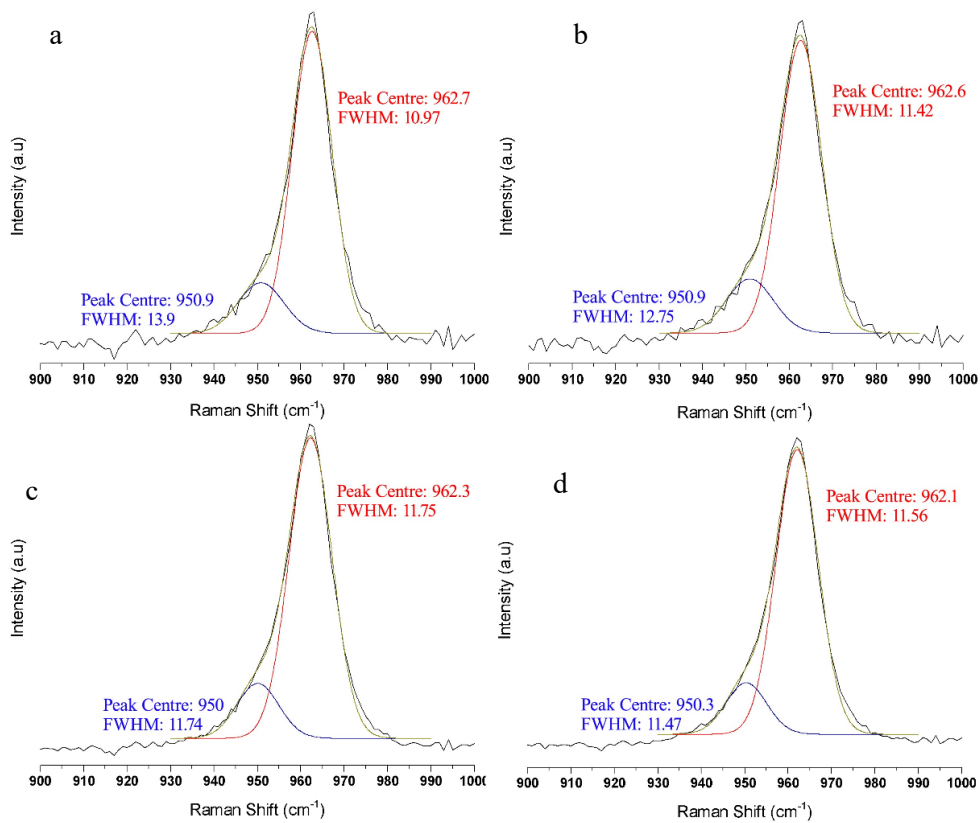


Figure 3.15: This figure represents deconvoluted PO<sub>4</sub> v<sub>1</sub> peak of a) H<sub>20</sub>, b) H<sub>40</sub>, c) H<sub>60</sub>, and d) H<sub>80</sub>.

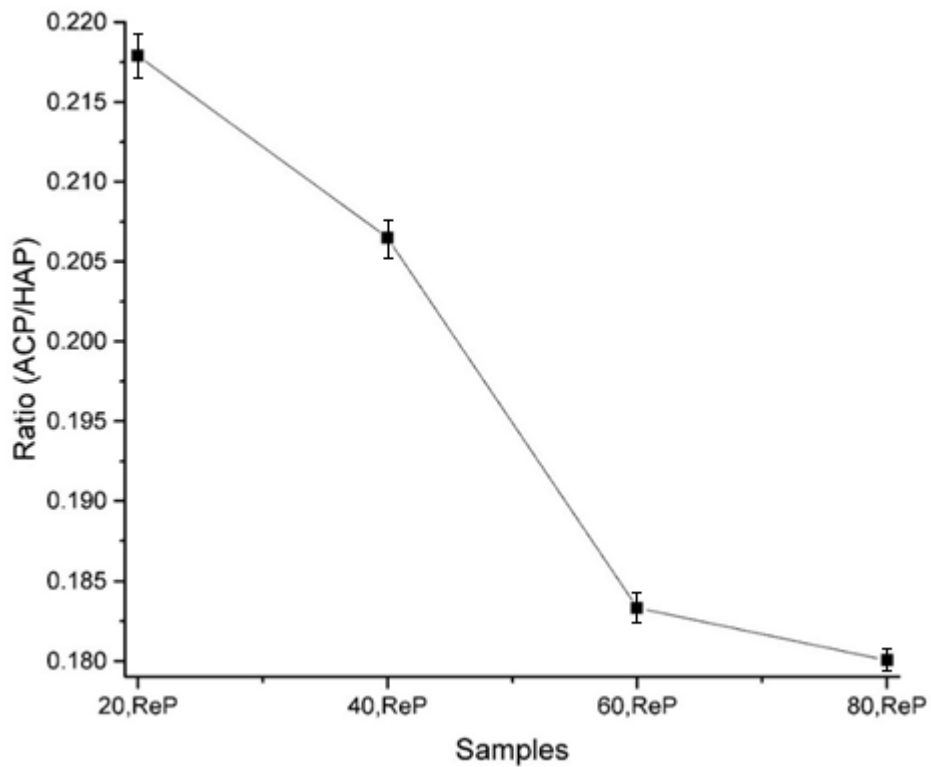


Figure 3.16: Ratio of ACP and HAP bands in Raman spectra, obtained after deconvolution of the PO<sub>4</sub> v<sub>1</sub> peak observed in Raman spectra of H<sub>20</sub>, H<sub>40</sub>, H<sub>60</sub> & H<sub>80</sub>.

### 3.3.4. Thermal Analysis

Simultaneous Thermogravimetry (TGA) – Differential Scanning Calorimetry (DSC) was carried out to understand heat induced changes in the HAp structure and corresponding heat flow (endothermic or exothermic) events. TGA thermograms of H<sub>20</sub>, H<sub>40</sub>, H<sub>60</sub> & H<sub>80</sub>, see Figure 3.17, appeared to display similar profiles (both during heating and cooling) however, detailed analysis revealed distinct features in each. In general, the thermal events occurring in all four TGA thermograms can be divided into four stages:

- i) Removal of adsorbed water, i.e., physisorbed water desorbs and evaporates.
- ii) Removal of more strongly chemically bonded water and other volatile matter.
- iii) Decarbonisation (i.e. decomposition of carbonate to release carbon dioxide), crystallisation of amorphous HAp and dehydroxylation.
- iv) Rehydroxylation (i.e., the chemisorption of atmospheric water)

Table 3.5: Breakdown of mass loss during heating of H<sub>20</sub>, H<sub>40</sub>, H<sub>60</sub> & H<sub>80</sub>.

		H <sub>20</sub>	H <sub>40</sub>	H <sub>60</sub>	H <sub>80</sub>
<b>Adsorbed water (1)</b>	TR (°C)	50-179.6	50-175.7	50-172.9	50-167.9
	WL (%)	2.67	2.85	1.80	1.00
<b>Chemically bonded water (2)</b>	TR (°C)	179.6-629.7	175.7-627.5	172.9-600.8	167.9-591.1
	WL (%)	2.94	3.47	2.80	2.22
<b>Decarbonisation &amp; Dehydroxylation (3)</b>	TR (°C)	710.5-1250	712.5-1250	702.4-1250	705.5-1250
	WL (%)	2.09	2.39	2.27	2.37
<b>Rehydroxylation (4)</b>	TR (°C)	1250-92	92.36-92	93.91-92	95.21-92
	WL (%)	0.42	0.77	0.78	0.80
<b>Overall WL (%)</b>		7.28	7.94	6.09	4.79

TR = Temperature Range WL= Weight Loss

Upon comparing decrement values of adsorbed and chemically bonded water, it is evident with increasing reaction temperatures, these values decreased, mainly due to differences in the morphology of particles. Similarly, decarbonisation and crystallisation weight loss is less in samples previously exposed to high reaction temperatures.

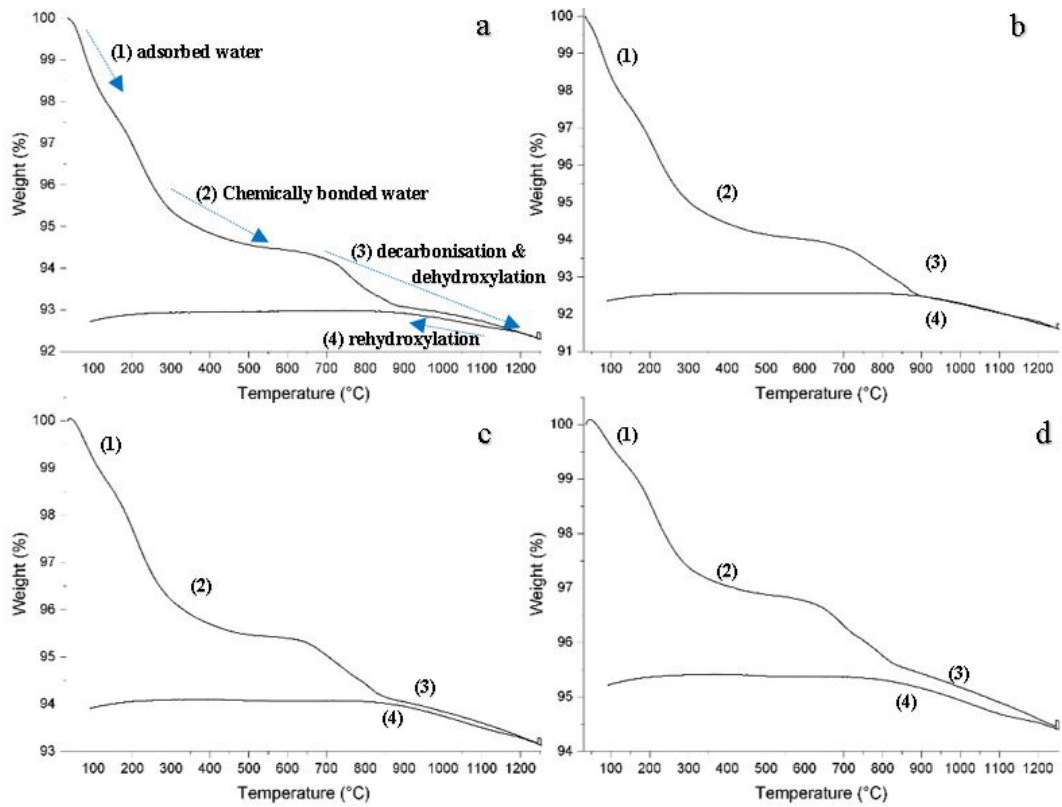


Figure 3.17: Thermal analysis (heating and cooling) of re-precipitated HAp samples a) H<sub>20</sub>, b) H<sub>40</sub>, c) H<sub>60</sub> & d) H<sub>80</sub>, with numbers (1) to (4) depicting important thermal events which are described fully in a).

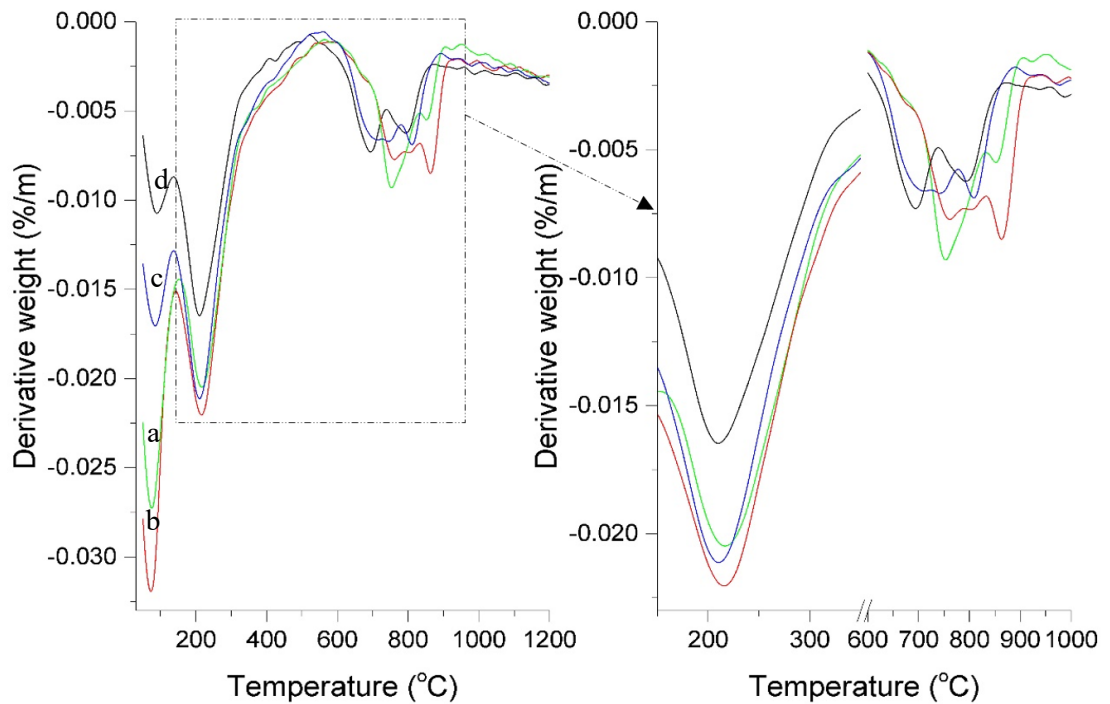


Figure 3.18: Derivative weight loss of a) H<sub>20</sub>, b) H<sub>40</sub>, c) H<sub>60</sub> and d) H<sub>80</sub>

Derivative weight loss (DTGA) of all four samples, also depicted the weight losses related to release of water (adsorbed and chemically bonded), decarbonisation and dehydroxylation, as shown in Figure 3.18. However, derivative heat flow (DDSC), Figure 3.19, revealed an additional thermal event at around 650 °C, which can be linked to crystallisation of an amorphous apatite surface layer [253, 269, 270].

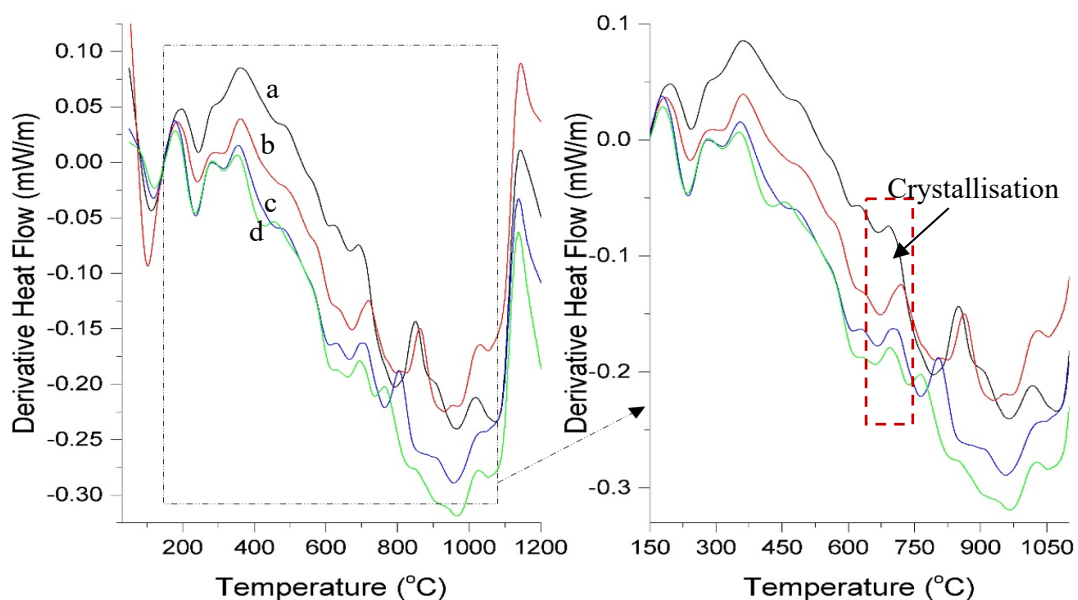


Figure 3.19: Derivative heat flow of a) H<sub>20</sub>, b) H<sub>40</sub>, c) H<sub>60</sub> and d) H<sub>80</sub>

### 3.3.5. Imaging

Electron Microscopy is a useful tool to study powdered material for their morphology and topology. In this study, SEM was used to access the evolving morphology of HAp due to different reaction temperatures during re-precipitation moreover, changes in the morphology of particles due to calcination was also assessed using this technique. Figure 3.20 shows the SEM images of the re-precipitated hydroxyapatite samples. In general, all samples displayed fine submicron-sized powdered structures however samples precipitated at higher temperatures (H<sub>60</sub> and H<sub>80</sub>) showed elongated morphology and agglomeration mainly because of diffusion growth and Ostwald ripening (i.e. the growth of larger particles at the expense of smaller ones). It is believed that the higher reaction temperatures caused diffusional growth of particles along the c-axis, which means elongation, however Ostwald ripening occurred during the 24-hour aging process[271].



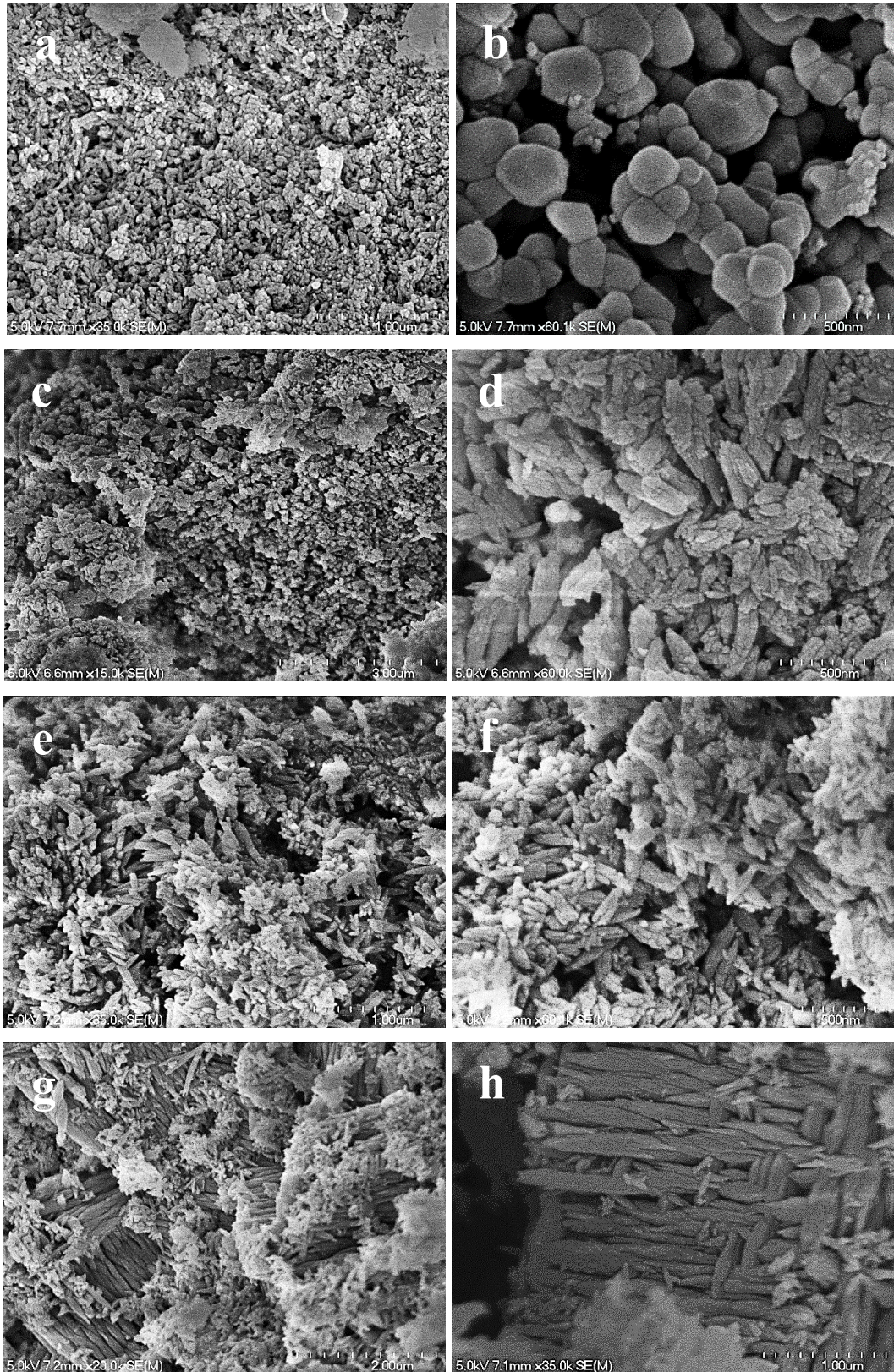


Figure 3.20: SEM images of HAp powders at different magnifications: a and b) H<sub>20</sub>, c and d) H<sub>40</sub>, e and f) H<sub>60</sub> and g and h) H<sub>80</sub>

Figure 3.21 shows the SEM images of the 800 °C calcined HAp samples (H<sub>20-800</sub>, H<sub>40-800</sub>, H<sub>60-800</sub> and H<sub>80-800</sub>). All samples displayed spherical morphology in their particles, with H<sub>60</sub> and H<sub>80</sub> showing minor neck formation which hints at diffusion and growth of

particles due to fusion. Particles sizes of all calcined samples varied from  $91.22 \pm 1.66$  to  $303.1 \pm 2.77$  nm as spherical particles (measured using SEM).

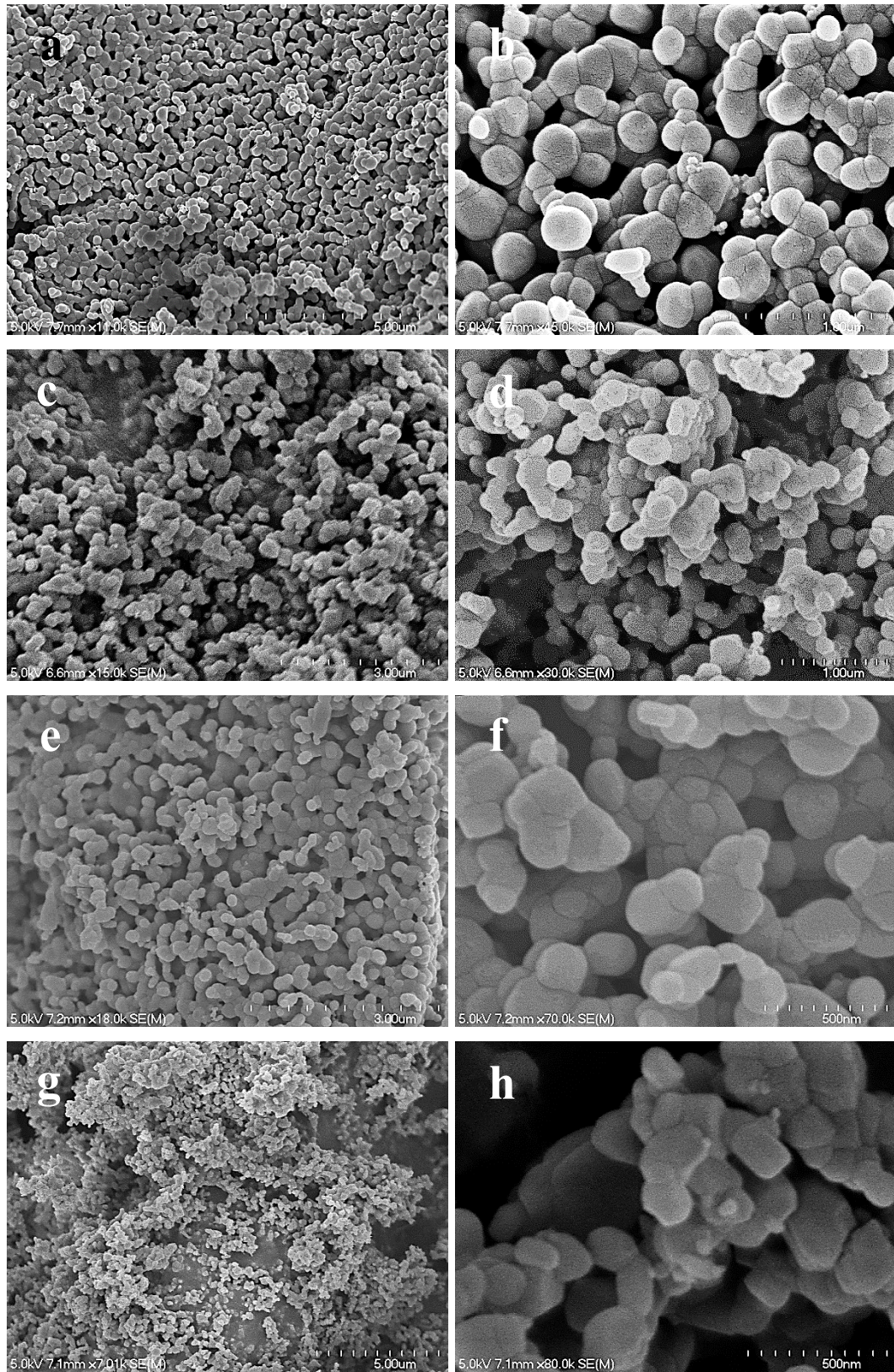
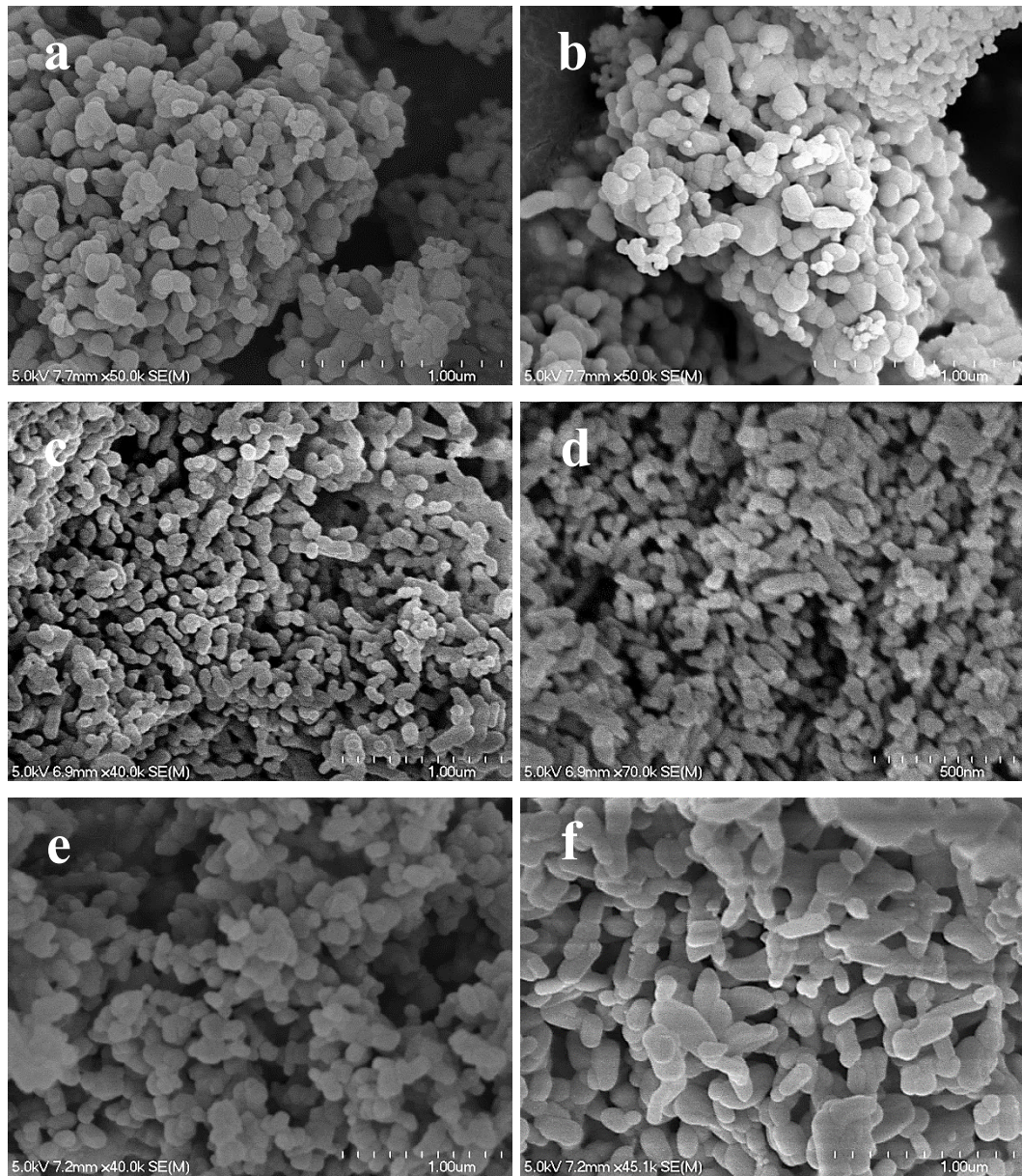


Figure 3.21: SEM images of HAp powders at different magnifications a & b) H<sub>20-800</sub>, c & d) H<sub>40-800</sub>, e & f) H<sub>60-800</sub> and g & h) H<sub>80-800</sub>

Figure 3.22 shows the SEM images of the 1000 °C calcined HAp samples (H<sub>20-1000</sub>, H<sub>40-1000</sub>, H<sub>60-1000</sub> and H<sub>80-1000</sub>). Although all samples showed signs of neck formation and fusion among particles, which is typical at such high temperatures, fusion is found to be more enhanced in H<sub>60</sub> & H<sub>80</sub> which signifies enhanced atomic diffusion among the particles. This fusion of particles due to the high temperature sintering effect has also been reported by other researchers[79, 272, 273].



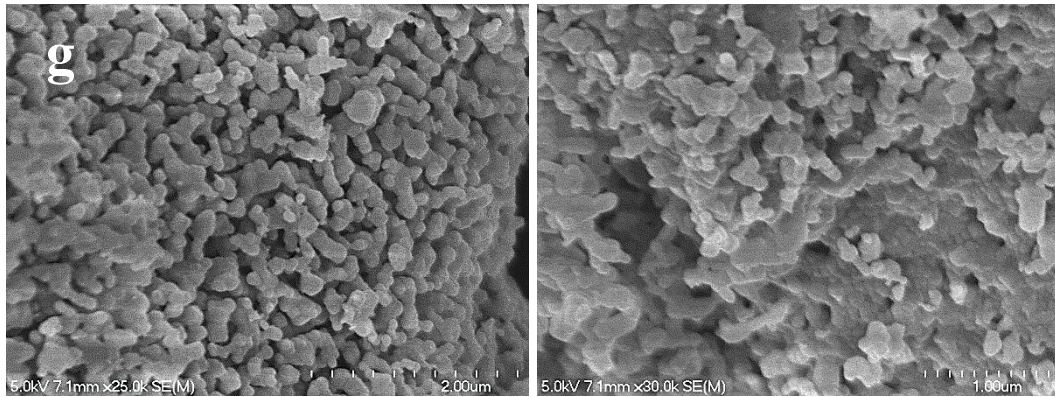


Figure 3.22: SEM images of HAp powders at different magnifications a & b) H<sub>20-1000</sub>, c & d) H<sub>40-1000</sub>, e & f) H<sub>60-1000</sub> and g & h) H<sub>80-1000</sub>

It was found that the sample that was reprecipitated at 80°C and calcined at 800°C, i.e., H<sub>80-800</sub> was found to be displaying the fusion and growth of HAp particles. Moreover, the 1000°C calcined version of this sample (i.e., H<sub>80-1000</sub>), was also found to be displaying sintering behaviour of smaller particles to form a solid structure, since composites will be sintered at 1000 °C hence H<sub>80-800</sub> will be a suitable morphology to start with. Furthermore, as per the XRD and FTIR studies, the H<sub>80-800</sub> displayed high purity HAp particles having an approx. 72 nm crystallite size (with much less compressive microstrain in the lattice) and a crystallinity index of approx. 0.95 (found using XRD). Based on all the results, it was expected that H<sub>80-800</sub>, was the most suitable matrix material for forming the composites with in this study.

### 3.4. Conclusions

This research reinforced that a re-precipitation-based strategy to synthesise HAp is an excellent approach to repurpose the waste animal bones but also to get the desired quality. This research added new information to the previous work done in this domain by exploring the effects of re-precipitation reaction temperature and calcination temperature on the morphology and shape of HAp particles, which is novel in the sense that the digest solution made by dissolving precipitated HAp (sintering defatted and deproteinised bovine bone at high temperature) in acid, may contain extra elements like Mg, which can influence the quality and morphology of reprecipitated HAp. As expected, increasing the re-precipitation temperature increased crystallinity and crystallite size, however the formation and stabilisation of disordered/amorphous calcium phosphate was also observed, which may be due to the presence of other elements in the solution. Finally, based on evolving morphology during calcination and crystallinity index, HAp reprecipitated at 80°C and calcined at 800°C, i.e., H<sub>80-800</sub> was selected as the most optimal matrix material to use for the intended composites.

# CHAPTER FOUR : SYNTHESIS OF CHARs FROM NEW ZEALAND PLANT FIBRES

---

## 4.1. Introduction

Thermochemical decomposition of biomass has a rich history of being used to produce, extremely useful products i.e., gas (syngas), liquid (bio-oil), and solid (biochar). Biochar, also known as the solid carbon rich product of biomass, is an environmentally friendly, inexpensive, chemically stable carbonaceous source, which in the past was mostly used for soil remediation, however modern research has led them to be used in advanced applications like in fuel cells and supercapacitors[207].

In this chapter, the results of research into the synthesis of char from natural plant fibres are described. This involved natural fibres from leaves of native New Zealand plants i.e., harakeke plant (*Phormium tenax*) and cabbage tree (*Cordyline australis*) which were harvested and charred. As described in chapter 2, both natural fibres are traditionally known for their strength, while harakeke plant fibres had been researched previously for different studies. The research described in this thesis on cabbage tree leaf fibres is pioneering. High temperature pyrolysis was used to obtain char from the natural plant fibres (i.e., carbonisation) and then fibrous char was further washed/modified using acid. Pyrolysis is a low cost, traditional technique to use for char development. The aim of all this is to develop suitable fibrous char that can be used in the HAp ceramic matrix as a reinforcement and so to create a composite of the two materials.

## 4.2. Materials and Methods

### 4.2.1. Materials

All chemicals and solvents used in the experimental work were employed as-received without further purification. Harakeke leaf fibres, which were processed through mechanical stripping (Foxton Flax Stripping Museum, NZ) and cabbage tree leaf fibres (sourced locally) were used to produce chars. The carbonisation of these samples was carried out in a muffle furnace under limited oxygen conditions. Sulphuric acid ( $H_2SO_4$ ) (Merck) and Hydrogen peroxide ( $H_2O_2$ ) (BDH) were used to make “piranha” solution (also known as “piranha etch” made using a 3:1 mixture of concentrated sulfuric acid ( $H_2SO_4$ ) with hydrogen peroxide ( $H_2O_2$ )). Ultra-pure water (Type 1) was used for all experimental and cleaning purposes. Sodium hydroxide (NaOH) (Merck) and sodium sulphite ( $Na_2SO_3$ )

(Merck) were used for alkali treatment. Ethanol was used for dispersion of the produced char.

#### 4.2.2. Fibre treatment

Fibre bundles were first defibrillated before being carbonised. Defibrillation of fibres was achieved by a high (170 °C) temperature alkali treatment. Initially long fibres were granulated using a lab scale granulator, as shown in Figure 4.1(a), and an 8 mm mesh followed by a high temperature alkali treatment. The as-received harakeke fibres were in bundle form and 5 wt% NaOH with 2 wt% sodium sulphite ( $\text{Na}_2\text{SO}_3$ ) treatment was carried out using a laboratory pulp digester. Debundling/separation of fibre bundles are traditionally carried out in paper industries using an appropriate alkali treatment so as to obtain elementary fibres by removing most of the lignin content (hence the process is also known as “delignification”). The fibre to solution ratio used was 1:8 by weight. The laboratory pulp digester as shown in Figure 4.1(b), has the capacity to hold four stainless steel canisters (approx. 1 L capacity) into which a pre weighed amount of fibres with pre-mixed solution were poured. The alkali treatment and heating parameters were taken from previous published research by Efendy and Pickering [274] on harakeke fibres i.e. heat treatment at 170 °C for 40 minutes. The volume of the chamber is approx. 15 L, so the remaining capacity of the chamber was filled by water, which allows heat transfer from the walls of the chamber to the canisters. The shell of the chamber is lined with heating elements regulated by a PID-controller which means the pressure inside the chamber was entirely dependent on the heating cycle. For achieving an even distribution of heat, the vessel is rotated through 110° (from an upright position).

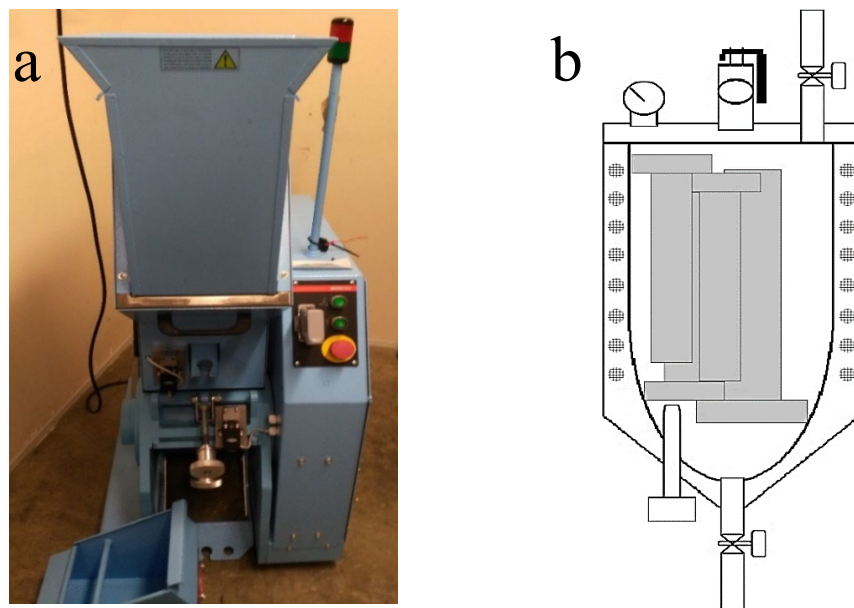


Figure 4.1: (a) Lab scale granulator and (b) schematic of a pulp digester.

After the pre-set time, the digester and its contents were rapidly cooled to approx. 30 °C, to avoid over exposure of fibres to alkali. Initially, steam was released followed by the draining of hot water. Before taking out the canisters, cold water was circulated and drained several times, to make sure the canisters reached manageable temperatures (i.e. were made safe to be handled manually (approx. 30 °C)). The warm digested fibres from canisters were placed onto a metallic wire mesh filter and washed for approx. 10 minutes using tap/flowing water. The cleaned fibres were then dried in a drying oven at 80°C for 48 hours.

It is found for harakeke fibres that a heat treatment of 170°C for 40 minutes produced optimal fibre separation, hence for comparison purposes cabbage tree fibres were also treated/defibrillated using the same parameters as used for the harakeke fibres.

#### **4.2.3. Preparation, modification, and dispersion of Biochar**

Biochars from both harakeke and cabbage tree defibrillated fibres were prepared in a covered & sealed crucible (with oxygen limited conditions) and placed in a muffle furnace. They were heated at  $\approx 10$  °C/min up to 850 °C and maintained at this temperature for 20 minutes, followed by natural cooling in the furnace. The temperature 850 °C, was chosen after performing the TGA analysis on both defibrillated harakeke (Hsep) and cabbage tree leaf fibres (Csep) (both thermograms are attached as Appendix D). It is important to minimise oxidative damage by allowing sufficient time for the samples to cool down below 100 °C. The biochar was initially washed using water and then 0.1 M HCl, to remove unwanted content following a previously reported procedure[275, 276]. For the modification & purification of biochar, piranha solution (i.e. the mixture of sulfuric acid (H<sub>2</sub>SO<sub>4</sub>) and hydrogen peroxide (H<sub>2</sub>O<sub>2</sub>)) was used, which is highly oxidative and can remove metals & organic contamination as well as being able to modify carbon structures[277]. The usage of piranha solution for purification and oxidation of carbonaceous structures is also reported in previous research[278]. The acid washed biochar was added to freshly prepared piranha solution (1 gram biochar in 50 mL solution) and was left to soak for approx. 20 minutes. After that the biochar was filtered and washed with water several times followed by dispersion in 70 vol.% ethanol-water solution. The piranha treated biochar was then subjected to characterisation. Figure 4.2 outlines, the complete process related to char synthesis.

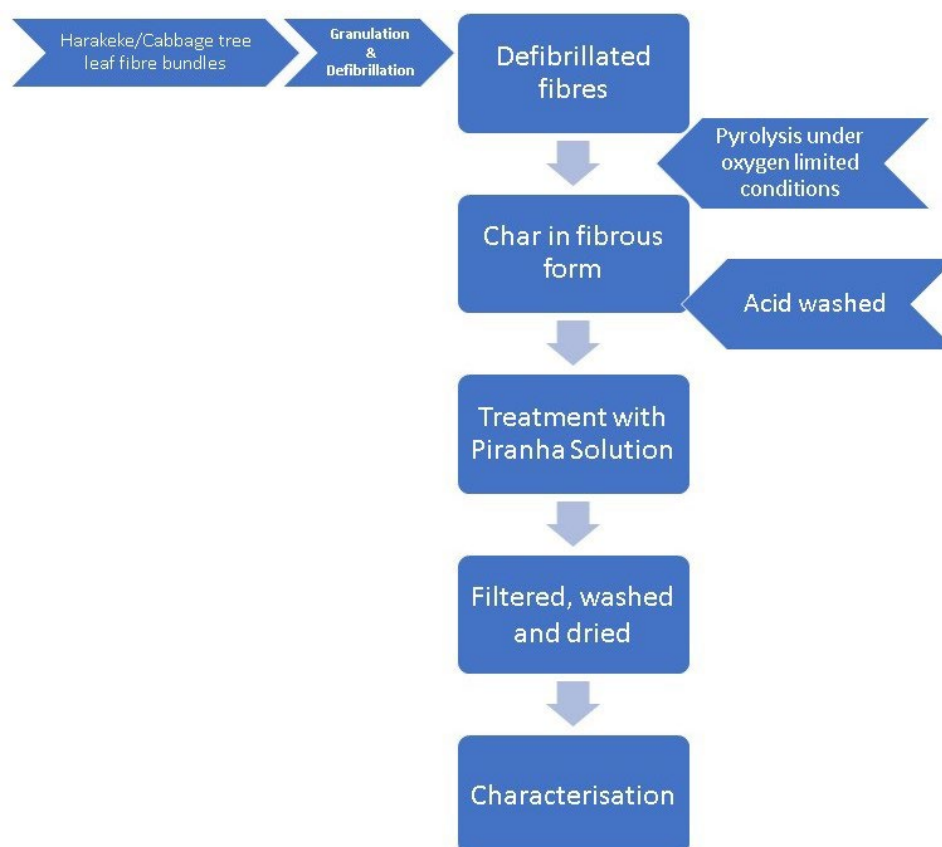


Figure 4.2: A pictorial representation of the processing steps summarizing the harvesting of char from New Zealand natural fibres.

#### 4.2.4. Characterisation

The evolving phase composition from natural fibres to purified biochar fibres was determined by X-ray diffractometry (Panalytical Empyrean Series 2 diffractometer) with Cu K $\alpha$  radiation at 45 kV and 40 mA ( $\lambda = 1.5406 \text{ \AA}$ ) with a step size of  $0.0260^\circ$ . A Fourier transform infrared (FTIR) spectrometer (Spectrum 100A Express, Perkin Elmer) was also utilised for recording IR spectra via the KBr disc method (recorded between  $4000 - 450 \text{ cm}^{-1}$ ) (5 samples, with 5 scans per sample). A spectral resolution of  $4 \text{ cm}^{-1}$  was used. Raman spectra of all biochars were recorded with a Raman station 400F (PerkinElmer) spectrometer with a spectral resolution of  $1 \text{ cm}^{-1}$  (using a 785 nm near-infrared laser) (5 samples, with 5 scans per sample). Samples were analysed by Raman while placed on aluminium foil, with the laser pointer visually focussed onto the surface of each location analysed on the carbonaceous samples. Laser power set to approximately 20 mW (20% of maximum, estimated to be  $\approx 6 \times 10^5 \text{ W/m}^2$  on the  $\approx 200 \text{ }\mu\text{m}$  diameter spot) was used to acquire spectra from all samples (after initial trials) for consistency across the range of materials analysed. Each spectrum was acquired as the sum of five repeats of 60 second exposures on the same location on the sample. Five separate spectra were acquired at different locations on each sample analysed. The morphological characteristics were recorded using a scanning electron microscope (SEM) (S-4700, Hitachi) instrument.



Thermogravimetric analysis (TGA) (STA 8000, Perkin Elmer) for proximate (the quantitative analysis of moisture, ash, volatile matter, and fixed carbon) analysis was also carried out. Table 4.1, outlines sample codes used to identify samples and their meaning.

Table 4.1: Sample coding and their brief descriptions.

S. No.	Sample	Description	Code
1	Raw harakeke fibres bundle	Raw harakeke fibres taken out of the leaves	H <sub>Bundle</sub>
2	Harakeke fibres defibrillated	Harakeke fibres obtained after defibrillation process	H <sub>Def</sub>
3	Raw cabbage tree leaf fibres bundle	Raw fibres taken out of the leaves	C <sub>Bundle</sub>
4	Cabbage tree leaf fibres defibrillated	Fibres obtained after defibrillation process	C <sub>Def</sub>
5	Harakeke char as formed	Char made from H <sub>Def</sub>	HC <sub>AF</sub>
6	Harakeke char acid washed	Char obtained after acid washing of HC <sub>AF</sub>	HC <sub>AW</sub>
7	Harakeke char piranha solution treated	Char obtained after piranha solution treatment of HC <sub>AW</sub>	HC <sub>PT</sub>
8	Cabbage tree leaf char as formed	Char made from C <sub>Def</sub>	CC <sub>AF</sub>
9	Cabbage tree leaf char acid washed	Char obtained after acid washing of CC <sub>AF</sub>	CC <sub>AW</sub>
10	Cabbage tree leaf char piranha solution treated	Char obtained after piranha solution treatment of CC <sub>AW</sub>	CC <sub>PT</sub>

## 4.3. Results and Discussion

### 4.3.1. Fourier transform infrared spectroscopy (FTIR) Analysis

FTIR was used to study the chemical structure of harakeke fibres (bundled (H<sub>Bundle</sub>) and defibrillated (H<sub>Def</sub>)). The identified peaks of interest are shown in IR spectra in Figure 4.3. Upon comparison of the spectra from both sample types, no visible change was found in the bands at 2922 and 2855 cm<sup>-1</sup>, which are usually attributed to the C–H stretching mode in cellulose, however a very small change in the intensity of the two characteristic lignin bands at 1508 and 1596 cm<sup>-1</sup> (which relate to the aromatic skeletal vibration of lignin) and the band at 1461 cm<sup>-1</sup> (attributed to the C–H deformations in lignin), was found in defibrillated fibres (H<sub>Def</sub>, Figure 4.3 (b)) and hence it is plausible to assume that a very small (almost negligible) amount of lignin was removed due to the mild alkali treatment. There was found, however, to be a considerable change in the intensity of the carbonyl band (>C=O) at 1734 cm<sup>-1</sup> in defibrillated fibres (H<sub>Def</sub>, Figure 4.3 (b)), which is a signature peak of hemicellulose. Similarly, the decrease in the intensity of the peak at approx. 1250 cm<sup>-1</sup> (stretching vibration of the C–O) peak) suggests the partial removal of hemicelluloses in the treated fibres. The peak at around 1638 cm<sup>-1</sup> is principally associated with absorbed water. The prominent band at around 1052 cm<sup>-1</sup> is attributed to the C–O, C–C stretching

and C–OH stretching vibrations in hemicellulose, cellulose and lignin. The sharp band at around  $899\text{ cm}^{-1}$  is due to the  $\beta$ -glycosidic bond, and is also representative of the occurrence of the crystalline phase of cellulose type I. The bands at 1461, 1381, 1328 and  $1250\text{ cm}^{-1}$  represent C–H, OH or  $\text{CH}_2$  bending [279-282].

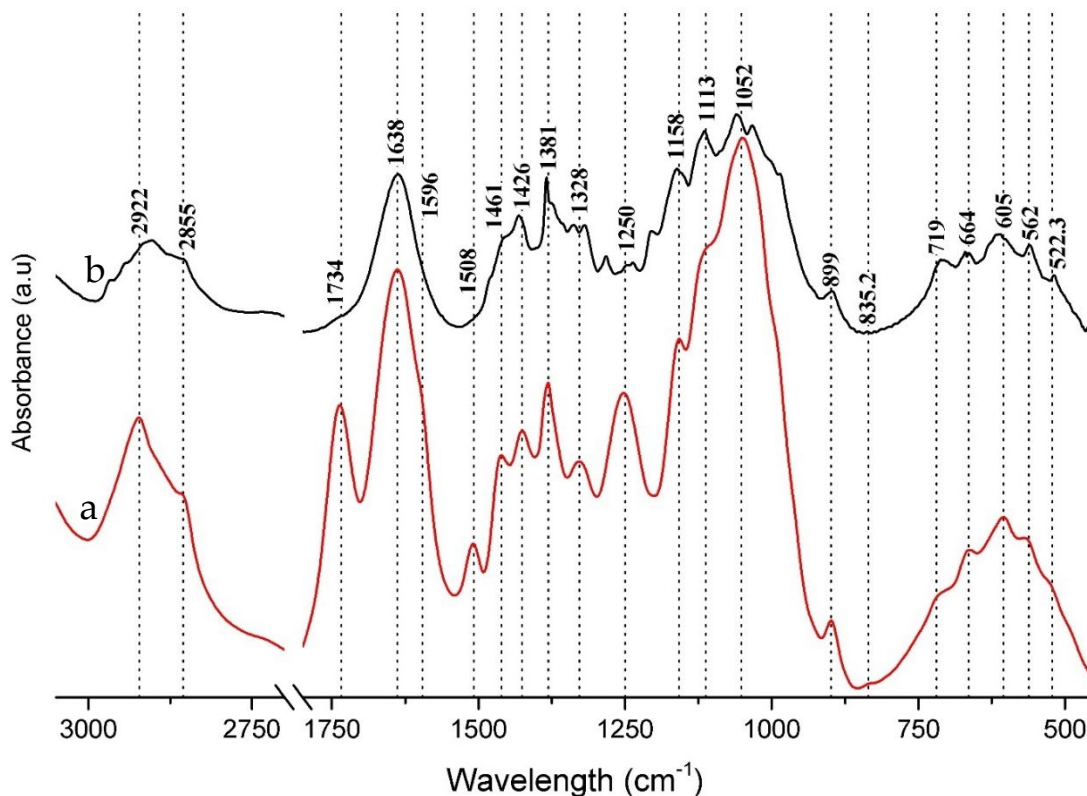


Figure 4.3: IR spectra of a)  $H_{\text{bundle}}$  and b)  $H_{\text{Def}}$ , representing decrease of lignin and hemicellulose due to the mild alkali treatment.

The molecular structures of char produced from harakeke fibres and their treated forms were also studied using FTIR and represented as Figure 4.4. All the identified IR peaks and their assignments are presented in table 4.2 and have been reported in previous studies[283-286]. The peaks at  $1636$  and  $1314\text{ cm}^{-1}$  corresponding to carbonyl groups, which appear to have increased with the piranha modification in defibrillated fibres ( $H_{\text{CPT}}$ , Figure 4.4 (c)), may be due to oxidation, which is consistent with findings from previous studies [287, 288]. The peaks in the range from  $2920$  to  $2855\text{ cm}^{-1}$  which are assigned to C–H bond stretching in aliphatic formation, is a solid indication of the presence of cellulose, hemicellulose and lignin in the precursor. The peak at around  $1620\text{ cm}^{-1}$  is attributed to the presence of C=C and C=O stretching in aromatic rings.

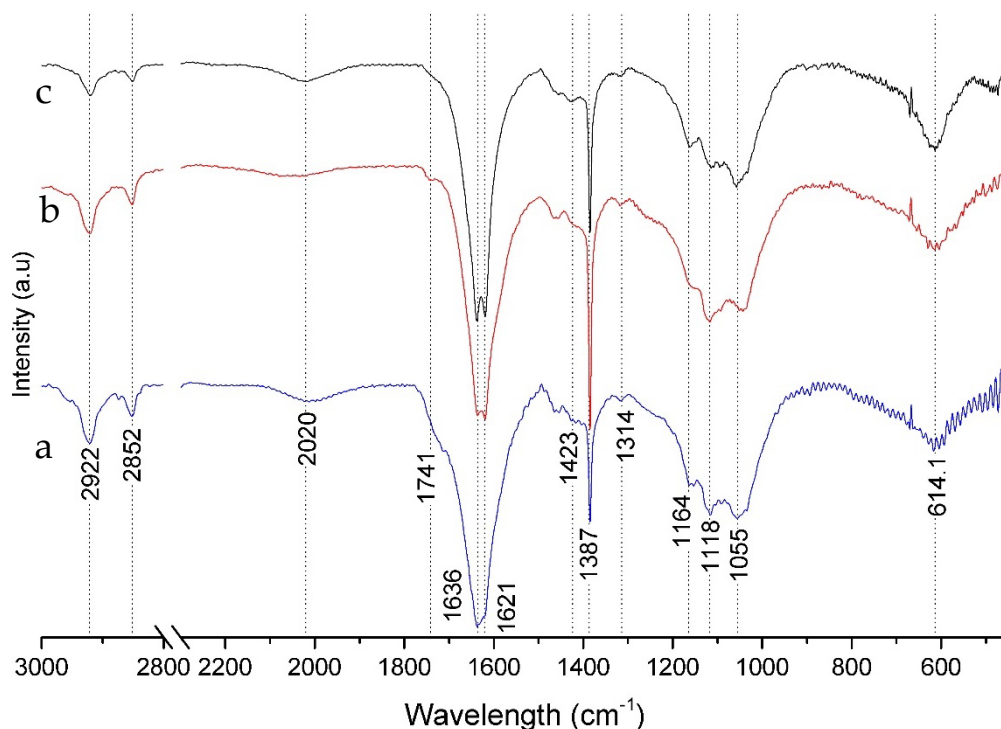


Figure 4.4: IR spectra of a) HC<sub>AF</sub> (harakeke char as formed), b) HC<sub>AW</sub> (harakeke char acid washed) and c) HC<sub>PT</sub> (harakeke char piranha solution treated).

Figure 4.5 details all the identified peaks related to the chemical structure of cabbage tree fibres (bundled ( $C_{\text{Bundle}}$ ) and defibrillated ( $C_{\text{Def}}$ )). An increase in the bands associated with the C–H stretching mode in cellulose at around 2922 and 2855  $\text{cm}^{-1}$  was found in the defibrillated fibres ( $C_{\text{Def}}$ , Figure 4.5 (b)). Moreover, a minor change, in defibrillated fibres ( $C_{\text{Def}}$ , Figure 4.5 (b)), was observed in the intensity of the characteristic lignin band at 1508  $\text{cm}^{-1}$  (due to aromatic skeletal vibrations of lignin) and the band at 1461  $\text{cm}^{-1}$  (attributed to the C–H deformations in lignin), which might be due to mild alkali treatment that caused removal of lignin. Furthermore, a minor decrease in the intensity of the carbonyl band ( $>\text{C}=\text{O}$ ) at 1734  $\text{cm}^{-1}$ , (a signature peak of hemicellulose) as well as in the intensity of the peak at approx. 1250  $\text{cm}^{-1}$  (stretching vibration of the C–O) peak suggests a modest removal of some of the hemicelluloses from the treated fibres ( $C_{\text{Def}}$ , Figure 4.5 (b)). The peak at around 1638  $\text{cm}^{-1}$  is associated with absorbed water. A significant increase in the peak at around 1059  $\text{cm}^{-1}$  (attributed to the C–O, C–C stretching and C–OH stretching vibrations in hemicellulose, cellulose and lignin) was noted, along with increase in the band at around 899  $\text{cm}^{-1}$  due to the  $\beta$ -glycosidic bond, which is also representative of the occurrence of the crystalline phase of cellulose type I [279-282, 289].

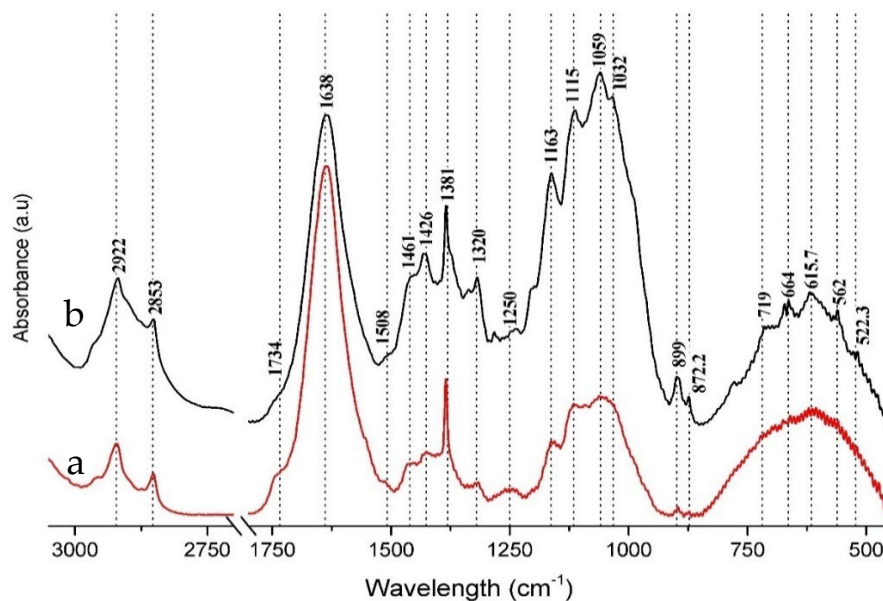


Figure 4.5: IR spectra of a)  $C_{\text{bundle}}$  and b)  $C_{\text{Def}}$ , representing key changes due to defibrillation.

Figure 4.6. presents the IR spectra of char produced from cabbage tree leaf fibres and their treated forms, with Table 4.2 summarising all the possible assignments of peaks observed in Fig. 4.6. The carbonyl peaks at  $1636$  and  $1320\text{ cm}^{-1}$  appeared to increase after acid washing ( $CC_{\text{AW}}$ , Figure 4.6 (b)) and piranha modification ( $CC_{\text{PT}}$ , Figure 4.6 (c)) which may be due to oxidation, an observation which is consistent with previous studies [287, 288]. The peak at around  $873\text{ cm}^{-1}$  which can be assigned to aromatic C–H but also possibly to C–O bending from carbonate, can be an indication of the presence of carbonate impurity, similarly peak at around  $1450\text{ cm}^{-1}$  can also be due to the presence of carbonate impurity.

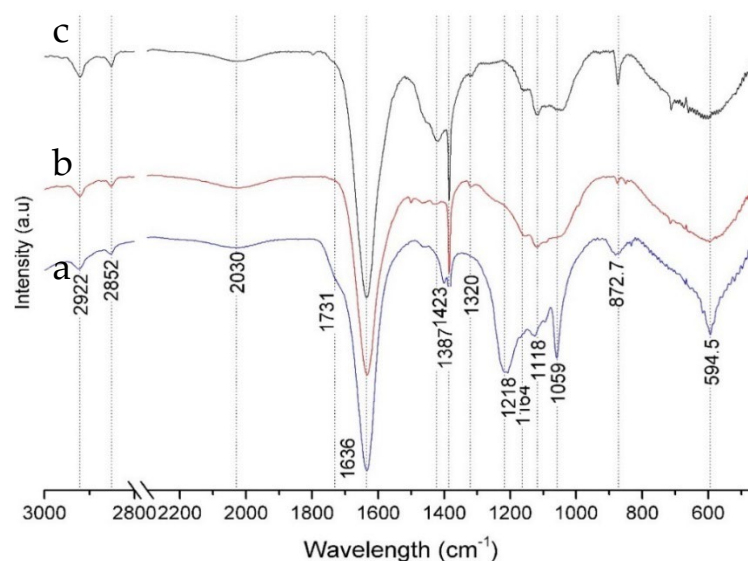


Figure 4.6: IR spectra of a)  $CC_{\text{AF}}$  (cabbage tree leaf char as formed), b)  $CC_{\text{AW}}$  (cabbage tree leaf char acid washed) and c)  $CC_{\text{PT}}$  (cabbage tree leaf char piranha solution treated).

Table 4.2: Possible IR assignments of char made from natural plant fibres.

IR Assignments	Harakeke leaf char			Cabbage tree leaf char		
	HC <sub>AF</sub>	HC <sub>AW</sub>	HC <sub>PT</sub>	CC <sub>AF</sub>	CC <sub>AW</sub>	CC <sub>PT</sub>
C-O-H Bending	614	614	614	594.5	594.5	594.5
Aromatic C-H as well as C-O from carbonate	--	--	--	872.7	872.7	872.7
C-O-C symmetric stretching in aliphatic groups and acid derivatives	1046	1046	1046	1059	1059	1059
C-O-C symmetric stretching in ester groups of cellulose and hemicellulose	1118	1118	1118	1118	1118	1118
C-O symmetric stretching in ester groups of cellulose and hemicellulose	1162	1162	1162	--	1164	1164
Aromatic C-O and phenolic -OH structures	--	--	--	1218	--	--
C-O stretching	1314	1314	1314	--	1320	1320
CH <sub>3</sub> deformation	1387	1387	1387	1387	1387	1387
In-plane OH bending and C-O stretch of dimmers	--	--	1423	--	1423	1423
C=C stretching of aromatic components, C=O stretching of conjugated ketones.	1620	1620	1620	--	--	--
C=O stretching	1636	1636	1636	1636	1636	1636
C=O stretching	--	1741	1741	1731	1731	1731
C=C stretching vibration of ketones, aldehydes or carboxylic group	2021	2021	2021	2030	2030	2030
Symmetric C-H stretching of aliphatic CH <sub>x</sub>	2853	2853	2853	2852	2852	2852
Aliphatic C-H stretching	2922	2922	2922	2922	2922	2922

#### 4.3.2. X-ray diffraction analysis

The X-ray diffractograms of raw harakeke fibres bundles (H<sub>Bundle</sub>) and its defibrillated form made using alkali treatment (H<sub>Def</sub>) are shown in Figure 4.7. The major crystalline peak for harakeke fibre bundles was found around 22.5° 2θ, corresponding to the cellulose crystallographic plane (0 0 2). The intensity of the cellulose crystallographic plane (0 0 2) peak was found to increase significantly as a result of alkali treatment implying the removal of pectins and other amorphous constituents. The other major peak at around 16° 2θ also corresponds to crystalline cellulose and, due to its high hemicellulose content, appeared as one single peak. However, after alkaline treatment, it appeared to start splitting, mainly due to the removal of a small amount of hemicellulose content.

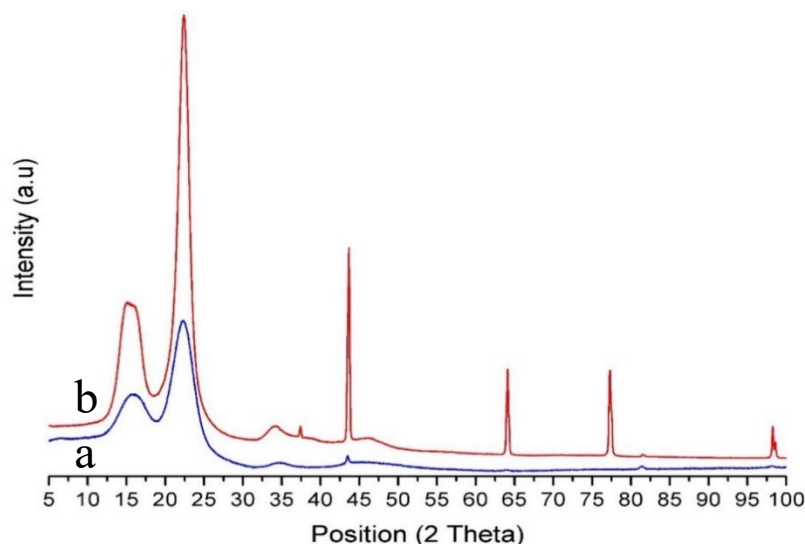


Figure 4.7: X-ray diffractogram of, a) raw harakeke fibres bundles ( $H_{\text{Bundle}}$ ) and, b) its defibrillated form made using alkali treatment ( $H_{\text{Def}}$ )

The XRD patterns of the harakeke biochars (as formed, acid washed and piranha treated) are represented in Figure 4.8. All three diffractograms showed diffuse graphite peaks at low and high 2theta values. The diffuse and broad bands indicate the existence of short range order in the carbon structure, while the sharp and narrow peaks is characteristic of crystalline phases in the carbon structure with long-range order. In the diffractogram of piranha solution treated harakeke leaf fibre char ( $HC_{\text{PT}}$ ) depicts both the broad bands related to short range carbon ordering, and a sharp peak at a  $2\theta$  value of  $25^\circ$  signified the presence of graphitic basal planes. These results closely match with previous studies[290, 291]. It appeared that acid washing, and piranha treatment had resulted in a removal of impurities.

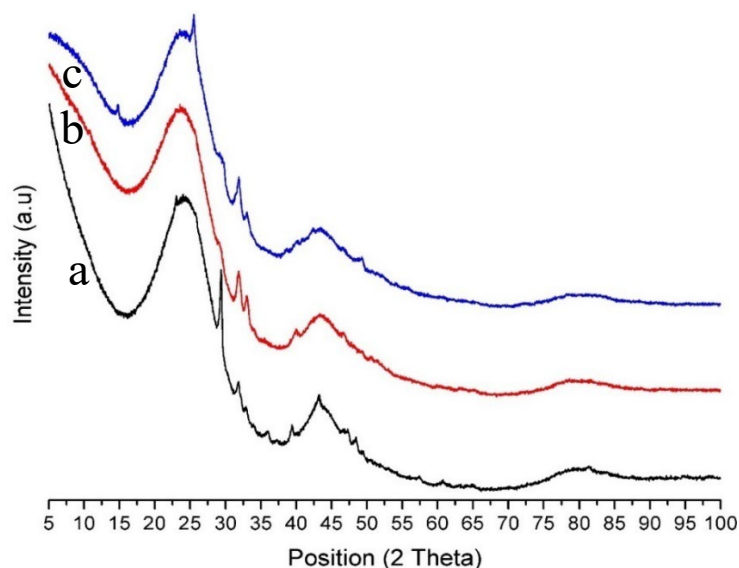


Figure 4.8: X-ray diffractogram of, a) char made from delignified harakeke leaf fibres ( $HC_{\text{AF}}$ ), b) Acid washed harakeke leaf fibre char ( $HC_{\text{AW}}$ ) and c) piranha solution treated harakeke leaf fibre char (previously acid washed) ( $HC_{\text{PT}}$ ).

Figure 4.9 displays the comparison of raw cabbage tree leaf bundles ( $C_{\text{Bundle}}$ ) and its defibrillated form which was prepared using alkali treatment ( $C_{\text{Def}}$ ). Similar to harakeke fibres, raw cabbage tree leaf bundles ( $C_{\text{Bundle}}$ ) also display a major crystalline peak at around  $22.5^\circ 2\theta$ , corresponding to the cellulose crystallographic plane (0 0 2), which significantly increased after alkali treatment due to removal of pectins and other amorphous constituents. The other important peak related to crystalline cellulose was also found at around  $16^\circ 2\theta$ , which after alkaline treatment also showed signs of splitting, due to the removal of a small amount of hemicellulose content. Other sharp peaks present in raw cabbage tree leaf bundles ( $C_{\text{Bundle}}$ ) are expected to be of biochar related impurities like iron oxide, calcite etc.

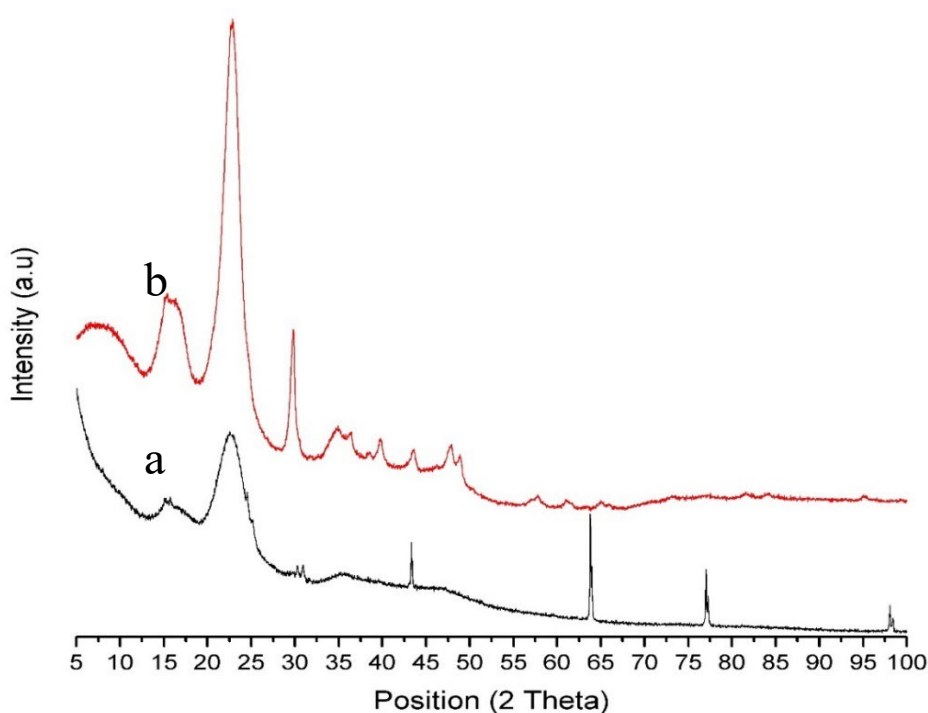


Figure 4.9: X-ray diffractogram of, a) raw cabbage tree leaf bundles ( $C_{\text{Bundle}}$ ) and, b) its defibrillated form made using alkali treatment ( $C_{\text{Def}}$ )

The XRD patterns of the cabbage tree leaf char (as formed, acid washed and piranha treated) are represented in Figure 4.10. Similar to harakeke char, broad bands of amorphous carbon along with a sharp peak at a  $2\theta$  value of  $25^\circ$  signifies the presence of graphitic basal planes. Here the effects of acid washing, and piranha treatment are much more pronounced, as it appeared more impurities had been removed.

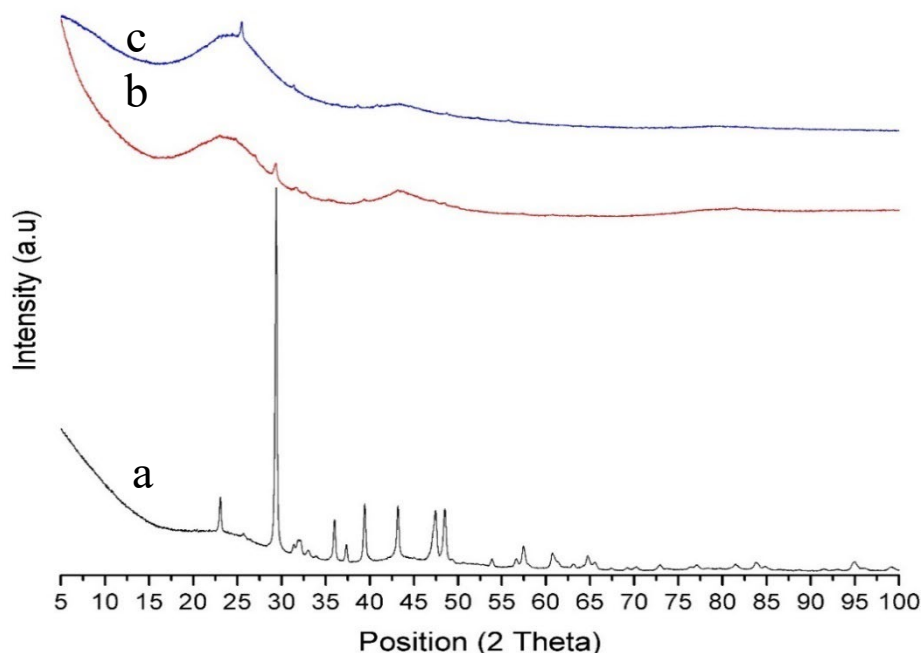


Figure 4.10: X-ray diffractogram of, a) char made from delignified cabbage tree leaf fibres ( $CC_{AF}$ ), b) Acid washed cabbage tree leaf fibre char ( $CC_{AW}$ ) and c) piranha solution treated cabbage tree leaf fibre char (previously acid washed) ( $CC_{PT}$ ).

#### 4.3.3. Raman Spectroscopy Analysis

Raman spectroscopy is useful for characterising carbonaceous materials. Its high sensitivity to  $sp^2$  carbon structures and high resolution makes it valuable for characterising biochar. Usually in case of carbonaceous materials two distinct bands (so-called G and D bands) are obtained. The D-band usually represents disordered amorphous graphite ( $sp^3$ -hybridized carbon atoms) while the G-band represents ordered graphitic crystallites ( $sp^2$ -hybrid carbon atoms). The G band is usually observed at approximately  $1580\text{ cm}^{-1}$ , and it represents the presence of organised  $sp^2$  domains, while the D band indicates the defects associated with the breaking of the hexagonal symmetry of the carbon atoms and can be observed at approximately  $1350\text{ cm}^{-1}$ . This means that for crystalline graphite, there will be only one peak (i.e. for a monocrystalline carbonaceous material) at around  $1580\text{ cm}^{-1}$ , however for disordered amorphous carbonaceous material there will be two peaks at  $1350$  and  $1600\text{ cm}^{-1}$ . Apart from the appearance of bands, the relationship between the intensities of both bands, can also be used to understand a number of important features of carbonaceous materials, including the crystallite size and can be related to the number of defects present. In depth Raman studies of carbonaceous material, involves the deconvolution of bands which are the summation of Raman scattering from many bonds.

The Raman spectra of the harakeke and cabbage tree leaf char are presented in Figure 4.11 and 4.12, respectively. All the spectra displayed the typical overlapping D and G bands as discussed above, which is a solid indication of formation of a well carbonised



char[292]. Both figures represent the changing D- and G-band positions as well as the intensity ratio ( $I_D/I_G$ ) of the acid washed and piranha solution treated sample (Appendix E describes the method used to analyse the Raman spectra, which is same as that used by McDonald-Wharry et.al. [205]). The Raman analysis of as formed harakeke ( $HC_{AF}$ ) and cabbage tree leaf ( $CC_{AF}$ ) chars displays the distribution and state of  $sp^2$  carbons, embedded in a disordered matrix of both  $sp^3$  and  $sp^2$  carbon. The observed changes in the D-band, and G-band positions as well as the intensity ratio ( $I_D/I_G$ ) are shown in Figures, 4.13, 4.14 and 4.15. It is to be noted one common problem with the Raman analysis is that excessive or concentrated laser irradiation can alter the surface of the sample, so resulting in false results, however in this Raman analysis, a reduced laser power (20% of maximum) and a relatively large spot size (approx. 200  $\mu m$ ) was used, to reduce the risk surface modification.

The intensity ratio of the D and G bands ( $I_D/I_G$ ) has an important meaning for char as it is directly related to the ordering of the graphitic structure, hence the extent of disorder in the carbon structure with respect to graphitic carbon can easily be estimated using the intensity ratio ( $I_D/I_G$ ). The intensity ratios ( $I_D/I_G$ ) of all char samples are presented in Figure 4.13, where for harakeke char, the ratio decreased sharply after acid washing ( $HC_{AW}$ ) and piranha treatment ( $HC_{PT}$ ) (with respect to as formed harakeke char i.e.,  $HC_{AF}$ ) which may be due to removal of amorphous carbon and increased ordering of the residual structures, however for cabbage tree leaf char, the ratio increased (both after acid washing ( $CC_{AW}$ ) and piranha treatment ( $CC_{PT}$ ) (with respect to as formed cabbage tree leaf char i.e.,  $CC_{AF}$ )) indicating an increase of defects caused by the acidic treatment. Depolymerisation during carbonisation resulted in the formation of isolated  $sp^2$  carbon atoms (having aromatic ring structures) so any increase in the  $I_D/I_G$  indicated the existence of more  $sp^3$  bonds i.e., more transitions of  $sp^2$  to  $sp^3$  which ultimately means, more induced defects and disorders[293].

The peak positions of the G and D bands vary with many factors including the laser wavelength, nanocrystallite size or intercalation of oxygen atoms. The changes in the wavenumber position of the G and D band (peak position) has specific interpretations, and in general, an increase in value is known as a blue shift and a decrease as a red shift. The presence of oxygen containing functional groups in the char structure, has a significant effect on the peak position of the G band, mainly because the G band is essentially strain related, hence a blue shift of the G band would be interpreted as modification of the carbon texture (or more precisely its nanotexture). Moreover, a red shift in G band position can be linked with tensile strain in the fullerene like structure (mainly curvature induced) as well as being due to the limited relaxation of compressive strain in the graphitic-like

network[294-296]. In this study, it was found that the harakeke char (figure 4.14) is showing a slight red shift in G band position, after piranha solution treatment, however cabbage tree leaf char (figure 4.15) showed appreciable blue shift in the position of G band, hence it can be inferred that piranha solution treatment has influenced/modified graphitic-like structure of both the chars, but in a different way. In the case of the D band, both samples showed a blue shift after piranha treatment which can be attributed to the induced compressive strain due to modification in the carbon texture[297, 298].

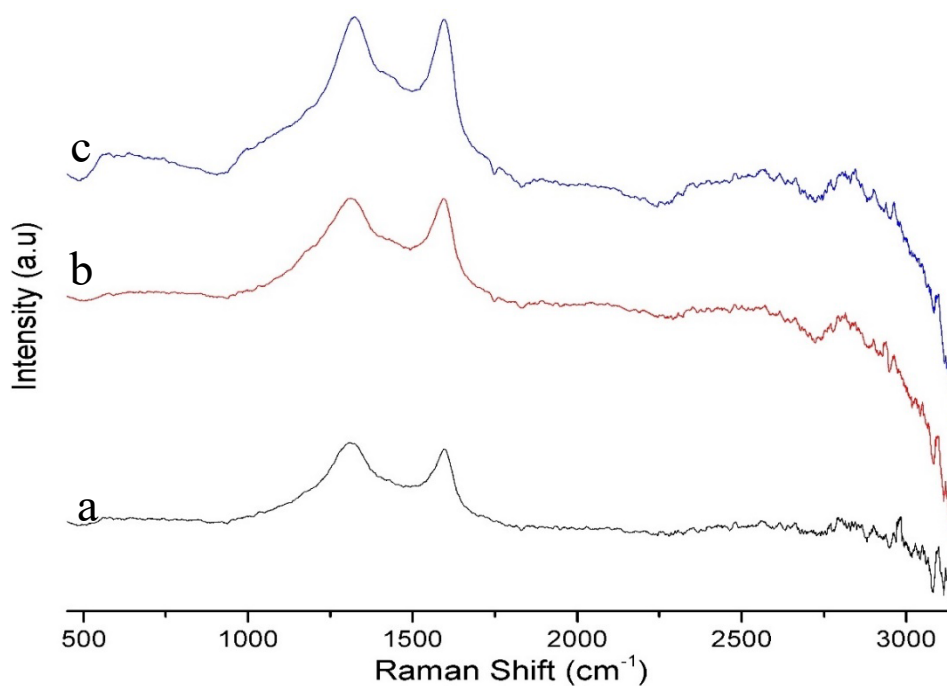


Figure 4.11: Raman spectra of a) HC<sub>AF</sub>, b) HC<sub>AW</sub> and c) HC<sub>PT</sub>

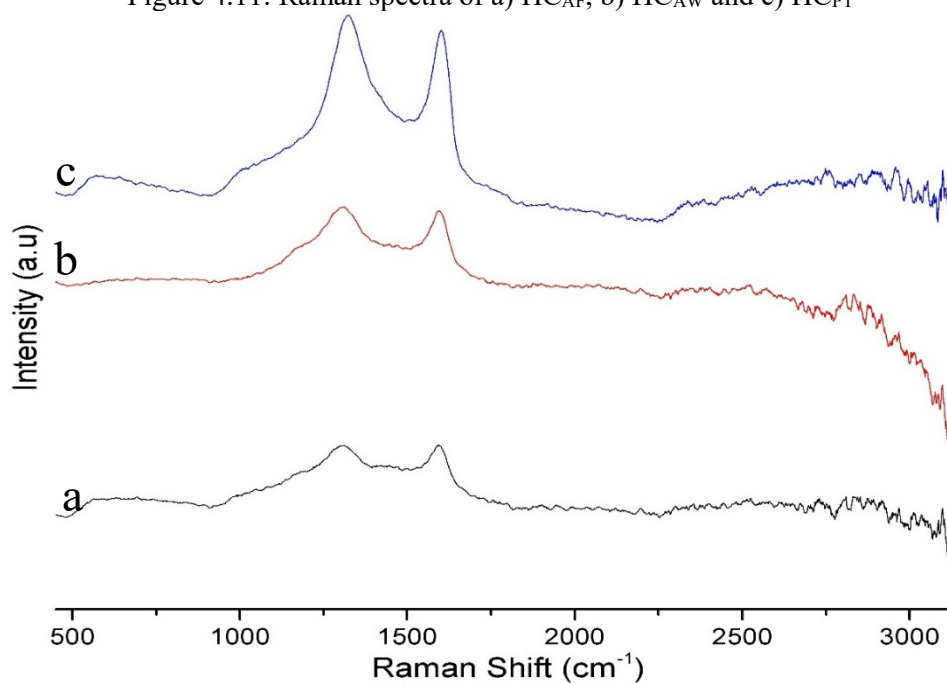


Figure 4.12: Raman spectra of a) CC<sub>AF</sub>, b) CC<sub>AW</sub> and c) CC<sub>PT</sub>.

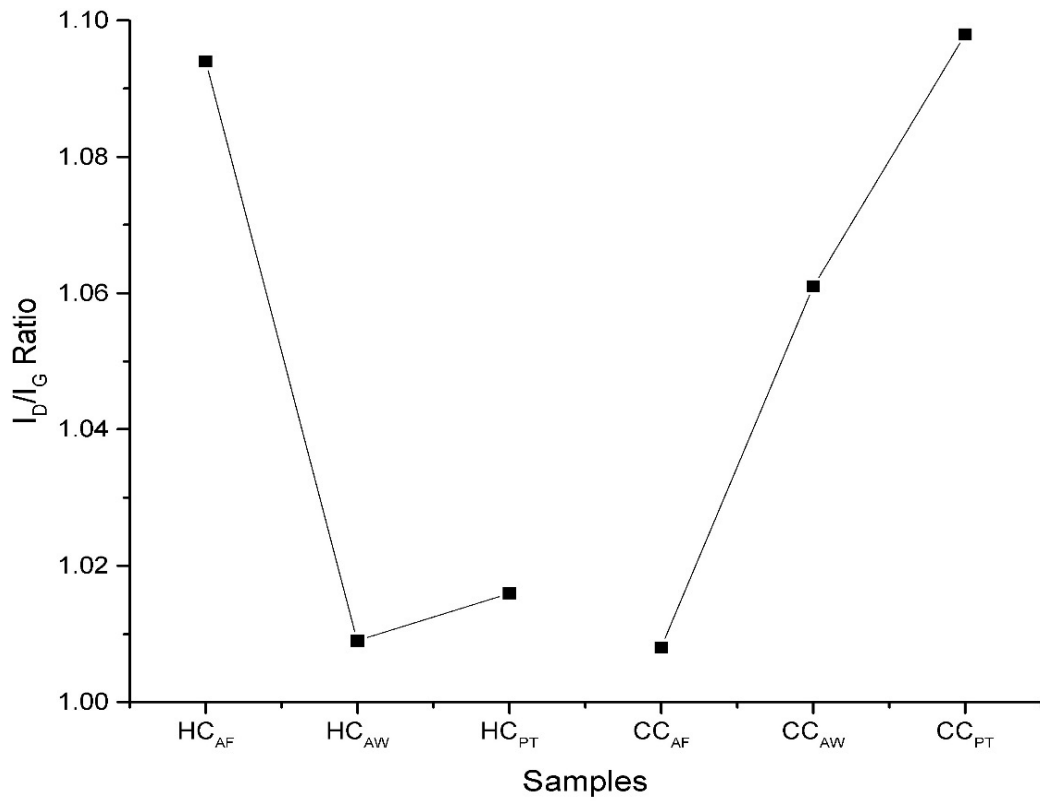


Figure 4.13: ( $I_D/I_G$ ) ratios of HC<sub>AF</sub>, HC<sub>AW</sub>, HC<sub>PT</sub>, CC<sub>AF</sub>, CC<sub>AW</sub> and CC<sub>PT</sub>.

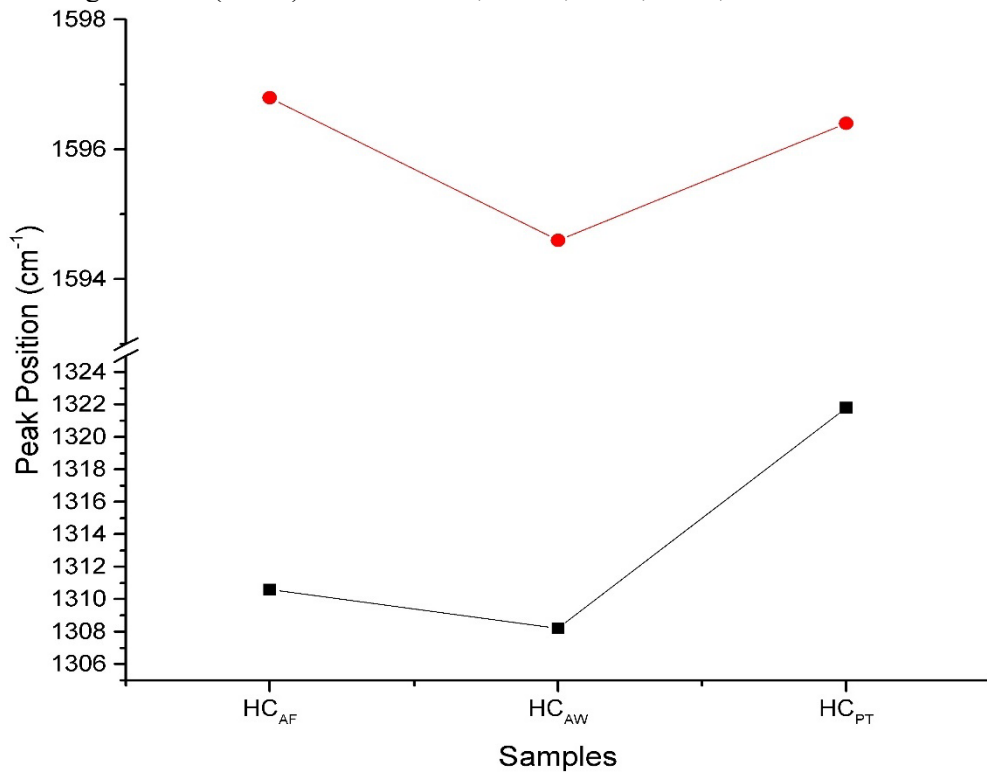


Figure 4.14: D and G band peak positions of HC<sub>AF</sub>, HC<sub>AW</sub> and HC<sub>PT</sub>.

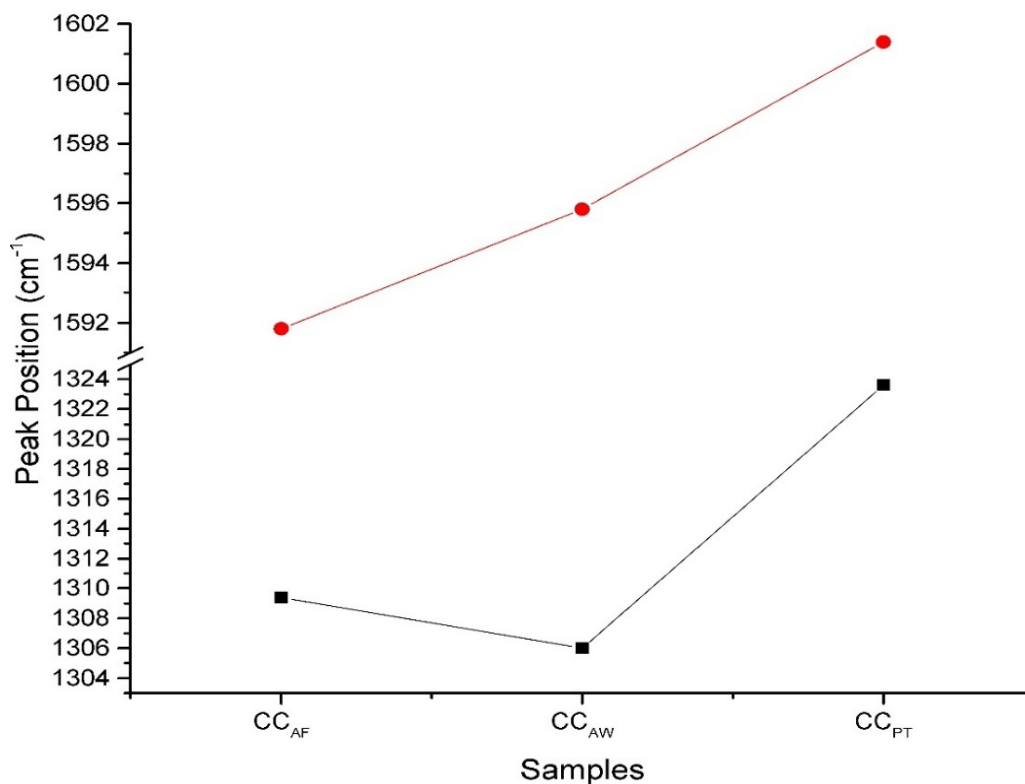


Figure 4.15: D and G band peak positions of CC<sub>AF</sub>, CC<sub>AW</sub> and CC<sub>PT</sub>.

#### 4.3.4. Proximate Analysis via TGA

In this study, proximate analysis of biomass (both defibrillated harakeke fibres (H<sub>Def</sub>) and cabbage tree leaf fibres (C<sub>Def</sub>)) and biochar samples (both piranha treated harakeke fibre char (HC<sub>PT</sub>) and cabbage tree leaf fibres (CC<sub>PT</sub>)) was also carried out using the TGA analyser, which is a useful and easier approach to find moisture, volatile matter, ash, and fixed carbon in a single step. The exact heating protocol method used to conduct analysis was adapted from another study reported by Ramos-Carmona et al. [299], which was prepared in accordance with the ASTM D 3174-12, however in the present study argon gas was used instead of nitrogen gas. The method used and the related calculations are presented in Table 4.3.

Table 4.3: TGA method for proximate analysis

Step	Procedure	Calculations
0	Start with high purity Ar (100 mL/min)	
1	Heat from 35°C to 105°C at 10°C/min	The weight loss after this will give moisture content, calculated from the thermogram.
2	Hold/isothermal for 15 min at 105°C	
3	Heat from 105°C to 900°C at 10°C/min	The weight loss after this will give volatile content, calculated from the thermogram
4	Hold/isothermal for 10 min at 900°C	

5	Cool from 900°C to 750°C (and equilibrate) at 10°C/min	The weight loss after this will give the fixed carbon content, calculated from the thermogram
6	Switch the Gas to Air at 100 mL/min	
7	Hold/isothermal for 20 min at 750°C	
		After all the combustion, the remaining residue will give the ash content, can be provided by the machine or can calculated by accurately weighing the crucible.

The proximate analysis result, provided in Table 4.4, showed that the cabbage tree leaf char has more volatile content and less fixed carbon, as compared to harakeke fibres. The higher volatile content in the cabbage tree leaf char can affect the sintering process of the composite mainly due to generation of gasses during heating.

Table 4.4: Results of proximate analysis carried out on biomass (both defibrillated harakeke fibres ( $H_{sep}$ ) and cabbage tree leaf fibre ( $C_{sep}$ )) and biochar samples (both piranha treated harakeke fibres char ( $HC_{PT}$ ) and cabbage tree leaf fibre ( $CC_{PT}$ ))

Proximate Analysis (wt %)	Harakeke		Cabbage Tree Leaf	
	$H_{Sep}$	$HC_{PT}$	$C_{Sep}$	$CC_{PT}$
<b>Moisture</b>	2.361 ± 0.145	6.266 ± 0.075	5.263 ± 0.443	4.352 ± 0.431
<b>Volatile Matter</b>	82.496 ± 0.256	19.769 ± 1.024	75.799 ± 0.591	44.477 ± 1.014
<b>Fixed Carbon</b>	12.564 ± 0.227	68.938 ± 1.022	13.082 ± 0.470	43.626 ± 0.951
<b>Ash Content</b>	2.577 ± 0.019	5.027 ± 0.010	5.855 ± 0.063	7.545 ± 0.007

#### 4.3.5. Imaging

Stereo microscopic inspection of the fibres pre and post alkali treatment revealed the extent of defibrillation due to delignification. A comparison of raw harakeke fibre bundles ( $H_{bundle}$ ) with its defibrillated form ( $H_{Def}$ ), figure 4.16, indicated the good separation of microfibrils as had been previously shown in the study by Efendy and Pickering [274], however the separation of cabbage tree leaf fibres shown in figure 4.17, did not appear to be as effective. Since, in this study similar alkaline treatment was tried on cabbage tree leaf fibres for pure comparison purposes, no further treatment was done to the cabbage tree leaf fibre specimens before carbonising them in order to preserve that level of comparability in processing of the two natural fibre materials.

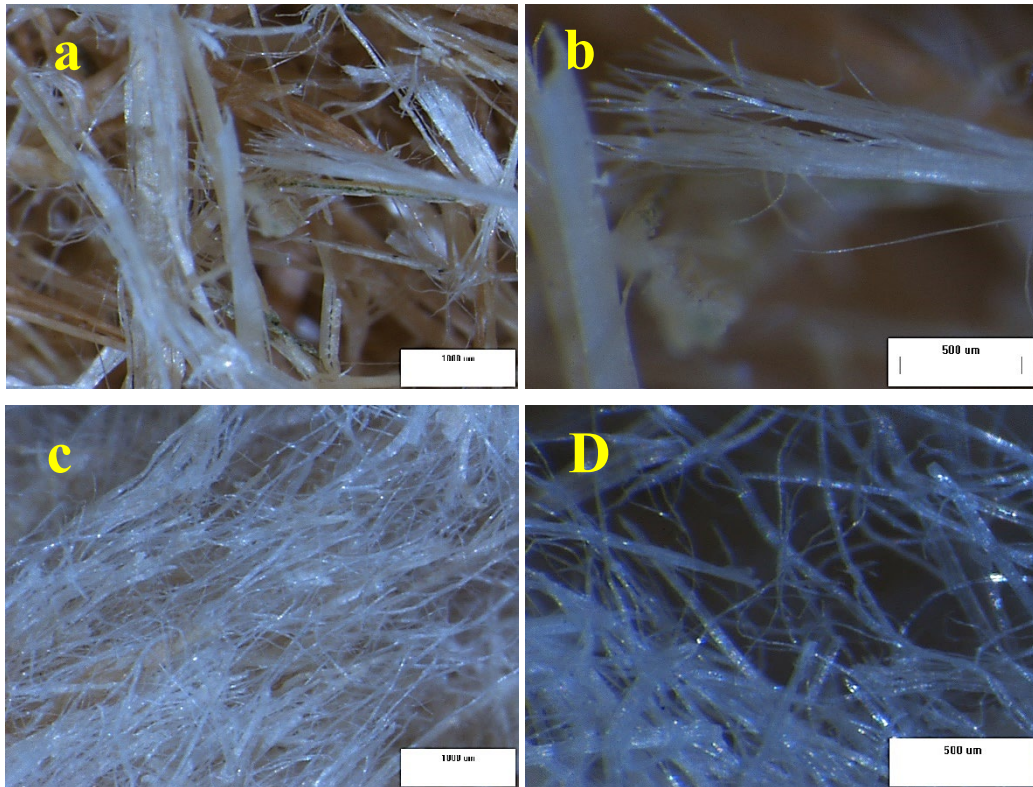


Figure 4.16: Stereo microscopy images of a, b)  $H_{\text{bundle}}$  and c, d)  $H_{\text{sep}}$

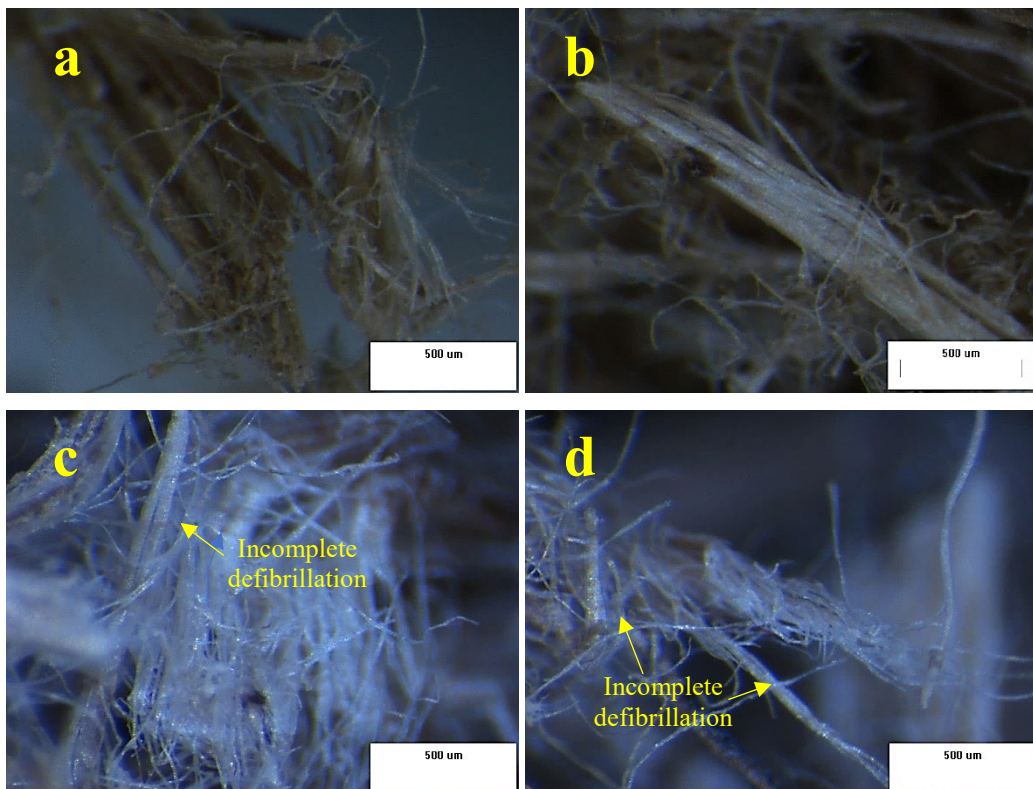


Figure 4.17: Stereo microscopy images of a, b)  $C_{\text{bundle}}$  and c, d)  $C_{\text{sep}}$ .

The scanning electron microscopy (SEM) images of harakeke and cabbage tree leaf char showed that the charring processes caused significant changes to the fibre

structure, in terms of shrinkage albeit while maintaining the natural architecture of the fibres. SEM was specifically used to study the topology of the developed chars, where effects of acid washing and piranha treatment on char could be directly observed. The surface topology of as formed harakeke char ( $HC_{AF}$ ), as shown in figure 4.18, appeared to be smooth and well formed, however acid washing and piranha solution treatment tended to make its surface rougher in nature. Figure 4.19 represents acid washed harakeke fibre char, and in this image, the surface of the fibres looked more rugged.

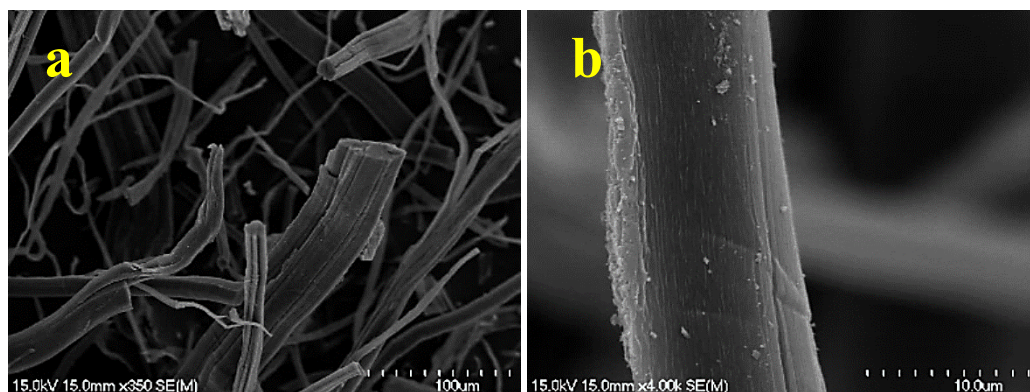


Figure 4.18: SEM images of as formed harakeke char ( $HC_{AF}$ )

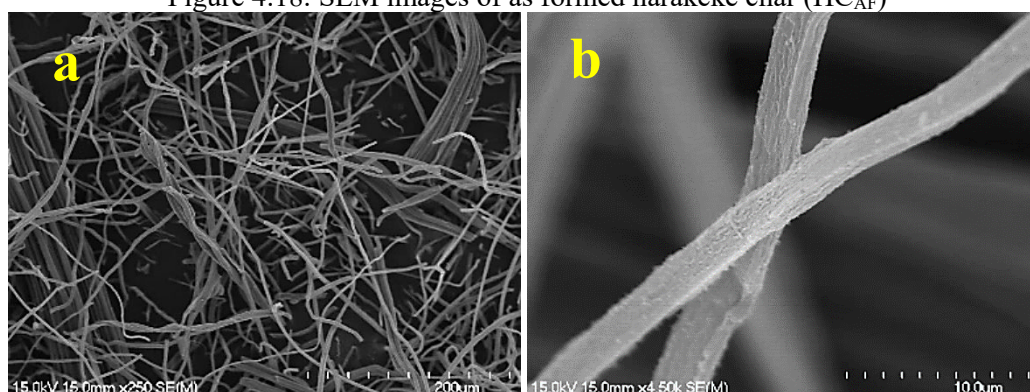


Figure 4.19: SEM images of harakeke char after acid washing ( $HC_{AW}$ )

The surface of piranha solution treated harakeke char fibres shown in Figure 4.20, appeared clean and rough mostly due to grooves and small craters. Figure 4.20 a and c represents the existence of fibrous char having a clean and rough surface, whereas Figure 4.20 b, depicts the presence of nanometric scale fibres attached to the micrometre sized carbon fibre. These nanometre-scale fibres were analysed further on. Figure 4.20 d displays the surface feature of the fibres, which is very rough and shows evidence of the existence of craters.

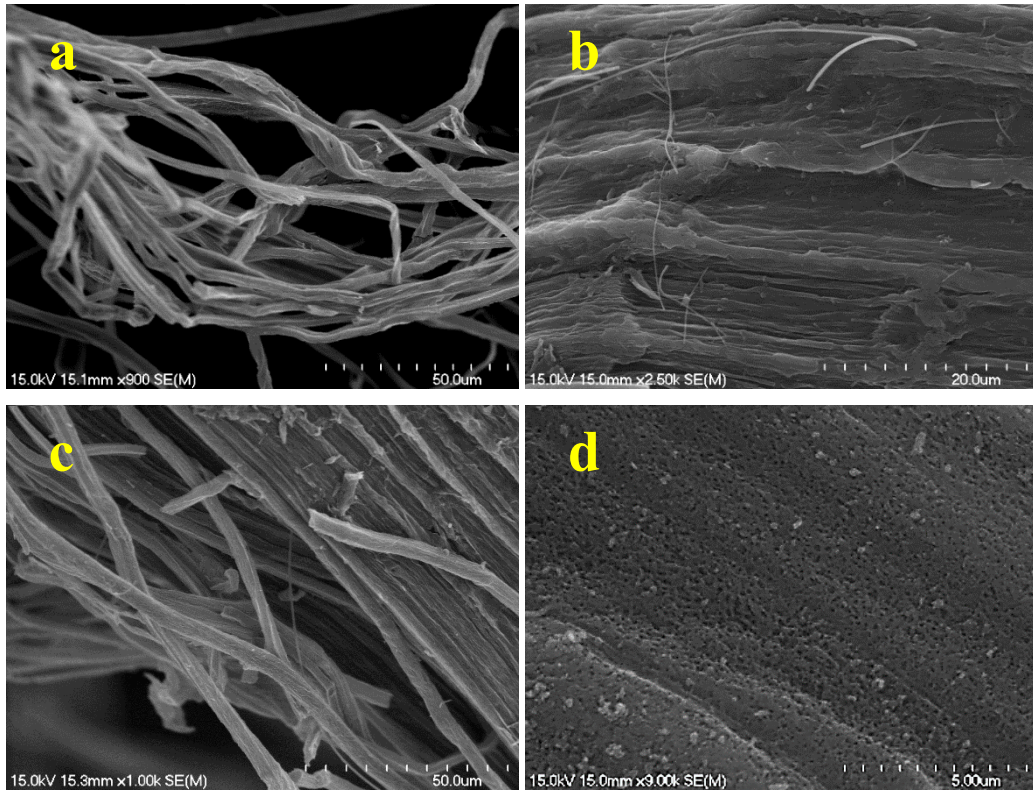
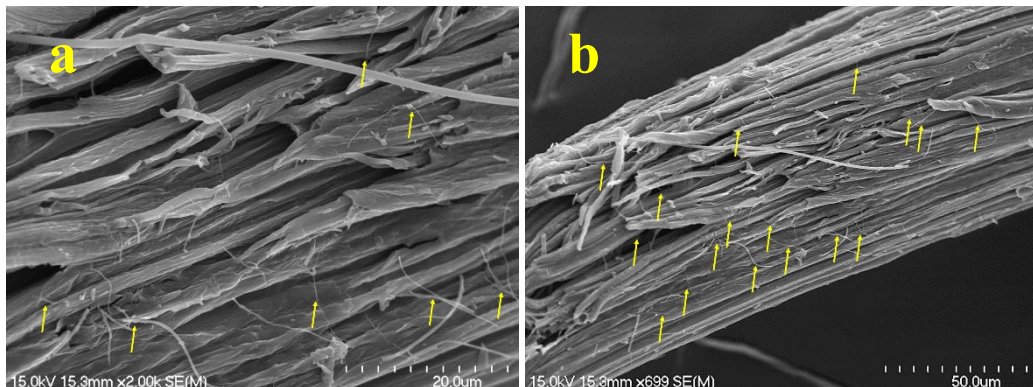


Figure 4.20: SEM images of piranha treated harakeke char (HC<sub>PT</sub>)

One of the most striking features noted during electron imaging of harakeke char fibres (i.e., after piranha treatment, HC<sub>PT</sub>), was the presence of nanotube like structures attached to their surface in abundant quantity (figure 4.21 & 4.22). The in-situ EDS measurements in SEM confirmed that those nanotube like structure are made up essentially of carbon and oxygen. Moreover, the average diameter measurements of these nano structures using SEM was found to be around  $96.3 \pm 53.2$  nm. This effect i.e., development of nanotube like structures, was found to be reproducible.





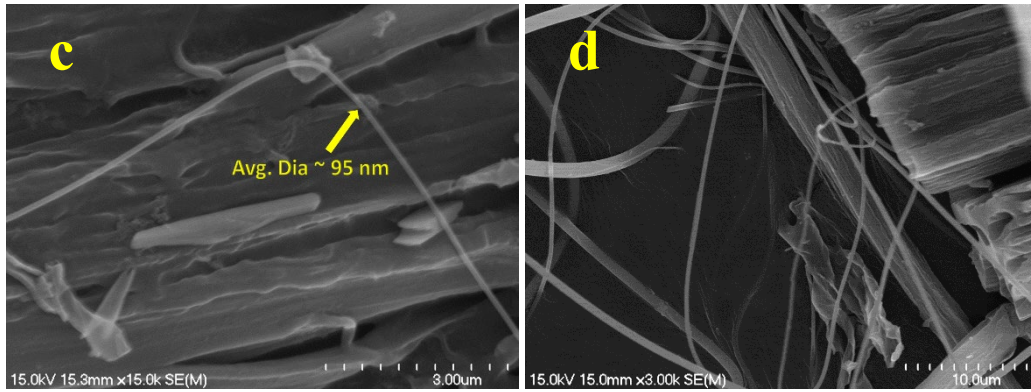


Figure 4.21: SEM images depicting the nanotube like structure present on the surface of piranha treated harakeke char

Closer inspection of these nanostructures under different SEM raster scanning rates (i.e., slow, and fast) revealed that the structures start to open (i.e. unscroll) on slow SEM scanning rates. Slow scanning rates in SEM deposit more electron concentration[300] on samples, so the higher electron concentration in the nanostructures resulted in their unscrolling as shown in Figure 4.23. Apparently, those nanostructures can be said to be similar to graphene nanoscrolls due to their chemical makeup, “un-scrolling” behaviour, and diameter. Graphene nanoscrolls consist of an open-ended continuous graphene sheet having spirally rolled-up geometry (tubular morphology and open inner cavity), due to which they naturally inherit most of graphene's properties but also demonstrate some of their own unique properties. There are various ways to synthesise the very small quantities of graphene nanoscrolls, which involve exfoliation of alkali metal-intercalated graphite, rolling the monolayer graphene made using evaporation of isopropyl alcohol solution.

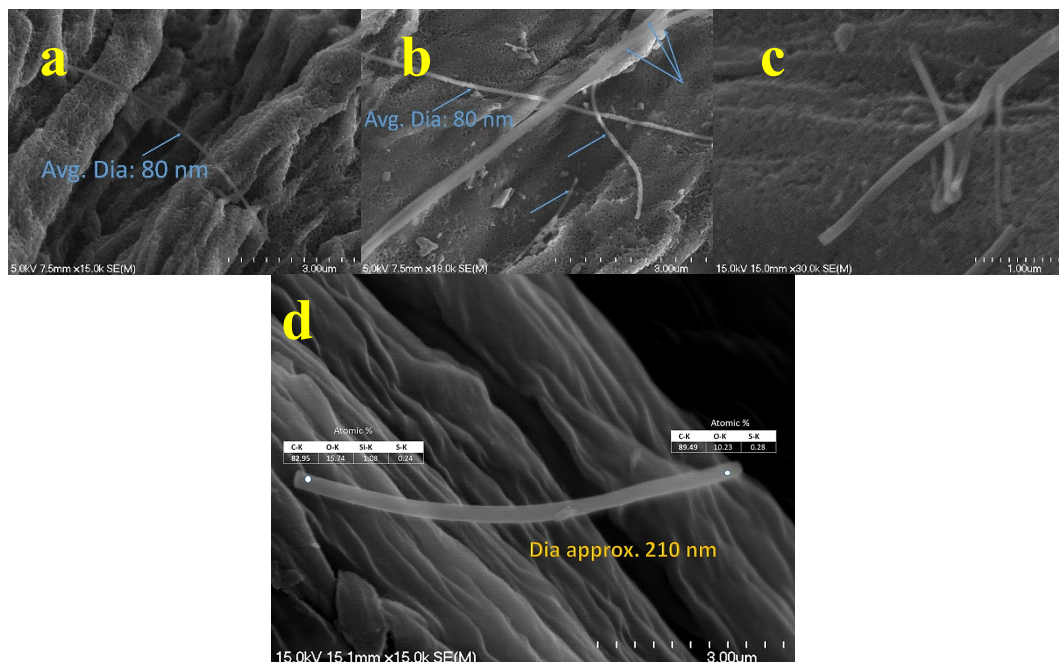


Figure 4.22: a-d) Close up view of nanotube like structures, where d) is showing the EDS analysis(as an inset) of one of the tube-like structures.

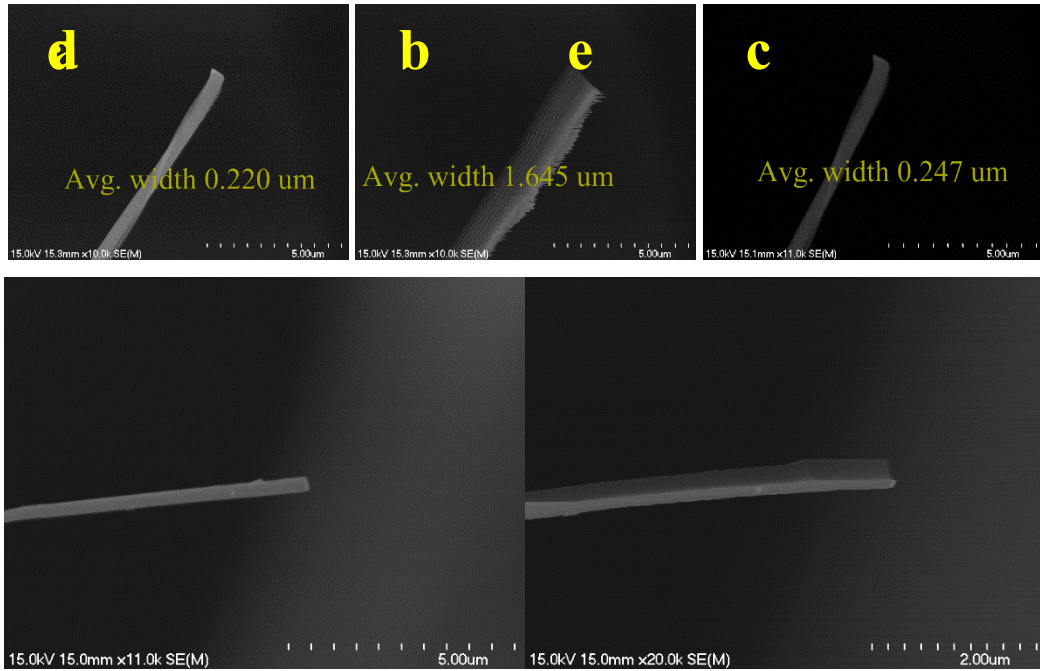


Figure 4.23: SEM images of nanoscrolls as developed in HC<sub>PT</sub>, where different scan rates revealed its un-scrolling structure.

The electron microscopy of cabbage tree leaf char and its modified form revealed interesting information about the impurities. Figure 4.24 displays SEM images of CC<sub>AF</sub> (cabbage tree leaf char as formed) where it can be seen that fibrous structure was formed, however it is also found that impurities most likely related to calcium carbonate (as per an in situ EDS analysis) were precipitated in a mushroom like structure developed during the heating of the natural fibres. Those impurities were removed by acid washing (CC<sub>AW</sub>) as shown in figure 4.25, and piranha treated cabbage char (CC<sub>PT</sub>) as shown in figure 4.26, revealed a clean but rough surface topology of char. Moreover, compared to harakeke char, cabbage tree leaf char also exhibited the occurrence of hollow tube like fibres as shown in figure 4.27.

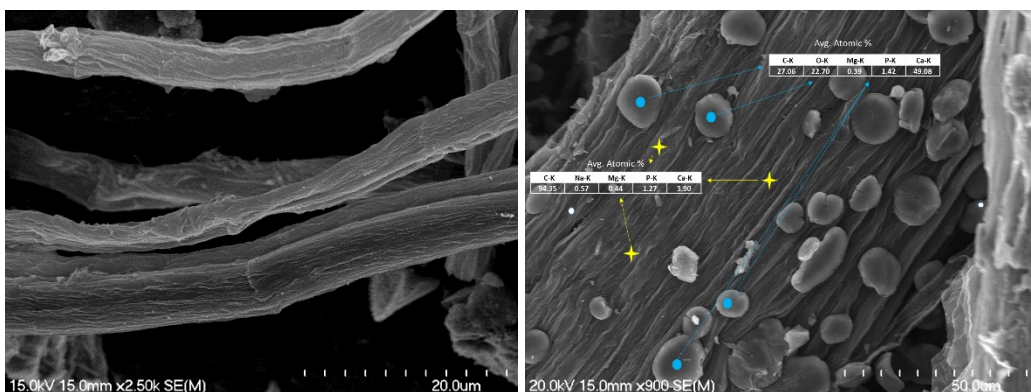


Figure 4.24: SEM images of as formed cabbage tree leaf char (CC<sub>AF</sub>), where b) is also showing EDS analysis of mushroom like structures developed by a calcite impurity.

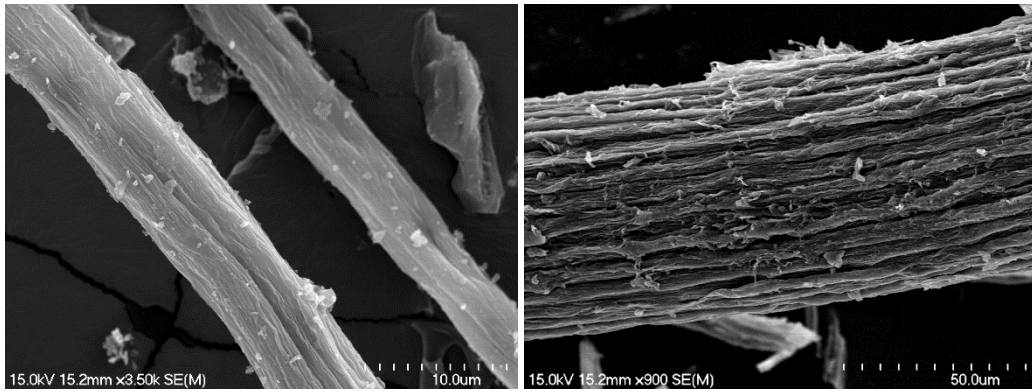


Figure 4.25:SEM images of acid washed cabbage tree leaf char (CC<sub>AW</sub>).

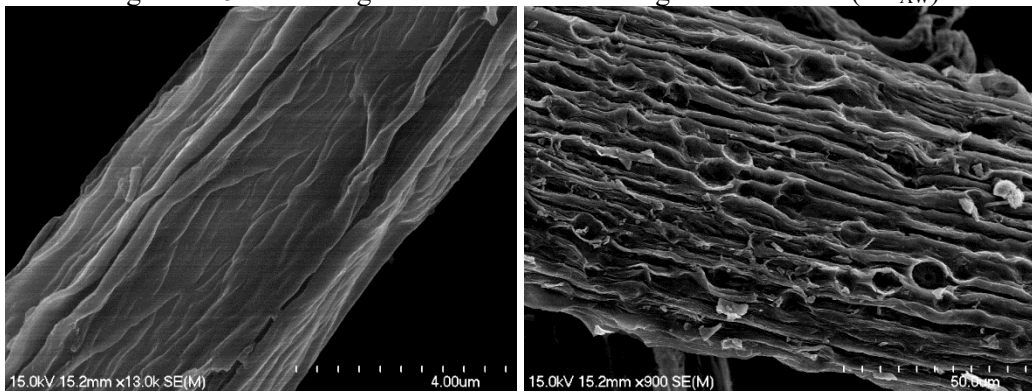


Figure 4.26:SEM images of piranha treated cabbage tree leaf char (CC<sub>PT</sub>).

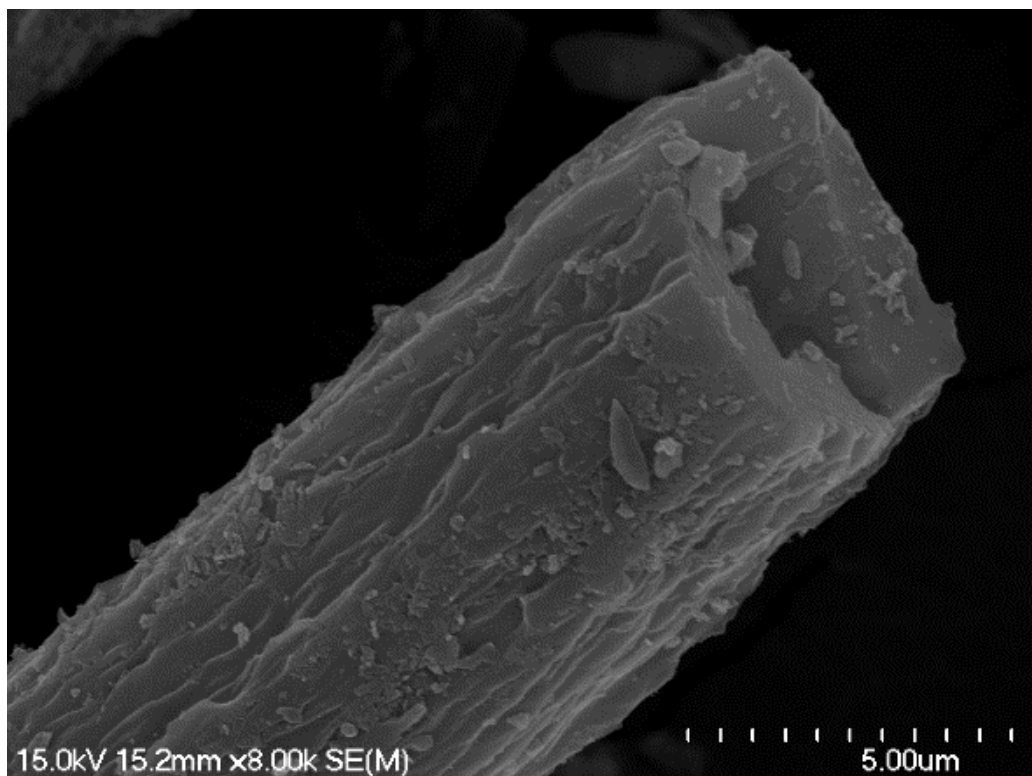


Figure 4.27:SEM image of a hollow fibre of cabbage tree leaf char.

## 4.4. Conclusions

In this part of the research, natural plant fibres were trialled to source carbon based fibrous structures (char) to use as a reinforcing agent in a HAp matrix. The natural fibres selected for this purpose are harakeke and cabbage tree leaf fibres, both these fibres are well known in New Zealand for their wide variety of uses and strength. Fibres were granulated and delignified before being subjected to pyrolysis in an oxygen deficient atmosphere to get the char. The as formed char (carbon-based fibrous structures) was acid washed and piranha solution treated to get high purity modified char. Both chars displayed fibrous morphology having rough topology, however piranha treated cabbage tree char displayed approx. 150% increased volatile content and approx., 50% increased ash content as compared to piranha treated harakeke char, moreover some of the fibres of cabbage tree leaf char was found to be hollow/tubular. It was found that the harakeke char formed carbon nanoscrolls on its surface, which was an interesting addition to study because this created a natural difference between the chars, i.e. with nanoscrolls (harakeke char) and without nanoscrolls (cabbage tree leaf char).

# CHAPTER FIVE : BOVINE BONE DERIVED HYDROXYAPATITE COMPOSITES REINFORCED WITH PLANT FIBRE CHARs

---

## 5.1. Introduction

Scientists working in the field of biomaterials, have extensively explored the possibilities of strengthening HAp using carbonaceous structures like carbon nanotubes, graphene etc to form composites. The composites were prepared in the form of coatings, scaffolds, powders and bulk structures, as each of those forms has different biomedical applications[129, 137, 145, 147, 301], like, for example, HAp-CNT composite coatings which can be used on metallic implants to improve their bone binding properties[301]. As indicated earlier, composites of HAp using carbon derived from natural sources like char, have not been trialled earlier, which is the main objective of this research. The idea to harvest carbon from natural sources and to use it in novel applications can also become one of the driving forces for a sustainable future where renewable resources are being utilised.

In this study, an attempt is made to develop a composite system comprising HAp derived from waste bovine bone and char harvested from natural plant fibres, in particular those endemic to New Zealand. This approach is a way forward for countries which are seriously committed to sustainability like New Zealand. As shown in Chapter 3, waste bovine bones were used to produce re-precipitated HAp powders. Most of the work related to derivation of HAp from waste animal bones follows a sequence of defatting the waste bone first and then heating the defatted bone at a high temperature (around 1000 °C) to initially get porous HAp structure, which was then powdered. This powdered HAp can be utilised as it is for various applications[56] but is not suitable for developing another structure from its compaction and then sintering it, mainly because of particle morphology which is limited to whatever developed during the high temperature treatment step. Moreover, their fusion behaviour during further sintering is also inferior because the particles have already been subjected to high temperature (around 1000 °C) and hence their surface energy will be low. This issue can be addressed by re-precipitation, which is based on acid digestion of the powdered HAp and then alkali assisted re-precipitation. In Chapter 3, different morphologies of re-precipitated HAp were developed and their behaviour at high temperatures was observed. One of these preparations of suitable morphology was chosen to make composites as described in this chapter.

Chapter 4 presented the sourcing of carbonaceous structures from natural plant fibres which are to be used as reinforcement in the composite samples with HAp. Natural fibres of harakeke plant leaves and cabbage tree leaves were initially granulated, defibrillated and pyrolyzed at 850 °C. This produced fibrous char, which was acid cleaned and then finally piranha solution-modified and it was in this form that it was incorporated into the HAp to make the composites. In this chapter, composites were trialled using the above-mentioned materials, with an intention to see the effect of fibrous char derived from plant fibres on the HAp materials generated from bovine bone. In embarking on this research, two possible issues were anticipated from using such carbon fibres in the HAp/carbon composites. The first one was related to the brittleness of the fibres, as it was suspected that they may get crushed during compaction (during forming of the cylindrical sample structures that were to be tested) and the second issue anticipated was related to the harmful by products formed during sintering like CaCO<sub>3</sub>. In the end, both of these issues were not actually experienced in samples examined which lend support to the idea that these carbon-based fibrous structures from natural plant fibres, are chemically and mechanically stable structures. The composite bodies were characterised for their chemical, topological and mechanical properties using a suite of characterisation techniques. An additional indirect measurement known as the “Diametral Tensile Strength (DTS)” test was made to further understand the mechanical behaviour of the composites under tensile stress. DTS is a mechanical property which was developed to examine friable/brittle materials which possess little or no plastic deformation. The aim of this test to assess the tensile strength of brittle materials, as it provides a simple and reproducible way and avoids the difficulties inherent to the flexural tensile strength testing methods commonly used on such materials.

## **5.2. Materials and Methods**

### **5.2.1. Materials**

All chemicals and solvents used in the experimental work were employed in as-received condition, without further purification. Reprecipitated HAp (H<sub>80-800</sub>, as synthesised and described/chartacterised in Chapter 3) and the piranha solution-treated chars (both harakeke (HC<sub>PT</sub>) and cabbage tree leaf chars (CC<sub>PT</sub>), as synthesised/described/characterised in Chapter 4) were used to make the composites. Ethanol (Merck) was used for the dispersion of the chars. Polyvinyl alcohol (PVA) (BDH, MW 14,000) solution acted as a ceramic binder and pore former. A graphite-based slurry was used for lubrication of the die, which was used to make cylindrical samples. Deionised water was used for all the work related to sample preparation and characterisation.

### 5.2.2. Composite Powder synthesis

In order to make sintered composites for characterisation, the powder used to form them needed to be made first. The composite powder formation involved initial ultrasonic dispersion of predetermined amounts of chars (0.1%, 0.5%, 1%, 1.5% & 2% of the amount of reprecipitated HAp) in a 70% ethanol/DI water mix. This specific volumetric mixture was used based on the research of Liu et.al.[302], in which this specific solvent mix proved to be highly successful in dispersing graphene. The powder to mixture ratio was 1:100 and ultrasonic dispersion was carried out for 1 hour (sometimes an ethanol top-up was also required during this time). After 1 h, a predetermined amount of H<sub>80-800</sub> (reprecipitated HAp) was added into the dispersion solution, which was then slowly stirred for 1 hour (sometimes more ethanol top-ups were required over this time), followed by drying at 80 °C for 12 hours in an oven. The dried powder tended sometimes to form agglomerates which required light crushing to redisperse. A pictorial representation of the process steps is represented in Figure 5.1. Dried, composite powders were subjected to chemical, thermogravimetric, microscopic and mechanical characterisation afterward.

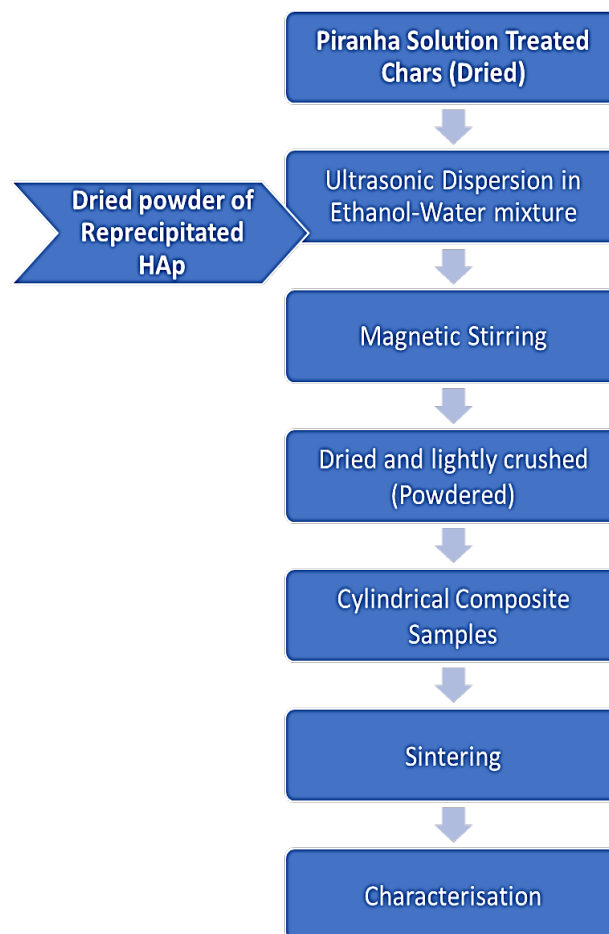


Figure 5.1: A pictorial representation of the processing steps, which summarises the production of the harakeke char and cabbage tree leaf char composites.

### 5.2.3. Composite body synthesis

To make the sintered composite body, it is important to initially make an unsintered structure having reasonable green strength and for a powder to acquire shape/green strength. For this reason, binders are usually added that can serve two important functions, the first being to help in binding the loose particles and the second being to leave the ceramic structure without residue after sintering (also known as “binder burnout”). Wei et al. [303] in their experimental and simulation study, showed that PVA polymer has good binding properties for HAp. In this study, a PVA solution (prepared using 10 wt% PVA powder dissolved in warm water) was physically mixed into the composite powders (the weight % of PVA solution to composite powder was 5%) to serve as a ceramic binder and also as a pore former. It is to be noted that the PVA powder was pretested (TGA analyses done in both argon and in air environments, see Figure 5.2) to make sure that it had a reasonably good binder burnout (i.e., removal of PVA without leaving residue) and it was found that almost all the weight was lost in the range from 250 – 650 °C. The binder mixed composite powders were then cold compacted into cylindrical tablets to acquire shape and green strength so that they could be sintered for compressive strength, hardness, porosity and indentation fracture toughness testing. The compaction pressure of 200 MPa was applied for a dwell time of 60 sec. Cylindrical samples for compressive strength testing had a height  $\geq 1.5$  times the diameter while for hardness, porosity and indentation fracture toughness testing, the minimum height was 3.5 mm). Sintering of composite powders was carried out in a tube furnace under an argon atmosphere. Compacted cylindrical samples were placed in an alumina boat, which was carefully pushed to the centre of the tube furnace. The ends of the tube were then carefully sealed with the inside of the tube being evacuated & backfilled with argon gas three times. The heating profile is mentioned in Figure 5.3, which is a combination of binder burnout (till soaking/isothermal hold at 650 °C) and sintering (till soaking/isothermal hold at 1050 °C) profiles. At the end of heating profile, all samples were furnace/naturally cooled. For comparison purposes, H<sub>80-800</sub> sintered cylindrical samples were also made through the same process however they were sintered in an air atmosphere (in a muffle furnace). Figure 5.4. displays the instruments used to make the green compacts as well as the tube furnace.



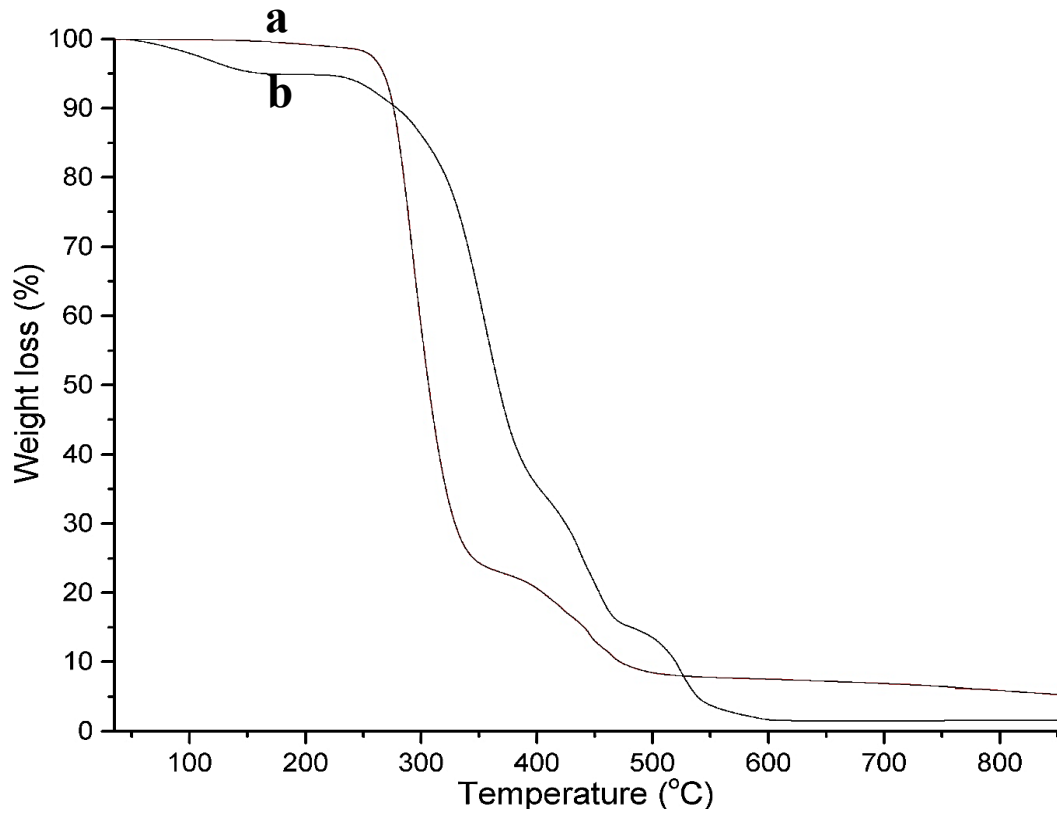


Figure 5.2: TGA thermograms of PVA powder, which was pre-tested to analyse its burnout behaviour in a) argon and b) air atmosphere

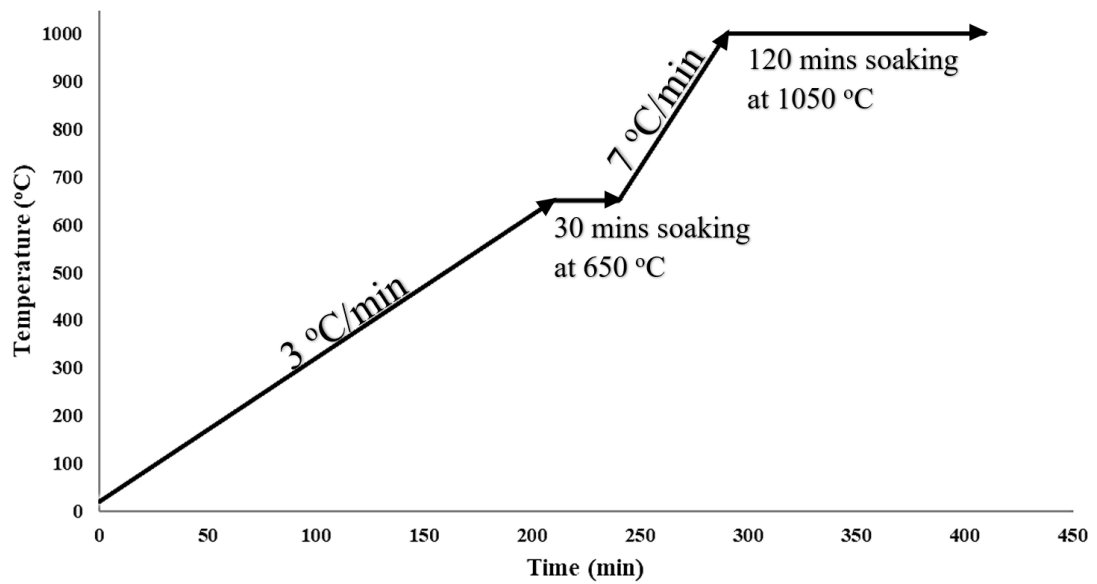


Figure 5.3: Heating profile of composites, depicting binder/PVA burnout (till soaking/isothermal hold at 650 °C) and sintering (till soaking/isothermal hold at 1050 °C) profiles.

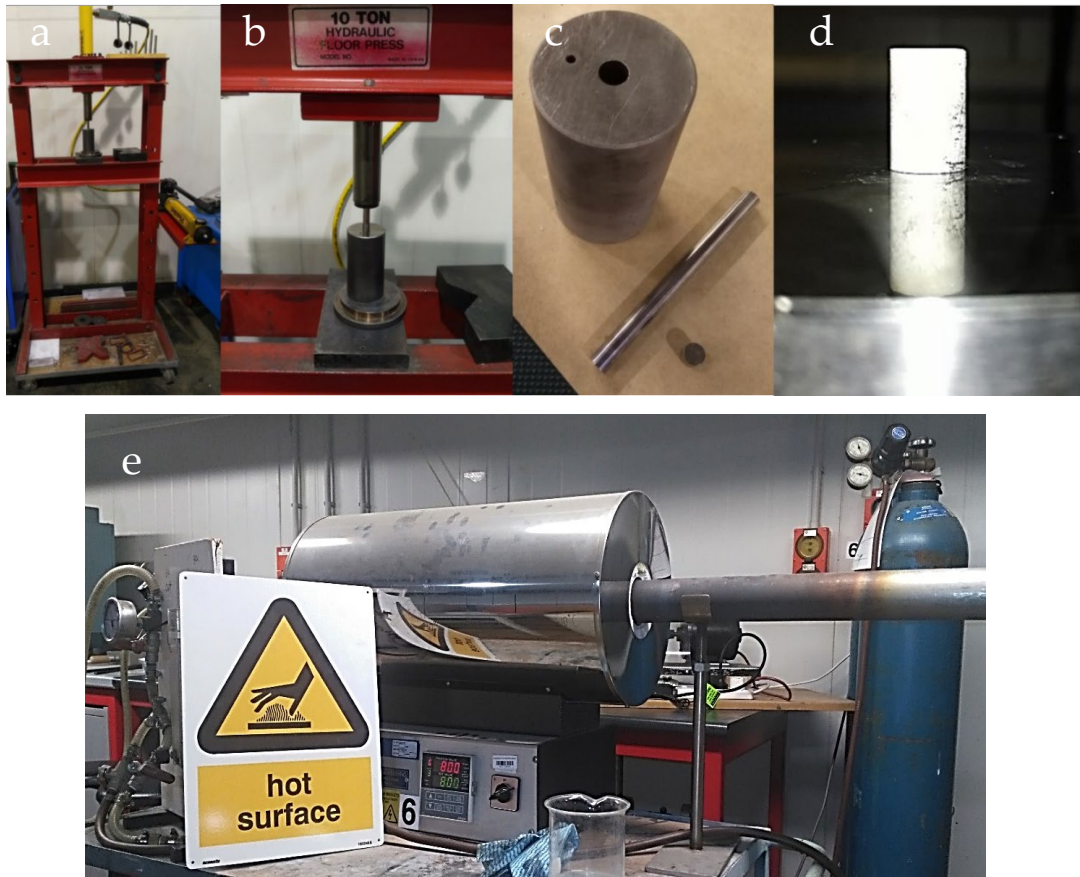


Figure 5.4: Tools/devices used to make cylindrical compacts, a) and b) represent a hydraulic floor press, c) is a 10 mm die (graphite used for lubrication), d) illustrates a sintered cylindrical composite sample and e) tube furnace.

#### 5.2.4. Characterisation

The phase composition of all powders used in the composite manufacture (i.e. with and without char addition) was determined by X-ray diffractometry (Panalytical Empyrean Series 2 diffractometer) which used Cu K $\alpha$  radiation at 45 kV and 40 mA ( $\lambda = 1.5406 \text{ \AA}$ ) and a step size of  $0.0260^\circ$ . A Fourier transform infrared (FTIR) spectrometer (Spectrum 100A Express, Perkin Elmer) was utilised for recording mid IR spectra via the KBr disc method (recorded between  $4000 - 450 \text{ cm}^{-1}$ ) (5 samples, with 5 scans per sample). A spectral resolution of  $4 \text{ cm}^{-1}$  was used. The elemental changes in the sintered composites and the calcium to phosphorus mole ratio were determined using ICP-MS (Agilent 8900 triple quadrupole (QQQ)). The morphological characteristics of the samples were recorded using a scanning electron microscope (SEM) (S-4700, Hitachi) instrument while compressive strength (6 samples per composition) and diametral tensile strength (an indirect tensile testing method for brittle materials) (5 samples per composition) were measured using an Instron universal testing machine (UTM). A micro-indentation hardness tester (3 samples per composition) (Leco LM700) was used to study hardness and indentation fracture toughness of the sintered samples. Surface preparation was carried out

by using an increasing grade of SiC grinding papers and polishing using a 1  $\mu\text{m}$  alumina slurry.

For XRD and FTIR (via KBr disc method) characterisation composite cylindrical samples were crushed (mini hydraulic press) and powdered, for ICP-MS composite powder was acid digested before being analysed, however for SEM imaging, broken samples from compressive testing were used.

Table 5.1: Sample coding and their brief description.

S. No.	Sample	Description	Code	
1	Re-precipitated HAp	Re-precipitation at 80 °C from the cow bone-derived digest solution and heat treated at 800 °C	H <sub>80-800</sub>	
2	Re-precipitated HAp (H <sub>80-800</sub> )-piranha solution treated <i>harakeke</i> char (HC <sub>PT</sub> ) composite powder	Char wt% added	0.1	HH <sub>0.1</sub>
			0.5	HH <sub>0.5</sub>
			1	HH <sub>1</sub>
			1.5	HH <sub>1.5</sub>
			2	HH <sub>2</sub>
3	Re-precipitated HAp (H <sub>80-800</sub> )-piranha solution treated <i>Cabbage tree leaf</i> char (CC <sub>PT</sub> ) composite powder	Char wt% added	0.1	HC <sub>0.1</sub>
			0.5	HC <sub>0.5</sub>
			1	HC <sub>1</sub>
			1.5	HC <sub>1.5</sub>
			2	HC <sub>2</sub>

## 5.3. Results & Discussion

### 5.3.1. Fourier transform infrared (FTIR) spectroscopic Analysis

Sintered *harakeke* char composite:

The FTIR spectra of the sintered composite powders (made via crushing sintered composite cylindrical samples) based on *harakeke* char (0.1%, 0.5%, 1%, 1.5% and 2%) as compared to just the sintered H<sub>80-800</sub> cylindrical sample are shown in Figure 5.5. All spectra display the characteristic peaks of hydroxyapatite, which signifies that no other side reactions had occurred on making the composites. Overall, changes in the intensities of some peaks and appearance of carbonate peaks are the main changes seen in the

composites FTIR spectra. All spectra displayed peaks centred around 1000–1100  $\text{cm}^{-1}$  as well as peaks at around 962  $\text{cm}^{-1}$  and 602  $\text{cm}^{-1}$  related to the  $\nu_1$  and  $\nu_4$  fundamental vibrational modes of the phosphate group of HAp. Composite FTIR spectra however, displayed additional bands around 875, 1414, and 1458  $\text{cm}^{-1}$  as well as a shoulder peak at around 1465  $\text{cm}^{-1}$  which indicated the presence of the  $\text{CO}_3^{2-}$  group (type-B i.e.,  $\text{CO}_3^{2-}$  substituting for  $\text{PO}_4^{3-}$ ). Considering the presence of the small signature peak for type-B ( $\text{CO}_3^{2-}$  substituting for  $\text{PO}_4^{3-}$ ) at  $\sim 1465 \text{ cm}^{-1}$  it can be inferred that carbonate manifests itself as a substitution group in HAp as well as a more labile presence (i.e., either adsorbed on the surface of HAp or present as a separate entity/compound). It could be assumed that during sintering char fibres generated a CO and/or  $\text{CO}_2$  atmosphere (partial oxidation) by combining with the dehydroxylated water from HAp or maybe with the oxygen attached to its structure (piranha modification). This CO and/or  $\text{CO}_2$  atmosphere could be held responsible for substitution and labile presence of carbonate in the composites. Merry, . et al. [304] also reports a similar condition where sintering of a CNT-HAp composite led to partial oxidation of the CNTs generating (as a result) carbon dioxide molecules. The band in the range of 3250-3700  $\text{cm}^{-1}$  and the peak at around 1633  $\text{cm}^{-1}$  is due to adsorbed  $\text{H}_2\text{O}$ /moisture. The band at 3573  $\text{cm}^{-1}$  is due to the O-H stretching modes of lattice hydroxyl groups in HA. A peak at around 1385  $\text{cm}^{-1}$  due to a nitrate impurity was also present in the sample.

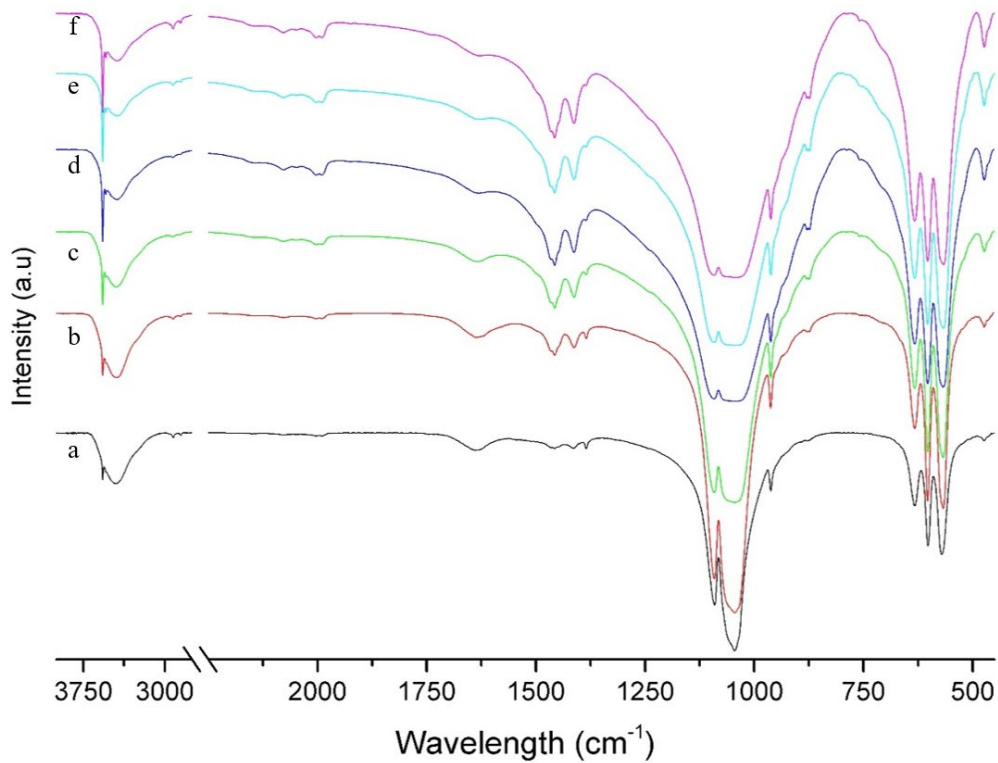


Figure 5.5: FTIR spectra of a)  $\text{H}_{80-800}$  b)  $\text{HH}_{0.1}$ , c)  $\text{HH}_{0.5}$ , d)  $\text{HH}_1$ , e)  $\text{HH}_{1.5}$  and f)  $\text{HH}_2$

Sintered cabbage tree leaf char composite:

Similarly, for sintered cabbage tree leaf char-based composites (0.1%, 0.5%, 1%, 1.5% and 2%) as compared to pure H<sub>80-800</sub>, (see Figure 5.6) the spectra also display the characteristic peaks of hydroxyapatite, which signifies that no other side reactions had occurred. Overall, changes in intensities of some peaks and appearance of carbonate peaks were the main differences seen in the spectra of the cabbage tree leaf char/HAp composites. The peaks detected and their assignments in these composites were identical to those for the harakeke leaf char composite with HAp as discussed above, moreover the source of carbonate substitution (and labile presence) could also be assumed to be the same as described earlier for harakeke leaf char composites.

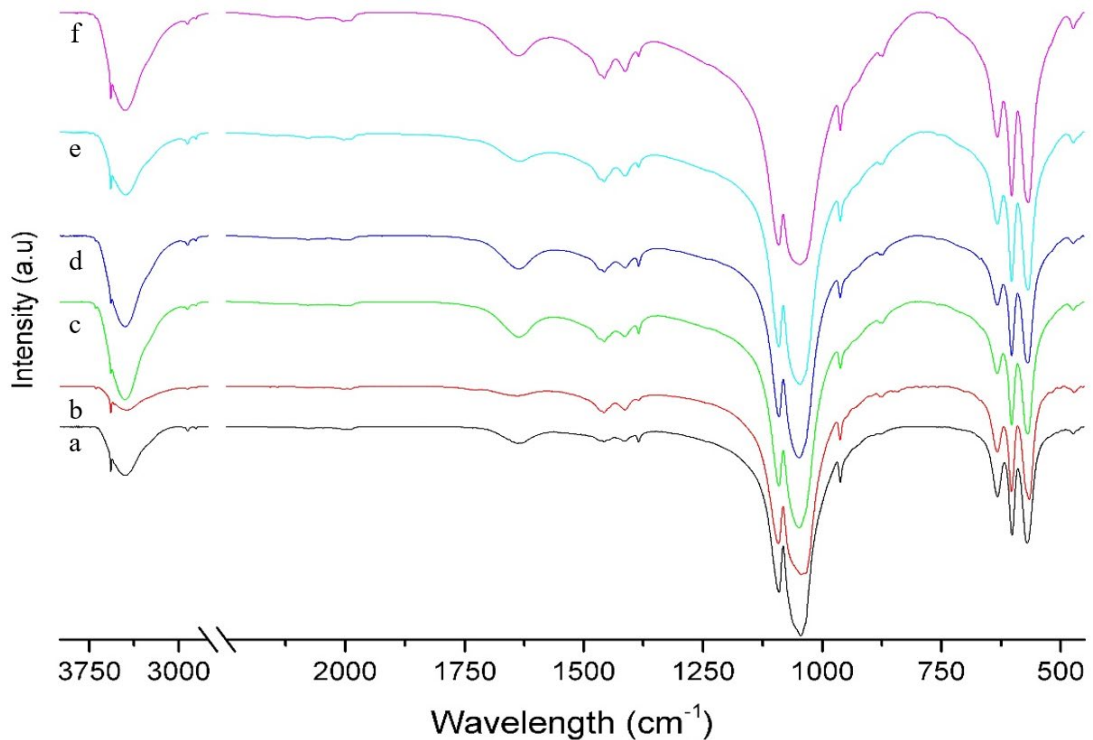


Figure 5.6: FTIR spectra of a) H<sub>80-800</sub> b) HC<sub>0.1</sub>, c) HC<sub>0.5</sub>, d) HC<sub>1</sub>, e) HC<sub>1.5</sub> and f) HC<sub>2</sub>

### 5.3.2. X-ray diffraction analysis

X-ray diffraction (XRD) was used to identify phase composition, crystallite size and crystallinity index in the composites and was compared with H<sub>80-800</sub>. For Rietveld refinement, SRM crystalline silicon was used for calibration of instrumental error. The instrumental error was automatically subtracted from the calculation using the software HighScore Plus[245].

Sintered *harakeke* char composite:

The X-ray diffractogram of H<sub>80-800</sub> and the harakeke char/HAp composites (0.1%, 0.5%, 1%, 1.5% and 2%) in the  $2\theta$  ranges  $20^\circ - 100^\circ$  are shown in Figure 5.7. The

diffraction patterns of the composites appear to have identical features to the XRD for H<sub>80-800</sub> (alone). This is an indication that no side reactions like formation of separate CaCO<sub>3</sub> phases had occurred. The diffraction peaks of the composites hence agree with those of pure H<sub>80-800</sub> indexed to the phase, hexagonal Ca<sub>10</sub>(PO<sub>4</sub>)<sub>6</sub>(OH)<sub>2</sub> in a P<sub>63m</sub> space group (ICDD-PDF number 9-432). Overall, all composites demonstrate that the powders exhibit HAp characteristics with good crystal structure with no other discrete impurity phases in evidence, hence the carbonate substitution (and labile presence) detected in FTIR was not so significant in extent to be detected in XRD.

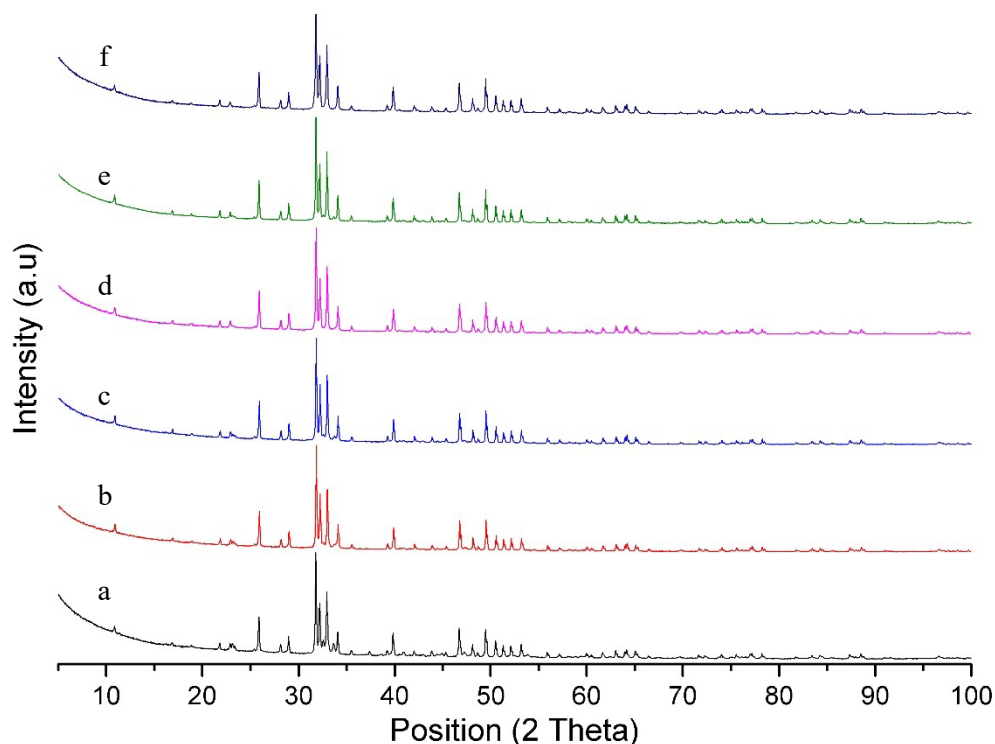


Figure 5.7: XRD diffractograms of a) H<sub>80-800</sub> b) HH<sub>0.1</sub>, b)HH<sub>0.5</sub>, c) HH<sub>1</sub>, d) HH<sub>1.5</sub> and e) HH<sub>2</sub>, which show the characteristic features of hydroxyapatite.

Sintered cabbage tree leaf char composite:

X-ray diffractograms of H<sub>80-800</sub> and cabbage tree leaf char composites (0.1%, 0.5%, 1%, 1.5% and 2%) in the 2 $\theta$  ranges 20 $^{\circ}$  –100 $^{\circ}$  are shown in Figure 5.8. In common with the harakeke char composites, the diffraction patterns of cabbage tree leaf char composites also appear to be same as that of the H<sub>80-800</sub> X-ray diffractogram and no side product was detected. All the diffractograms of sintered cabbage tree leaf char composites are showing the characteristic XRD peaks of hydroxyapatite. As with the harakeke char composite, the peaks in the XRD of the composites involving cabbage tree char can be indexed to hexagonal Ca<sub>10</sub>(PO<sub>4</sub>)<sub>6</sub>(OH)<sub>2</sub> in a P<sub>63m</sub> space group (ICDD-PDF number 9-432).

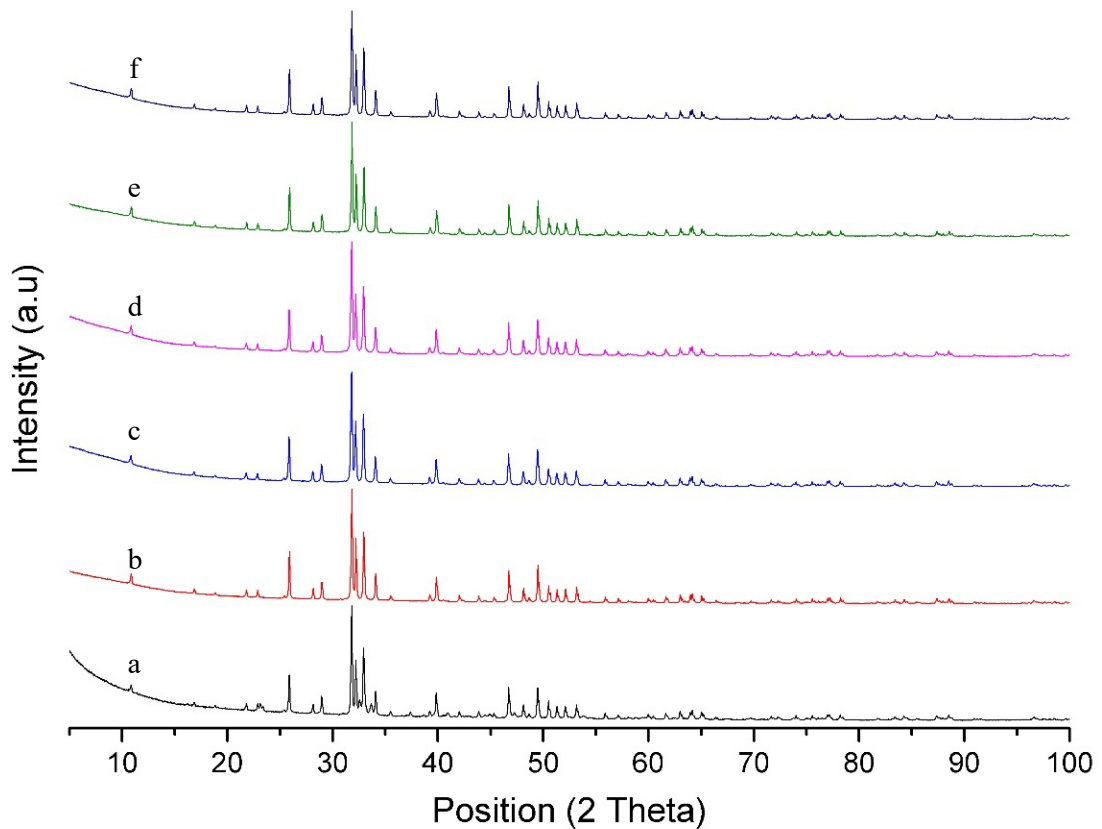


Figure 5.8: XRD diffractograms of a) H<sub>80-800</sub> b) HC<sub>0.1</sub>, c) HC<sub>0.5</sub>, d) HC<sub>1</sub>, e) HC<sub>1.5</sub> and f) HC<sub>2</sub>, which show the characteristic features of hydroxyapatite.

### 5.3.3. Inductively coupled plasma-mass spectrometry (ICP-MS)

Inductively coupled plasma-mass spectrometry (ICP-MS) was used to analyse sintered composites to monitor changes in the elemental composition of composites as compared to unaltered H<sub>80-800</sub>. The control sample i.e., H<sub>80-800</sub>, was found to have a Ca:P mole ratio of approx. 1.63, which is close to the stoichiometric HAp Ca:P mole ratio i.e., 1.67.

Sintered *harakeke* char composite:

Apparently, increasing percentages of char resulted in a gradual increase in P, S and Si content, which can be introduced by the partial oxidation of reinforcing char fibres. The Ca:P mole ratio had also changed, which could be due to the partial absorption/reaction with CO<sub>2</sub> to form carbonated apatite. The increased Si content is an impurity, which could be due to processing conditions (like from glassware), whereas the amount of Na present in samples may be due to the use of NaOH during reprecipitation. Table 5.2, presents the elemental composition of all *harakeke* leaf char composites.

Table 5.2: Elemental composition of all harakeke leaf char composites as determined by ICP-MS and comparison with (uncomposited) H<sub>80-800</sub>

	H <sub>80-800</sub>	HH <sub>0.1</sub>	HH <sub>0.5</sub>	HH <sub>1</sub>	HH <sub>1.5</sub>	HH <sub>2</sub>
Ca	28.542	30.789	30.789	30.978	30.444	29.890
P	13.494	15.641	16.200	16.567	16.558	16.964
Na	2.692	2.809	2.266	1.620	2.081	1.640
Mg	0.512	0.561	0.574	0.566	0.571	0.548
Si	0.140	0.269	0.205	0.236	0.303	0.236
S	0.046	0.071	0.073	0.076	0.093	0.108
Al	0.022	0.029	0.021	0.023	0.023	0.020
Ca:P	1.63	1.52	1.47	1.44	1.42	1.36

Sintered cabbage tree leaf char composite:

As in the harakeke composites, P and Si were found to be increased in the sintered cabbage tree leaf char composites, and Ca:P mole ratio was also found to be higher, which was likely due to localised formation of carbonate apatite. The increased Si content may be due to processing conditions (like from glassware) , and Na present in samples may be due to the use of NaOH during reprecipitation as stated earlier for the harakeke-HAp composites. Table 5.3 presents the elemental composition of all cabbage tree leaf char composites.

Table 5.3: Elemental composition of all cabbage tree leaf char-based composites found using ICP-MS as compared to H<sub>80-800</sub>

	H <sub>80-800</sub>	HC <sub>0.1</sub>	HC <sub>0.5</sub>	HC <sub>1</sub>	HC <sub>1.5</sub>	HC <sub>2</sub>
Ca	28.542	34.100	36.214	36.691	35.370	35.135
P	13.494	15.435	16.387	17.165	17.341	17.699
Na	2.692	2.456	2.079	1.512	1.913	1.574
Mg	0.512	0.500	0.531	0.538	0.542	0.550
Si	0.140	0.335	0.266	0.220	0.274	0.230
S	0.046	0.224	0.240	0.266	0.309	0.366
Al	0.022	0.025	0.018	0.021	0.022	0.020
Ca:P	1.63	1.71	1.71	1.65	1.58	1.53

#### 5.3.4. Imaging

Electron microscopic examination was carried out to study and find microstructural changes in the HAp due to addition of char to form the composites. The microstructural development of sintered H<sub>80-800</sub> (both for the unbroken and broken (compressive strength tested) samples) presented in Figure 5.9, was found to be similar to



that of a typical porous apatitic structure as is usually observed in HAp precipitated from animal bones (Appendix F). It was observed that transgranular fractures dominate as a fracture mode in the broken sample, and moreover that well dispersed porosity was also observed. Figure 5.9 c) presents the low magnification image of the sample, which clearly demonstrates the presence also of a well sintered structure.

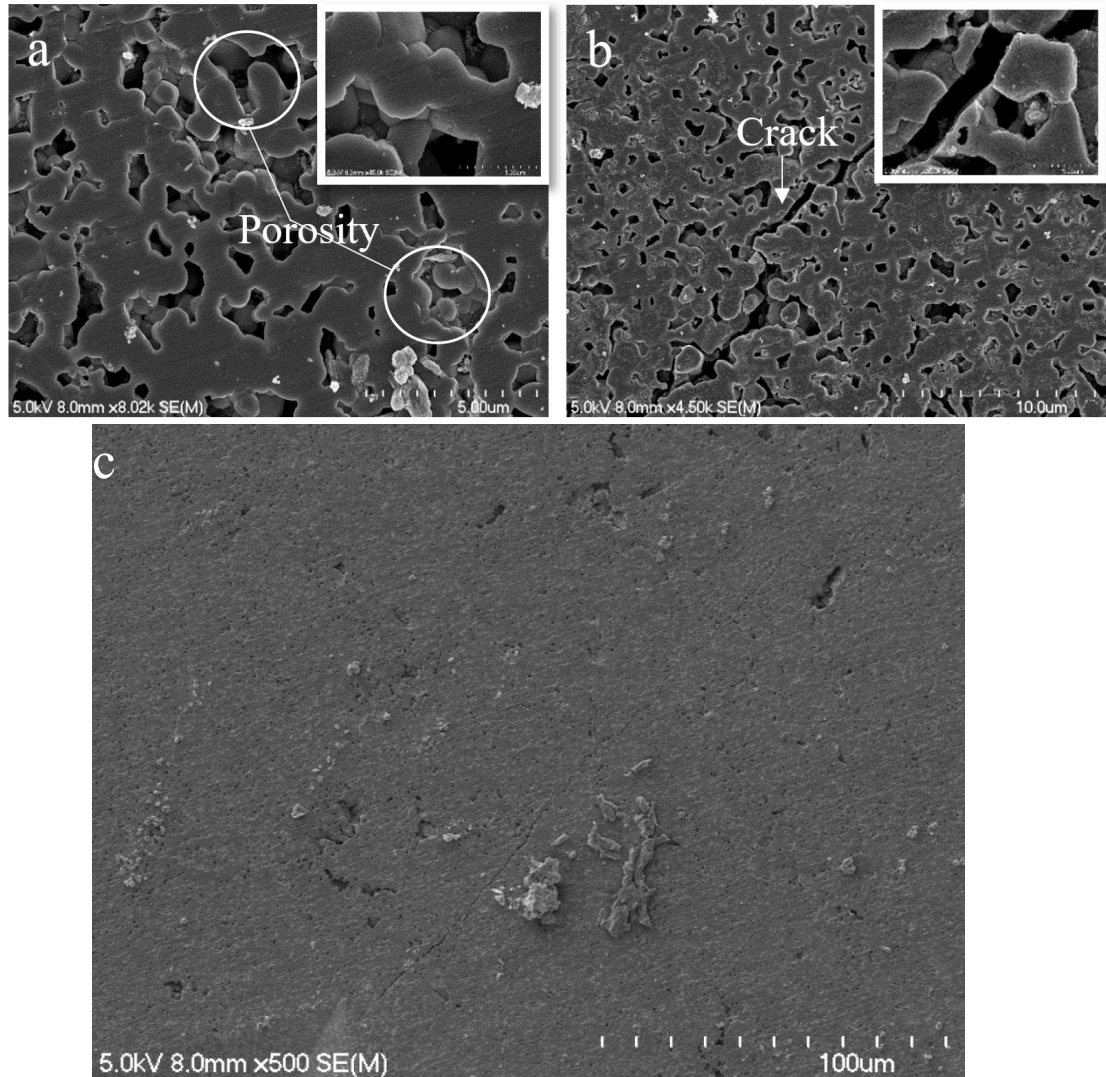


Figure 5.9: SEM micrograph of H<sub>80-800</sub>, a) unfractured sample, b) fractured sample (compression tested/broken specimen) and c) low magnification image of sintered sample.

Sintered *harakeke* char composite:

Figure 5.10-5.13 represents the electron microscopy images of harakeke char fibre composites. The microstructural examination of composites revealed evolving changes in the HAp structures especially adjacent to the char fibres in the items examined. In general, it was noted that incorporation of char in the HAp, was found to affect the matrix microstructure immediately adjacent to the fibres as it appeared to have small grains (refined structure). Similar grain refinement was reported in previous studies because of

increasing carbonaceous structures content [305, 306]. One possible reason for this is due to the increased thermal conductivity because of char structures, which allows the localised temperature to be raised up to the temperature of grain refinement.

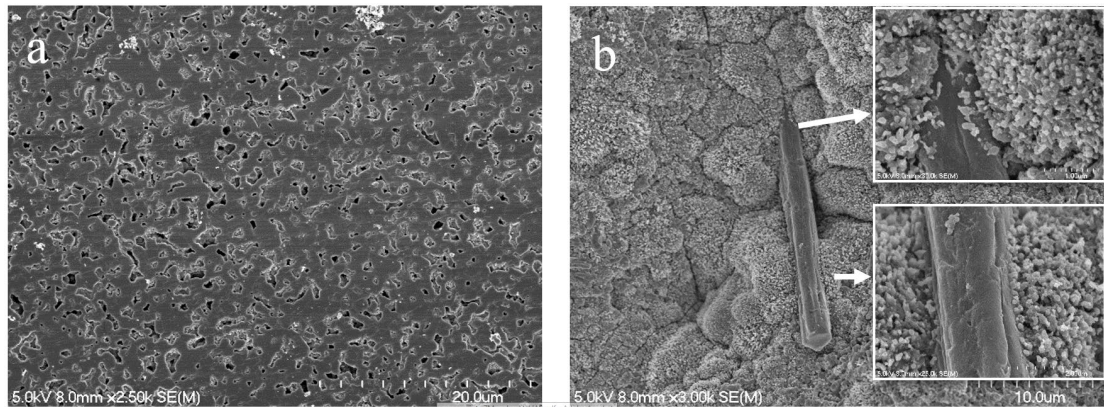


Figure 5.10: Topological microscopy of HH<sub>0.1</sub>, a) matrix and b) area near char fibre

The overall structure of HH<sub>0.1</sub> appears to be the same as that of H<sub>80-800</sub>, however the microstructure of matrix adjacent to char fibres appeared to be fine grained, as shown in Figure 5.10. A possible reason for this behaviour i.e., refinement of grains near the char fibres, is explained earlier. The same effect was found to be more enhanced in composites with higher char content. In Figures 5.11 and 5.12 there is clear indication of the formation of needle like HAp structure in areas adjacent to char fibres in HH<sub>1</sub>, and in HH<sub>2</sub> most of its structure appears needle-like.

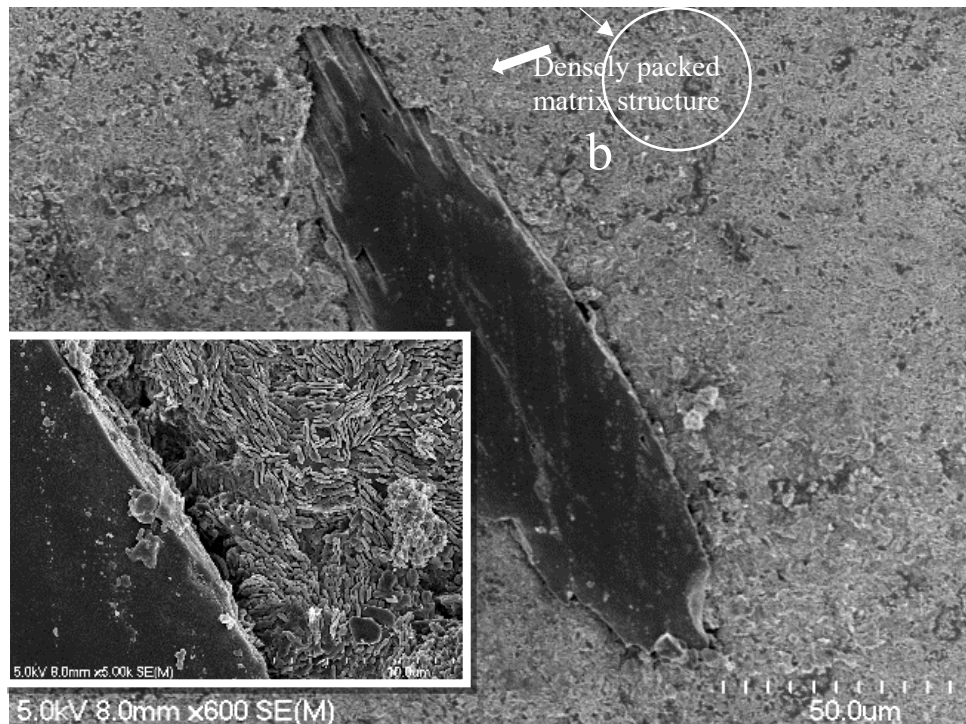


Figure 5.11: Topological microscopy of HH<sub>1</sub>, representing needle like structure near the char fibre.

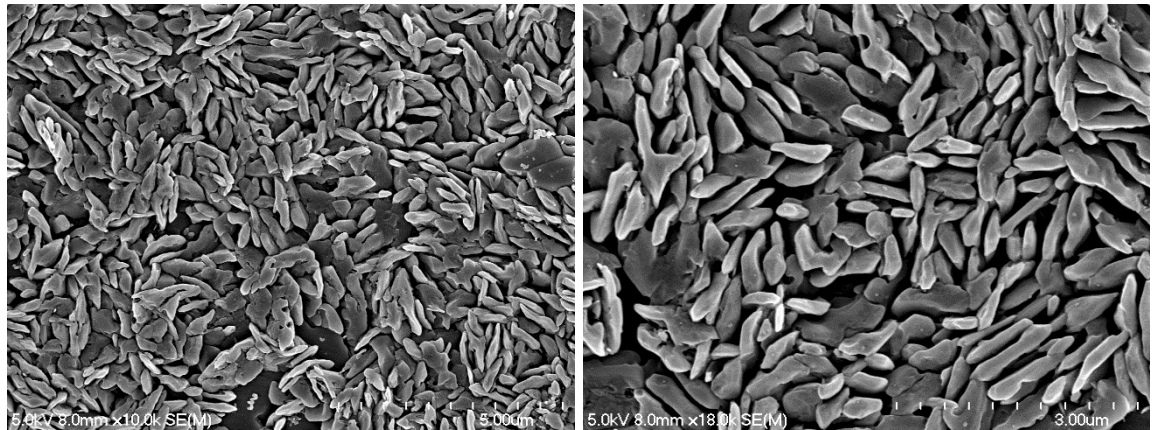


Figure 5.12: Topological microscopy of HH<sub>2</sub>, representing the growth of needle like structure throughout the sintered body.

The fractured sample of HH<sub>0.1</sub> is compared to HH<sub>0.5</sub> in Figure 5.13(a) and (b) respectively. It can be observed that HH<sub>0.5</sub> is displaying fibrous/reinforcement bridging effects. This is one of the modes of strengthening (as presented earlier in Figure 2.3). Similar effects were presented in another study [307] where reduced graphene oxide induced crack bridging strengthening.

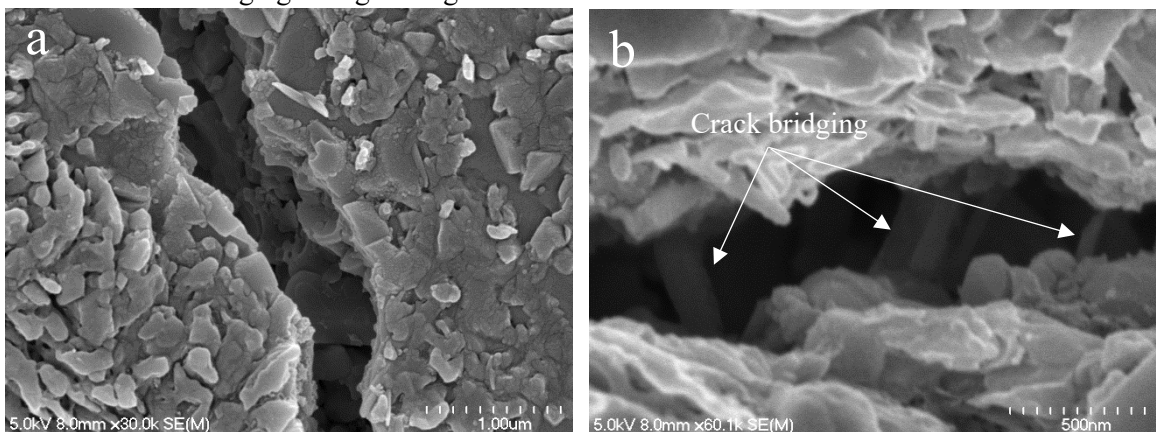


Figure 5.13: Fracture microscopy of a) HH<sub>0.1</sub> and b) HH<sub>0.5</sub>, where the latter is showing a bridging effect that provided resistance to a growing crack.

Sintered cabbage tree leaf char composite:

The microstructural development in the cabbage tree leaf char-based composites was found to be significantly different from that observed in the harakeke-HAP composites. The matrix structure in HC<sub>0.1</sub> as shown in Figure 5.14 a) and b) represents a fine grained mesoporous-like matrix structure. Moreover, in the area adjacent to the cabbage tree leaf char fibre, there appeared to be different or a combination of microstructures that looked needle-like, elongated and fine grained. HAp matrix appeared to be well attached with the char fibres as shown in Figure 5.15. This makes these samples different from the harakeke char composites, where only areas adjacent to the fibres were

highly influenced/refined, whereas in case of cabbage tree leaf fibre char composite, the whole structure including the matrix is somewhat influenced.

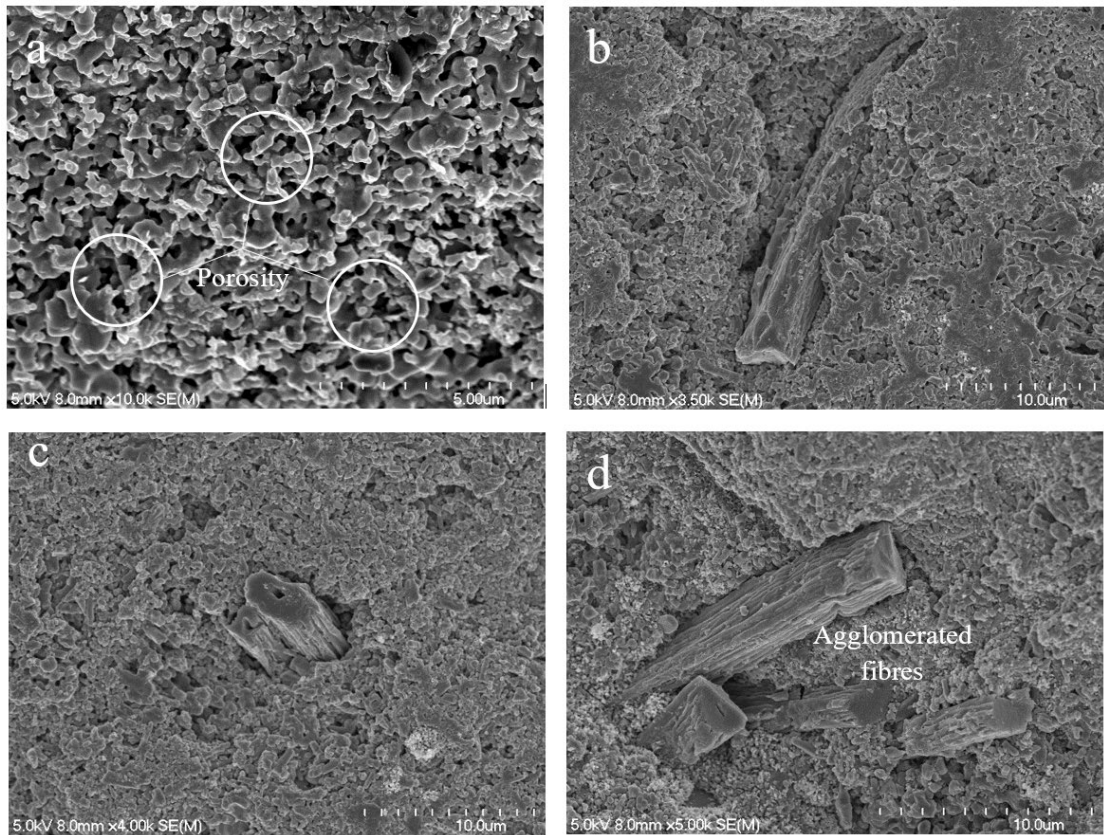


Figure 5.14: Development of microstructure in a)  $HC_{0.1}$  matrix and area near char fibres in b)  $HC_{0.1}$ , c)  $HC_{0.5}$  and d)  $HC_1$ .

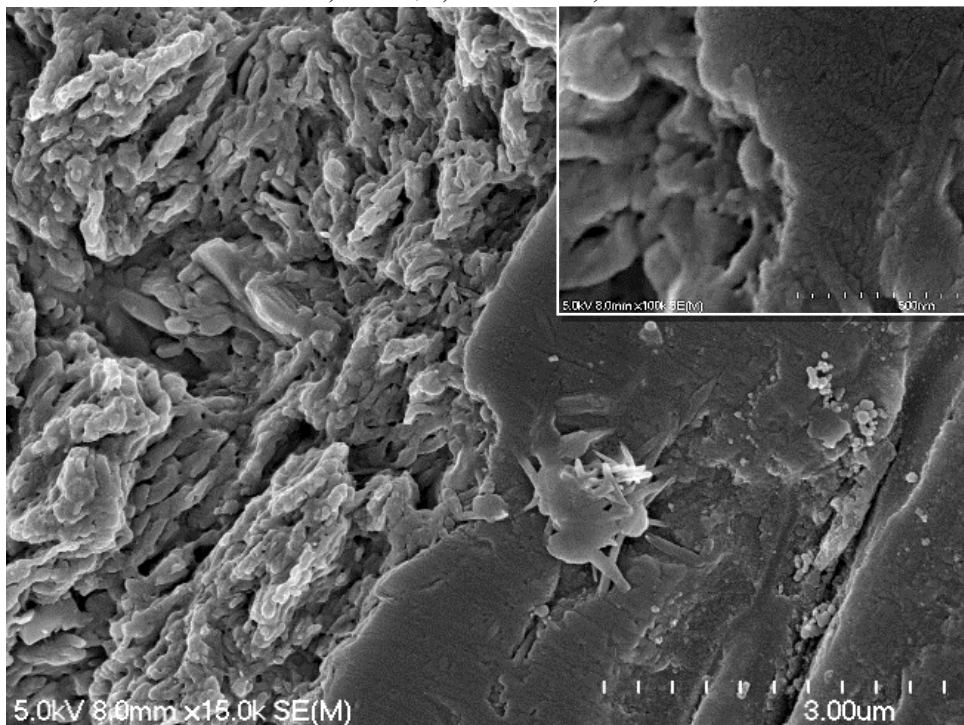
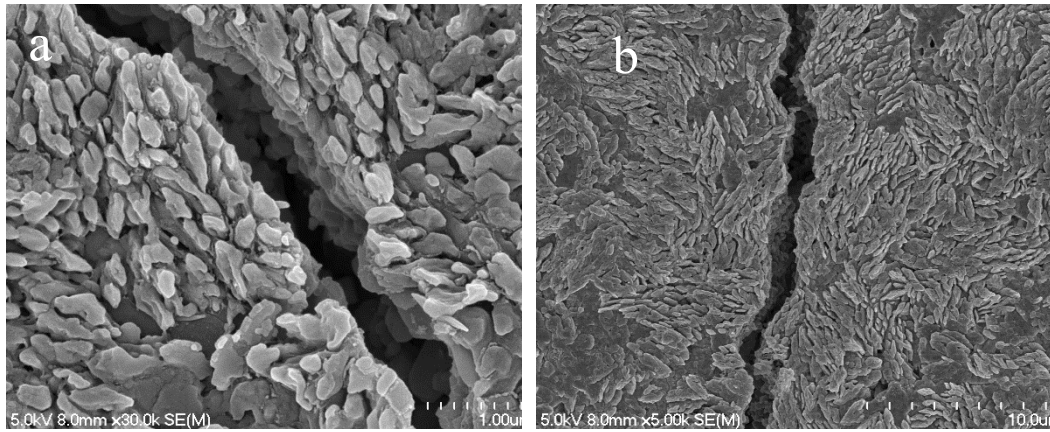


Figure 5.15: Structural development and bonding of HAp with the cabbage tree leaf char fibre in  $HC_1$ . (the solid region represents the structure of the char fibre).

Similarly, the higher loadings of char also affected the matrix microstructure ( and also areas adjacent to fiber), where it was observed that 0.5% char resulted in elliptical morphology of HAp (Figure 5.16 a), 1% char resulted in rod like (Figure 5.16 b) and 2% char resulted in needle like morphology (Figure 5.17 b). All morphologies have a very fine level of porosity. Figure 5.17 a), presents composites having 1.5% char, whereas Figure 5.17 b) presents composites having 2% char.



5.16: Structure and fracture pattern of HAp in a) HC<sub>0.5</sub> and b) HC<sub>1</sub>

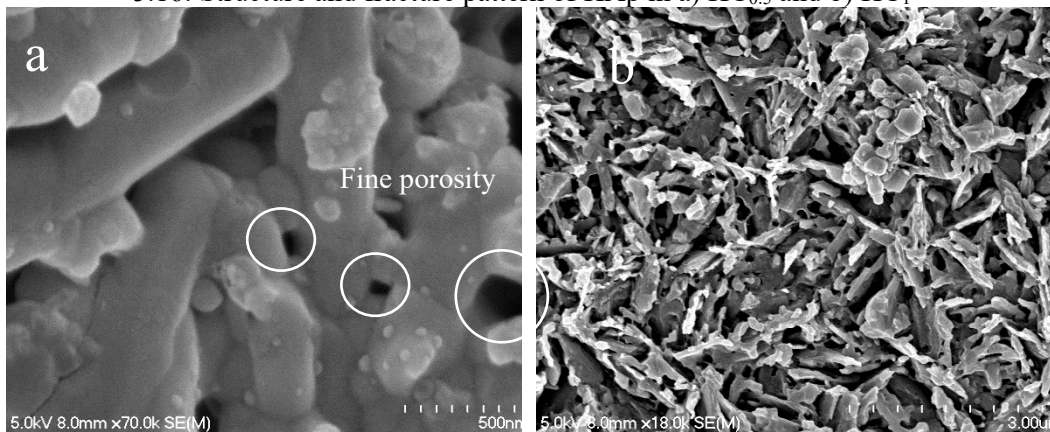


Figure 5.17: Structure of HAp in a) HC<sub>1.5</sub> and b) HC<sub>2</sub>

### 5.3.5. Vickers Hardness Measurements:

For a ceramic material or ceramic matrix composite, hardness is an important property to measure, as it relates the property of the ceramic to withstand penetration of the surface by a combination of brittle fracture and plastic flow. The hardness is usually accessed by the quotient of the applied load (P) and the contact area (A) of the indenter with the sample. There are many hardness testing standards available, however, for ceramics. Vickers and Knoop are mostly preferred based on the accuracy and repeatability. For Vickers testing, a 136° pyramidal diamond indenter is used that produces a square indentation when pressed against the ceramic surface. The testing procedure was carried

out in accordance with the testing procedures outlined in ASTM E384. The hardness was then calculated using the standard formula:

$$H_v = A_o \frac{P}{d^2} \text{ (eq. 7)}$$

where the constant  $A_o$  is the contact area of the Vickers pyramidal geometry defined by:  $A_o = 1.8544$  for [GPa]. The size of the indentation diagonal ( $d$ ) was measured using SEM images of the indented area. A typical indentation image from SEM is presented in Figure 5.18 d). Both diagonals were measured, and the mean value was then used to calculate the Vickers hardness of the sample using equation 5.1. The Vickers hardness values of  $H_{80-800}$ , are found to be around  $192.68 \pm 26.79$  HV, which is much higher than values obtained previously for both of cortical and cancellous bone[308].

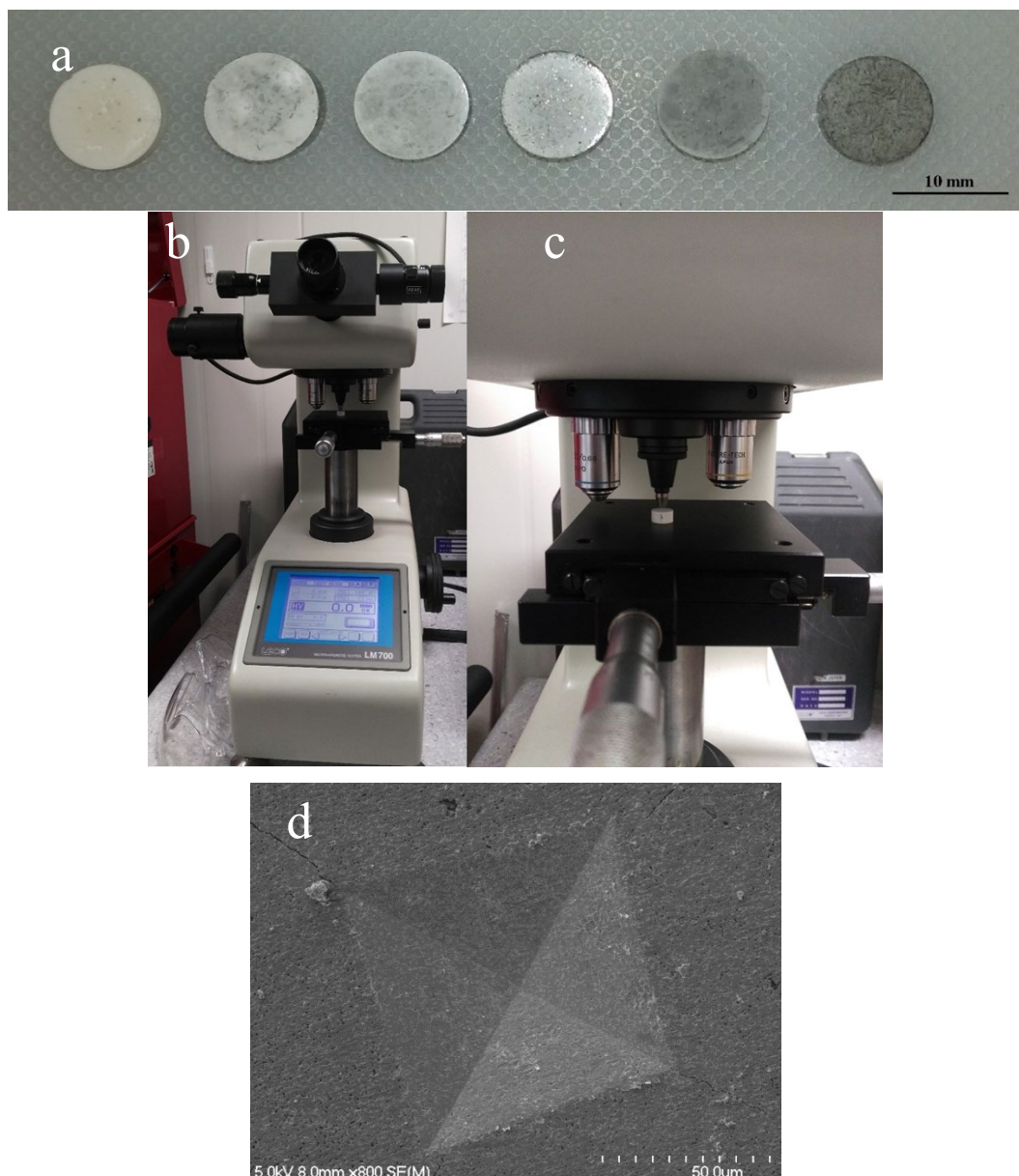


Figure 5.18: a) Harakeke composites for Vickers hardness b & c) Vickers hardness tester and d) SEM image of an indent.

Sintered *harakeke* char composite:

The Vickers hardness measurements on *harakeke* char composites are presented in Figure 5.19. A clear trend of rise and fall of hardness values was observed around 0.5% of char incorporation. 0.1% addition of char resulted in minor increment of hardness, followed by a massive increase because of the 0.5% addition. Further additions resulted in a decrease in hardness, however additions up to 1.5% gave values still greater than for the H<sub>80-800</sub> alone. The decrease in hardness values may be the result of unavoidable agglomeration of char fibres in areas of the composite, as they tend to become the source of the crack upon being loaded[306]. As per results presented by Barabashko et. al. [309] 0.5% CNT addition gave the values close to 500 HV, which is close to values found in HH<sub>0.5</sub>.

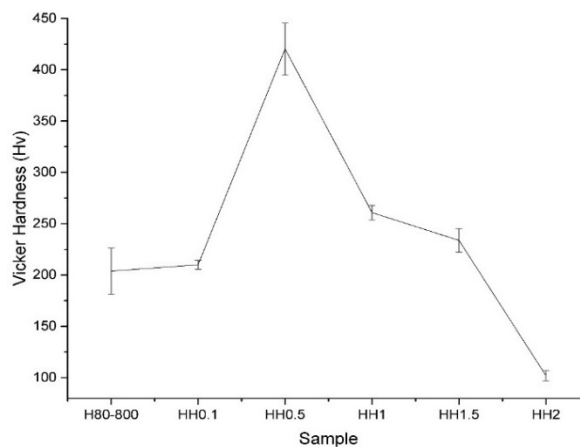


Figure 5.19: Micro Vickers hardness measurements performed on *harakeke* char composite samples.

Sintered cabbage tree leaf char composite:

The micro-Vickers hardness values of cabbage tree leaf char composite are presented in Figure 5.20. This showed a continuous increase in hardness values up to 1% char addition, followed by a massive drop with further additions.

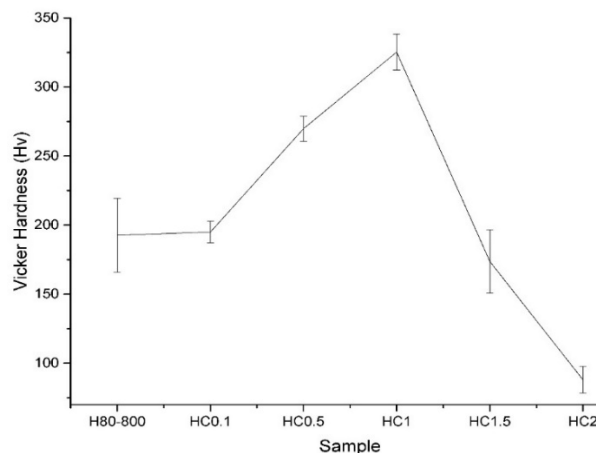


Figure 5.20: Micro Vickers hardness measurements carried out on cabbage tree leaf char composite.

### 5.3.6. Apparent Porosity and Relative Density Measurement:

Apparent porosity and relative density calculations of all composites (both harakeke char and cabbage tree leaf char) and H<sub>80-800</sub>, was done using Archimedes' method, for which three replicate samples of each prepared type of material were measured. The apparent porosity measurement is a reflection of the open & interconnected porosity existing in the test piece, and can easily be determined by the following equation:

$$\% \text{Apparent porosity} = \frac{W_W - W_D}{W_W - W_S} * 100 \text{ (eq. 8)}$$

Where,  $W_D$  is the weight of dry ceramic,  $W_S$  is the reweighing again while immersed in water (using a special hanging weight measurement setup) and  $W_W$  is the weight of sample after it is removed from the water (undried).

The relative densities of all samples were also calculated by relating the bulk densities of samples with the theoretical density of HAp which is 3.156 g/cm<sup>3</sup>. The bulk density was calculated using:

$$\% \text{Bulk Density} = \frac{W_D * \rho_w}{W_W - W_S} * 100 \text{ (eq. 9)}$$

Where  $\rho_w = 0.997 \text{ g/cm}^3$  at 25°C which is the density of water at that temperature. Figure 5.21 shows the setup to measure porosity and the evolving bubbles during soaking in water due to displacement of gas bubbles from the pores.



Figure 5.21: a) Archimedes setup for porosity measurement and b) evolving bubbles from the sintered sample when immersed in water



Sintered *harakeke* char composite:

Fig. 5.22 is a graph showing the apparent porosity and density value measurements for the *harakeke* char composites with HAp. Changes in the apparent porosity and density values in the *harakeke* char composites were noted when compared to the H<sub>80-800</sub>, however the changes were not found to be too significant, as shown in Figure 5.22. The minor addition of 0.1% *harakeke* fibre char, increased the relative density due to the decrease of apparent porosity which may occur as a result of the bridging effect from the nano carbonaceous structures in the composite however, further additions yielded the reverse effect. The decrease of relative density and increase of porosity at higher concentrations of char, may be due to agglomeration of micron sized char in areas of the composite as mentioned earlier or may be due to the structural porosities of the char itself, which would be exacerbated upon being loaded.

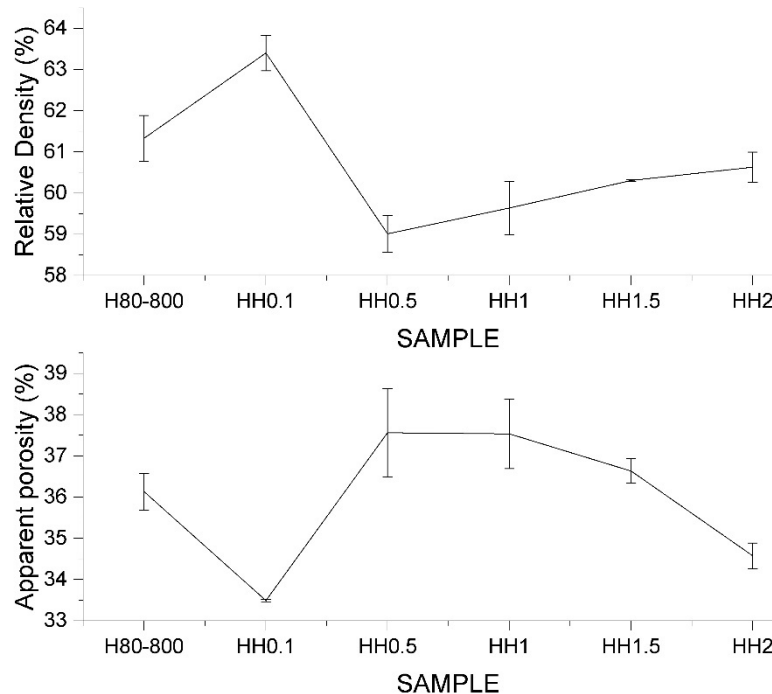


Figure 5.22: Relative density and apparent porosity measurements conducted on *harakeke* char composites relative to H<sub>80-800</sub>.

Sintered cabbage tree leaf char composite:

Fig. 5.23 is a graph showing the apparent porosity and density values measurement for the cabbage tree leaf char composites with HAp. In common with the *harakeke* char composites, the values measured did not show much difference in the relative density and apparent porosity values compared to the H<sub>80-800</sub> sample, as shown in Figure 5.23. At low levels of char addition, the changes were the same as that of *harakeke* fibre char, however, higher additions of 1.5% and 2% char, resulted in higher density values and lower

porosities. This effect indicates the growth of particles, which have led to closure of porosity.

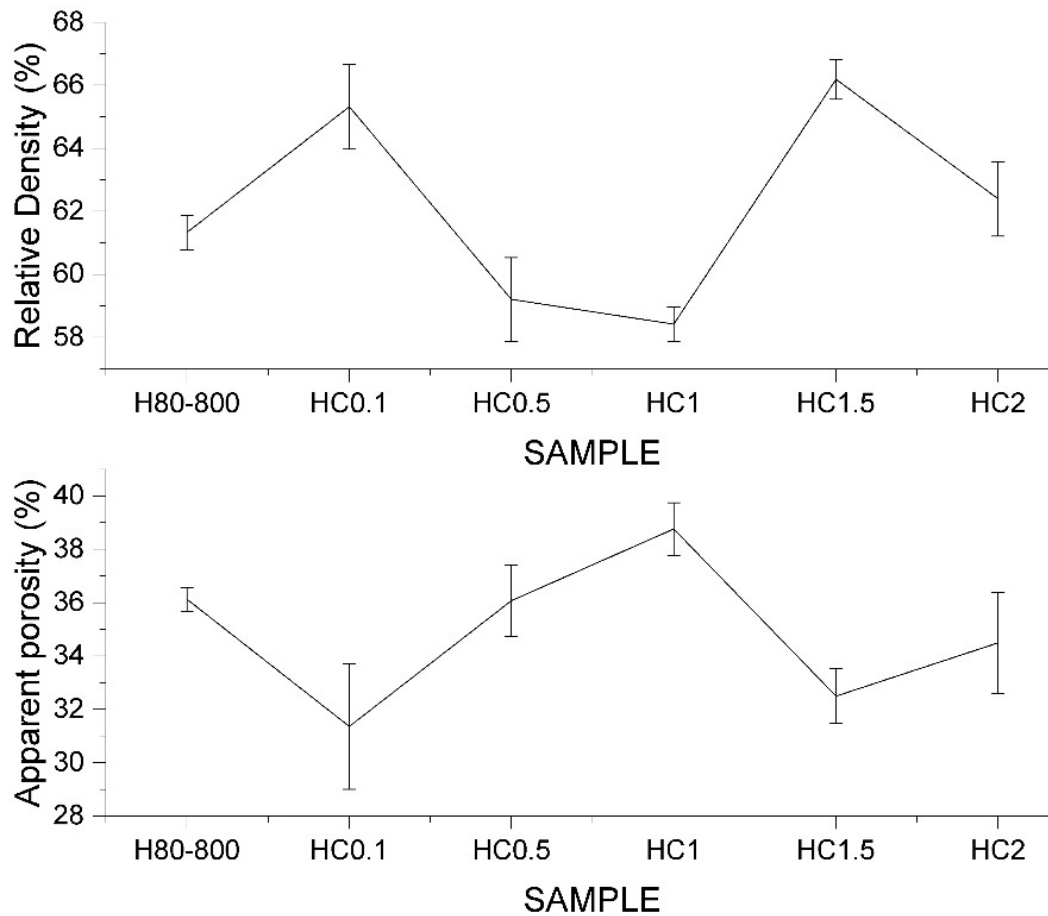


Figure 5.23: Relative density and apparent porosity measurements conducted on cabbage tree leaf char composites relative to H<sub>80-800</sub>.

### 5.3.7. Indentation Fracture Toughness and Brittleness Index

Indentation fracture toughness was measured using the method outlined in previously reported research[117], and precise measurements of indent diagonals and crack lengths were measured using SEM. Appendix G presents the process of measurement of crack length using SEM images. The brittleness index of all samples was calculated by dividing hardness values by  $K_{IC}$ , which in this case refers to indentation fracture toughness values.

Sintered *harakeke* char composite:

Figure 5.24, presents a steady rise of indentation fracture toughness values which was observed when the H<sub>80-800</sub> was loaded with 0.1 and 0.5% harakeke char. It was found that 0.5% addition yielded the maximum fracture toughness value. Further additions of char decreased the fracture toughness values. The brittleness index drops sharply with the

addition of 0.1% char and almost remained the same in samples up to the one with 1% loading, which indicates the induced ductility and fracture resistance in the composite.

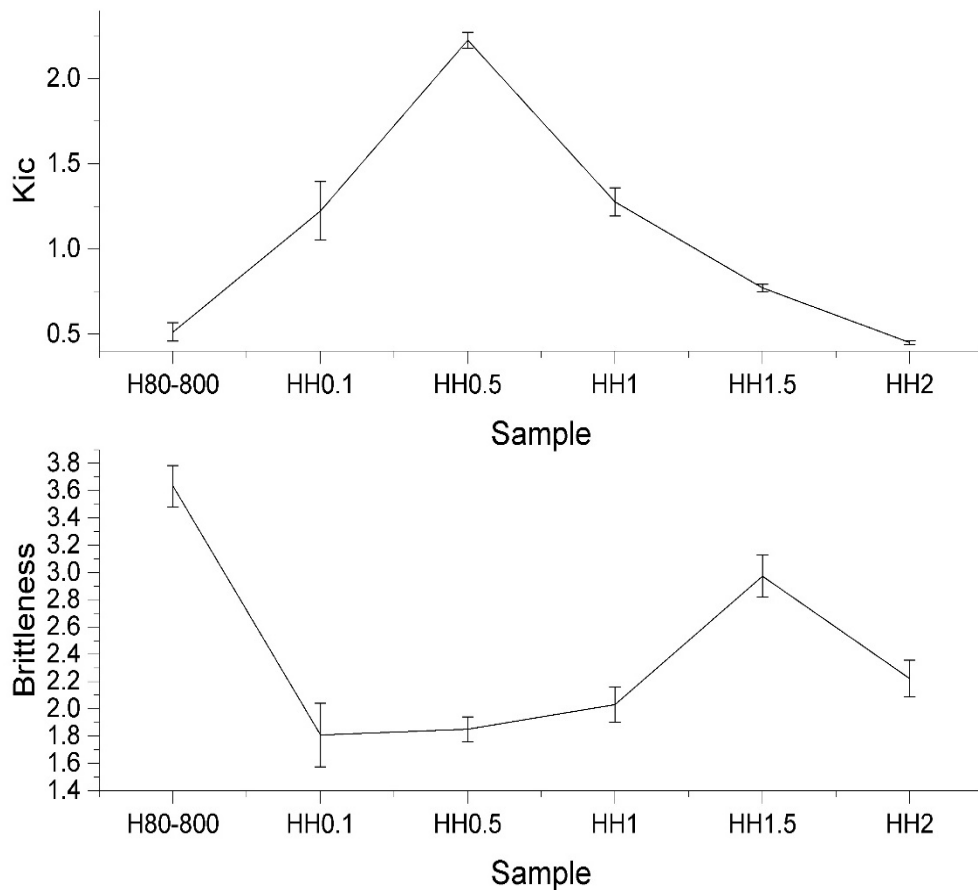


Figure 5.24: K<sub>IC</sub> and Brittleness index in harakeke leaf char-containing HAp composites.

Sintered cabbage tree leaf char composite:

The fracture toughness values of the composites were also increased with the addition of cabbage tree leaf char, however in contrast to the harakeke char composite samples, 1% addition of cabbage tree leaf char gave a sample exhibiting the maximum fracture toughness value (for that sample set), as shown in Figure 5.25. The maximum value obtained through cabbage tree leaf char reinforcement, was, however, much lower than the maximum obtained with harakeke char. For the brittleness index values, the trend was the same as that observed for harakeke char containing samples, which indicate the introduction of ductility with an increasing amount of cabbage tree leaf char up to a level of 0.5% addition.

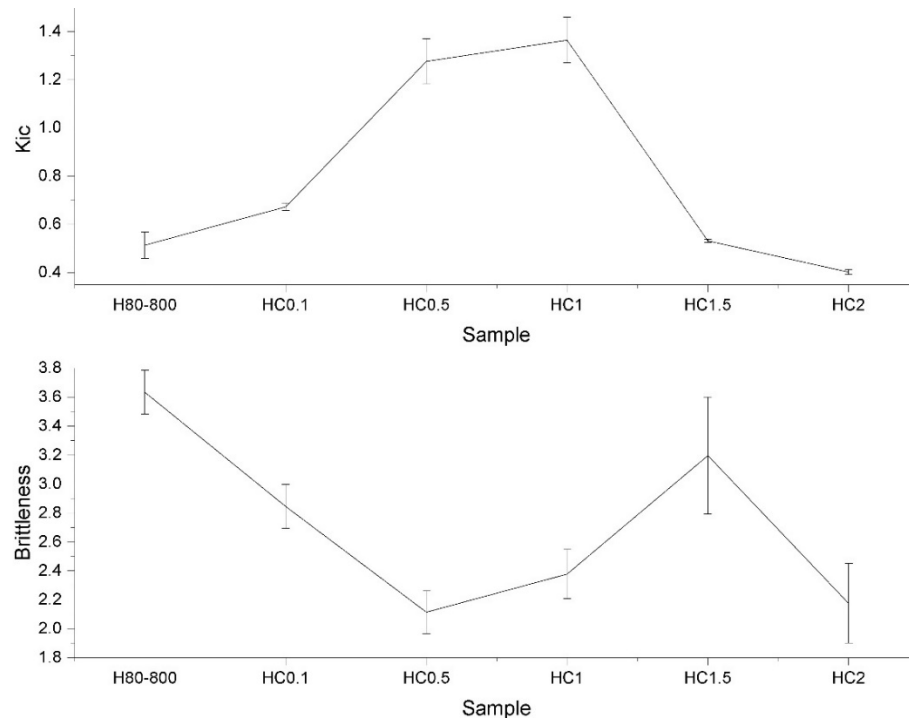


Figure 5.25:  $K_{Ic}$  and Brittleness index in cabbage tree leaf char composites.

### 5.3.8. Compressive Strength:

Compressive testing is used to assess how materials behave under compressive loading conditions and is considered a very important measurement for deducing the elastic and compressive fracture properties of low ductility or brittle materials. Figure 5.26 is a closeup view of the universal testing machine (UTM) with the composite sample placed on its platform.



Figure 5.26: Composite sample ready to be compression tested on the universal testing machine (UTM).

Sintered *harakeke* char composite:

The compressive strength test results of the H<sub>80-800</sub> (control) and all the Harakeke char reinforced composite samples are presented in Figure 5.27. In general, a significant increase of approx. 93% in compressive strength was observed with just 0.1% addition of fibrous char, followed by a continuous decrease of up to 51% (when compared to the H<sub>80-800</sub> control sample) when char addition to the HAp had reached 2%. Even at an addition of 0.5% char, an increase of approx. 47% was realised when compared to the control HAp sample. Since, nanoscrolls are essentially rolled graphene sheets, and graphene sheets are known for their strengthening effects in HAp matrix (as described earlier in chapter 2) so it was expected that the presence of nanoscrolls may have positively influenced the strength of the composites. The maximum strength displayed by the HH<sub>0.1</sub> sample, indicates the strengthening effect of nanostructured carbonaceous material (carbon nanoscrolls), as found in harakeke char. As per the interpolation of the compressive strength results presented by Barabashko et. al. [309] in their study involving MWCNT-HAp composite, 0.1% CNT addition yielded same values of compressive strength as that found in this study, however their study was only limited to max 0.5% CNTs addition.

The decrease in compressive strength with the addition of 1% and above, may be due (as indicated previously) to the agglomeration of the fibrous char in the ceramic body, which, itself, can generate new cracks upon being loaded.

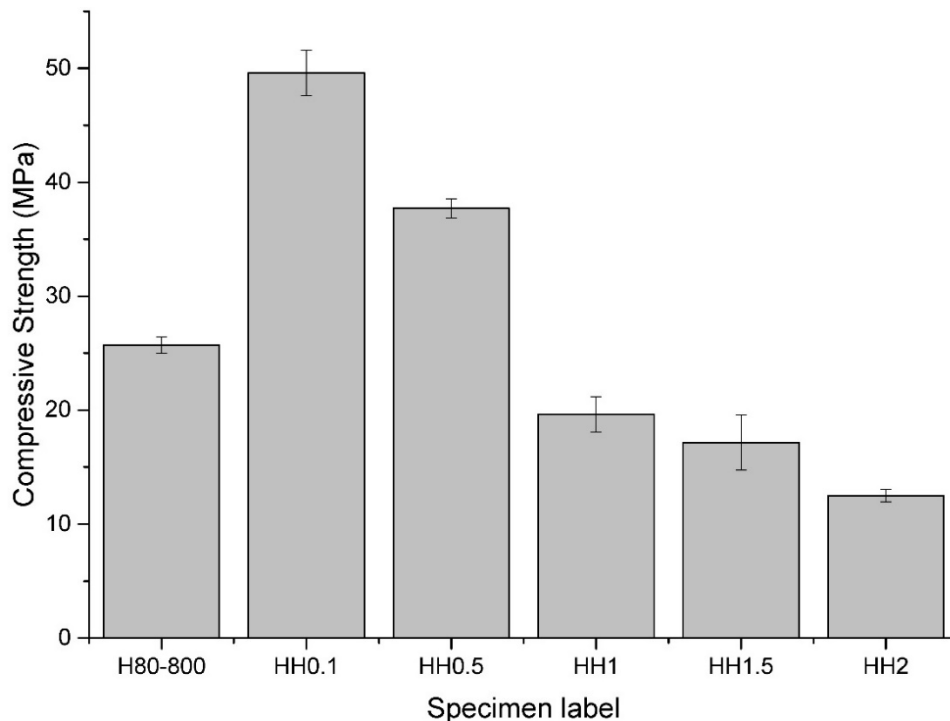


Figure 5.27: Compressive strength measurements conducted on harakeke char composite as a function of char loading.

Sintered cabbage tree leaf char composite:

Figure 5.28, outlines the compressive strength value measured for cabbage tree leaf char reinforced composite compared to pure H<sub>80-800</sub> HAp (control). The compressive trend is different from what was observed when harakeke char reinforcement was used. The 0.1% addition of cabbage tree leaf char resulted in only a modest 6% increase in compressive strength, which was further increased to 47% with the addition of 0.5% char, however further additions resulted in a decrease in compressive strength relative to 0.5% char composite. When compared to harakeke char reinforcement, it can be observed that the trend and the values of compressive strength are different and this may be because of the absence of the nanostructured carbon (nano scrolls) in the cabbage tree leaf char, as the presence of rolled graphene sheets could have induced strengthening affects like crack bridging in the composites.

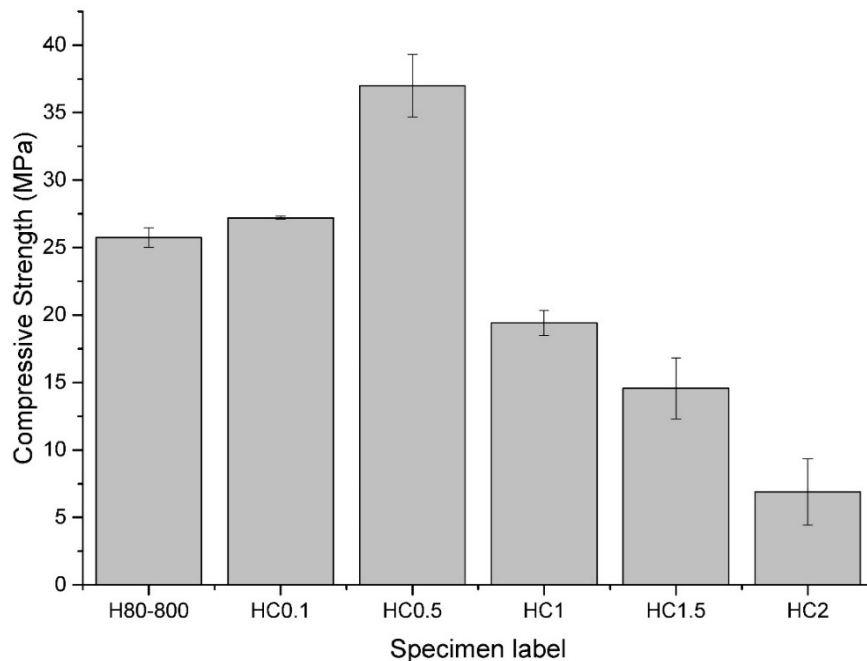


Figure 5.28: Compressive strength measurements of cabbage tree leaf char composite specimens as a function of char loading.

### 5.3.9. Diametral tensile strength (DTS)

The so called diametral tensile strength test is also known as an indirect tensile strength test, where when carrying out this testing, a cylindrical specimen is subjected to a compressive load in the diametral plane which is perpendicular to the longitudinal axis, as shown in Figure 5.29. The compressive vertical forces generate, tensile stresses perpendicular to the vertical plane that pass through the centre of the disc and the fracture occurs along the vertical plane. The tensile stresses produced are directly proportional to the applied compressive load. The DTS of the control sample (H<sub>80-800</sub>) which had

approximately 36% apparent porosity was found to be around  $5.37 \pm 0.10$  MPa which is very close to the DTS values reported in an another study[310].

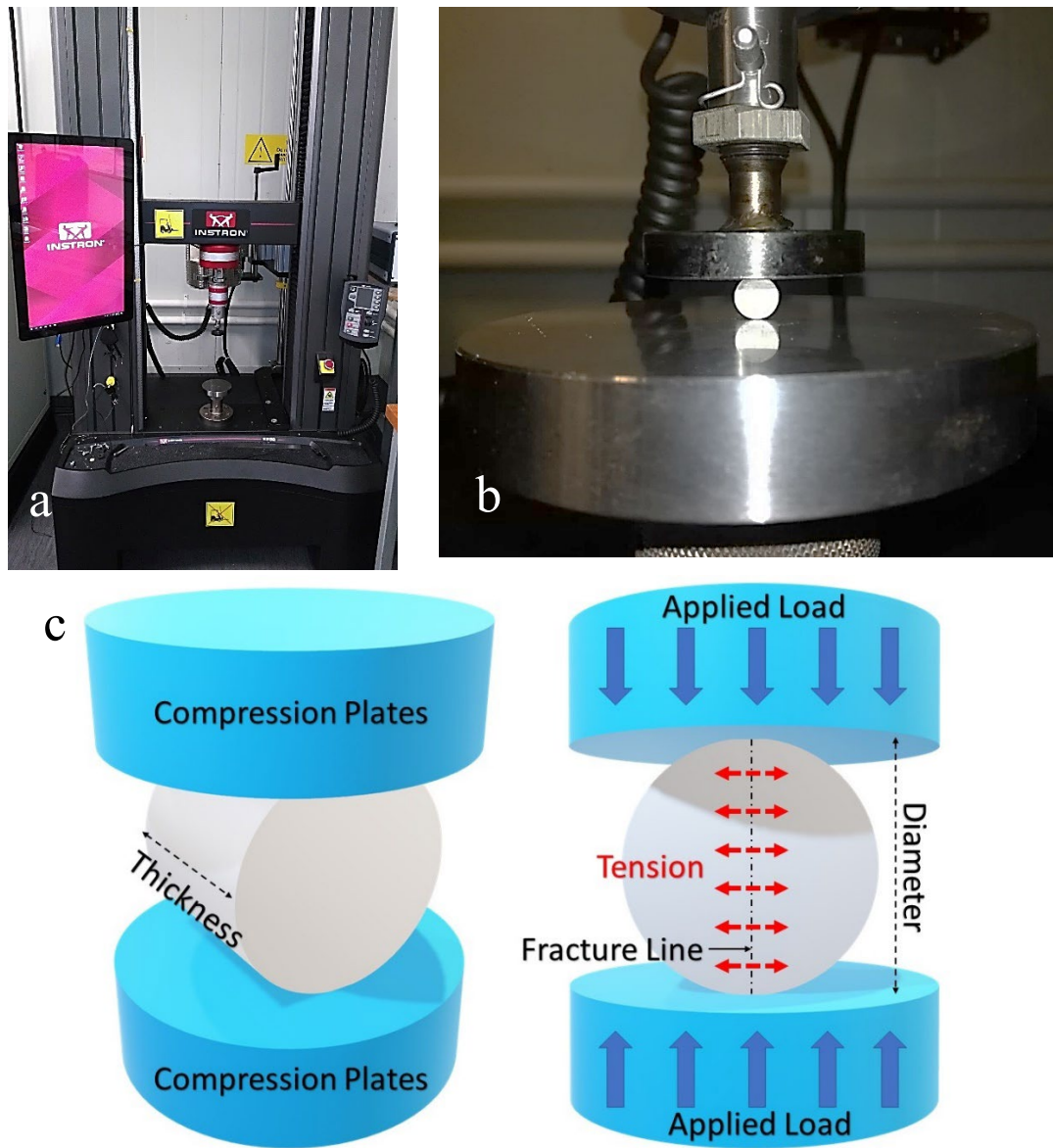


Figure 5.29: a) Compression testing machine, b) sample undergoing DTS test and c) schematic of DTS test.

Sintered *harakeke* char composite:

The diametral tensile strength of *harakeke* char composites is given in Figure 5.30. It can be observed that addition of 0.1% and 0.5% *harakeke* char improved the DTS by 103% and 175% respectively, however further additions resulted in a decrease in DTS relative to 0.5% *harakeke* char composite. An important observation related to the fracture behaviour of samples is that 0.5%, 1% and 1.5% *harakeke* char composite samples remained intact (not powdered) even after failing/developing fractures. However, the 2% *harakeke* char composite sample became powdered after failing. This was probably due to

the irregularities in the distribution of char which caused agglomeration, which generates cracks upon being loaded. The figure 5.31 shows the top and lateral views of the fracture samples.

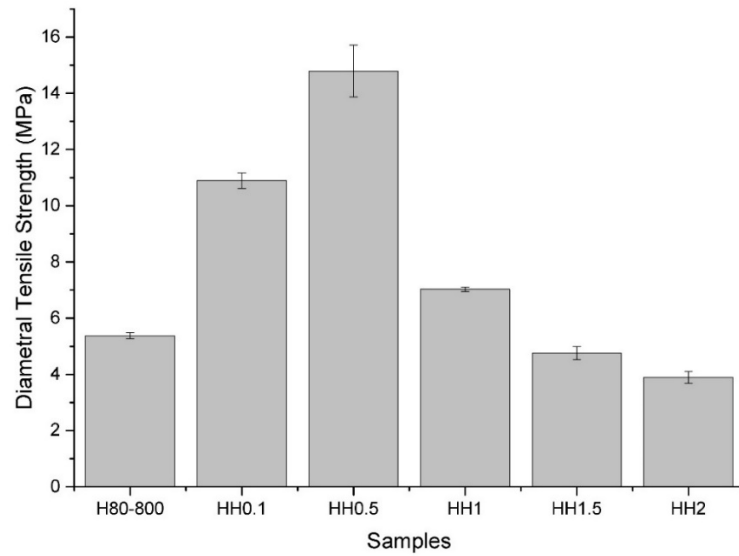


Figure 5.30: DTS measurements conducted on harakeke leaf char composite samples.

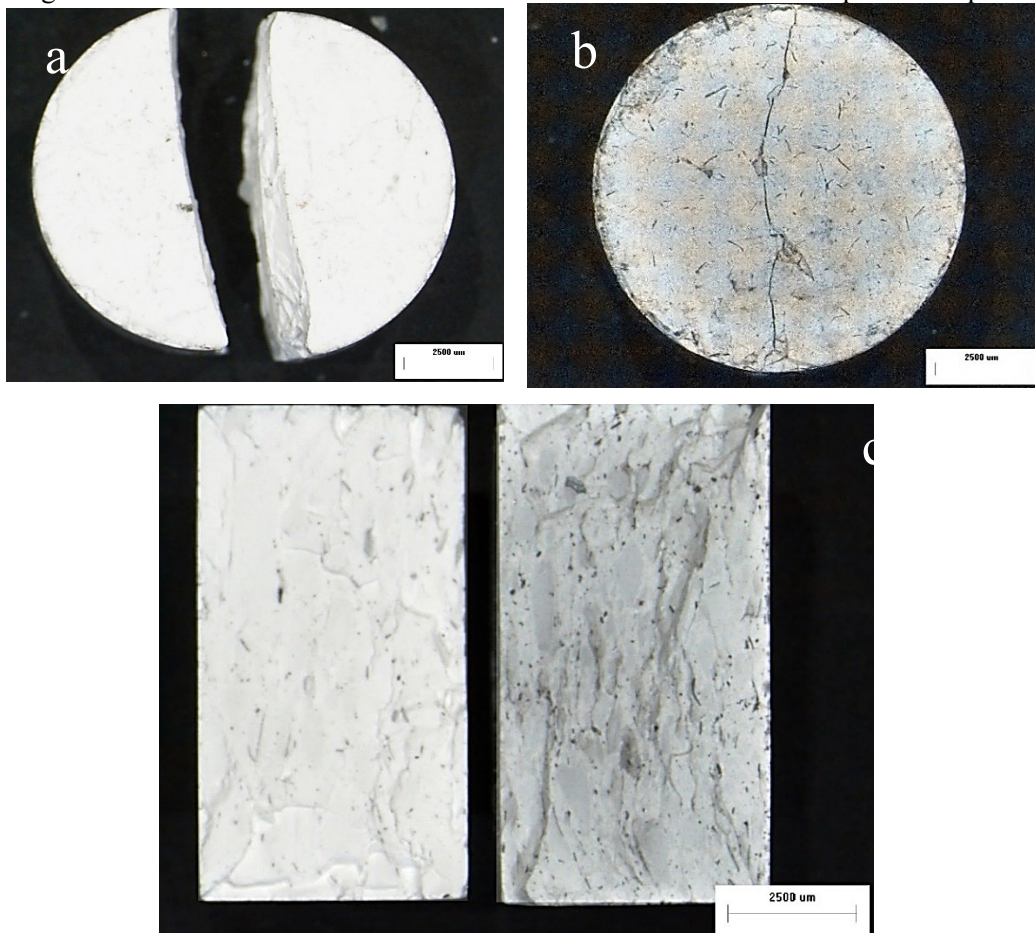


Figure 5.31: a) Diametral tensile strength test fractured H<sub>80-800</sub>, b) diametral tensile strength test fractured HH<sub>1</sub> and c) lateral view of both fractured samples.



Sintered cabbage tree leaf char composite:

The diametral tensile strength of H<sub>80-800</sub> and cabbage tree leaf char composites is presented in Figure 5.32. It can be observed that addition of 0.1% and 0.5% cabbage tree leaf char improved the DTS by 11% and 66% respectively, however further additions resulted in a dramatic decrease in DTS. For the composites that had 1%, 1.5% and 2% char addition, fractures into several pieces or powdering occurred on failure. This was probably due (as in the harakeke leaf fibre char case) to the agglomeration of the char within these ceramic test specimens which has been attributed to the degradation of other mechanical properties measured for composites of these char loadings.

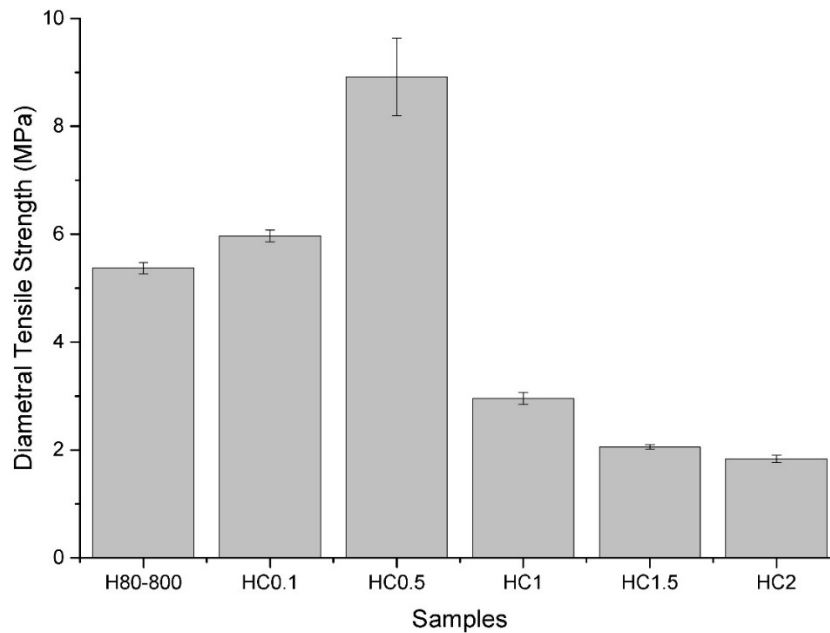


Figure 5.32: DTS measurements conducted on cabbage tree leaf char composite samples.

## 5.4. Conclusions

The control sample (H<sub>80-800</sub>) displayed a well sintered structure with approx. 61% porosity and 36% apparent porosity. It had a compressive strength, diametral tensile strength, Vickers hardness, brittleness index and indentation fracture toughness of approx.  $25.73 \pm 0.72$  MPa,  $5.37 \pm 0.10$  MPa,  $192.69 \pm 26.79$  HV,  $3.63 \pm 0.15$  and  $0.513 \pm 0.054$  Mpa.m<sup>1/2</sup> respectively. Comparatively, in both types of composites, char addition up to a certain level was found to have enhanced the mechanical properties of HAp. There was, however a very significant difference in the values of the properties across loadings. For example, 0.1% addition of piranha treated harakeke char (HC<sub>PT</sub>) raised the values of compressive strength by approx. 93%, diametral tensile strength by approx. 103%, Vickers hardness by approx. 8.97% and indentation fracture toughness by approx. 138%, whereas a 0.1% addition of cabbage tree leaf char raised the values of compressive strength only

by approx. 6%, diametral tensile strength by approx. 11%, Vickers hardness by approx. 1.23% and indentation fracture toughness by approx. 31%. For both composites, it was noted that brittleness index decreased as compared to control sample (H<sub>80-800</sub>), which means introduction of char in the HAp increases ductility and crack resistance. Electron microscopy revealed refinement of particles near the fibres, which may be due to the increased thermal conductivity because of char structures, which allowed the localised temperature to be raised up to the temperature of grain refinement.

# CHAPTER SIX : BIOMORPHIC CALCIUM DEFICIENT HYDROXYAPATITE FIBRES DERIVED FROM A NATURAL HARAKEKE (PHORMIUM TENAX) LEAF FIBRE TEMPLATE

---

## 6.1. Introduction

The research in the field of “Biomimetic materials” has led to the development of various useful materials having a design motif of naturally produced materials. A variety of multifunctional materials especially biomorphic ceramics have been developed using several biotemplating techniques [311-313]. The development process of a biomorphic ceramic is relatively simple and effective, as ceramics easily inherit microstructural features of natural materials without too much modification. Ceramic materials composed of  $\text{Al}_2\text{O}_3$ ,  $\text{SiC}$ ,  $\text{TiO}_2$  and  $\text{ZrO}_2$  have been trialled for forming structures (like fibres, porous structures, coatings) using the biotemplating techniques, for e.g. Dong et. al. [314] utilized eggshell membrane (ESM) density, bio-inertness well structures with interconnected porosity and improved mechanical properties. They proposed this material as an alternative to titanium and titanium alloy for as a biotemplate and an aqueous soaking technique to synthesize biomorphic mesoporous  $\text{TiO}_2$  with an interwoven meshwork formation. These biomorphic ceramics were found to be suitable for applications like heat insulation, electrical capacitors and membranes for sensors [211, 212, 315, 316]. One significant use of biomorphic ceramics is as a biomedical material. González et al. [317] developed bioactive glass-coated biomorphic  $\text{SiC}$  thin films that were found to possess low medical purposes. Similarly, Rambo et al. [318] developed biomorphic alumina sponges coated with bioactive calcium phosphate layers for biomedical applications. Recent developments in bone tissue engineering revealed the importance of porous scaffolds as an effective approach to promote the repair and regeneration of diseased or damaged bone tissue. An ideal porous scaffold is required to possess excellent bioactivity, osteoconductivity, controlled biodegradability, reasonable mechanical strength and a network of interconnected porosity to serve as a template for bone ingrowth, [319-321].

Porous hydroxyapatite ( $\text{Ca}_{10}(\text{PO}_4)_6(\text{OH})_2$ , HAp) ceramics mostly fulfil the criteria required for ideal implant material, although an obvious and classical problem has been the poor mechanical properties that the material has [17, 322]. A number of studies has reported

the formation of a bone-like apatite layer on porous HAp material surfaces in vitro and stimulation of new bone formation and growth into the interconnected porosity of a scaffold/implant [323-325]. To synthesise HAp with a natural porous network and to imitate the porous structure of spongy bone, scientists have tried different techniques such as polymeric sponge replication [326], animal bone conversion[70], electrospinning [327], phase-separation [328], freeze-drying [329], and gel-casting techniques [330], however templated synthesis of hydroxyapatite based materials have attracted considerable interest in the last 10 years[331-333]. One of the most important criteria for any template-assisted synthesis of HAp is the selection of a suitable template and its possible contribution to the apatitic mineralisation. In terms of using natural templating materials for making bio-inspired materials, research workers in the last 20 years have utilised many natural biological materials like soft- and hardwoods, silk, cotton, coral and coir fibres to synthesise different ceramic materials. The microstructure produced, retains the natural biological features and uniformity of the template used. Wood is a natural biopolymeric composite composed of hemicellulose, cellulose and lignin. It displays a complex macro/micro/nano-structure with ordered cellular honeycomb-like channels, which resembles the structure of cancellous bone[211, 212]. One study reported the successful use of heat-treated birch wood directly as an implant for osteochondral bone defects in a rabbit [214]. Many different types of wood (or wood-derived materials) due to their open trabecular structure, have been used as templates for making porous ceramics providing flexibility for the manufacture of complex shapes, biological properties, and inherent 3D interconnected porous structure. In this chapter, a combination of biotemplating and HAp re-precipitation processing, techniques were trialled for the first time on *harakeke* fibres, to develop novel biomorphic HAp ceramic materials.

## 6.2. Materials and Methods

### 6.2.1. Materials

All chemicals and solvents used in the experimental work were employed in as-received condition, without further purification. Nitric acid (HNO<sub>3</sub>) (65%, Merck Germany) was used to carry out digestions. The natural mechanically stripped *harakeke* (*Phormium tenax*) leaf fibres (supplied by Foxton Flax Stripping Museum, NZ) were used as the biotemplate. Ultra-pure water (Type 1) was used for all experimental and cleaning purposes. Raw sectioned bovine femur bones (in frozen condition, breed unknown) were used as a source of calcium and phosphate ions and were purchased from the butcher's section of a major supermarket chain in New Zealand. The pre-sectioned frozen bones were defrosted in water at room temperature for 24 hours before defatting was carried out.

### 6.2.2. Solution preparation

The first step for developing biomorphic HAp fibres is the making of a solution containing  $\text{Ca}^{2+}$  and  $\text{PO}_4^{3-}$  ions. This solution was produced from bovine femur bone, which was processed to remove most of the unwanted, extraneous organic matter. The cleaning (defatting) process involved boiling of the raw bones for 8 hours with a change of water after every 2 hours followed by drying at 105 °C for 12 hours in an oven. Defatted and dried bones were subjected subsequently to heat treatment at 1000 °C for 4 hours. This temperature (1000 °C) was chosen after performing a thermogravimetric analysis of the defatted bone. The heat treatment was designed in a way to ensure that removal of all organic matter namely collagenous protein and carbonate occurs such that crystalline hydroxyapatite is achieved/precipitated. The bone obtained after heat treatment was white in colour and fragile in nature. These bones are referred to as “sintered cow bone” in this paper. After this heating process, sintered cow bones were crushed to obtain powder which was subsequently digested in dilute (20%) nitric acid. This solution is referred to as “digest solution”. The pH of 20% nitric acid solution and digest solution was found to be -0.03 and -0.01 respectively. The initial concentration of  $\text{Ca}^{2+}$  and  $\text{PO}_4^{3-}$  ions in the digest solution was experimentally found (using ICP-MS/analysed as Ca and P) to be approx. 330 ug/L and 180 ug/L respectively.

### 6.2.3. Harakeke leaf fibre formation and initial treatments

The natural *harakeke* (*Phormium tenax*) leaf fibres were treated with 0.5 M NaOH solution for 2 hours at room temperature (to increase surface roughness and/or wettability), thoroughly washed with water and then dried overnight at 60 °C. The dried and loose alkali-treated *harakeke* leaf fibres were then immersed in the digest solution for 24 hours (solid to liquid ratio 1:10) to allow infiltration of the inorganic ions. The left-over digest was found to be brownish in colour and had a pH of approx. 0. After drying at 60 °C for 8 hours, the fibres were then oxidised at 1000 °C for 3 hours in an alumina crucible. This results in the formation of long entangled white fibres, which may have ash content due to burning of plant fibres. These fibres are referred to as “biomorphic fibres (as formed)” in this paper. A sample of “biomorphic fibres (as formed)” was taken for additional analysis by Fourier transform infrared (FTIR) and powder X-ray diffraction (XRD) only. The resultant long entangled fibres were subsequently subjected to 0.1 M NaOH solution washing treatment for 10 minutes to remove ash content. A pictorial representation of the process steps is represented in Figure 6.1. The short fibres; namely “biomorphic fibres (final product)”; obtained were then subjected to chemical, thermogravimetric and microscopic characterisation.

#### 6.2.4. Characterisation

An FTIR spectrometer (Spectrum 100A Express, Perkin Elmer) was utilised for recording IR spectra of the *harakeke* fibres, sintered cow bone and biomorphic fibres (both as formed and final product), via the potassium bromide (KBr) disc method (spectra were recorded between 4000 – 450  $\text{cm}^{-1}$ ) (5 samples, with 5 scans per sample). A spectral resolution of 4  $\text{cm}^{-1}$  was used. Raman spectra of biomorphic fibres (final product) were recorded with a Raman station 400F (Perkin Elmer) spectrometer with a spectral resolution of 1  $\text{cm}^{-1}$  (laser 785 nm near-infrared laser) (5 samples, with 3 scans per sample). Thermogravimetric analysis (TGA) (STA 8000, Perkin Elmer) was also carried out to study the loss of weight associated with the different heating events of the raw and digest solution-treated fibres. Thermograms were recorded from room temperature to 800 °C in an air atmosphere. The thermogram of the imbibed fibres provides information on the formation of the biomorphic fibres from the *harakeke* fibres imbibed with digest solution. The phase composition of biomorphic fibres (final product) was determined by an X-ray diffractometry (Panalytical Empyrean Series 2 diffractometer) with Cu K $\alpha$  radiation at 45 kV & 40 mA ( $\lambda = 1.5406 \text{ \AA}$ ) and a step size of 0.0260°. An XRD study of raw *harakeke* and digest treated fibres heated at various temperatures was performed to understand the biomorphic formation of HAp. The elemental analysis of sintered cow bone, biomorphic fibres (as formed and final product) was done using an inductively coupled plasma mass spectrometer (ICP-MS, Agilent 8900 triple quadrupole (QQQ)). A sample of biomorphic fibres (final product) was also tested for elemental analysis, through an external analytical company (Analytica Ltd, Hamilton, New Zealand) to verify the Ca/P mole ratio value. The morphological characteristics of the samples were recorded using a scanning electron microscope (SEM) (S-4700, Hitachi) instrument in the form of fibres placed on an aluminium stub using high purity conductive double sided adhesive carbon tape. Prior to imaging, all samples were sputter coated with platinum to avoid surface charging issues.



Figure 6.1: A pictorial representation of the processing steps, which summarises production of the digest solution containing calcium and phosphate ions and the soaking and calcination of the NaOH treated *harakeke* fibres in the solution, resulting in the production of the biomorphic fibres.

## 6.3. Results & Discussion

### 6.3.1. FTIR Analysis

The chemical structure of *harakeke* fibres (raw and alkaline-treated) were analysed using FTIR, as it is an appropriate technique for observing any changes introduced in the chemical structure of natural fibres due to the different treatments. The main IR absorbance peaks of interest have been identified and are shown for comparison in Figure 6.2. Upon comparison of both spectra, no visible change was found in the bands at 2922 and 2855  $\text{cm}^{-1}$ , which are usually attributed to the C–H stretching modes in cellulose, however a very small change in the intensity of the two characteristic lignin bands at 1508 and 1596  $\text{cm}^{-1}$  (which relate to the aromatic skeletal vibrations of lignin) and the band at 1461  $\text{cm}^{-1}$  (attributed to the C–H deformations in lignin), was found and hence it is plausible to assume that a very small and negligible amount of lignin was removed due to the mild alkali treatment. There was found to be a considerable change in the intensity of the carbonyl band ( $>\text{C}=\text{O}$ ) at 1734  $\text{cm}^{-1}$ , which is a signature peak of hemicellulose. Similarly, the decrease in the intensity of the peak at approx. 1250  $\text{cm}^{-1}$  (stretching vibration of the C–O single bond) suggests the partial removal of hemicelluloses in the treated fibres. The peak at around 1638  $\text{cm}^{-1}$  is principally associated with adsorbed water. The prominent band at around 1052  $\text{cm}^{-1}$  is attributed to the C–O, C–C stretching and C–OH stretching vibrations in hemicellulose, cellulose and lignin. The sharp band at around 899  $\text{cm}^{-1}$  is due to the  $\beta$ -glycosidic bond, and is also representative of the occurrence of the crystalline phase of cellulose type I. The bands at 1461, 1381, 1328 and 1250  $\text{cm}^{-1}$  represent C–H, OH or  $\text{CH}_2$  bending [279-282].

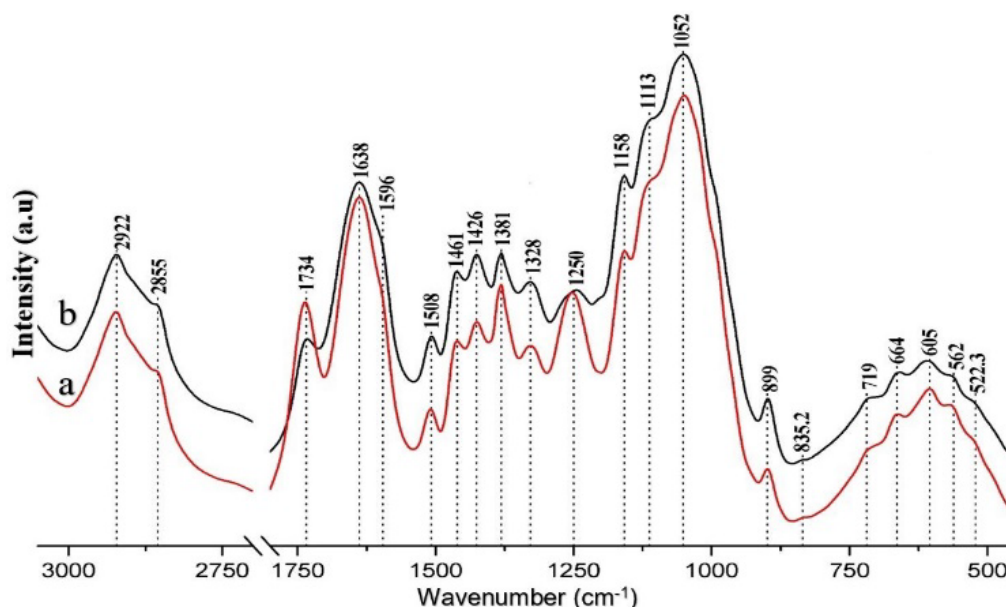


Figure 6.2: FTIR spectra of (a) raw harakeke fibres, and (b) mild alkaline treated harakeke fibres. Spectra were recorded as pressed KBr discs.

FTIR analysis was also carried out on sintered cow bone, Figure 6.3 (a), to confirm HAp had been prepared, as well as to ensure that during sintering complete deproteinisation had taken place. The complete deproteinisation is important to avoid xanthoproteic-associated reactions that can result in impurities and discolouration during its digestion in nitric acid[26]. The IR spectra of sintered cow bone depicts all the characteristic peaks of the HAp lattice, which include peaks related to  $\text{PO}_4^{3-}$ , hydroxyl modes and  $\text{CH}_n$  stretching vibrations [56, 70, 237, 334-336]. The small peak at around  $1385\text{ cm}^{-1}$  which appeared in all the spectra is most likely due to a nitrate impurity which would have emanated from the nitric acid used to form the digest solution. Hence it can be deduced that at  $1000\text{ }^\circ\text{C}$ , crystalline hydroxyapatite has been produced from raw cow bone after complete deproteinisation.

The FTIR analysis of the biomorphic fibres (both as formed and final product) was carried out to monitor for the formation of HAp in the fibres, as well as to assess qualitatively their crystallinity. Figure 6.3 (b), which represents the spectra of biomorphic fibres (as formed), shows the characteristic peaks of stoichiometric hydroxyapatite. The band centred around  $1000\text{--}1100\text{ cm}^{-1}$  is the main peak confirming the formation of hydroxyapatite. The peaks at around  $961.6\text{ cm}^{-1}$  and  $602\text{ cm}^{-1}$  are related to the  $\nu_1$  and  $\nu_4$  fundamental vibrational modes of the phosphate group [56, 70, 237, 334-336]. The bands at around  $875$ ,  $1414$  and  $1458\text{ cm}^{-1}$  indicate the presence of the  $\text{CO}_3^{2-}$  group (type-B i.e.  $\text{CO}_3^{2-}$  substituting for  $\text{PO}_4^{3-}$ ) however it is generally observed that  $\sim 1465$ ,  $\sim 1413$ , and  $\sim 873\text{ cm}^{-1}$  are characteristic bands for type-B substitution. The missing band at approx.  $1465\text{ cm}^{-1}$  point towards the possibility of labile (free) carbonate being present rather than substituted carbonate, as carbonate in HAp can either be substituted in the lattice or labile (labile meaning adsorbed on its surface or present by association as a separate entity/compound). Studies by Ren and Leng[237] and Ren, Ding and Leng [336] showed that along with the different bands of carbonate, the presence of a specific band (which they termed the “signature band”) is essential to deduce whether there is substitution of  $\text{CO}_3^{2-}$  in the lattice. If that specific band is absent, the carbonate can be considered labile rather than substituted. They found out that the signature band for type-B ( $\text{CO}_3^{2-}$  substituting for  $\text{PO}_4^{3-}$ ) is at  $\sim 1465\text{ cm}^{-1}$ . Hence in the case of biomorphic fibres (as formed) the absence of the  $\sim 1465\text{ cm}^{-1}$  signature band indicate that the carbonate identified in the IR spectrum is labile in nature, most probably adsorbed on the surface (due to highly porous nature of fibres) during cooling in the furnace. Moreover, a new peak at around  $1617\text{ cm}^{-1}$  might be adsorbed  $\text{CO}_2$ , in line with the previous studies based on the adsorption of  $\text{CO}_2$  on the HAp surface[337, 338], where the appearance of different bands in the range of  $1600\text{--}1700\text{ cm}^{-1}$  were reported after the successful adsorption of  $\text{CO}_2$  on the HAp



surface. The band in the range of 3250-3700  $\text{cm}^{-1}$  and the peak at around 1633  $\text{cm}^{-1}$  is due to adsorbed  $\text{H}_2\text{O}$ /moisture[339]. This was found to be increased in the biomorphic fibres (as formed) from sintered cow bone (Figure 6.3(a)) and is most likely the result of the fibres' extensive porous network that will be favourable for adsorbing water from the ambient air. The band at 3573  $\text{cm}^{-1}$  is due to the O-H stretching modes of lattice HAp hydroxyl groups, which shows the presence of hydroxyapatite. Comparison of the IR spectra of biomorphic fibres (as formed) with the biomorphic fibres (final product), (Figure 6.3(c)), reveals the effect of NaOH washing treatment on fibres. All the characteristic peaks of HAp remained unaltered, however there was found to be an increase in the intensities of bands due to adsorbed (labile) carbonate (at 875, 1414 and 1458  $\text{cm}^{-1}$ ). This would have resulted from the formation of a small amount of free calcium carbonate (confirmed from XRD) that would normally accompany any exposure to an alkaline solution under ambient conditions. Moreover, an increase in the band intensity of adsorbed water (3442 and 1633  $\text{cm}^{-1}$ ) was also noted, which indicates the increased uptake of water during washing treatment. Table 6.1 enlists all the identified peaks of biofibre (as formed and final product). In general, the IR readily confirms the formation of crystalline HAp in the form of fibres via the aqueous soaking and sintering technique.

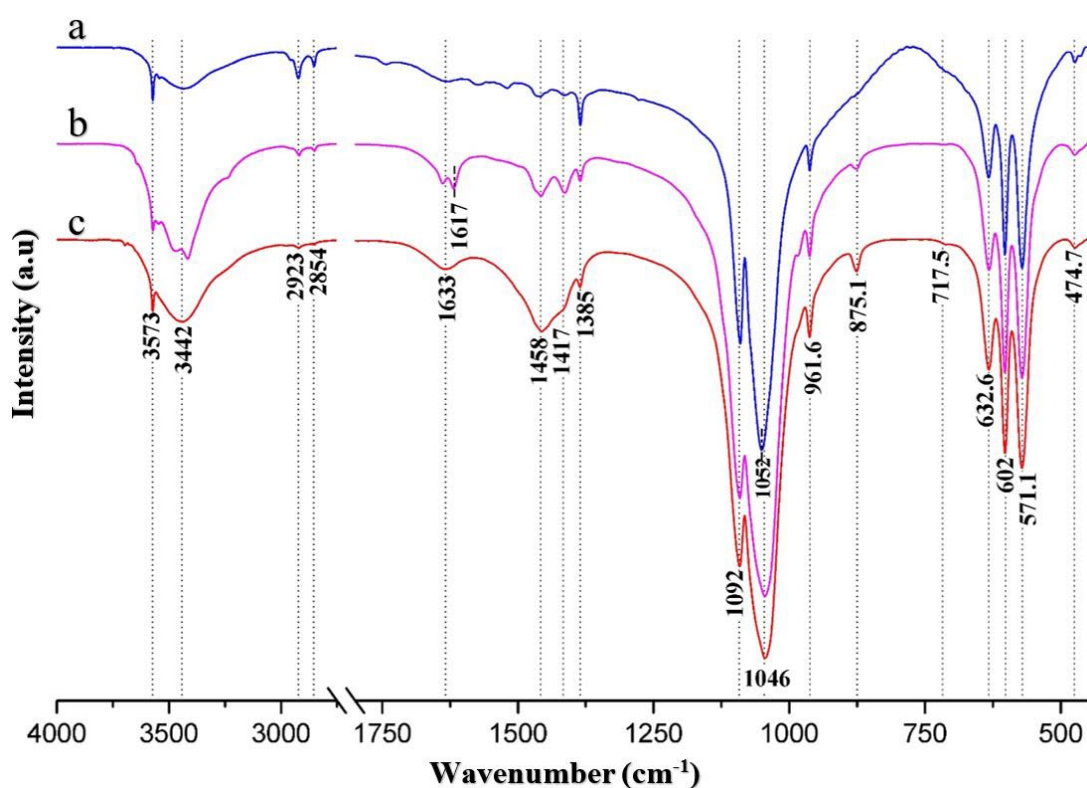


Figure 6.3: FTIR spectrum of (a) sintered cow bone (b) Biomorphic fibres (as formed) (c) Biomorphic fibres (final product)

Table 6.1: Assignment of the FTIR spectra of the calcium phosphate samples acquired in this study

Vibration Band	Biomorphic Fibres (As formed)	Biomorphic Fibres (final product)
PO <sub>4</sub> <sup>3-</sup> (ν <sub>2</sub> ) bending mode	474.4	474.4
PO <sub>4</sub> <sup>3-</sup> (ν <sub>4</sub> ) asymm. bending mode	571.1	571.1
PO <sub>4</sub> <sup>3-</sup> (ν <sub>4</sub> ) asymm. bending mode	602	602
OH libration	632.6	632.6
PØP Q <sup>3</sup> , Q <sup>2</sup> and Q <sup>1</sup> units symm. stretching	717.5	717.5
HPO <sub>4</sub> <sup>2-</sup> ion vibrations CO <sub>3</sub> <sup>2-</sup> (ν <sub>2</sub> ) asymm. bending mode	875.1	875.1
PO <sub>4</sub> <sup>3-</sup> (ν <sub>1</sub> ) symm. stretching mode	961.6	961.6
PO <sub>4</sub> <sup>3-</sup> (ν <sub>3</sub> ) asymm. stretching mode	1043-1092	1043-1092
Nitrate impurity (from nitric acid used)	1385	1385
CO <sub>3</sub> <sup>2-</sup> (ν <sub>3</sub> ) asymm. C-O stretching mode	1417 1458	1417 1458
Adsorbed CO <sub>2</sub>	1617	--
H-O-H (ν <sub>2</sub> ) bending mode	1633	1633
sp <sup>3</sup> – and sp <sup>2</sup> –hybridized CH <sub>n</sub> stretching vibrations	2923, 2854	2923, 2854
ν <sub>1</sub> and ν <sub>3</sub> stretching modes of hydrogen-bonded H <sub>2</sub> O molecules	3250-3700	3250-3700

Results obtained from FTIR were also used to calculate the crystallinity index (CI), which is generally defined as the measure of fraction of crystallinity of one phase in a given sample. The CI helps in accessing the extent of splitting in the PO<sub>4</sub><sup>3-</sup> band (which actually reflects increase in crystallinity) and is defined by [239, 340]:

$$CI = \frac{A_x + A_y}{A_z} \text{ [or as per notation in Figure 6.4, } CI = \frac{AA' + CC'}{BB'} \text{] (eq. 1, also previously reported in chapter 3)}$$

where, A<sub>x</sub>, A<sub>y</sub> and A<sub>z</sub>, represent the absorbance values at wavenumber x, y and z, respectively which in the present study are defined to be 602, 571 and 590 cm<sup>-1</sup>. However, in carrying out this calculation using absorbance intensities the relevant portion of the IR spectrum (like in the case of the biomorphic fibres, 750 – 450 cm<sup>-1</sup>) needs to be baseline corrected (see Figure 6.4). The heights of the 602 cm<sup>-1</sup> and 571 cm<sup>-1</sup> absorptions are summed and then divided by the height of the valley between them. Crystallinity indices (CI) of the biomorphic fibres (final product) was found to be 4.60.

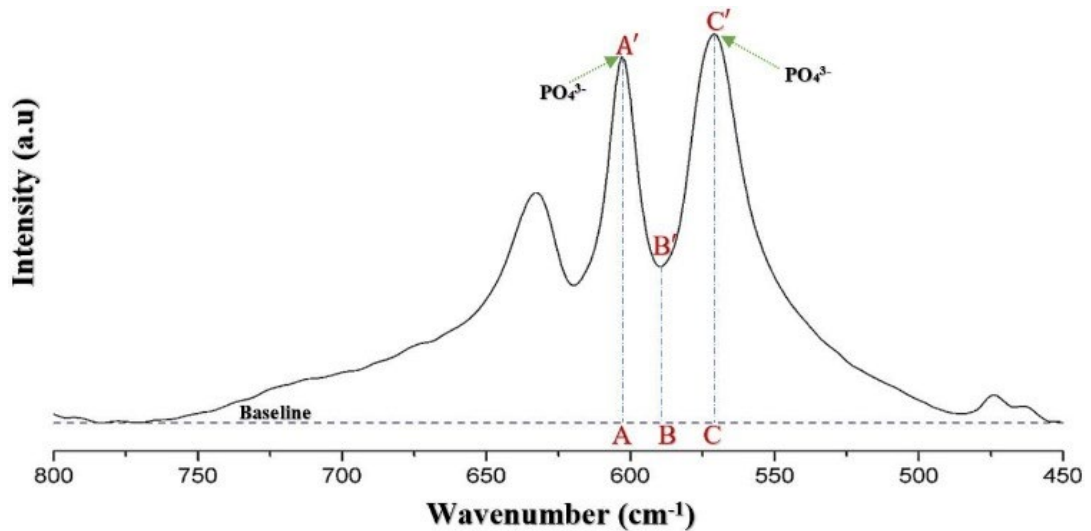


Figure 6.4: Portion of the IR spectrum of biomorphic fibres (final product) used to calculate CI.

### 6.3.2. Raman Spectroscopy Analysis

Raman spectroscopy, which has been used to complement results obtained through IR spectroscopy, can also be used to calculate crystallinity index (CI). The Raman spectrum of biomorphic fibres (final product) displayed the characteristically strong  $\text{PO}_4 \nu_1$  peak at around  $962 \text{ cm}^{-1}$ , which is the strongest signal in the Raman confirming the presence of hydroxyapatite (see Figure 6.5). Apart from this, peaks corresponding to the vibrational modes of phosphate groups, i.e.  $\nu_2(\text{PO}_4)$  at  $431$  &  $447.0 \text{ cm}^{-1}$ ,  $\nu_3(\text{PO}_4)$  at  $1076$ ,  $1047$ ,  $1041$  &  $1028 \text{ cm}^{-1}$  and  $\nu_4(\text{PO}_4)$  at  $615.6$ ,  $607.5$ ,  $591$  &  $579.3 \text{ cm}^{-1}$  peaks were also observed, which matches with available literature[341, 342].

Researchers have also used Raman spectral peaks to study crystallinity index, carbonate-to-phosphate ratio and mineral maturity of bone[264-268]. In this study, the crystallinity index (CI) from Raman spectra was calculated using the formula[343]:

$$CI_{\text{Raman}} = FWHM_{962} \text{ (eq. 10)}$$

Where,  $FWHM_{962}$  is the full-width at half maximum of the peak representing the  $-\text{PO}_4 \nu_1$  symmetric stretching mode at around  $962 \text{ cm}^{-1}$ . The  $CI_{\text{Raman}}$  values represent the degree of atomic order, the larger the values, the wider is the peak and the more atomically disordered the material is [344]. The  $CI_{\text{Raman}}$  value of biomorphic fibres (final product) was found to be 5.528.

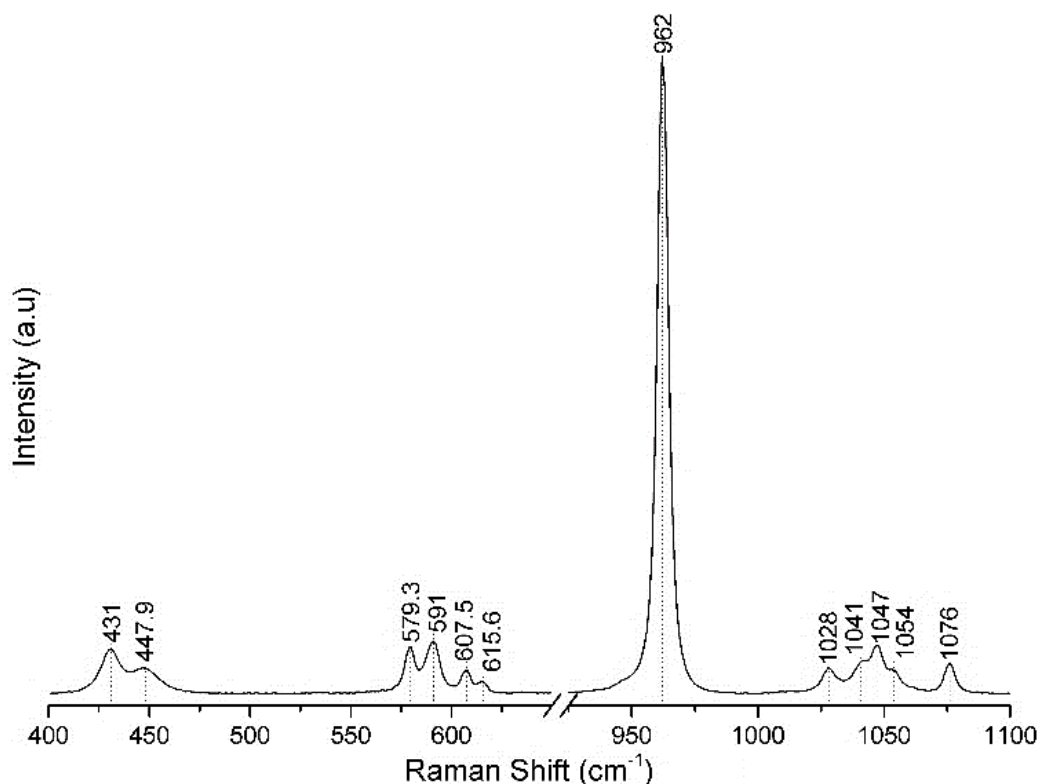


Figure 6.5: This figure represents the Raman spectrum of biomorphic Fibres (final product).

### 6.3.3. Thermal Analysis

Thermogravimetric analysis (TGA) of pre (raw *harakeke* fibres) and post soaked fibres (digest solution-treated fibres) is a vital characterisation tool that helps in analysing processing steps which involve mass losses (mainly due to the combustion of cellulose, hemicellulose and lignin associated with the sample) and also helps in gaining insight into the eventual formation of the hydroxyapatite cast structure. Simultaneous differential scanning calorimetry (DSC) helps in detecting and correlating all the heat flow (either endothermic or exothermic) events occurring during degradation of the organic matrix and formation of HAp. Figure 6.6, shows the thermogram depicting weight loss curve and the corresponding heat flow curve of the raw *harakeke* fibre bundles. Raw *harakeke* fibres displayed an initial weight loss between 50 to 120°C, mainly due to the removal of volatile content and free/adsorbed water in the fibres. It can be observed that the raw fibres did not show any noticeable thermal degradation below 200 °C. More significant weight losses (up to approx. 90%) were observed between 200°C and 500°C. At the onset of 250°C, fibres started to lose their weight mainly as a result of the thermal depolymerisation of hemicellulose and pectin, while the cellulose undergoes cleavage in its glycosidic linkages[345]. This stage was completed when the temperature reached approximately 350°C during which the fibres had lost almost 60% of their original mass. A broad exothermic peak can also be observed in the same temperature zone which supports the

depolymerisation. The next and final stage of the thermal degradation occurred in the range of 400 to 500°C when the *harakeke* had lost almost 97.5% of its initial weight leaving behind ash and residual minerals. The degradation of the  $\alpha$ -cellulose and lignin occurred during this stage [221, 274, 346].

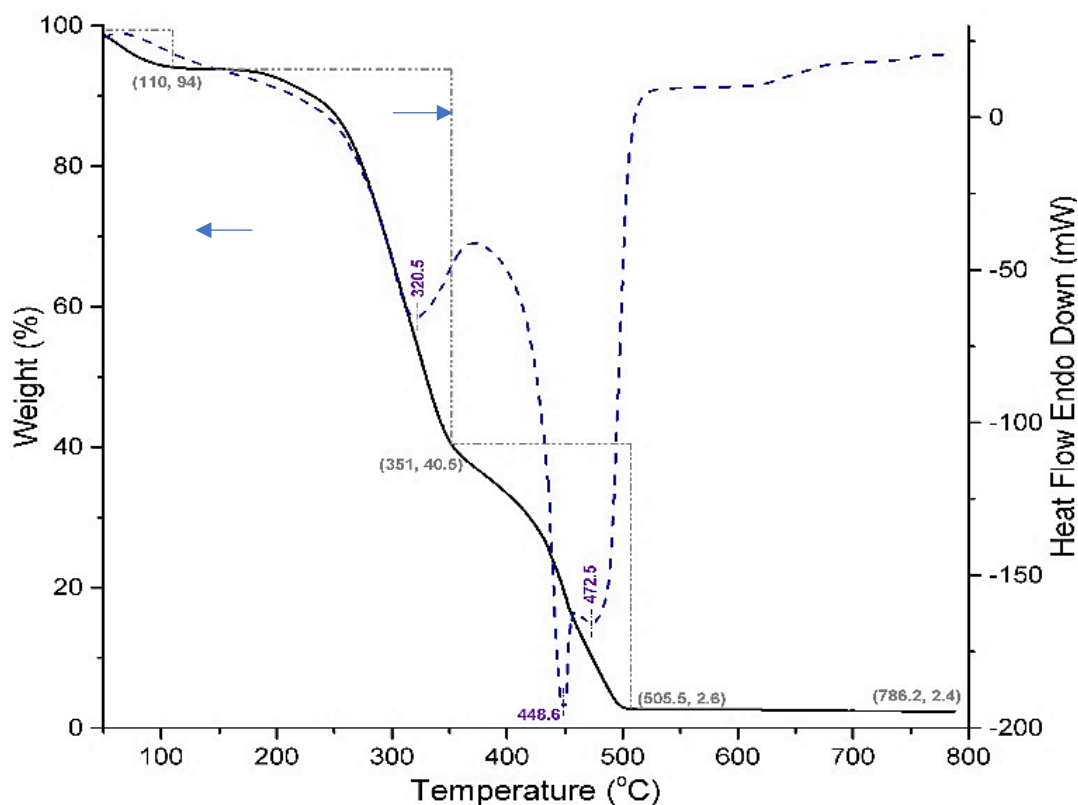


Figure 6.6: Thermogram (TGA-DSC) of raw harakeke fibres, representing the degradation of its constituents.

While studying the associated thermogram of *harakeke* fibres (Figure 6.7) that had previously been soaked/imbibed with the digest solution (apart from the initial weight loss due to the removal of free moisture and volatile content in the temperature range of 50-120°C) three distinct stages were observed in comparison to the thermogram of the raw (untreated) fibres which showed contrastingly only two stages. Wang et al. [347] while developing a different biomorphic material i.e.  $\text{Al}_2\text{O}_3$  using silk as a template and  $\text{AlCl}_3$  as an alumina source, also found an additional stage before burning/degradation of the silk template, which they referred to as the development of biomorphic alumina fibres. The thermogram in the present study depicts a stage in the temperature range of 140 - 200°C, where approx. 20% of the weight was lost, which corresponds to the development of phases involving calcium and phosphate. The presence of the two exothermic peaks in the range of 140 - 200°C also supports this phase formation. After this, two broad peaks at around 330°C and 410°C were observed, which can be assigned to the depolymerisation of hemicellulose and degradation of cellulose respectively. On comparison of the area under the curve of associated peaks of hemicellulose, cellulose and lignin, it can be assumed that

their content in the digest solution imbibed fibres was less in amount compared to the raw (unsoaked) fibres, which could be due to the pre-soaking in the highly acidic digest solution. The weight loss of approx. 3.5% from 500 °C to 800 °C can be due to the burning of char, which may have caused the initial formation of a protective layer of calcium phosphate on the fibres. An analysis of the weight loss curve shows a mass loss in the fibres of approx. 64% which indicates that the remaining 36% mass is due to biomorphic fibre and ash content.

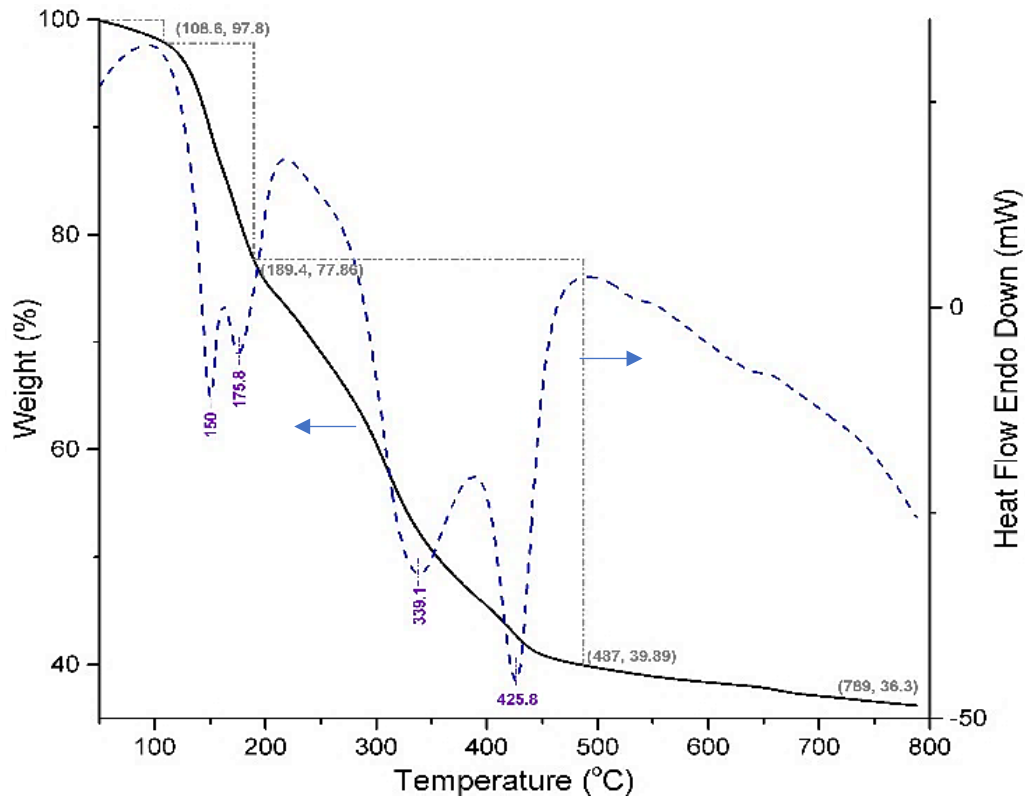


Figure 6.7: Thermogram (TGA-DSC) of solution-treated harakeke fibres, representing the formation of HAp.

The derivative thermogravimetric analysis (DTG i.e. the first derivative of weight loss with respect to time) of both pre and post digest solution soaked fibres is presented in Figure 6.8. DTG curve of raw fibres clearly represent the major weight losses at around 300 °C and 450 °C as describe earlier, hence only a two-stage decomposition of raw fibres is evident, which is also found in other studies involving lignocellulosic-type fibres[348, 349]. The DTG curve of soaked fibres also depicts an additional stage in the range of 140 - 200°C having two weight loss peaks. A minor hump at around 650 °C can be associated with the either the burning of char or the degradation of the carbonate moiety which would have been introduced during the alkali treatment done to the increase in roughness/wettability of the fibres.

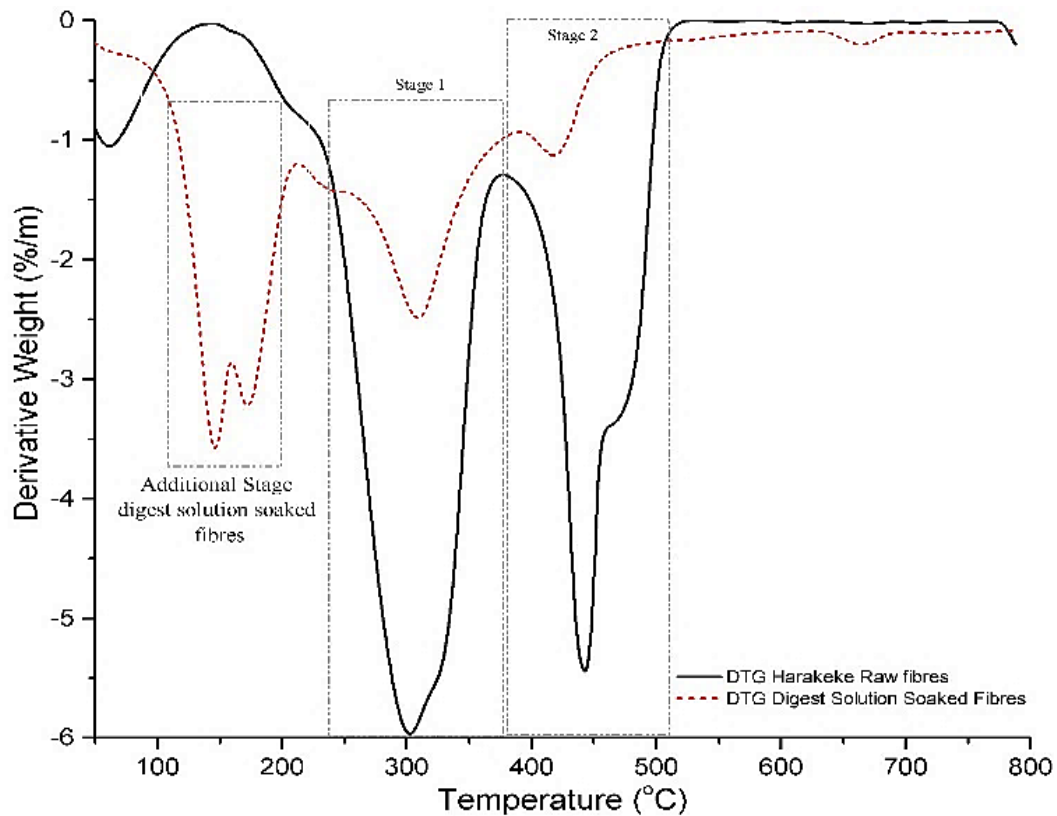


Figure 6.8: Derivative weight loss of raw and solution-treated harakeke fibres.

#### 6.3.4. X-ray diffraction analysis

Phase identification of biomorphic fibres (final product) was carried out via powder X-ray diffraction analysis. Figure 6.9 shows the XRD pattern of biomorphic fibres (final product) compared with the reference pattern from the database. The obtained spectra were imported into the Philips “HighScore Plus” software[245] and compared to the reference spectra from the ICDD PDF-4 database (The International Centre for Diffraction Data, 2019). The identified peaks matches with hydroxyapatite (“ $\text{Ca}_5(\text{PO}_4)_3(\text{OH})$ ”, reference number 04-010-6315) and, additionally, minor peaks of  $\beta$ -tricalcium phosphate ( $\beta\text{-Ca}_3(\text{PO}_4)_2$ , reference number 04-008-8714) and calcium carbonate ( $\text{CaCO}_3$ , reference number 01-078-4614) were also detected. Later it was identified that the formation of calcium carbonate in the “biomorphic fibres (final product)” was likely associated with the NaOH washing treatment and formed by uptake of  $\text{CO}_2$  from the ambient atmosphere. Figure 6.12 shows the comparison of pre- and post-NaOH-washed biomorphic fibres, where it is evident that  $\text{CaCO}_3$  is appearing after the treatment.

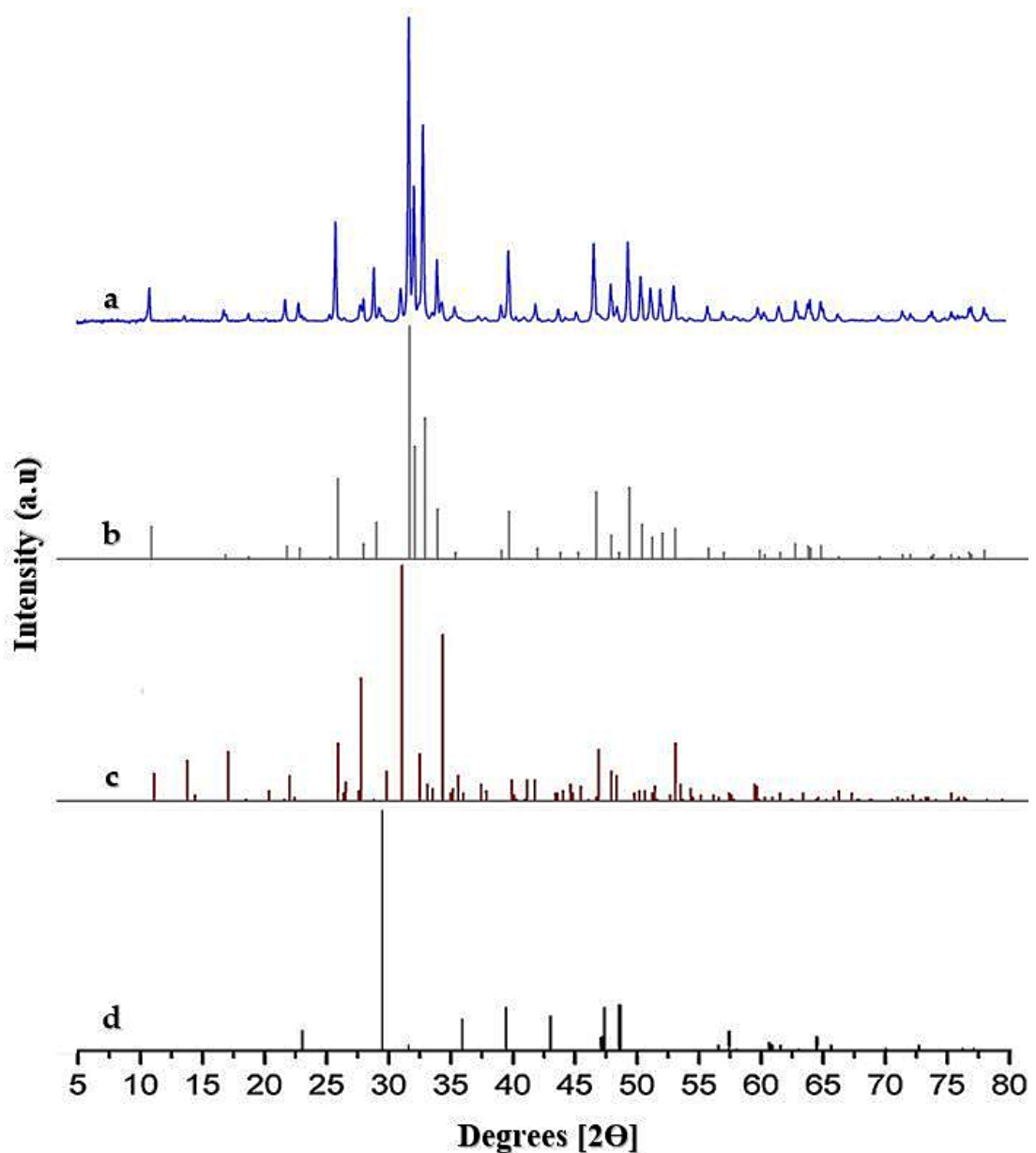


Figure 6.9: XRD diffractograms of (a) biomorphic fibres (final product) compared with the XRD from (b) standard “hydroxyapatite” (reference number 04-010-6315), (c) standard  $\beta$ -tri calcium phosphate (reference number 04-008-8714) and (d) standard calcium carbonate (reference number 01-078-4614).

The Scherrer equation was used to find the mean the crystallite size ( $D$ ) from the XRD line-broadening measurement for both sintered cow bone and the biomorphic fibres (final product) [340]:

$$D = \frac{0.89\lambda}{\beta \cos\theta} \text{ (eq. 3, also reported in chapter 3)}$$

Where  $\lambda$  is the wavelength ( $\text{CuK}\alpha$ ),  $\beta$  is the full width at half-maximum of the chosen diffraction line and  $\theta$  the diffraction angle. The diffraction peak at approx.  $2\theta = 25.9^\circ$  (corresponding to the (0 0 2) Miller plane) was chosen for calculating crystallite size ( $D$ ),



as this was found to be sufficiently isolated from the other peaks to allow measurement, as well as being sharper and more representative of the crystal growth along the c-axis. Similarly, the degree of crystallinity which reflects the fraction of the crystalline phase ( $\chi_c$ ) present in biomorphic fibres (final product) was calculated using equation 4 [246]:

$$\chi_c = 1 - \frac{v_{112/300}}{I_{300}} \text{ (eq. 2, also reported in chapter 3)}$$

Where  $I_{300}$  is the intensity of (300) diffraction peak and  $v_{112/300}$  is the intensity of the hollow between the (1 1 2) and (3 0 0) diffraction peaks (measured by averaging the intensities), as seen in Figure 6.12. The crystallite size and degree of crystallinity was found to be 56.59 nm and 0.93 respectively. Rietveld refinement was also carried out using Philips “HighScore Plus” software[245, 247, 248] (based on the Rietveld code from Wiles & Young [249]). Lattice parameters of biomorphic fibres (final product) were found to be  $a = b = 9.41961 \text{ \AA}$  and  $c = 6.88476 \text{ \AA}$  and upon comparison with the lattice parameters of hydroxyapatite  $a = b = 9.4218 \text{ \AA}$  and  $c = 6.8813 \text{ \AA}$  (taken from [350]), no major significant difference was noted. Unit cell volume was found to be  $529.04 \text{ \AA}^3$  calculated using  $V = \frac{\sqrt{3}}{2} a^2 c$ , where a and c are the unit cell axes dimensions[351].

XRD analysis of raw and digest solution treated *harakeke* fibres at different heat treatment temperatures (identified from TGA-DSC analysis) was also performed to investigate the formation of HAp. Figure 6.10 presents the diffraction spectra of raw *harakeke* fibres, solution treated-dried fibres and the solution treated fibres heat treated in the range  $120 \text{ }^\circ\text{C}$  to  $220 \text{ }^\circ\text{C}$  at an interval of  $20 \text{ }^\circ\text{C}$ . The XRD pattern of raw *harakeke* fibre represents a typical diffraction spectra of cellulose which is also matching with the literature [274]. The XRD pattern of solution treated-dried fibres revealed the substantial decrease in cellulose peaks and development of several other peaks, which corresponds to crystalline form of monocalcium phosphate monohydrate (PDF # 04-011-5377). Monocalcium phosphate monohydrate (MCPM), also known as calcium dihydrogen phosphate having formula  $\text{Ca}(\text{H}_2\text{PO}_4)_2 \cdot \text{H}_2\text{O}$ , is an important member of calcium phosphate family. MCPM possesses a Ca/P mole ratio of 0.5 and is highly acidic in nature. MCPM decomposes and converts into monetite ( $\text{CaHPO}_4$ ) in water while forming free phosphoric acid. However, in one study involving spray drying of MCPM initial dissociation into monetite had been noted, however further heating of monetite to dryness resulted in the reformation of MCPM due to the reaction of monetite with the previously dissociated phosphoric acid[352]. It is believed that the reactive functional groups at the surface of *Harakeke* fibres may have aided the nucleation and growth of MCPM.

XRD analysis of 120 °C, 140 °C and 160 °C, displayed the sequential diminishing peaks of MCPM, which is related with the conversion of MCPM into monetite and free phosphoric acid, however the newly produced phosphoric acid may have itself started to dehydrate, which resulted in its dissociation. It has been reported in the literature that when phosphoric acid is heated above 200°C, dehydrates and dissociates into a series of products ranging from pyrophosphoric acid ( $H_4P_2O_7$ ) to metaphosphoric acid  $(H_3PO_4)_n$  [353]. XRD analysis at 180 °C, 200 °C & 220 °C, depicts a pure and crystalline form of monetite (PDF # 00-009-0080).

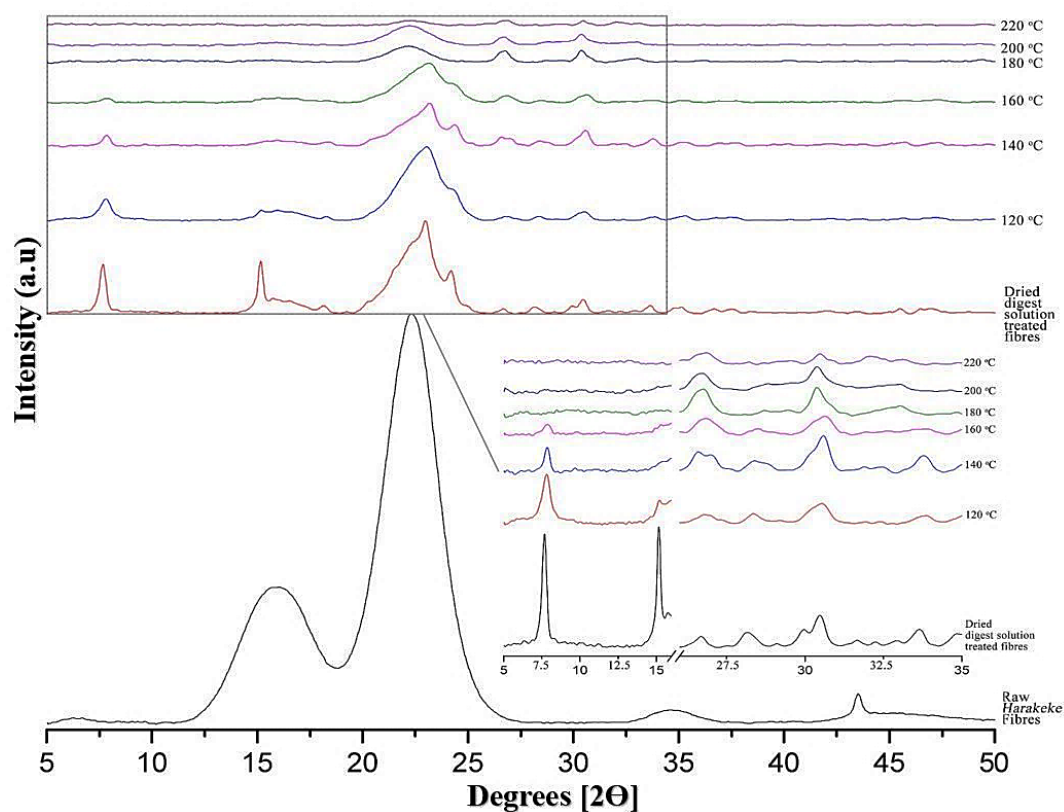


Figure 6.10: XRD diffractograms of raw and digest treated fibres representing evolving changes due to heating in the range from 120-220 °C

Figure 6.11 presents the diffraction spectra of solution treated fibres at incrementally higher temperatures. XRD analysis at 300, 400 and 500 °C revealed the dissociation of monetite into poorly crystalline/amorphous calcium phosphate depicted by the presence of a broad hump in the range of 25-35° 2θ. In this range complete decomposition of the fibres' cellulose moiety also takes place. The XRD pattern obtained for fibres heated to 500 °C represents a near complete dissociation of monetite into amorphous calcium phosphate. It is believed that the associated burning of cellulose, the releasing of  $CO_2$  and possible formation of char might have brought about conditions favourable to the transformation to HAp, as the diffraction pattern for the material heated to 600 °C showed the formation of poorly crystalline HAp and TCP. XRD patterns obtained of the material heated to 850 and 1000 °C showed an increase in the crystallinity of the formed HAp.

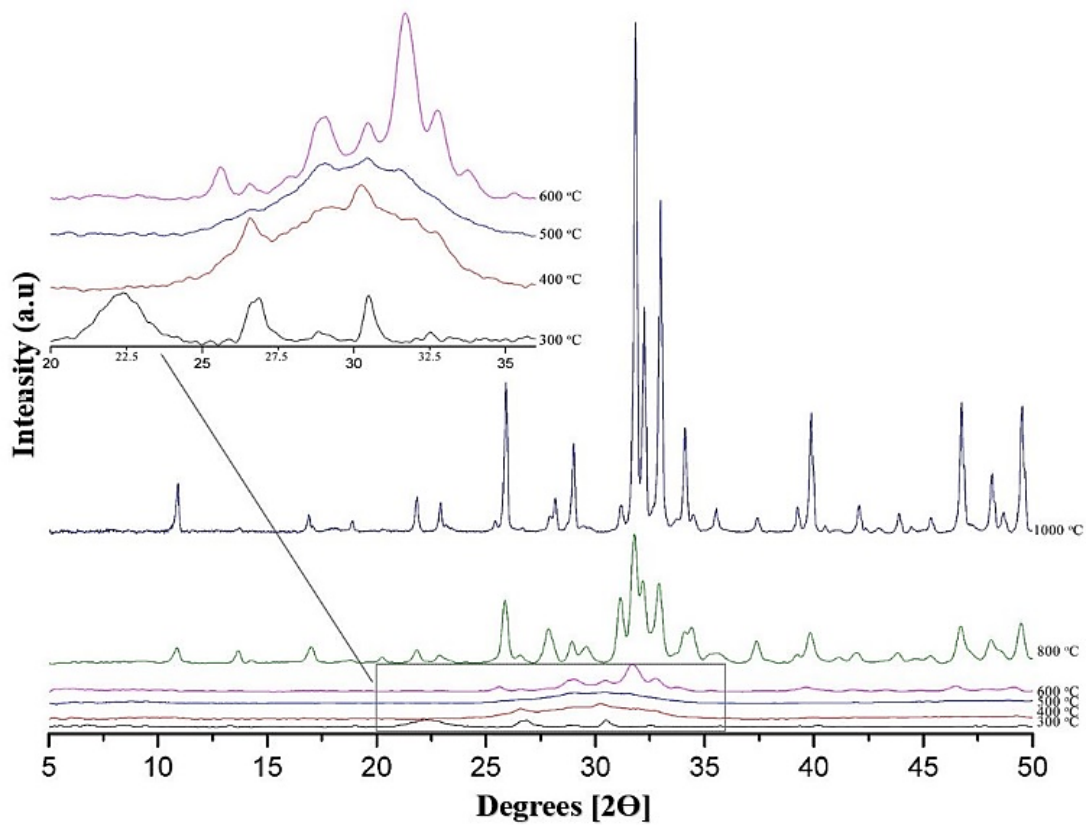


Figure 6.11: XRD diffractograms of raw and digest treated fibres representing the evolving phase changes occurring due to heating in the range of 300-1000 °C

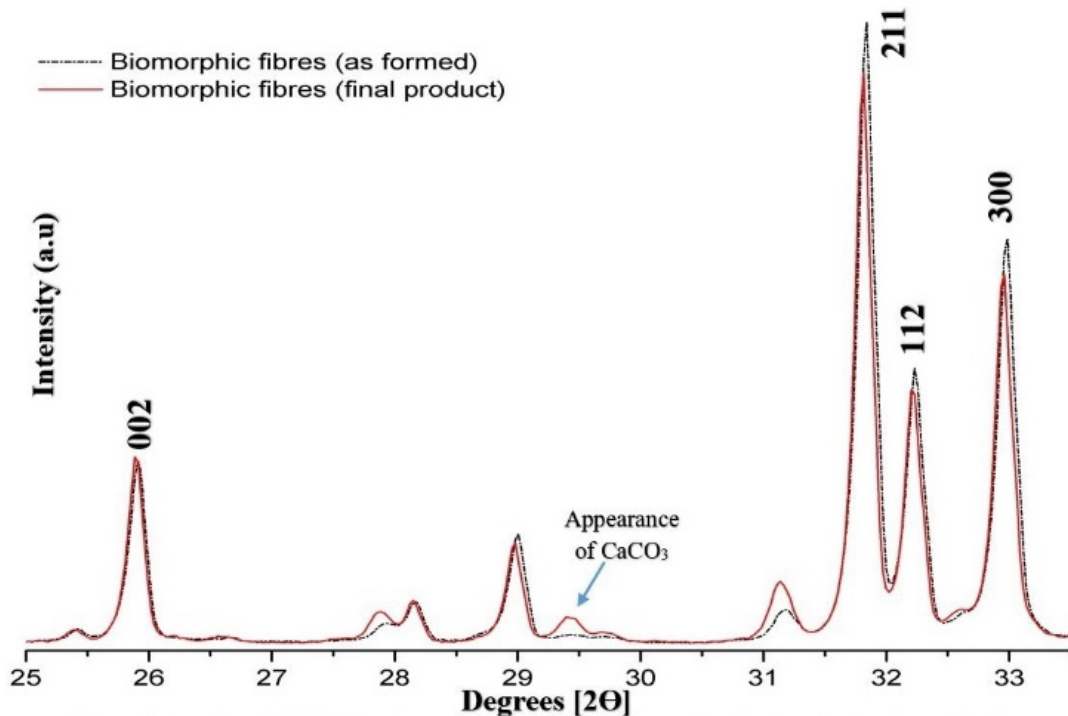


Figure 6.12: A portion of the XRD diffractogram of biomorphic fibres, revealing the important peaks used for the calculations of the crystallite size and degree of crystallinity.

### 6.3.5. Imaging

Microscopic characterisation was carried out to study the structures and morphology of the as-received *harakeke* raw fibres, mild alkali-treated *harakeke* fibres and biomorphic fibres (final product). Microscopic imaging of as-received (Figure 6.13) and 0.5 M NaOH-treated *harakeke* fibres (Figure 6.14) revealed minor fibrillation ((Figure 6.6.13 (a)), as fibres in the alkali-treated sample showed minor separation/desizing, whereas the as-received *harakeke* fibres contained bundles of fibres held together by hemicellulose, lignin and pectin [279](Figure 6.14 (a-b)). Alkali-treated fibre surfaces were found to be more groove-like and rougher in texture (Figure 6.14(b)), which would be expected to give a more wettable surface [354].

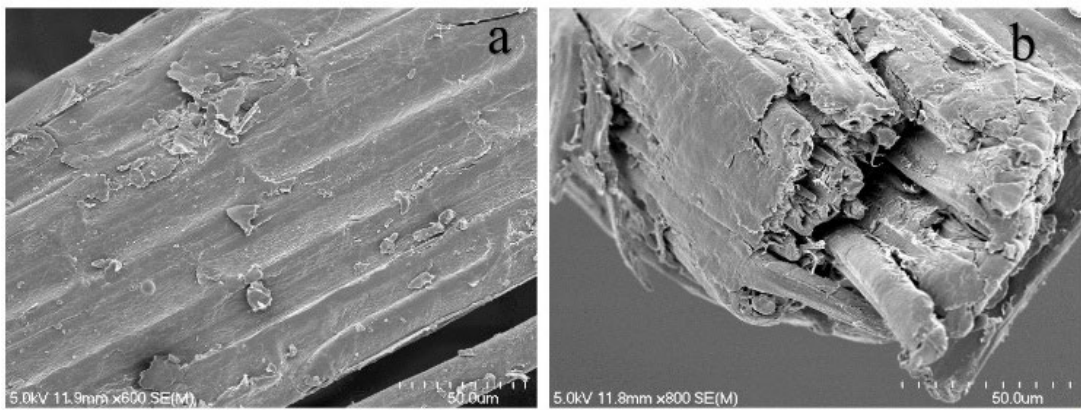


Figure 6.13: SEM images of as received harakeke fibres, with (a) showing bundles of fibres and b) representing a cross-sectional view of the fibre bundle in the as-received fibres.

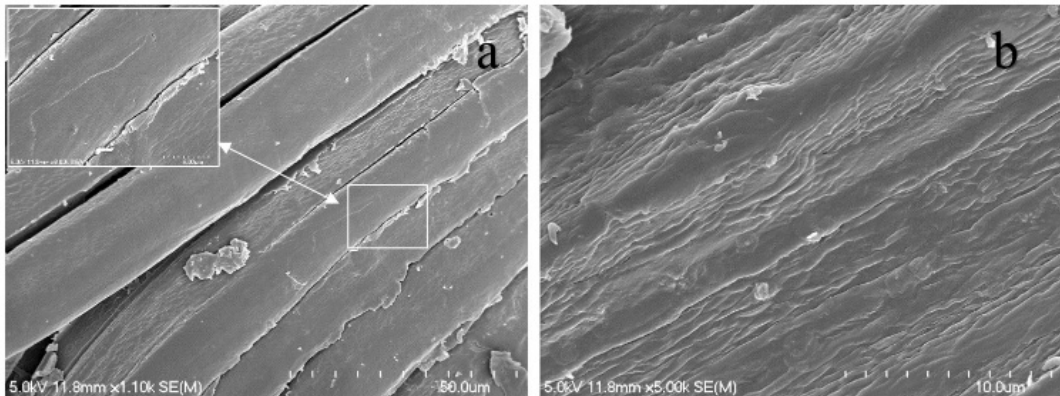


Figure 6.14: SEM images of the NaOH-treated harakeke fibres with (a) representing defibrillation in the fibres and, (b) representing surface roughness/ruggedness in the fibre.

Electron microscopic analysis of the biomorphic fibres (final product) (Figure 6.15) revealed the surface topology and internal structure of fibres with their surfaces appearing smooth, but their internal structure being noticeably porous and hollow. Surface imaging also revealed the coalescence of grains along with the presence of microporosity and cracks, which is a typical result of ceramic sintering. The internal structure revealed a complex network of interconnected porosities in between several protruding structures, so

resembling a fibrillar structure. The overall structure of the HAp fibres looked well developed but porous, which could be beneficial if such fibres were utilised in drug delivery or water purification systems or even as bioactive bone substitute materials in non-load bearing areas.

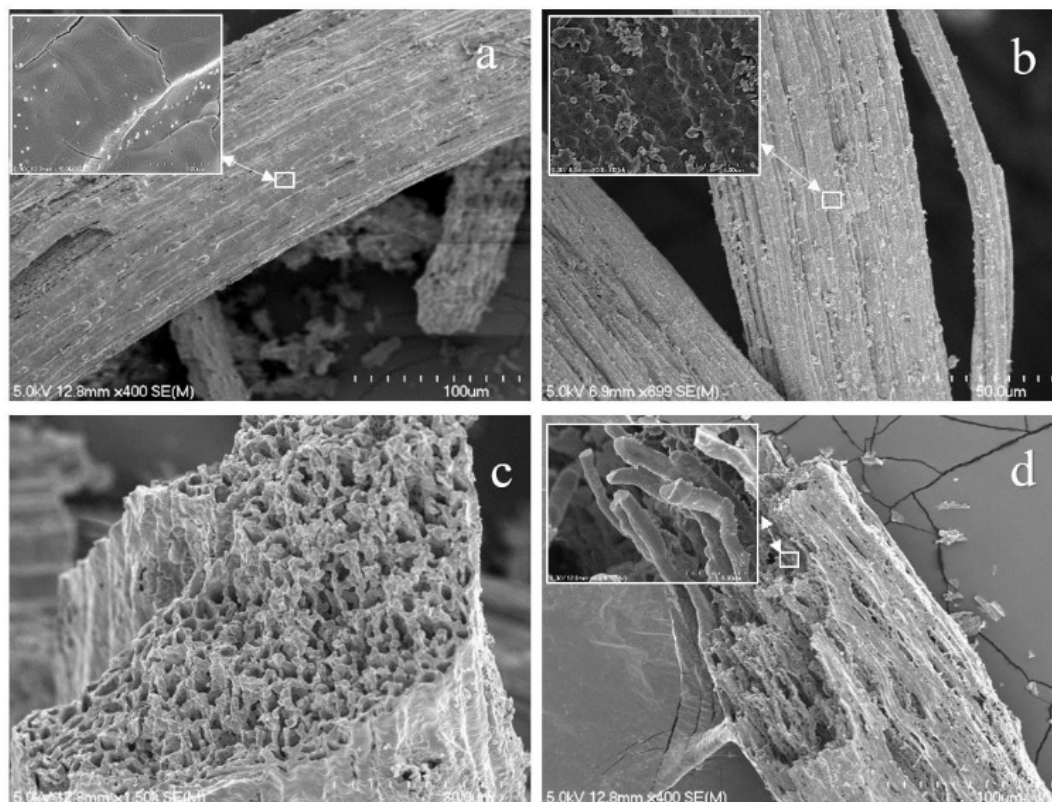


Figure 6.15: Electron microscopic images of biomorphic fibres (final product) images (a, b) represent surface features, while images (c, d) depict internal structures and porosity.

Optical images of solution-treated fibres at different heat treatment temperatures are shown in Figure 6.16. Translucent MCPM deposition is clearly visible in the 100 °C and 120 °C samples, however, the 140 °C and 160 °C samples did not show any extra surface features on the fibres. Decolourisation of the fibres started at 160 °C and continued up to 220 °C, while a deposition of an off-white solid phase identified as monetite started to appear from 180 °C. The depositions were not found to be homogenous but more patchy in nature.

Samples heat treated from 300 °C, showed a white powdery surface layer on the fibres, which appeared to grow into heavy depositions up until a temperature of 600 °C. An important feature noticed at 500 and 600 °C was the charring of the fibres. Samples heated at 800 °C, showed the growth of a white surface layer (composed of HAp and TCP as identified by XRD studies) on the charred fibres. Samples formed at 1000 °C showed complete formation of the biomorphic fibres.

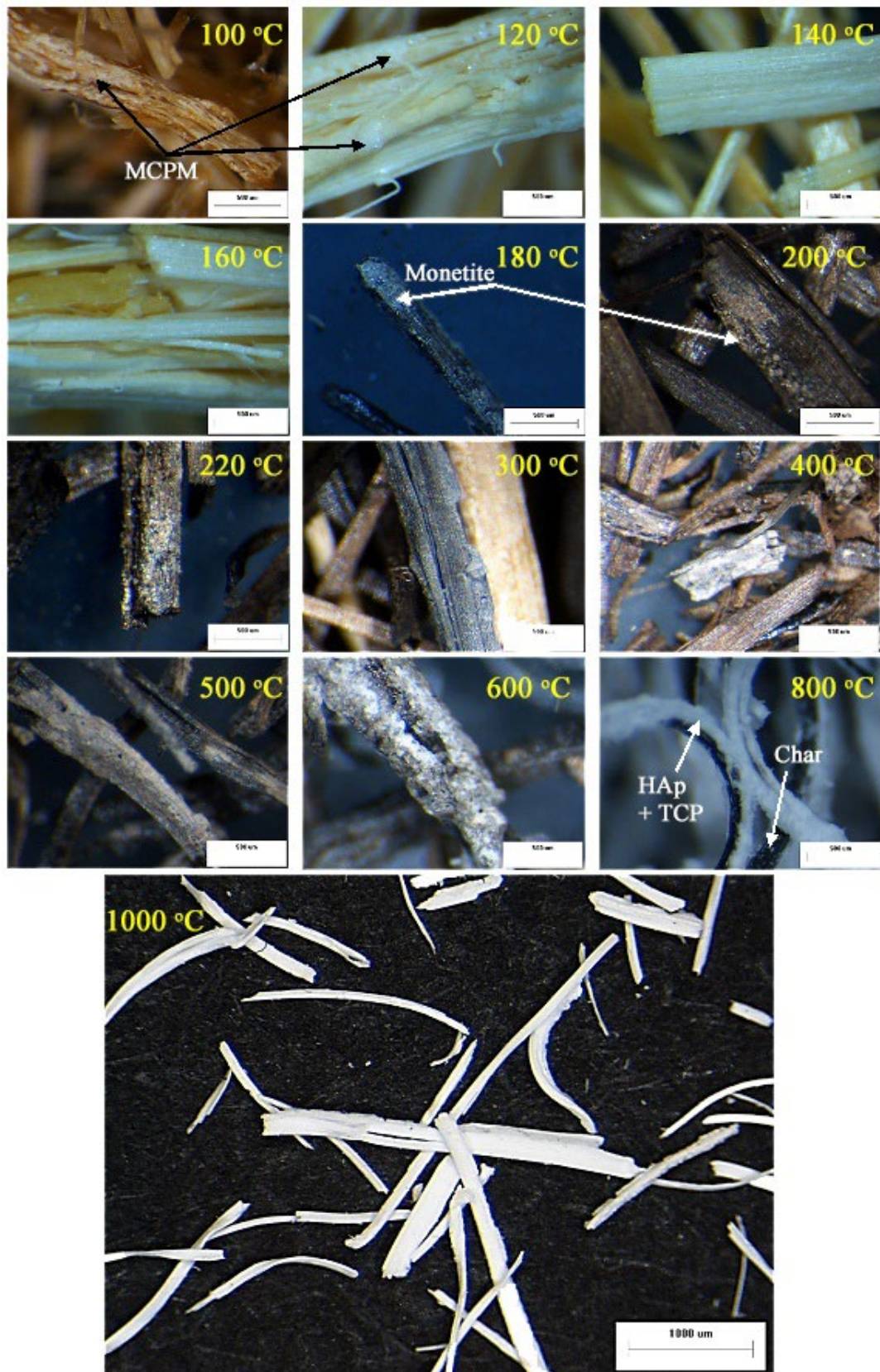


Figure 6.16: Optical images of digest solution treated fibres at different heating temperatures.

Hence the cast structure development of hydroxyapatite occurred along with the degradation of the fibre matrix itself so the biomorphic fibres were hence able to maintain

their shape because the cast HAp assumed the morphological shape of the fibres effectively as a replica after combustive removal.

### 6.3.6. Inductively coupled plasma-mass spectrometry (ICP-MS)

Inductively coupled plasma-mass spectrometry (ICP-MS) has been regularly used for quantification of Ca and P in CaP samples[355-357] and is key to providing values of Ca/P mole ratios of CaP phases present. In the present study, sintered cow bone and biomorphic fibres (as formed and final product) were dissolved in nitric acid solution, diluted, filtered and analysed by ICP-MS. The elemental composition and Ca/P mole ratios are summarised in Table 6.2. The Ca/P mole ratio of biomorphic fibre (final product) sample (analysed in triplicate) was found through testing on two independent ICP-MS instruments to be 1.48 and 1.54. Although this is close to the value expected for tricalcium phosphate; XRD and FTIR data show clearly that HAp is present. The Ca/P mole ratio obtained suggests that calcium deficient HAp has been produced. Standard XRD patterns for stoichiometric and Ca-deficient HAp are similar in appearance hence the diffractogram of biomorphic fibres (final product), Figure 6.9(a) can be considered to be that of calcium deficient HAp [358]. The elemental quantitative comparison of biofibre (as formed) with the sintered cow bone showed that certain elements (like S, Al, and Fe) have increased quantities which is reasoned to be due to the presence of *harakeke* ash. The NaOH washing treatment of biofibre (as formed) to produce biofibre (final product) was found to have reduced Ca and P content, while some of the ash related elements (like S and Fe) had also reduced in amount however the Na %, presumably arising from the NaOH treatment, was found to increase.

Table 6.2: The elemental composition obtained using ICP-MS

Element	Unit	Sintered cow bone	Biofibre (as formed)	Biofibre (final product)
Ca	%	35.160	37.070	35.101
P		18.045	17.703	17.584
Na		0.669	0.660	1.660
Mg		0.491	0.476	0.452
S		0.157	0.251	0.176
Sr		0.061	0.050	0.048
Ba		0.060	0.046	0.042
Al		0.001	0.025	0.027
K		0.025	0.020	0.017
Fe		0.002	0.011	0.010
Ca/P mole ratio	--	1.54	1.62	1.54

## 6.4. Conclusions

This chapter reports the novel formation of calcium deficient biomorphic HAp fibres via an aqueous soaking technique of *harakeke* Fibres in a bovine digest solution followed by calcination. Bovine bone was used as a biogenic source of  $\text{Ca}^{2+}$  and  $\text{PO}_4^{3-}$  ions instead of resorting to the use of commercial HAp powder. This approach potential allows repurposing of agricultural by-products. *harakeke* fibres were used as a unique biotemplate due to their abundance in nature and thermal stability (up to 200 °C). These allowed the development of potentially useful bio-inspired biomedical materials from the natural plant fibres. The final product realised was not only able to retain the original shape of the *harakeke* fibres but was also found to form a phase of bone like apatite in the form of a porous matrix that could be used as a xenografting material.



# CHAPTER SEVEN : SYNOPSIS & FUTURE RECOMMENDATIONS

---

## 7.1. Synopsis

The research work presented in this thesis was focused on the developing HAp based bio-ceramic composite using char as reinforcement. Char was developed using natural fibres from indigenous New Zealand plants. Chapter 3 dealt with the repurposing of waste bovine bones to develop useful morphology of HAp for composites, while Chapter 4 dealt with the harvesting and processing of the carbonaceous/char structures from the natural plant fibres. Chapter 5 presented the development and properties of composites. Chapter 6 presented the synthesis of biomorphic HAp fibres. In this last chapter, all logical conclusions are presented and discussed, which finally all lead up to discussion of the composite.

## 7.2. Re-purposing waste Bovine Bones

As stated earlier, the driving force for bovine bone to develop HAp is its sheer volume as a by-product in New Zealand mainly due to heavy dairying practices to satisfy national and international demands. Historically the concept of cleaning/deproteinisation of bovine bone is now an acceptable way to source HAp as they would be more bioactive and suitable for its use in body.

This research work is directly linked with the work already done at the Department of Chemistry, University of Waikato led by Dr. Michael Mucalo. The concept of previous and this work is first to achieve HAp from waste animal bones via high temperature treatment and then acid dissolution & alkaline reprecipitation of HAp obtained from waste bovine bone. Utilising the available techniques in the department, this research successfully produced reprecipitated HAp, which can be evidenced from IR (Figure 3.4), XRD (Figure 3.9) and Raman (Figure 3.14) results. The novelty of this research is the evaluation of morphology and crystallinity of reprecipitated HAp as a function of reprecipitation and calcination temperatures. The idea of this research work is to promote the sense that HAp from waste bovine bones can be as useful as that of synthesis from chemical salt-based precipitation methods for developing a range of HAp morphologies.

### 7.2.1. Effect of reprecipitation temperature on HAp crystallinity and morphology

The easiest and the most common method to synthesize HAp is the precipitation from a solution containing dissolved  $\text{Ca}^{2+}$  ions and  $\text{PO}_4^{3-}$  ions. Calcium salts (like  $\text{CaCl}_2$  [359],  $\text{Ca}(\text{NO}_3)_2$  [360],  $\text{Ca}(\text{OH})_2$  [361],  $\text{CaCO}_3$ , [362]) and Phosphate salts (like  $\text{H}_3\text{PO}_4$ ,

(NH<sub>4</sub>)<sub>2</sub>HPO<sub>4</sub>, NH<sub>4</sub>H<sub>2</sub>PO<sub>4</sub>, Na<sub>3</sub>PO<sub>4</sub>, and KH<sub>2</sub>PO<sub>4</sub>) are used to provide the calcium and phosphate ions which are reacted in alkaline conditions (pH > 9). This leads to precipitation of nanostructured, nonstoichiometric, and poorly crystalline HAp with high yield. Other types of calcium phosphates can also form. Eanes et al. [104] investigated the HAp precipitation at room temperature conditions and found that well-crystallized HAp precipitates for at least 24 hrs at room temperature. They described that precipitation progressed in stages, where the ACP or amorphous calcium phosphate forms initially, which gradually decreased till complete disappearance \*(replaced by crystalline HAp). Webster et al. [363] demonstrated that precipitation at 90 °C yields bigger sized HAp grains as compared to those precipitated at room temperature, similarly Ishikawa et al. [364] demonstrated that XRD peak sharpening occurred with increasing reaction temperatures which indicates increasing crystallinity.

In this study, similar trends were also noted where XRD diffractograms (Figure 3.10) clearly showed peak sharpening with the execution of reprecipitation of HAp at higher temperatures. Further to this, in FTIR spectra, the deconvoluted IR region ( $\nu_2$ PO<sub>4</sub>) of all four types of reprecipitated HAp (Figure 3.8') indicated an increase in apatitic phosphate signals and a decrease in non-apatitic phosphate signals (PO<sub>4</sub><sup>3-</sup> and HPO<sub>4</sub><sup>2-</sup>, see table 3.2), which is also a sign of increasing crystallinity. Figure 7.1, displays the increasing crystallinity (calculated using IR and XRD data ) and crystallite size.

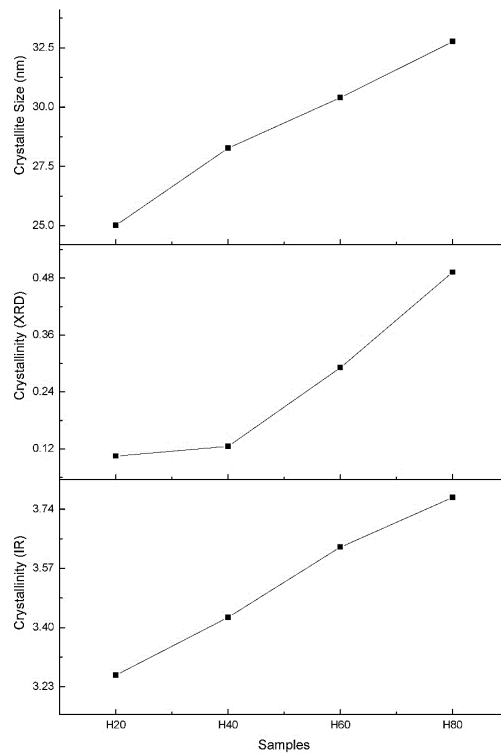


Figure 7.1: Crystallinity Index (calculated using IR and XRD) and crystallite size of reprecipitated HAp used in the composites in this study.

The SEM observations (Figure 3.21) of reprecipitated HAp, in general displayed elongation & growth of particles with increasing reaction temperature mainly due to diffusional growth and Ostwald ripening. One way to access and compare the morphology of samples was to calculate the shape factor, which is:

$$\text{Shape Factor} = L/D \text{ (eq. 11)}$$

Where, L is the length of particle and D is the diameter, both in nanometres. In order to determine this, approximately 75 particles were located from different SEM images and used to calculate the shape factor. Figure 7.2 illustrates this

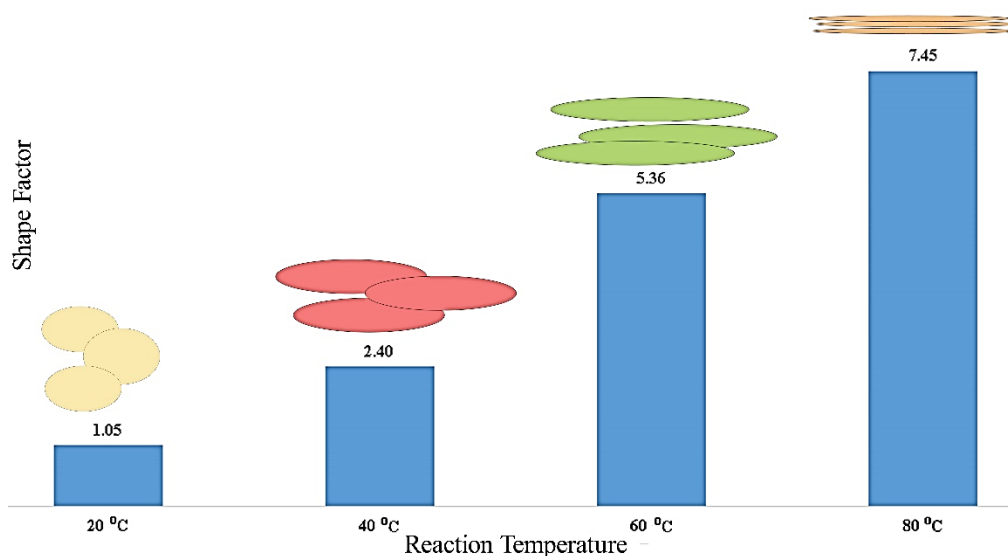


Figure 7.2: Calculated shape factor of all reprecipitated samples of HAp as used in the current study.

H<sub>20</sub> only displayed spherical shaped particles, with a shape factor close to 1, with minimal agglomeration and clumping. H<sub>40</sub>, H<sub>60</sub> & H<sub>80</sub> were all found to possess a non-spherical morphology, as shown by the trend of increasing shape factor values, which means effectively the shifting of the particle morphology from spherical to more needle like. This is expected as increasing temperature provided enough energy for particles to cause Ostwald ripening.

### 7.2.2. Effect of reprecipitation temperature on the development of disordered/amorphous calcium phosphate

Disordered/amorphous calcium phosphate (ACP) is sometimes referred to as one of the best third-generation biomaterials due mainly to its high bioactivity and biodegradation properties. ACP is also important in biomineralization and helps in osteogenesis. In this work, it was noted that an ACP layer readily forms on an ordered HAp

during re-precipitation and freely transformed into more thermodynamically stable crystalline HAp possibly due to surface nucleation and solution-mediated transformation. Similarly, ACP formation & formation via precipitation from the solution made using chemicals has also been previously reported. XRD (Figure 3.10) and Raman (Figure 3.15) spectroscopy clearly demonstrated the presence and decrease of ACP with the increase of re-precipitation temperature, however this part of the research needs further investigation because the digest solution's composition is different from the solution made using chemical salts hence it can have different effects on the formation and stabilisation of ACP.

## **7.3. Natural plant fibres as a source of carbonaceous micro and nano structures**

The purpose of this study was to harvest carbon based fibrous structures from natural plant fibres. The natural fibres selected for this purpose were known for their strength i.e., harakeke and cabbage tree leaf fibres. The idea was to see, if their natural strength translates into their carbon form. The original scientific motivation behind this work in the current study was the research done by McDonald Wharry et al. [205, 292, 365] on harakeke char, which showed the presence of a crystalline graphitic structure embedded in the amorphous structure of the fibrous char. In this study, it was aimed to test those embedded graphitic structures for load bearing. The as formed carbon-based fibrous structures were subjected to acid cleaning to remove ash content and were further purified & modified by piranha solution (piranha solution can be used for oxidation and removal of organic impurities from carbon structures). The modification was meant to increase the bonding compatibility with HAp. One of the important highlights of that study was the formation of carbon nanoscrolls on the surface of harakeke char. Their presence was abundant, in every sample, even in repeat ones. Based on this, a natural difference was created between the two-carbon based fibrous structures i.e., with nanoscrolls (harakeke char) and without nanoscrolls (cabbage tree leaf char). Both chars displayed fibrous morphology having rough topology, however piranha treated cabbage tree leaf char displayed approx. 150% increased volatile content and approx., 50% increased ash content as compared to piranha treated harakeke char, moreover a minor fraction of cabbage tree leaf char was found to be hollow/tubular structured.

### **7.3.1. Harakeke char-HAp composites**

Harakeke char-HAp composites were made using piranha treated harakeke char (HC<sub>PT</sub>) and re-precipitated HAp (H<sub>80-800</sub>). The control sample i.e., H<sub>80-800</sub> displayed a well

sintered structure having approx. 61% porosity and 36% apparent porosity. This level of porosity was purposefully developed (in all samples) using PVA polymer, which served dual purposes, firstly as a binder and secondly as a pore former. The cylindrical samples of H<sub>80-800</sub> were found to have approx. 26 MPa compressive strength and 5.7 MPa diametral tensile strength, along with approx. 48 HV Vickers hardness and 0.513 Mpa M<sup>1/2</sup> indentation fracture toughness. The addition of piranha treated harakeke char increased the overall mechanical properties of the composite to a certain level before being dropped to values even lower than the control sample. The relative density and apparent porosity values of all the composites remained close to that of the control sample. Except compressive strength values, all of the mechanical properties increased to the maximum values just by the addition of 0.5% char, whereas the maximum compressive strength was achieved with only 0.1% addition of char. Hence, the 0.5% addition of char, increased hardness by 118%, DTS by 158%, indentation fracture toughness by 334% and the corresponding values of compressive strength at 0.5% char were found to be increased by 147%. Sarkar et. al. [150] developed a HAP-CNT composite via SPS, where 2.5 vol% CNT at 1100 °C SPS temperature produced a composite with 97.39% density and with 469.6 HV hardness as well as with a fracture toughness of 1.27 Mpam<sup>1/2</sup>. Compared to their results, in this study, 0.5 wt% harakeke char produced a composite of approx. 59% relative density having 420 HV hardness and 2.22 Mpam<sup>1/2</sup> fracture toughness, which proves that the harakeke char is an effective carbonaceous source of reinforcement in HAp. A comparison of percent increase/decrease in properties with respect to the control sample is presented in Table 7.1.

### **7.3.2. Cabbage tree leaf fibre char-HAp Composites**

The composites made using cabbage tree leaf char displayed different values and trends. The overall values of cabbage tree leaf char fibre were much lower than that of harakeke char composites. The 0.1% addition of piranha treated cabbage tree leaf char to HAp, raised the values of compressive strength only by approx. 6%, diametral tensile strength by approx. 11%, Vickers hardness by approx. 1.2% and indentation fracture toughness by approx. 31%. The addition of 0.5% char further increased the values of (as compared to control sample) of compressive strength by approx. 43%, Vickers hardness by approx. 40%, diametral tensile strength by 66%, indentation fracture toughness by 148%, whereas 1% addition of char proved mostly detrimental because except for hardness and indentation fracture toughness values, the rest of the properties were found to be inferior. The maximum rise in hardness and indentation fracture toughness values was found to be approx. 69% and 164.4%, when 1% char was added. A comparison of

percent increase/decrease in properties with respect to the control sample is presented in Table 7.1.

Table 7.1: Percent change in mechanical properties of composites with respect to control sample.

Sample		Percentage increase change in			
		Fracture Toughness	Compressive Strength	Vicker Hardness	Diametral Tensile Strength
Harakeke leaf fibre char composites	0.10%	138.5	92.8	3.1	102.7
	0.50%	333.5	46.5	106.3	175.3
	1%	149.0	-23.6	28.0	30.9
	1.50%	50.4	-33.3	14.7	-11.4
	2%	-12.0	-51.4	-50.0	-27.5
Cabbage tree leaf fibre char composites	0.10%	31.0	5.7	-4.2	11.1
	0.50%	148.6	43.8	32.4	66.0
	1%	165.7	-24.5	59.7	-45.0
	1.50%	3.5	-43.4	-14.7	-61.8
	2%	-21.8	-73.2	-56.7	-65.8

## 7.4. Calcium deficient biomorphic HAp fibres

The research reported is an attempt to repurpose agricultural by-products to develop calcium deficient biomorphic HAp fibres. An aqueous soaking technique of harakeke fibres in a bovine digest solution followed by calcination, was used to develop fibres. Waste bovine bone was used as a biogenic source to generate a solution of  $\text{Ca}^{2+}$  and  $\text{PO}_4^{3-}$  ions instead of resorting to the use of commercial HAp powder. The final product realised was not only able to retain the original shape of the harakeke fibres but was also found to form a phase of bone like apatite in the form of a porous matrix that could be used as a xenografting material.

## 7.5. Future Recommendations

During the course of the research, a number of potential areas were identified which had the potential for further study to produce more fruitful results. Some of the recommendations for future studies from this work are:

- 1) Optimising the natural fibre charring process to enhance the strength of fibrous char used in composites or in other applications. This will result in development of char fibres having more strength and toughness.
- 2) Optimising acid treatments of harakeke char, to enhance the development of nanoscrolls and also to provide a way to separate out the nanoscrolls from the

remaining char structure. This can result in the development of a process of harvesting nano carbonaceous structures from a natural source.

- 3) Evaluating different sintering atmospheres (i.e. using different gases or combination of gases like CO + H<sub>2</sub> + H<sub>2</sub>O bubbled through ice water as reported in a previous research[366]) to see its effects on the final properties of composites, as it is believed that this will result in the realisation of greater compressive strengths in the composite materials.
- 4) Optimising suitable times and treatments for cabbage tree leaf fibres to realise optimal defibrillation. This can result in getting good dispersion of its char fibres.
- 5) Sintering composites with the same compositions as used in this study but instead using spark plasma sintering which is considered the best method to use for this purpose when the materials involve HAp. This will result in an increase of compressive and toughness values.

## Reference

1. Hildebrand, H.F., *Biomaterials – a history of 7000 years*. BioNanoMaterials, 2013. **14**(3-4): p. 119-133.
2. Nerlich, A.G., et al., *Ancient Egyptian prosthesis of the big toe*. The Lancet, 2000. **356**(9248): p. 2176-2179.
3. Huebsch, N. and D.J. Mooney, *Inspiration and application in the evolution of biomaterials*. Nature, 2009. **462**(7272): p. 426-432.
4. Ratner, B.D. and G. Zhang, *1.1.2 - A History of Biomaterials*, in *Biomaterials Science (Fourth Edition)*, W.R. Wagner, et al., Editors. 2020, Academic Press. p. 21-34.
5. Chen, F.-M. and X. Liu, *Advancing biomaterials of human origin for tissue engineering*. Progress in polymer science, 2016. **53**: p. 86-168.
6. Chen, Q. and G. Thouas, *Biomaterials a basic introduction*. 2015, Boca Raton, Fla: CRC Press.
7. Ehrlich, H., *Biomaterials and Biological Materials*, in *Marine Biological Materials of Invertebrate Origin*. 2019, Springer International Publishing: Cham. p. 3-18.
8. Baino, F., S. Hamzehlou, and S. Kargozar, *Bioactive Glasses: Where Are We and Where Are We Going?* Journal of functional biomaterials, 2018. **9**(1): p. 25.
9. Park, J. and R.S. Lakes, *Biomaterials: An introduction: Third edition*. Biomaterials: An introduction: Third edition, 2007: p. 1-561.
10. Sarikaya, M., et al., *Molecular biomimetics: nanotechnology through biology*. Nature Materials, 2003. **2**(9): p. 577-585.
11. Thevenot, P., W. Hu, and L. Tang, *Surface chemistry influences implant biocompatibility*. Current topics in medicinal chemistry, 2008. **8**(4): p. 270-280.
12. Williams, D.F., *Challenges With the Development of Biomaterials for Sustainable Tissue Engineering*. Frontiers in bioengineering and biotechnology, 2019. **7**: p. 127-127.
13. Velnar, T., et al., *Biomaterials and host versus graft response: a short review*. Bosnian journal of basic medical sciences, 2016. **16**(2): p. 82-90.
14. Ucar, S., et al., *Formation of Hydroxyapatite via Transformation of Amorphous Calcium Phosphate in the Presence of Alginate Additives*. Crystal Growth & Design, 2019. **19**(12): p. 7077-7087.
15. Zhao, J., et al., *Amorphous calcium phosphate and its application in dentistry*. Chemistry Central journal, 2011. **5**: p. 40-40.
16. Termine, J.D. and A.S. Posner, *Amorphous/crystalline interrelationships in bone mineral*. Calcified Tissue Research, 1967. **1**(1): p. 8-23.
17. Siddiqui, H.A., K.L. Pickering, and M.R. Mucalo, *A Review on the Use of Hydroxyapatite-Carbonaceous Structure Composites in Bone Replacement Materials for Strengthening Purposes*. Materials, 2018. **11**(10): p. 1813.
18. Plenk Jr, H., *The Role of Materials Biocompatibility for Functional Electrical Stimulation Applications*. Artificial Organs, 2011. **35**(3): p. 237-241.
19. Prasad, K., et al., *Metallic Biomaterials: Current Challenges and Opportunities*. Materials (Basel, Switzerland), 2017. **10**(8): p. 884.



20. Oonishi, H., et al., *Comparative bone growth behavior in granules of bioceramic materials of various sizes*. J Biomed Mater Res, 1999. **44**(1): p. 31-43.
21. Overgaard, S., et al., *The influence of crystallinity of the hydroxyapatite coating on the fixation of implants. Mechanical and histomorphometric results*. J Bone Joint Surg Br, 1999. **81**(4): p. 725-31.
22. Kokubo, T., et al., *Novel Ceramics for Biomedical Applications*. Vol. 36. 2000. 37-46.
23. Johnson, G., et al., *The processing and characterization of animal-derived bone to yield materials with biomedical applications. Part II: milled bone powders, reprecipitated hydroxyapatite and the potential uses of these materials*. Journal of Materials Science: Materials in Medicine, 2000. **11**(11): p. 725-741.
24. Worth, A., et al., *The evaluation of processed cancellous bovine bone as a bone graft substitute*. Clin Oral Implants Res, 2005. **16**(3): p. 379-86.
25. Laird, D.F., M.R. Mucalo, and G.J. Dias, *Vacuum-assisted infiltration of chitosan or polycaprolactone as a structural reinforcement for sintered cancellous bovine bone graft*. J Biomed Mater Res A, 2012. **100**(10): p. 2581-92.
26. Mucalo, M. and D. Foster, *A method for avoiding the xanthoproteic-associated discolouration in reprecipitated (nitric-acid-digested) hydroxyapatite prepared from mammalian bone tissue*. Croatica Chemica Acta, 2004. **77** (3): p. 509-517.
27. Roberts, A. *Fertiliser industry*. Te Ara - the Encyclopedia of New Zealand; Available from: <http://www.TeAra.govt.nz/mi/fertiliser-industry/print>
28. Weiner, S. and W. Traub, *Bone structure: from angstroms to microns*. Faseb j, 1992. **6**(3): p. 879-85.
29. Reznikov, N., R. Shahaar, and S. Weiner, *Bone hierarchical structure in three dimensions*. Acta Biomater, 2014. **10**(9): p. 3815-26.
30. Clarke, B., *Normal Bone Anatomy and Physiology*. Clinical Journal of the American Society of Nephrology, 2008. **3**(Supplement 3): p. S131.
31. Florencio-Silva, R., et al., *Biology of Bone Tissue: Structure, Function, and Factors That Influence Bone Cells*. BioMed Research International, 2015. **2015**: p. 421746.
32. Feng, X., *Chemical and Biochemical Basis of Cell-Bone Matrix Interaction in Health and Disease*. Current chemical biology, 2009. **3**(2): p. 189-196.
33. Cacciotti, I., *Cationic and Anionic Substitutions in Hydroxyapatite*, in *Handbook of Bioceramics and Biocomposites*, I.V. Antoniac, Editor. 2016, Springer International Publishing: Cham. p. 145-211.
34. Jiang, Y., Z. Yuan, and J. Huang, *Substituted hydroxyapatite: a recent development*. Materials Technology, 2020. **35**(11-12): p. 785-796.
35. Orlovskii, V.P., V.S. Komlev, and S.M. Barinov, *Hydroxyapatite and Hydroxyapatite-Based Ceramics*. Inorganic Materials, 2002. **38**(10): p. 973-984.
36. Hill, P.A., *Bone Remodelling*. British Journal of Orthodontics, 1998. **25**(2): p. 101-107.
37. Swetha, M., et al., *Biocomposites containing natural polymers and hydroxyapatite for bone tissue engineering*. International Journal of Biological Macromolecules, 2010. **47**(1): p. 1-4.

38. Kanhed, S., et al., *Porosity distribution affecting mechanical and biological behaviour of hydroxyapatite bioceramic composites*. Ceramics International, 2017. **43**(13): p. 10442-10449.
39. Mauffrey, C., et al., *Bone graft harvest site options in orthopaedic trauma: A prospective in vivo quantification study*. Injury. **43**(3): p. 323-326.
40. Gao, C., et al., *Carbon nanotube, graphene and boron nitride nanotube reinforced bioactive ceramics for bone repair*. Acta Biomaterialia, 2017. **61**(Supplement C): p. 1-20.
41. Patel, N.R. and P. Gohil, *A Review on Biomaterials: Scope, Applications & Human Anatomy Significance*. Vol. 2. 2012. 91-101.
42. Wang, L.J. and G.H. Nancollas, *Calcium Orthophosphates: Crystallization and Dissolution*. Chemical Reviews, 2008. **108**(11): p. 4628-4669.
43. Dorozhkin, S.V., *Calcium Orthophosphates in Nature, Biology and Medicine*. Materials, 2009. **2**(2): p. 399-498.
44. LeGeros, R.Z., *Calcium Phosphate-Based Osteoinductive Materials*. Chemical Reviews, 2008. **108**(11): p. 4742-4753.
45. Meyers, M.A., et al., *Biological materials: Structure and mechanical properties*. Progress in Materials Science, 2008. **53**(1): p. 1-206.
46. Dorozhkin, S.V., *Bioceramics of calcium orthophosphates*. Biomaterials, 2010. **31**(7): p. 1465-1485.
47. Hench, L., *Biomaterials*. Science, 1980. **208**(4446): p. 826-831.
48. Hench, L.L. and I. Thompson, *Twenty-first century challenges for biomaterials*. Journal of the Royal Society Interface, 2010. **7**(Suppl 4): p. S379-S391.
49. Tan, L., et al., *Biodegradable Materials for Bone Repairs: A Review*. Journal of Materials Science & Technology, 2013. **29**(6): p. 503-513.
50. Navarro, M., et al., *Biomaterials in orthopaedics*. Journal of The Royal Society Interface, 2008. **5**(27): p. 1137-1158.
51. Stevens, M.M., *Biomaterials for bone tissue engineering*. Materials Today, 2008. **11**(5): p. 18-25.
52. O'Brien, F.J., *Biomaterials & scaffolds for tissue engineering*. Materials Today, 2011. **14**(3): p. 88-95.
53. Taichman, R.S., *Blood and bone: two tissues whose fates are intertwined to create the hematopoietic stem-cell niche*. Blood, 2005. **105**(7): p. 2631-9.
54. Suchanek, W. and M. Yoshimura, *Processing and properties of hydroxyapatite-based biomaterials for use as hard tissue replacement implants*. Journal of Materials Research, 1998. **13**(1): p. 94-117.
55. Farraro, K.F., et al., *Revolutionizing orthopaedic biomaterials: The potential of biodegradable and bioresorbable magnesium-based materials for functional tissue engineering*. Journal of biomechanics, 2014. **47**(9): p. 1979-1986.
56. Mucalo, M.R., *Animal-bone derived hydroxyapatite in biomedical applications*, in *Hydroxyapatite (Hap) for Biomedical Applications*. 2015, Woodhead Publishing. p. 307-342.
57. Aoki, H., *Science and medical applications of hydroxyapatite*. 1991: Ishiyaku Euroamerica.
58. Kraay, M.J. and V.M. Goldberg, *Hydroxyapatite*, in *Surgical Techniques in Total Knee Arthroplasty*, G.R. Scuderi and A.J. Tria, Jr., Editors. 2002, Springer-Verlag New York: New York, US. p. 277-286.
59. Shackelford, J.F., *Bioceramics*. 2003: Taylor & Francis.

60. Basu, B., D.S. Katti, and A. Kumar, *Advanced Biomaterials: Fundamentals, Processing, and Applications*. 2010: Wiley.
61. Fihri, A., et al., *Hydroxyapatite: A review of syntheses, structure and applications in heterogeneous catalysis*. Coordination Chemistry Reviews, 2017. **347**(Supplement C): p. 48-76.
62. Rey, C., et al., *Bone mineral: update on chemical composition and structure*. Osteoporos Int, 2009. **20**(6): p. 1013-21.
63. Ana, I.D., S. Matsuya, and K. Ishikawa, *Engineering of Carbonate Apatite Bone Substitute Based on Composition-Transformation of Gypsum and Calcium Hydroxide*. Vol. 02. 2010.
64. Hench, L.L., *An Introduction to Bioceramics: Second Edition*. 2013: World Scientific Publishing Company.
65. Paul, W. and C. Sharma, *Development of porous spherical hydroxyapatite granules: application towards protein delivery*. Journal of Materials Science: Materials in Medicine, 1999. **10**(7): p. 383-388.
66. Weinlander, M., et al., *TCP- Impurities in HA- Granules and Crystallinity Changes in Plasmaflamesprayed HA- Coatings Detected by Spectroscopical Methods and their Consequence*, in *Bioceramics and the human body*, A. Ravaglioli and A. Krajewski, Editors. 1992, New York: Elsevier Science Publishers.
67. Zhou, H. and J. Lee, *Nanoscale hydroxyapatite particles for bone tissue engineering*. Acta Biomaterialia, 2011. **7**(7): p. 2769-2781.
68. Hing, K., et al., *Quantification of bone ingrowth within bone-derived porous hydroxyapatite implants of varying density*. Journal of Materials Science: Materials in Medicine, 1999. **10**(10-11): p. 663-670.
69. Yamamoto, M., et al., *Promotion of fibrovascular tissue ingrowth into porous sponges by basic fibroblast growth factor*. Journal of Materials Science: Materials in Medicine, 2000. **11**(4): p. 213-218.
70. Johnson, G.S., M.R. Mucalo, and M.A. Lorier, *The processing and characterization of animal-derived bone to yield materials with biomedical applications Part 1: Modifiable porous implants from bovine condyle cancellous bone and characterization of bone materials as a function of processing*. Journal of Materials Science: Materials in Medicine, 2000. **11**(7): p. 427-441.
71. Callan, D.P. and M.D. Rohrer, *Use of bovine-derived hydroxyapatite in the treatment of edentulous ridge defects: a human clinical and histologic case report*. J Periodontol, 1993. **64**(6): p. 575-82.
72. Yukna, R.A., et al., *Multi-center clinical evaluation of combination anorganic bovine-derived hydroxyapatite matrix (ABM)/cell binding peptide (P-15) as a bone replacement graft material in human periodontal osseous defects. 6-month results*. J Periodontol, 1998. **69**(6): p. 655-63.
73. Sunil, B.R. and M. Jagannatham, *Producing hydroxyapatite from fish bones by heat treatment*. Materials Letters, 2016. **185**: p. 411-414.
74. Cahyanto, A., et al., *Fabrication of hydroxyapatite from fish bones waste using reflux method*. IOP Conference Series: Materials Science and Engineering, 2017. **172**(1): p. 012006.
75. Boutinguiza, M., et al., *Biological hydroxyapatite obtained from fish bones*. Materials Science and Engineering: C, 2012. **32**(3): p. 478-486.

76. Vecchio, K.S., et al., *Conversion of bulk seashells to biocompatible hydroxyapatite for bone implants*. Acta Biomaterialia, 2007. **3**(6): p. 910-918.
77. Lee, S.-W., et al., *Comparative Study of hydroxyapatite prepared from seashells and eggshells as a bone graft material*. Tissue Engineering and Regenerative Medicine, 2014. **11**(2): p. 113-120.
78. Raya, I., et al., *Synthesis and Characterizations of Calcium Hydroxyapatite Derived from Crabs Shells (Portunus pelagicus) and Its Potency in Safeguard against to Dental Demineralizations*. International Journal of Biomaterials, 2015. **2015**: p. 469176.
79. Wu, S.-C., et al., *Effects of calcination on synthesis of hydroxyapatite derived from oyster shell powders*. Journal of the Australian Ceramic Society, 2019. **55**.
80. Wu, S.-C., et al., *Synthesis of hydroxyapatite from eggshell powders through ball milling and heat treatment*. Journal of Asian Ceramic Societies, 2016. **4**(1): p. 85-90.
81. Rivera, E.M., et al., *Synthesis of hydroxyapatite from eggshells*. Materials Letters, 1999. **41**(3): p. 128-134.
82. Kattimani, V.S., et al., *Eggshell Derived Hydroxyapatite as Bone Graft Substitute in the Healing of Maxillary Cystic Bone Defects: A Preliminary Report*. Journal of International Oral Health : JIOH, 2014. **6**(3): p. 15-19.
83. Ibrahim, A.R., et al., *Synthesis of spongy-like mesoporous hydroxyapatite from raw waste eggshells for enhanced dissolution of ibuprofen loaded via supercritical CO<sub>2</sub>*. Int J Mol Sci, 2015. **16**(4): p. 7960-75.
84. Nga, N.K., N.T. Thuy Chau, and P.H. Viet, *Facile synthesis of hydroxyapatite nanoparticles mimicking biological apatite from eggshells for bone-tissue engineering*. Colloids and Surfaces B: Biointerfaces, 2018. **172**: p. 769-778.
85. Yunus Basha, R., T.S. Sampath Kumar, and M. Doble, *Design of biocomposite materials for bone tissue regeneration*. Mater Sci Eng C Mater Biol Appl, 2015. **57**: p. 452-63.
86. John, M. and S. Thomas, *Biofibres and biocomposites*. Carbohydrate Polymers, 2008. **71**(3): p. 343-364.
87. Herliansyah, M.K., et al., *Preparation and Characterization of Natural Hydroxyapatite: A Comparative Study of Bovine Bone Hydroxyapatite and Hydroxyapatite from Calcite*. Materials Science Forum, 2007. **561-565**: p. 1441-1444.
88. Herliansyah, M.K., et al., *The influence of sintering temperature on the properties of compacted bovine hydroxyapatite*. Materials Science and Engineering: C, 2009. **29**(5): p. 1674-1680.
89. Ayatollahi, M.R., et al., *Mechanical and tribological properties of hydroxyapatite nanoparticles extracted from natural bovine bone and the bone cement developed by nano-sized bovine hydroxyapatite filler*. Ceramics International, 2015. **41**(9, Part A): p. 10818-10827.
90. Nasiri-Tabrizi, B., A. Fahami, and R. Ebrahimi-Kahrizsangi, *A comparative study of hydroxyapatite nanostructures produced under different milling conditions and thermal treatment of bovine bone*. Journal of Industrial and Engineering Chemistry, 2014. **20**(1): p. 245-258.

91. Ruksudjarit, A., et al., *Synthesis and characterization of nanocrystalline hydroxyapatite from natural bovine bone*. Current Applied Physics, 2008. **8**(3): p. 270-272.
92. Mucalo, M.R., et al., *The novel use of waste animal bone from New Zealand agricultural sources as a feedstock for forming plasma sprayed hydroxyapatite coatings on biomedical implant materials*. J Appl Biomater Biomech, 2004. **2**(2): p. 96-104.
93. Gunduz, O., et al., *Composites of bovine hydroxyapatite (BHA) and ZnO*. Journal of Materials Science, 2008. **43**(8): p. 2536-2540.
94. Rakmae, S., et al., *Effect of silane coupling agent treated bovine bone based carbonated hydroxyapatite on in vitro degradation behavior and bioactivity of PLA composites*. Materials Science and Engineering: C, 2012. **32**(6): p. 1428-1436.
95. Nirmala, R., et al., *Structural, thermal, mechanical and bioactivity evaluation of silver-loaded bovine bone hydroxyapatite grafted poly( $\epsilon$ -caprolactone) nanofibers via electrospinning*. Surface and Coatings Technology, 2010. **205**(1): p. 174-181.
96. Murugan, R., T.S. Sampath Kumar, and K. Panduranga Rao, *Fluorinated bovine hydroxyapatite: preparation and characterization*. Materials Letters, 2002. **57**(2): p. 429-433.
97. Mucalo, M.R., et al., *The Use of New Zealand Animal Bone as Bioceramic Bone Xenografts: Concept to Clinical Study*. Key Engineering Materials, 2002. **240-242**: p. 427-432.
98. Niakan, A., et al., *Sintering behaviour of natural porous hydroxyapatite derived from bovine bone*. Ceramics International, 2015. **41**(2, Part B): p. 3024-3029.
99. Murugan, R., K.P. Rao, and T.S. Sampath Kumar, *Heat-deproteinated xenogeneic bone from slaughterhouse waste: Physico-chemical properties*. Bulletin of Materials Science, 2003. **26**(5): p. 523-528.
100. Khoo, W., et al., *Preparation of Natural Hydroxyapatite from Bovine Femur Bones Using Calcination at Various Temperatures*. Procedia Manufacturing, 2015. **2**: p. 196-201.
101. Kusriani, E. and M. Sontang, *Characterization of x-ray diffraction and electron spin resonance: Effects of sintering time and temperature on bovine hydroxyapatite*. Radiation Physics and Chemistry, 2012. **81**(2): p. 118-125.
102. Bahrololoom, M., et al., *Characterisation of natural hydroxyapatite extracted from bovine cortical bone ash*. Journal of Ceramic Processing Research, 2009. **10**: p. 129-138.
103. Ooi, C.Y., M. Hamdi, and S. Ramesh, *Properties of hydroxyapatite produced by annealing of bovine bone*. Ceramics International, 2007. **33**(7): p. 1171-1177.
104. Eanes, E., I. Gillissen, and A. Posner, *Intermediate states in the precipitation of hydroxyapatite*. Nature, 1965. **208**(5008): p. 365-367.
105. Launey, M.E. and R.O. Ritchie, *On the Fracture Toughness of Advanced Materials*. Advanced Materials, 2009. **21**(20): p. 2103-2110.
106. Ritchie, R.O., *The conflicts between strength and toughness*. Nature Materials, 2011. **10**: p. 817.
107. Anderson, T.L., *Fracture Mechanics: Fundamentals and Applications, Third Edition*. 2005: Taylor & Francis.

108. Gogotsi, G.A., *Fracture toughness of ceramics and ceramic composites*. Ceramics International, 2003. **29**(7): p. 777-784.
109. Lemons, J.E., *Ceramics: past, present, and future*. Bone, 1996. **19**(1 Suppl): p. 121s-128s.
110. Yin, H., et al., *Griffith Criterion for Brittle Fracture in Graphene*. Nano Letters, 2015. **15**(3): p. 1918-1924.
111. Sitarz, M., et al., *Optical and Mechanical Characterization of Zirconium Based Sol-Gel Coatings on Glass*, in *Archives of Metallurgy and Materials*. 2016. p. 1747.
112. Ohji, T., et al., *Strengthening and Toughening Mechanisms of Ceramic Nanocomposites*. Journal of the American Ceramic Society, 1998. **81**(6): p. 1453-1460.
113. Wang, G.C., Z.F. Lu, and H. Zreiqat, *8 - Bioceramics for skeletal bone regeneration A2 - Mallick, Kajal*, in *Bone Substitute Biomaterials*. 2014, Woodhead Publishing. p. 180-216.
114. Zhao, G., et al., *A study on in-situ synthesis of TiB<sub>2</sub>-SiC ceramic composites by reactive hot pressing*. Ceramics International, 2014. **40**(1, Part B): p. 2305-2313.
115. Naslain, R.R., et al., *Ceramic Matrix Composites [and Discussion]*. Philosophical Transactions: Physical Sciences and Engineering, 1995. **351**(1697): p. 485-496.
116. Quinn, G., *Fracture Toughness of Ceramics by the Vickers Indentation Crack Length Method: A Critical Review*. A Critical Review, 2006. **27**: p. 45-62.
117. Rocha-Rangel, E., *Fracture Toughness Determinations by Means of Indentation Fracture*. 2011.
118. Quinn, G.D. and R.C. Bradt, *On the Vickers Indentation Fracture Toughness Test*. Journal of the American Ceramic Society, 2007. **90**(3): p. 673-680.
119. Plaza, L., *Determination of Uncertainties in Plane Toughness (K<sub>IC</sub>) Testing*. Seminario Sobre la Evaluación de la Incertidumbre en Ensayos Mecánicos, 2003.
120. Weisbrod, G. and D. Rittel, *A method for dynamic fracture toughness determination using short beams*. International Journal of Fracture, 2000. **104**(1): p. 89-103.
121. Niihara, K., R. Morena, and D. Hasselman, *Evaluation of K<sub>IC</sub> of brittle solids by the indentation method with low crack-to-indent ratios*. Journal of materials science letters, 1982. **1**(1): p. 13-16.
122. Wang, C., *Introduction to Fracture Mechanics; Stress analysis of cracked bodies, Aeronautical and Maritime Research Laboratory, Victoria 3001, Melbourne*. 1996, DSTO-GD-0103.
123. Hirsch, A., *The era of carbon allotropes*. Nature Materials, 2010. **9**: p. 868.
124. Okwundu, O., E. Aniekwe, and C. Nwanno, *Unlimited potentials of carbon: different structures and uses (a Review)*. Metallurgical and Materials Transactions A, 2018. **24**: p. 145-171.
125. Zahra, K., M. Majid, and V.D. Mircea, *Main Allotropes of Carbon: A Brief Review*, in *Sustainable Nanosystems Development, Properties, and Applications*, V.P. Mihai and M. Marius Constantin, Editors. 2017, IGI Global: Hershey, PA, USA. p. 185-213.

126. Falcao Eduardo, H.L. and F. Wudl, *Carbon allotropes: beyond graphite and diamond*. Journal of Chemical Technology & Biotechnology, 2007. **82**(6): p. 524-531.
127. Bharath, K.N. and S. Basavarajappa, *Applications of biocomposite materials based on natural fibers from renewable resources: a review*. Science and Engineering of Composite Materials, 2016. **23**(2).
128. Fan, X., et al., *Part I: porosity dependence of the Weibull modulus for hydroxyapatite and other brittle materials*. J Mech Behav Biomed Mater, 2012. **8**: p. 21-36.
129. Nahorny, S., et al., *Multi-walled carbon nanotubes/graphene oxide hybrid and nanohydroxyapatite composite: A novel coating to prevent dentin erosion*. Mater Sci Eng C Mater Biol Appl, 2017. **79**: p. 199-208.
130. Georgakilas, V., et al., *Broad Family of Carbon Nanoallotropes: Classification, Chemistry, and Applications of Fullerenes, Carbon Dots, Nanotubes, Graphene, Nanodiamonds, and Combined Superstructures*. Chemical Reviews, 2015. **115**(11): p. 4744-4822.
131. Awaji, H., S.-M. Choi, and E. Yagi, *Mechanisms of toughening and strengthening in ceramic-based nanocomposites*. Mechanics of Materials, 2002. **34**(7): p. 411-422.
132. Khanal, S.P., et al., *Improvement of the fracture toughness of hydroxyapatite (HAp) by incorporation of carboxyl functionalized single walled carbon nanotubes (CfSWCNTs) and nylon*. Materials Science and Engineering: C, 2016. **60**: p. 204-210.
133. Gao, L. and J. Lin, *Electrophoretic coating of Hydroxyapatite on pyrolytic carbon using glycol as dispersion medium*. Journal of Wuhan University of Technology-Mater. Sci. Ed., 2008. **23**(3): p. 293-297.
134. Buddy D. Ratner, A.S.H., Frederick J. Schoen, Jack E. Lemons, *Biomaterials Science, Third Edition: An Introduction to Materials in Medicine*. 2012, Academic Press.
135. Hetherington, V.J., C.E. Lord, and S.A. Brown, *Mechanical and histological fixation of hydroxylapatite-coated pyrolytic carbon and titanium alloy implants: a report of short-term results*. J Appl Biomater, 1995. **6**(4): p. 243-8.
136. Fitzer, E., A. Gkogkidis, and M. Heine, *Carbon Fibers and their Composites (A Review)*. Vol. HTHP. 1984. pp. 363-392.
137. Zakharov, N.A., et al., *Synthesis and properties of calcium hydroxyapatite/carbon fiber composites*. Russian Journal of Inorganic Chemistry, 2017. **62**(9): p. 1162-1172.
138. Ślósarczyk, A., et al., *Hot Pressed Hydroxyapatite–Carbon Fibre Composites*. Vol. 20. 2000. 1397-1402.
139. Dorner-Reisel, A., et al., *Unreinforced and carbon fiber reinforced hydroxyapatite: Resistance against microabrasion*. Vol. 24. 2004. 2131-2139.
140. Boehm, A., et al., *The Mechanical Properties of Biocompatible Apatite Bone Cement Reinforced with Chemically Activated Carbon Fibers*. Materials, 2018. **11**(2): p. 192.
141. Arora, N. and N.N. Sharma, *Arc discharge synthesis of carbon nanotubes: Comprehensive review*. Diamond and Related Materials, 2014. **50**: p. 135-150.

142. Sekhar, S. and S. Bal, *Carbon Nanotube Reinforced Ceramic Matrix Composites A Review*. Vol. 07. 2008.
143. Chrzanowska, J., et al., *Synthesis of carbon nanotubes by the laser ablation method: Effect of laser wavelength*. *physica status solidi (b)*, 2015. **252**(8): p. 1860-1867.
144. Akasaka, T., et al., *Apatite formation on carbon nanotubes*. *Materials Science and Engineering: C*, 2006. **26**(4): p. 675-678.
145. Aryal, S., et al., *Carbon nanotubes assisted biomimetic synthesis of hydroxyapatite from simulated body fluid*. *Materials Science and Engineering: A*, 2006. **426**(1): p. 202-207.
146. Chen, Y., et al., *Laser-surface-alloyed carbon nanotubes reinforced hydroxyapatite composite coatings*. *Applied Physics Letters*, 2005. **86**(25): p. 251905.
147. Lahiri, D., et al., *Carbon nanotube toughened hydroxyapatite by spark plasma sintering: Microstructural evolution and multiscale tribological properties*. *Carbon*, 2010. **48**(11): p. 3103-3120.
148. Lei, T., et al., *In Situ Preparation and Enhanced Mechanical Properties of Carbon Nanotube/Hydroxyapatite Composites*. *International Journal of Applied Ceramic Technology*, 2011. **8**(3): p. 532-539.
149. Ye, M., Q. Wenjiang, and P. Jingqin, *Preparation and characterization of mechanical properties of carbon nanotube reinforced hydroxyapatite composites consolidated by spark plasma sintering*. *IOP Conference Series: Materials Science and Engineering*, 2017. **231**(1): p. 012164.
150. Sarkar, S., et al., *Fabrication of CNT-Reinforced HAp Composites by Spark Plasma Sintering*. Vol. 534–536. 2007. 893-896.
151. Balani, K., et al., *Plasma-sprayed carbon nanotube reinforced hydroxyapatite coatings and their interaction with human osteoblasts in vitro*. *Biomaterials*, 2007. **28**(4): p. 618-624.
152. Lee, H.C., et al., *Synthesis of Single-layer Graphene: A Review of Recent Development*. *Procedia Chemistry*, 2016. **19**: p. 916-921.
153. Allen, M.J., V.C. Tung, and R.B. Kaner, *Honeycomb Carbon: A Review of Graphene*. *Chemical Reviews*, 2010. **110**(1): p. 132-145.
154. Ghuge, A.D., A.R. Shirode, and V.J. Kadam, *Graphene: A Comprehensive Review*. *Curr Drug Targets*, 2017. **18**(6): p. 724-733.
155. Liu, Y., J. Huang, and H. Li, *Synthesis of hydroxyapatite-reduced graphite oxide nanocomposites for biomedical applications: oriented nucleation and epitaxial growth of hydroxyapatite*. *Journal of Materials Chemistry B*, 2013. **1**(13): p. 1826-1834.
156. Zhang, L., et al., *A tough graphene nanosheet/hydroxyapatite composite with improved in vitro biocompatibility*. *Carbon*, 2013. **61**(Supplement C): p. 105-115.
157. Chen, D., H. Feng, and J. Li, *Graphene Oxide: Preparation, Functionalization, and Electrochemical Applications*. *Chemical Reviews*, 2012. **112**(11): p. 6027-6053.
158. Zaaba, N.I., et al., *Synthesis of Graphene Oxide using Modified Hummers Method: Solvent Influence*. *Procedia Engineering*, 2017. **184**(Supplement C): p. 469-477.
159. Pei, S. and H.-M. Cheng, *The reduction of graphene oxide*. *Carbon*, 2012. **50**(9): p. 3210-3228.



160. Schafhaeuti, C., *LXXXVI. On the combinations of carbon with silicon and iron, and other metals, forming the different species of cast iron, steel, and malleable iron*. The London, Edinburgh, and Dublin Philosophical Magazine and Journal of Science, 1840. **16**(106): p. 570-590.
161. Brodie, B.C., *XIII. On the atomic weight of graphite*. Philosophical Transactions of the Royal Society of London, 1859. **149**: p. 249-259.
162. Hummers, W.S. and R.E. Offeman, *Preparation of Graphitic Oxide*. Journal of the American Chemical Society, 1958. **80**(6): p. 1339-1339.
163. Li, Y., et al., *Biomimetic graphene oxide-hydroxyapatite composites via in situ mineralization and hierarchical assembly*. RSC Advances, 2014. **4**(48): p. 25398-25403.
164. Fathyunes, L. and J. Khalil-Allafi, *Characterization and corrosion behavior of graphene oxide-hydroxyapatite composite coating applied by ultrasound-assisted pulse electrodeposition*. Ceramics International, 2017. **43**(16): p. 13885-13894.
165. Li, M., et al., *Graphene oxide/hydroxyapatite composite coatings fabricated by electrophoretic nanotechnology for biological applications*. Carbon, 2014. **67**: p. 185-197.
166. Abdolhosseinzadeh, S., H. Asgharzadeh, and H. Seop Kim, *Fast and fully-scalable synthesis of reduced graphene oxide*. Scientific Reports, 2015. **5**: p. 10160.
167. Baradaran, S., et al., *Mechanical properties and biomedical applications of a nanotube hydroxyapatite-reduced graphene oxide composite*. Carbon, 2014. **69**: p. 32-45.
168. Öztürk, E., B. Özbek, and İ. Şenel, *Production of biologically safe and mechanically improved reduced graphene oxide/hydroxyapatite composites*. Materials Research Express, 2017. **4**(1): p. 015601.
169. Mengesha, A.E. and B.B.C. Youan, *8 - Nanodiamonds for drug delivery systems A2 - Narayan, R*, in *Diamond-Based Materials for Biomedical Applications*. 2013, Woodhead Publishing. p. 186-205.
170. Ansari, S.A., et al., *Role of Nanodiamonds in Drug Delivery and Stem Cell Therapy*. Iranian Journal of Biotechnology, 2016. **14**(3): p. 130-141.
171. Mochalin, V.N., et al., *The properties and applications of nanodiamonds*. Nature Nanotechnology, 2011. **7**: p. 11.
172. Chen, X., et al., *Mechanical properties of nanodiamond-reinforced hydroxyapatite composite coatings deposited by suspension plasma spraying*. Applied Surface Science, 2018. **439**: p. 60-65.
173. Pecheva, E., et al., *Effect of Nanodiamond Particles Incorporation in Hydroxyapatite Coatings*. Vol. 25. 2009.
174. Li, D., et al., *Synthesis and Vacuum Cold Spray Deposition of Biofunctionalized Nanodiamond/Hydroxyapatite Nanocomposite for Biomedical Applications*. Advanced Engineering Materials, 2017. **19**(12): p. 1700363.
175. Geng, J., et al., *Fullerene-Related Nanocarbons and Their Applications*. Journal of Nanotechnology, 2012. **2012**: p. 2.
176. Taylor, R., et al., *Isolation, separation and characterisation of the fullerenes C60 and C70: the third form of carbon*. Journal of the Chemical Society, Chemical Communications, 1990(20): p. 1423-1425.
177. Prato, M., *[60]Fullerene chemistry for materials science applications*. Journal of Materials Chemistry, 1997. **7**(7): p. 1097-1109.

178. Djordjevic, A., et al., *Synthesis and Characterization of Hydroxyapatite/Fullerenol Nanocomposites*. Vol. 15. 2015. 1538-1542.
179. Kobayashi, S. and W. Kawai, *Development of carbon nanofiber reinforced hydroxyapatite with enhanced mechanical properties*. Composites Part A: Applied Science and Manufacturing, 2007. **38**(1): p. 114-123.
180. Wu, M., et al., *Biomimetic synthesis and characterization of carbon nanofiber/hydroxyapatite composite scaffolds*. Carbon, 2013. **51**: p. 335-345.
181. Evis, Z. and T.J. Webster, *Nanosize hydroxyapatite: doping with various ions*. Advances in Applied Ceramics, 2011. **110**(5): p. 311-321.
182. Sallam, S.M., et al., *Synthesis and characterization of hydroxyapatite contain chromium*. Journal of Biophysical Chemistry, 2012. **Vol.03No.04**: p. 5.
183. Zilm, M.E., et al., *Hydroxyapatite substituted by transition metals: experiment and theory*. Physical Chemistry Chemical Physics, 2016. **18**(24): p. 16457-16465.
184. Herkendell, K., et al., *Domination of volumetric toughening by silver nanoparticles over interfacial strengthening of carbon nanotubes in bactericidal hydroxyapatite biocomposite*. Materials Science and Engineering: C, 2014. **34**: p. 455-467.
185. Chen, L., et al., *Synthesis and characterization of chitosan-multiwalled carbon nanotubes/hydroxyapatite nanocomposites for bone tissue engineering*. J Mater Sci Mater Med, 2013. **24**(8): p. 1843-51.
186. Sharma, A., V. Pareek, and D. Zhang, *Biomass pyrolysis—A review of modelling, process parameters and catalytic studies*. Renewable and Sustainable Energy Reviews, 2015. **50**: p. 1081-1096.
187. Yaman, S., *Pyrolysis of biomass to produce fuels and chemical feedstocks*. Energy Conversion and Management, 2004. **45**(5): p. 651-671.
188. Fitz, H.C., et al., *Development of a general ecosystem model for a range of scales and ecosystems*. Ecological Modelling, 1996. **88**(1): p. 263-295.
189. Xu, R.-k., et al., *Chapter One - Adsorption Properties of Subtropical and Tropical Variable Charge Soils: Implications from Climate Change and Biochar Amendment*, in *Advances in Agronomy*, D.L. Sparks, Editor. 2016, Academic Press. p. 1-58.
190. R, R. and J. Sankar, *Biochar for Sustainable Agriculture – A Review*. Vol. 2. 2016. 173-184.
191. Manyà, J.J., *Pyrolysis for Biochar Purposes: A Review to Establish Current Knowledge Gaps and Research Needs*. Environmental Science & Technology, 2012. **46**(15): p. 7939-7954.
192. Jien, S.-H. and C.-S. Wang, *Effects of biochar on soil properties and erosion potential in a highly weathered soil*. CATENA, 2013. **110**(Supplement C): p. 225-233.
193. Li, X., et al., *Functional Groups Determine Biochar Properties (pH and EC) as Studied by Two-Dimensional (13)C NMR Correlation Spectroscopy*. PLoS ONE, 2013. **8**(6): p. e65949.
194. Cheng, C.-H., et al., *Oxidation of black carbon by biotic and abiotic processes*. Organic Geochemistry, 2006. **37**(11): p. 1477-1488.
195. Baumann, B.B., *The botanical aspects of ancient Egyptian embalming and burial*. Economic Botany, 1960. **14**(1): p. 84-104.

196. Sombroek, W.G., *Amazon soils : a reconnaissance of the soils of the Brazilian Amazon region / W.G. Sombroek ; with a foreword by P. Lemos de Oliveira*. 1966, Wageningen, [The Netherlands]: Centre for Agricultural Publications and Documentation.
197. J. Eden, M., et al., *Terra Preta Soils and Their Archaeological Context in the Caqueta Basin of Southeast Colombia*. Vol. 49. 1984. 125.
198. Pandolfo, A.G., M. Amini-Amoli, and J.S. Killingley, *Activated carbons prepared from shells of different coconut varieties*. *Carbon*, 1994. **32**(5): p. 1015-1019.
199. Gergova, K. and S. Eser, *Effects of activation method on the pore structure of activated carbons from apricot stones*. *Carbon*, 1996. **34**(7): p. 879-888.
200. Karaosmanoglu, F., A. Isigigur-Ergudenler, and A. Sever, *Biochar from the Straw-Stalk of Rapeseed Plant*. Vol. 14. 2000. 336-339.
201. Purevsuren, B. and Y. Davaajav, *Thermal Analysis of Casein*. *Journal of Thermal Analysis and Calorimetry*, 2001. **65**(1): p. 147-152.
202. Purevsuren, B. and Y. Davaajav, *Investigation on Pyrolysis of Casein*. *Journal of Thermal Analysis and Calorimetry*, 2001. **66**(3): p. 743-748.
203. Marris, E., *Putting the carbon back: Black is the new green*. *Nature*, 2006. **442**(7103): p. 624-626.
204. Özçimen, D. and A. Ersoy-Meriçboyu, *A study on the carbonization of grapeseed and chestnut shell*. *Fuel Processing Technology*, 2008. **89**(11): p. 1041-1046.
205. McDonald-Wharry, J., M. Manley-Harris, and K. Pickering, *Carbonisation of biomass-derived chars and the thermal reduction of a graphene oxide sample studied using Raman spectroscopy*. *Carbon*, 2013. **59**(Supplement C): p. 383-405.
206. Qian, K., et al., *Recent advances in utilization of biochar*. *Renewable and Sustainable Energy Reviews*, 2015. **42**(Supplement C): p. 1055-1064.
207. Sun Cha, J., et al., *Production and Utilization of Biochar: A Review*. Vol. 40. 2016.
208. Choi, Y.-K. and S.-J. Park, *Hydrogen storage capacity of highly porous carbons synthesized from biomass-derived aerogels*. Vol. 16. 2015. 127-131.
209. Ramesh, T., N. Rajalakshmi, and K.S. Dhathathreyan, *Activated carbons derived from tamarind seeds for hydrogen storage*. Vol. 4. 2015. 89-95.
210. Oleszczuk, P., et al., *Characterization of nanoparticles of biochars from different biomass*. *Journal of Analytical and Applied Pyrolysis*, 2016. **121**(Supplement C): p. 165-172.
211. Ramirez-Rico, J., J. Martinez-Fernandez, and M. Singh, *Biomorphic ceramics from wood-derived precursors*. *International Materials Reviews*, 2017. **62**(8): p. 465-485.
212. Studart, A.R., et al., *Processing Routes to Macroporous Ceramics: A Review*. *Journal of the American Ceramic Society*, 2006. **89**(6): p. 1771-1789.
213. Ilvessalo-Pfäffli, M.-S., *Structure of Wood*, in *Fiber Atlas: Identification of Papermaking Fibers*, M.-S. Ilvessalo-Pfäffli, Editor. 1995, Springer Berlin Heidelberg: Berlin, Heidelberg. p. 6-32.
214. Aho, A., et al., *Natural composite of wood as replacement material for osteochondral bone defects*. 2007. **83**: p. 64-71.

215. Wehi, P.M. and B.D. Clarkson, *Biological flora of New Zealand 10. Phormium tenax, harakeke, New Zealand flax*. New Zealand Journal of Botany, 2010. **45**(4): p. 521-544.
216. Carr, D.J., et al., *Fibers from Three Cultivars of New Zealand Flax (Phormium tenax)*. Textile Research Journal, 2016. **75**(2): p. 93-98.
217. Daniels, V., *Factors affecting the deterioration of the cellulosic fibres in black-dyed New Zealand flax (phormium tenax)*. Studies in Conservation, 2013. **44**(2): p. 73-85.
218. Ansell, M.P. and L.Y. Mwaikambo, *The structure of cotton and other plant fibres*, in *Handbook of Textile Fibre Structure*, S.J. Eichhorn, et al., Editors. 2009, Woodhead Publishing. p. 62-94.
219. Duchemin, B., K. Luijk, and M. Staiger. *New Zealand Flax (Phormium tenax) Reinforced Eco-Composites*. in *2nd international conference on eco-composites*. 2003. Queen Mary, University of London, London, UK.
220. Alzeer, M. and K. MacKenzie, *Synthesis and mechanical properties of novel composites of inorganic polymers (geopolymers) with unidirectional natural flax fibres (phormium tenax)*. Applied Clay Science, 2013. **75-76**: p. 148-152.
221. De Rosa, I.M., C. Santulli, and F. Sarasini, *Mechanical and thermal characterization of epoxy composites reinforced with random and quasi-unidirectional untreated Phormium tenax leaf fibers*. Materials & Design (1980-2015), 2010. **31**(5): p. 2397-2405.
222. Siddiqui, H.A., K.L. Pickering, and M.R. Mucalo, *Study of biomorphic calcium deficient hydroxyapatite fibres derived from a natural Harakeke (Phormium tenax) leaf fibre template*. Bioinspiration & Biomimetics, 2020. **16**(1): p. 016015.
223. Orwin, J. *Shrubs and small trees of the forest - Cabbage trees*. [cited 2017 23 November]; Available from: <http://www.TeAra.govt.nz/en/shrubs-and-small-trees-of-the-forest/page-6>.
224. Simpson, P., *Dancing Leaves: The Story of New Zealand's Cabbage Tree, Tī Kōuka*. 2000: Canterbury University Press.
225. Ferraz, M.P., F.J. Monteiro, and C.M. Manuel, *Hydroxyapatite Nanoparticles: A Review of Preparation Methodologies*. Journal of Applied Biomaterials and Biomechanics, 2004. **2**(2): p. 74-80.
226. Gentile, P., et al., *Process Optimisation to Control the Physico-Chemical Characteristics of Biomimetic Nanoscale Hydroxyapatites Prepared Using Wet Chemical Precipitation*. Materials, 2015. **8**(5): p. 2297-2310.
227. Şimşek, D., et al., *Preparation and Characterization of Hydroxyapatite/Calcium Phosphate Powders*. Key Engineering Materials, 2004. **264-268**: p. 2075-2078.
228. Lazić, S., et al., *The effect of temperature on the properties of hydroxyapatite precipitated from calcium hydroxide and phosphoric acid*. Thermochemica Acta, 2001. **374**: p. 13-22.
229. Fulmer, M.T. and P.W. Brown, *Effects of temperature on the formation of hydroxyapatite*. Journal of Materials Research, 1993. **8**(7): p. 1687-1696.
230. Rahavi, S.S., et al., *A comparative study on physicochemical properties of hydroxyapatite powders derived from natural and synthetic sources*. Russian Journal of Non-Ferrous Metals, 2017. **58**(3): p. 276-286.

231. Jaber, H.L., A.S. Hammood, and N. Parvin, *Synthesis and characterization of hydroxyapatite powder from natural Camelus bone*. Journal of the Australian Ceramic Society, 2018. **54**(1): p. 1-10.
232. Sun, R.-X., et al., *Physicochemical and biological properties of bovine-derived porous hydroxyapatite/collagen composite and its hydroxyapatite powders*. Ceramics International, 2017. **43**(18): p. 16792-16798.
233. Zhang, Y. and J. Lu, *A simple method to tailor spherical nanocrystal hydroxyapatite at low temperature*. Journal of Nanoparticle Research, 2007. **9**(4): p. 589-594.
234. Uskoković, V. and D.P. Uskoković, *Nanosized hydroxyapatite and other calcium phosphates: chemistry of formation and application as drug and gene delivery agents*. J Biomed Mater Res B Appl Biomater, 2011. **96**(1): p. 152-91.
235. Rodriguez-Lorenzo, L., J. Hart, and K. Gross, *Structural and Chemical Analysis of Well-Crystallized Hydroxyfluorapatites*. Vol. 34. 2003.
236. Gilbert, K., et al., *CO<sub>2</sub> solubility in aqueous solutions containing Na<sup>+</sup>, Ca<sup>2+</sup>, Cl<sup>-</sup>, SO<sub>4</sub><sup>2-</sup> and HCO<sub>3</sub><sup>-</sup>: The effects of electrostricted water and ion hydration thermodynamics*. Applied Geochemistry, 2016. **67**.
237. Ren, F.Z. and Y. Leng, *Carbonated Apatite, Type-A or Type-B?* Key Engineering Materials, 2011. **493-494**: p. 293-297.
238. Reyes-Gasga, J., et al., *XRD and FTIR crystallinity indices in sound human tooth enamel and synthetic hydroxyapatite*. Vol. 33. 2013. 4568-4574.
239. Weiner, S. and O. Bar-Yosef, *States of preservation of bones from prehistoric sites in the Near East: A survey*. Journal of Archaeological Science, 1990. **17**(2): p. 187-196.
240. Wojdyr, M., *Fityk: a general-purpose peak fitting program*. Journal of Applied Crystallography, 2010. **43**(5-1): p. 1126-1128.
241. Pasteris, J., *A mineralogical view of apatitic biomaterials*. American Mineralogist, 2016. **101**: p. 2594-2610.
242. Rey, C., et al., *Nanocrystalline apatites in biological systems: characterisation, structure and properties*. Materialwissenschaft und Werkstofftechnik, 2007. **38**(12): p. 996-1002.
243. Ortali, C., et al., *Consolidation of bone-like apatite bioceramics by spark plasma sintering of amorphous carbonated calcium phosphate at very low temperature*. Journal of the European Ceramic Society, 2018. **38**: p. 2098-2109.
244. Drouet, C., et al., *Nanocrystalline apatites: From powders to biomaterials*. Powder Technology, 2009. **190**(1): p. 118-122.
245. Degen, T., et al., *The HighScore suite*. Powder Diffraction, 2014. **29**(S2): p. S13-S18.
246. Landi, E., et al., *Densification behaviour and mechanisms of synthetic hydroxyapatites*. Journal of the European Ceramic Society, 2000. **20**(14-15): p. 2377-2387.
247. Friederichs, R.J., et al., *Synthesis, characterization and modelling of zinc and silicate co-substituted hydroxyapatite*. Journal of The Royal Society Interface, 2015. **12**(108): p. 20150190.
248. Moslim, N.A., N. Ahmad, and S.R. Kasim, *XRD Analysis of Calcined Magnesium Substituted Biphasic Calcium Phosphate (Mg-BCP)*. Journal of Physics: Conference Series, 2018. **1082**: p. 012025.

249. Wiles, D.B. and R.A. Young, *A new computer program for Rietveld analysis of X-ray powder diffraction patterns*. Journal of Applied Crystallography, 1981. **14**(2): p. 149-151.
250. Dunne, C., et al., *Co-blasting of titanium surfaces with an abrasive and hydroxyapatite to produce bioactive coatings: Substrate and coating characterisation*. Journal of biomaterials applications, 2014. **28**: p. 767-778.
251. Combes, C. and C. Rey, *Amorphous calcium phosphates: synthesis, properties and uses in biomaterials*. Acta Biomater, 2010. **6**(9): p. 3362-78.
252. Eanes, E.D., *Amorphous Calcium Phosphate: Thermodynamic and Kinetic Considerations*, in *Calcium Phosphates in Biological and Industrial Systems*, Z. Amjad, Editor. 1998, Springer US: Boston, MA. p. 21-39.
253. Vecstaudza, J., M. Gasik, and J. Locs, *Amorphous calcium phosphate materials: Formation, structure and thermal behaviour*. Journal of the European Ceramic Society, 2019. **39**(4): p. 1642-1649.
254. Boskey, A.L. and A.S. Posner, *Conversion of amorphous calcium phosphate to microcrystalline hydroxyapatite. A pH-dependent, solution-mediated, solid-solid conversion*. The Journal of Physical Chemistry, 1973. **77**(19): p. 2313-2317.
255. Posner, A.S. and F. Betts, *Synthetic amorphous calcium phosphate and its relation to bone mineral structure*. Accounts of Chemical Research, 1975. **8**(8): p. 273-281.
256. Posner, A.S. and F. Betts, *Synthetic amorphous calcium phosphate and its relation to bone mineral structure*. Accounts of Chemical Research, 2002. **8**(8): p. 273-281.
257. Yin, X. and M.J. Stott, *Biological calcium phosphates and Posner's cluster*. The Journal of Chemical Physics, 2003. **118**(8): p. 3717-3723.
258. Dorozhkin, S.V., *Amorphous calcium (ortho)phosphates*. Acta Biomater, 2010. **6**(12): p. 4457-75.
259. Wang, L., et al., *Posner's cluster revisited: direct imaging of nucleation and growth of nanoscale calcium phosphate clusters at the calcite-water interface*. CrystEngComm, 2012. **14**(19): p. 6252-6256.
260. Mancardi, G., et al., *Detection of Posner's clusters during calcium phosphate nucleation: a molecular dynamics study*. Journal of Materials Chemistry B, 2017. **5**(35): p. 7274-7284.
261. Berkum, J., et al., *The optimum standard specimen for X-ray diffraction line-profile analysis*. Powder Diffraction - POWDER DIFFR, 1995. **10**: p. 129-139.
262. Santra, K., P. Chatterjee, and S.P. Sen Gupta, *Voigt modelling of size-strain analysis: Application to  $\alpha$ -Al<sub>2</sub>O<sub>3</sub> prepared by combustion technique*. Bulletin of Materials Science, 2002. **25**(3): p. 251-257.
263. Venkateswarlu, K., A. Chandra Bose, and N. Rameshbabu, *X-ray peak broadening studies of nanocrystalline hydroxyapatite by Williamson–Hall analysis*. Physica B: Condensed Matter, 2010. **405**(20): p. 4256-4261.
264. Farlay, D., et al., *Mineral maturity and crystallinity index are distinct characteristics of bone mineral*. J Bone Miner Metab, 2010. **28**(4): p. 433-45.
265. Rey, C., et al., *Characterization of Calcium Phosphates Using Vibrational Spectroscopies*, in *Advances in Calcium Phosphate Biomaterials*, B. Ben-Nissan, Editor. 2014, Springer Berlin Heidelberg: Berlin, Heidelberg. p. 229-266.

266. Wong, W.Y. and A.-F.M. Noor, *Synthesis and Sintering-wet Carbonation of Nano-sized Carbonated Hydroxyapatite*. Procedia Chemistry, 2016. **19**: p. 98-105.
267. Mandair, G.S. and M.D. Morris, *Contributions of Raman spectroscopy to the understanding of bone strength*. Bonekey Rep, 2015. **4**: p. 620.
268. Morris, M.D. and G.S. Mandair, *Raman assessment of bone quality*. Clin Orthop Relat Res, 2011. **469**(8): p. 2160-9.
269. Garskaite, E., et al., *Effect of processing conditions on the crystallinity and structure of carbonated calcium hydroxyapatite (CHAp)*. CrystEngComm, 2014. **16**(19): p. 3950-3959.
270. Wang, S., et al., *Low temperature preparation of  $\alpha$ -tricalcium phosphate and its mechanical properties*. Processing and Application of Ceramics, 2017. **11**: p. 100-105.
271. Uskokovic, V. and D. Uskoković, *Nanosized Hydroxyapatite and Other Calcium Phosphates: Chemistry of Formation and Application as Drug and Gene Delivery Agents*. Journal of biomedical materials research. Part B, Applied biomaterials, 2011. **96**: p. 152-91.
272. Patel, N., et al., *Calcining Influence on the Powder Properties of Hydroxyapatite*. Journal of materials science. Materials in medicine, 2001. **12**: p. 181-8.
273. The, Y.C., et al., *Effect of calcination on the sintering behaviour of hydroxyapatite*. Ceramics - Silikaty, 2014. **58**: p. 320-325.
274. Aruan Efendy, M.G. and K.L. Pickering, *Comparison of harakeke with hemp fibre as a potential reinforcement in composites*. Composites Part A: Applied Science and Manufacturing, 2014. **67**: p. 259-267.
275. Meri, N., et al., *Effect of Chemical Washing Pre-treatment of Empty Fruit Bunch (EFB) biochar on Characterization of Hydrogel Biochar composite as Bioadsorbent*. IOP Conference Series: Materials Science and Engineering, 2018. **358**: p. 012018.
276. Fan, R., *Biochars for removal of ammonium, phosphate, and hydrogen peroxide from aqueous solutions: potential applications in agricultural and semiconductor industrial waters*, in *Department of Civil and Environmental Engineering*. 2018, University of Delaware. p. 241.
277. Almgheer, T. and F. Abdulrazzak, *Oxidation of multi-walled carbon nanotubes in acidic and basic Piranha mixture*. Frontiers in Nanoscience and Nanotechnology, 2016. **2**.
278. Wei, C., et al., *Mechano-Fenton–Piranha Oxidation of Carbon Nanotubes for Energy Application*. Advanced Sustainable Systems, 2019. **3**(11): p. 1900065.
279. Duchemin, B. and M.P. Staiger, *Treatment of Harakeke fiber for biocomposites*. Journal of Applied Polymer Science, 2009. **112**(5): p. 2710-2715.
280. Puglia, D., et al., *Effect of alkali and silane treatments on mechanical and thermal behavior of Phormium tenax fibers*. Fibers and Polymers, 2013. **14**(3): p. 423-427.
281. Lowe, B.J., et al., *Light-ageing characteristics of Māori textiles: Colour, strength and molecular change*. Journal of Cultural Heritage, 2017. **24**: p. 60-68.

282. Fortunati, E., et al., *Extraction of Cellulose Nanocrystals from Phormium tenax Fibres*. Journal of Polymers and the Environment, 2012. **21**(2): p. 319-328.
283. Reza, M.S., et al., *Acacia Holosericea: An Invasive Species for Bio-char, Bio-oil, and Biogas Production*. Bioengineering, 2019. **6**(2): p. 33.
284. Popescu, C.-M., et al., *Spectral Characterization of Eucalyptus Wood*. Applied Spectroscopy, 2007. **61**(11): p. 1168-1177.
285. Reza, M.S., et al., *Evaluation of the bioenergy potential of invasive Pennisetum purpureum through pyrolysis and thermogravimetric analysis*. Energy, Ecology and Environment, 2020. **5**(2): p. 118-133.
286. Antonangelo, J.A., et al., *Physicochemical properties and morphology of biochars as affected by feedstock sources and pyrolysis temperatures*. Biochar, 2019. **1**(3): p. 325-336.
287. Xue, Y., et al., *Hydrogen peroxide modification enhances the ability of biochar (hydrochar) produced from hydrothermal carbonization of peanut hull to remove aqueous heavy metals: Batch and column tests*. Chemical Engineering Journal, 2012. **200-202**: p. 673-680.
288. Huff, M.D. and J.W. Lee, *Biochar-surface oxygenation with hydrogen peroxide*. Journal of Environmental Management, 2016. **165**: p. 17-21.
289. Cui, X., et al., *Transformation of Phosphorus in Wetland Biomass during Pyrolysis and Hydrothermal Treatment*. ACS Sustainable Chemistry & Engineering, 2019. **7**.
290. Waqas, M., et al., *Development of Biochar as Fuel and Catalyst in Energy Recovery Technologies*. Journal of Cleaner Production, 2018. **188**: p. 477-488.
291. Zhao, B. and O. Nartey, *Characterization and evaluation of biochars derived from agricultural waste biomass from Gansu, China*. 2014.
292. McDonald-Wharry, J., *2013–2014 Survey of Chars Using Raman Spectroscopy*. C, 2021. **7**: p. 63.
293. Ferrari, A.C., *Raman spectroscopy of graphene and graphite: Disorder, electron–phonon coupling, doping and nonadiabatic effects*. Solid state communications, 2007. **143**(1-2): p. 47-57.
294. Campos-Delgado, J., et al., *CVD synthesis of mono- and few-layer graphene using alcohols at low hydrogen concentration and atmospheric pressure*. Chemical Physics Letters, 2013. **584**: p. 142-146.
295. Chu, P.K. and L. Li, *Characterization of amorphous and nanocrystalline carbon films*. Materials Chemistry and Physics, 2006. **96**(2): p. 253-277.
296. Kudin, K.N., et al., *Raman Spectra of Graphite Oxide and Functionalized Graphene Sheets*. Nano Letters, 2008. **8**(1): p. 36-41.
297. Nzihou, A., *Handbook on Characterization of Biomass, Biowaste and Related By-products*. 2020.
298. Cong, C., et al., *Visualization of arrangements of carbon atoms in graphene layers by Raman mapping and atomic-resolution TEM*. Scientific Reports, 2013. **3**(1): p. 1195.
299. Ramos-Carmona, S., S. Delgado-Balcázar, and J. Pérez, *Physicochemical characterization of torrefied wood biomass under air as oxidizing atmosphere*. BioResources, 2017. **12**: p. 5428-5448.
300. Thong, J.T.L., K.W. Lee, and W.K. Wong, *Reduction of charging effects using vector scanning in the scanning electron microscope*. Scanning, 2001. **23**(6): p. 395-402.



301. Kaya, C., I. Singh, and A.R. Boccaccini, *Multi-walled Carbon Nanotube-Reinforced Hydroxyapatite Layers on Ti6Al4V Medical Implants by Electrophoretic Deposition (EPD)*. *Advanced Engineering Materials*, 2008. **10**(1-2): p. 131-138.
302. Liu, W.-W., et al., *Exfoliation and dispersion of graphene in ethanol-water mixtures*. *Frontiers of Materials Science*, 2012. **6**.
303. Wei, Q., et al., *Study the bonding mechanism of binders on hydroxyapatite surface and mechanical properties for 3DP fabrication bone scaffolds*. *Journal of the Mechanical Behavior of Biomedical Materials*, 2016. **57**: p. 190-200.
304. Merry, J.C., et al., *Synthesis and characterization of carbonate hydroxyapatite*. *Journal of Materials Science: Materials in Medicine*, 1998. **9**(12): p. 779-783.
305. Liu, Y., et al., *Inhibited grain growth in hydroxyapatite-graphene nanocomposites during high temperature treatment and their enhanced mechanical properties*. *Ceramics International*, 2016. **42**(9): p. 11248-11255.
306. Zhao, X., et al., *Carbon fiber reinforced hydroxyapatite composites with excellent mechanical properties and biological activities prepared by spark plasma sintering*. *Ceramics International*, 2020. **46**.
307. Nosrati, H., et al., *Low temperature consolidation of hydroxyapatite-reduced graphene oxide nano-structured powders*. *Materials Advances*, 2020. **1**(5): p. 1337-1346.
308. Pramanik, S., A. Agarwal, and K. Rai, *Development of High Strength Hydroxyapatite for Hard Tissue Replacement*. *Trends in Biomaterials and Artificial Organs*, 2005. **19**: p. 46-51.
309. Barabashko, M.S., et al., *Variation of Vickers microhardness and compression strength of the bioceramics based on hydroxyapatite by adding the multi-walled carbon nanotubes*. *Applied Nanoscience*, 2020. **10**(8): p. 2601-2608.
310. Evis, Z. and F. Ozturk, *Investigation of tensile strength of hydroxyapatite with various porosities by diametral strength test*. *Materials Science and Technology*, 2008. **24**(4): p. 474-478.
311. Glaser, D.E. and C. Viney, *Biomimetic Materials*. *Biomaterials Science*, 2013: p. 349-360.
312. Ripley, R.L. and B. Bhushan, *Bioarchitecture: bioinspired art and architecture--a perspective*. *Philos Trans A Math Phys Eng Sci*, 2016. **374**(2073): p. 20160192.
313. Paris, O., I. Burgert, and P. Fratzl, *Biomimetics and Biotemplating of Natural Materials*. 2010. **35**: p. 219-225.
314. Dong, Q., et al., *Synthesis and characterizations of hierarchical biomorphic titania oxide by a bio-inspired bottom-up assembly solution technique*. *Journal of Solid State Chemistry*, 2007. **180**(3): p. 949-955.
315. Luo, M., et al., *Synthesis of wood-derived ceramics from biological templates*. *Progress in Chemistry*, 2008. **20**(6): p. 989-1000.
316. Baino, F. and M. Ferraris, *Learning from Nature: Using bioinspired approaches and natural materials to make porous bioceramics*. *International Journal of Applied Ceramic Technology*, 2017. **14**(4): p. 507-520.

317. Gonzalez, P., et al., *New biomorphic SiC ceramics coated with bioactive glass for biomedical applications*. *Biomaterials*, 2003. **24**(26): p. 4827-32.
318. Rambo, C., et al., *Biomimetic Apatite Coating on Biomorphous Alumina Scaffolds*. 2006. **26**: p. 92-99.
319. Wu, S., et al., *Biomimetic porous scaffolds for bone tissue engineering*. *Materials Science and Engineering: R: Reports*, 2014. **80**: p. 1-36.
320. Neto, A.S. and J.M.F. Ferreira, *Synthetic and Marine-Derived Porous Scaffolds for Bone Tissue Engineering*. *Materials (Basel)*, 2018. **11**(9): p. 1702.
321. Zhang, K., et al., *Effect of microporosity on scaffolds for bone tissue engineering*. *Regen Biomater*, 2018. **5**(2): p. 115-124.
322. LeGeros, R.Z., *Properties of osteoconductive biomaterials: calcium phosphates*. *Clin Orthop Relat Res*, 2002. **395**(395): p. 81-98.
323. Gu, Y.W., K.A. Khor, and P. Cheang, *Bone-like apatite layer formation on hydroxyapatite prepared by spark plasma sintering (SPS)*. *Biomaterials*, 2004. **25**(18): p. 4127-34.
324. Kim, H.M., et al., *The mechanism of biomineralization of bone-like apatite on synthetic hydroxyapatite: an in vitro assessment*. *Journal of the Royal Society, Interface*, 2004. **1**(1): p. 17-22.
325. Czikó, M., et al., *In vitro biological activity comparison of some hydroxyapatite-based composite materials using simulated body fluid*. *Open Chemistry*, 2013. **11**(10): p. 1583-1598.
326. C. B. M. Fook, A., et al., *Porous Hydroxyapatite Scaffolds by Polymer Sponge Method*. 2009. **396-398**: p. 703-706.
327. Lee, J.-H. and Y.-J. Kim, *Hydroxyapatite nanofibers fabricated through electrospinning and sol-gel process*. *Ceramics International*, 2014. **40**(2): p. 3361-3369.
328. G, R., et al., *A novel nano-hydroxyapatite - PMMA hybrid scaffolds adopted by conjugated thermal induced phase separation (TIPS) and wet-chemical approach: Analysis of its mechanical and biological properties*. *Mater Sci Eng C Mater Biol Appl*, 2017. **75**: p. 221-228.
329. Hattori, T., et al., *Preparation of Hydroxyapatite Powder Using a Freeze-Drying Method*. *Journal of the Ceramic Association, Japan*, 1987. **95**(1104): p. 825-827.
330. Sepulveda, P., et al., *Production of Porous Hydroxyapatite by the Gel-Casting of Foams and Cytotoxic Evaluation*. 2000. **50**: p. 27-34.
331. Carreño, N.L.V., et al., *Nano and Micro Ceramic Membranes from Degradable Templates*. *Materials Research*, 2016. **19**: p. 1017-1025.
332. Utara, S. and J. Klinkaewnarong, *Synthesis and characterization of hydroxyapatite nanoparticles templated by ozonolysed natural rubber latex*. *Journal of Sol-Gel Science and Technology*, 2016. **80**(3): p. 728-737.
333. Verma, G., et al., *Rod-like micelle templated synthesis of porous hydroxyapatite*. *Ceramics International*, 2013. **39**(8): p. 8995-9002.
334. Barakat, N.A.M., et al., *Extraction of pure natural hydroxyapatite from the bovine bones bio waste by three different methods*. *Journal of Materials Processing Technology*, 2009. **209**(7): p. 3408-3415.
335. Akindoyo, J.O., et al., *Characterization and Elemental Quantification of Natural Hydroxyapatite Produced from Cow Bone*. *Chemical Engineering & Technology*, 2019. **42**(9): p. 1805-1815.

336. Ren, F., Y. Ding, and Y. Leng, *Infrared spectroscopic characterization of carbonated apatite: a combined experimental and computational study*. J Biomed Mater Res A, 2014. **102**(2): p. 496-505.
337. Matsumura, Y. and J.B. Moffat, *Partial Oxidation of Methane to Carbon-Monoxide and Hydrogen with Molecular-Oxygen and Nitrous-Oxide over Hydroxyapatite Catalysts*. Journal of Catalysis, 1994. **148**(1): p. 323-333.
338. Cheng, Z.H., et al., *FTIR Study of Adsorption of CO<sub>2</sub> on Nonstoichiometric Calcium Hydroxyapatite*. Langmuir, 1998. **14**(23): p. 6681-6686.
339. Raynaud, S., et al., *Calcium phosphate apatites with variable Ca/P atomic ratio I. Synthesis, characterisation and thermal stability of powders*. Biomaterials, 2002. **23**(4): p. 1065-72.
340. Reyes-Gasga, J., et al., *XRD and FTIR crystallinity indices in sound human tooth enamel and synthetic hydroxyapatite*. 2013. **33**: p. 4568-4574.
341. Koutsopoulos, S., *Synthesis and characterization of hydroxyapatite crystals: a review study on the analytical methods*. J Biomed Mater Res, 2002. **62**(4): p. 600-12.
342. De Aza, P., et al., *Vibrational properties of calcium phosphate compounds. 2. Comparison between hydroxyapatite and  $\beta$ -tricalcium phosphate*. Chemistry of Materials, 1997. **9**(4): p. 916-922.
343. Sa, Y., et al., *Are different crystallinity-index-calculating methods of hydroxyapatite efficient and consistent?* New Journal of Chemistry, 2017. **41**(13): p. 5723-5731.
344. Li, Z. and J.D. Pasteris, *Chemistry of bone mineral, based on the hypermineralized rostrum of the beaked whale Mesoplodon densirostris*. Am Mineral, 2014. **99**(4): p. 645-653.
345. Rojas, J., M. Bedoya, and Y. Ciro, *Current Trends in the Production of Cellulose Nanoparticles and Nanocomposites for Biomedical Applications*. Cellulose - Fundamental Aspects and Current Trends, 2015: p. 193-228.
346. Puglia, D., et al., *Thermal and mechanical characterisation of Phormium tenax-reinforced polypropylene composites*. Journal of Thermoplastic Composite Materials, 2013. **27**(11): p. 1493-1503.
347. Wang, T., et al., *Synthesis and Thermal Conductivities of the Biomorphic Al<sub>2</sub>O<sub>3</sub> Fibers Derived from Silk Template*. 2013. **10**: p. 285-292.
348. Liu, W., et al., *Effects of alkali treatment on the structure, morphology and thermal properties of native grass fibers as reinforcements for polymer matrix composites*. Journal of Materials Science, 2004. **39**(3): p. 1051-1054.
349. Albano, C., et al., *Thermal stability of blends of polyolefins and sisal fiber*. Polymer Degradation and Stability, 1999. **66**(2): p. 179-190.
350. Rodríguez-Lorenzo, L.M., J.N. Hart, and K.A. Gross, *Structural and Chemical Analysis of Well-Crystallized Hydroxyfluorapatites*. The Journal of Physical Chemistry B, 2003. **107**(33): p. 8316-8320.
351. Tilley, R.J.D., *Crystals and Crystal Structures*. 2006: Wiley.
352. Nasri, K., et al., *Spray-Dried Monocalcium Phosphate Monohydrate for Soluble Phosphate Fertilizer*. Industrial & Engineering Chemistry Research, 2015. **54**(33): p. 8043-8047.
353. Considine, G.D., *Phosphoric Acid*, in *Van Nostrand's Scientific Encyclopedia*, G.D. Considine, Editor. 2006.
354. Chen, H., et al., *Effect of alkali treatment on wettability and thermal stability of individual bamboo fibers*. Journal of Wood Science, 2018. **64**(4): p. 398-405.


355. Giraldo-Betancur, A.L., et al., *Comparison of physicochemical properties of bio and commercial hydroxyapatite*. Current Applied Physics, 2013. **13**(7): p. 1383-1390.
356. Wang, Y., et al., *In situ fabrication of hollow hydroxyapatite microspheres by phosphate solution immersion*. Journal of Crystal Growth, 2011. **327**(1): p. 245-250.
357. Salma-Ancane, K., L. Stipniece, and Z. Irbe, *Effect of biogenic and synthetic starting materials on the structure of hydroxyapatite bioceramics*. Ceramics International, 2016. **42**(8): p. 9504-9510.
358. Beaufils, S., et al., *Synthesis of calcium-deficient hydroxyapatite nanowires and nanotubes performed by template-assisted electrodeposition*. Mater Sci Eng C Mater Biol Appl, 2019. **98**: p. 333-346.
359. Eiden-Aßmann, S., et al., *The influence of amino acids on the biomineralization of hydroxyapatite in gelatin*. Journal of inorganic biochemistry, 2002. **91**(3): p. 481-486.
360. Pelin, I.M., et al., *Preparation and characterization of a hydroxyapatite–collagen composite as component for injectable bone substitute*. Materials Science and Engineering: C, 2009. **29**(7): p. 2188-2194.
361. Guo, X., et al., *Fabrication of nanostructured hydroxyapatite via hydrothermal synthesis and spark plasma sintering*. Journal of the american ceramic society, 2005. **88**(4): p. 1026-1029.
362. Krishna, D.S.R., et al., *A novel route for synthesis of nanocrystalline hydroxyapatite from eggshell waste*. Journal of Materials Science: Materials in Medicine, 2007. **18**(9): p. 1735-1743.
363. Webster, T.J., et al., *Enhanced functions of osteoblasts on nanophase ceramics*. Biomaterials, 2000. **21**(17): p. 1803-1810.
364. Ishikawa, K., et al., *Effects of preparation conditions in aqueous solution on properties of hydroxyapatites*. Dental materials journal, 1990. **9**(1): p. 58-69,123.
365. McDonald-Wharry, J., M. Manley-Harris, and K. Pickering, *A comparison of the charring and carbonisation of oxygen- rich precursors with the thermal reduction of graphene oxide*. Philosophical Magazine, 2015. **95**(36): p. 4054-4077.
366. White, A., et al., *Optimization of the sintering atmosphere for high-density hydroxyapatite - Carbon nanotube composites*. Journal of the Royal Society, Interface / the Royal Society, 2010. **7 Suppl 5**: p. S529-39.

# APPENDIX A



Review

## A Review on the Use of Hydroxyapatite-Carbonaceous Structure Composites in Bone Replacement Materials for Strengthening Purposes

Humair A. Siddiqui <sup>1,2</sup>, Kim L. Pickering <sup>1</sup>  and Michael R. Mucalo <sup>3,\*</sup>

<sup>1</sup> School of Engineering, Faculty of Science & Engineering, University of Waikato, Hamilton 3240, New Zealand; ahumair@hotmail.com (H.A.S.); klp@waikato.ac.nz (K.L.P.)

<sup>2</sup> Department of Materials Engineering, Faculty of Chemical & Process Engineering, NED University of Engineering & Technology, Karachi 75270, Pakistan

<sup>3</sup> School of Science, Faculty of Science & Engineering, University of Waikato, Hamilton 3240, New Zealand

\* Correspondence: michael.mucalo@waikato.ac.nz

Received: 31 August 2018; Accepted: 22 September 2018; Published: 24 September 2018



**Abstract:** Biomedical materials constitute a vast scientific research field, which is devoted to producing medical devices which aid in enhancing human life. In this field, there is an enormous demand for long-lasting implants and bone substitutes that avoid rejection issues whilst providing favourable bioactivity, osteoconductivity and robust mechanical properties. Hydroxyapatite (HAp)-based biomaterials possess a close chemical resemblance to the mineral phase of bone, which give rise to their excellent biocompatibility, so allowing for them to serve the purpose of a bone-substituting and osteoconductive scaffold. The biodegradability of HAp is low ( $K_{sp} \approx 6.62 \times 10^{-126}$ ) as compared to other calcium phosphates materials, however they are known for their ability to develop bone-like apatite coatings on their surface for enhanced bone bonding. Despite its favourable bone regeneration properties, restrictions on the use of pure HAp ceramics in high load-bearing applications exist due to its inherently low mechanical properties (including low strength and fracture toughness, and poor wear resistance). Recent innovations in the field of bio-composites and nanoscience have reignited the investigation of utilising different carbonaceous materials for enhancing the mechanical properties of composites, including HAp-based bio-composites. Researchers have preferred carbonaceous materials with hydroxyapatite due to their inherent biocompatibility and good structural properties. It has been demonstrated that different structures of carbonaceous material can be used to improve the fracture toughness of HAp, as they can easily serve the purpose of being a second phase reinforcement, with the resulting composite still being a biocompatible material. Nanostructured carbonaceous structures, especially those in the form of fibres and sheets, were found to be very effective in increasing the fracture toughness values of HAp. Minor addition of CNTs (3 wt.%) has resulted in a more than 200% increase in fracture toughness of hydroxyapatite-nanorods/CNTs made using spark plasma sintering. This paper presents a current review of the research field of using different carbonaceous materials composited with hydroxyapatite with the intent being to produce high performance biomedically targeted materials.

**Keywords:** hydroxyapatite; carbon; graphene; strengthening; toughening; fracture; crack bridging; nanotechnology; fracture mechanics

# APPENDIX B

---

## Bioinspiration & Biomimetics

---



### PAPER

RECEIVED  
5 May 2020

REVISED  
25 August 2020

ACCEPTED FOR PUBLICATION  
28 September 2020

PUBLISHED  
1 December 2020

## Study of biomorphic calcium deficient hydroxyapatite fibres derived from a natural *Harakeke* (*Phormium tenax*) leaf fibre template

Humair A Siddiqui<sup>1,2</sup> , Kim L Pickering<sup>1</sup> and Michael R Mucalo<sup>3,\*</sup> 

<sup>1</sup> School of Engineering, University of Waikato, Hamilton 3240, New Zealand

<sup>2</sup> Department of Materials Engineering, Faculty of Chemical & Process Engineering, NED University of Engineering & Technology, Karachi 75270, Pakistan

<sup>3</sup> School of Science, University of Waikato, Hamilton 3240, New Zealand

\* Author to whom any correspondence should be addressed.

E-mail: [ahumair@hotmail.com](mailto:ahumair@hotmail.com), [klp@waikato.ac.nz](mailto:klp@waikato.ac.nz) and [michael.mucalo@waikato.ac.nz](mailto:michael.mucalo@waikato.ac.nz)

**Keywords:** hydroxyapatite, biomorphic, Harakeke/flax, fibres, bioceramic, bovine bone repurposing

### Abstract

The complex structure of natural bio-organic matter has inspired scientists to utilise these as templates to design 'biomorphic materials', which retain the intricate architecture of the materials while acting as a useful bioactive material. Biomorphic hydroxyapatite-based fibres were synthesised using *Harakeke* leaf fibre as a template, which constitutes a powerful method for manufacturing bioactive ceramic fibres. Furthermore, in creating the hydroxyapatite-based fibres, a natural source of calcium and phosphate ions (from bovine bone) was utilised to create the digest solution in which the leaf fibres were immersed prior to their calcination to form the inorganic fibres. Chemical, thermogravimetric and microscopic characterisation confirmed that the final product was able to successfully replicate the shape of the fibres and furthermore be transformed into calcium deficient, bone-like hydroxyapatite.

---

## APPENDIX C

---

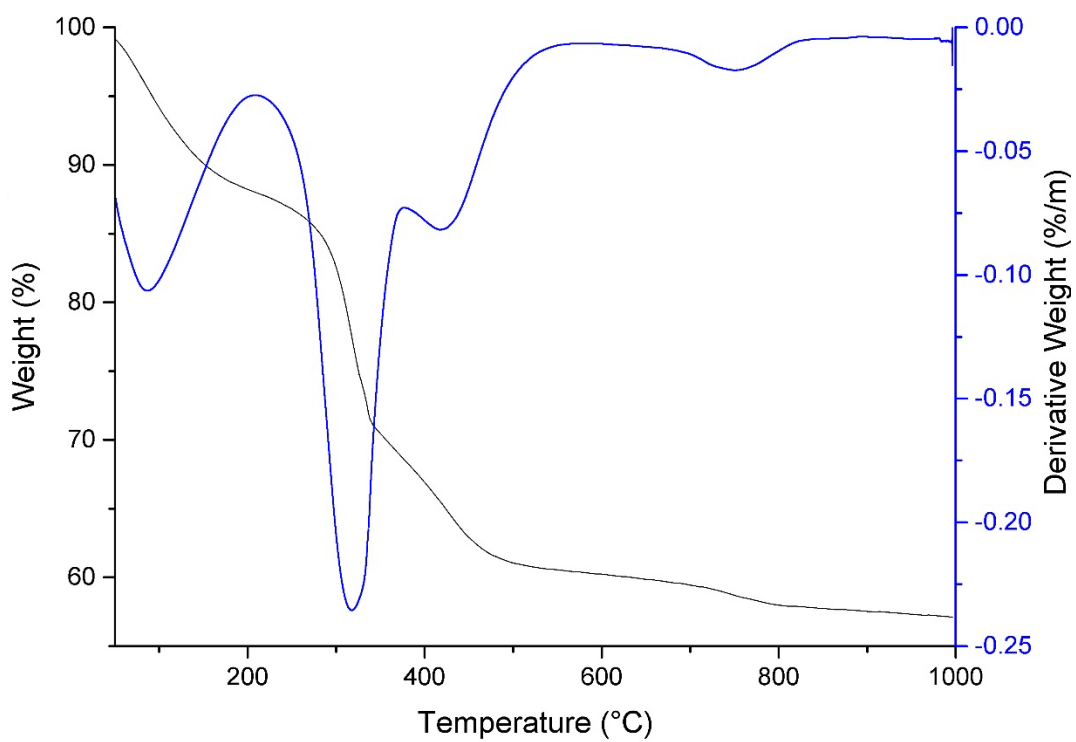


Figure C.1: Weight loss and derivative weight of raw cow bone.

# APPENDIX D

---

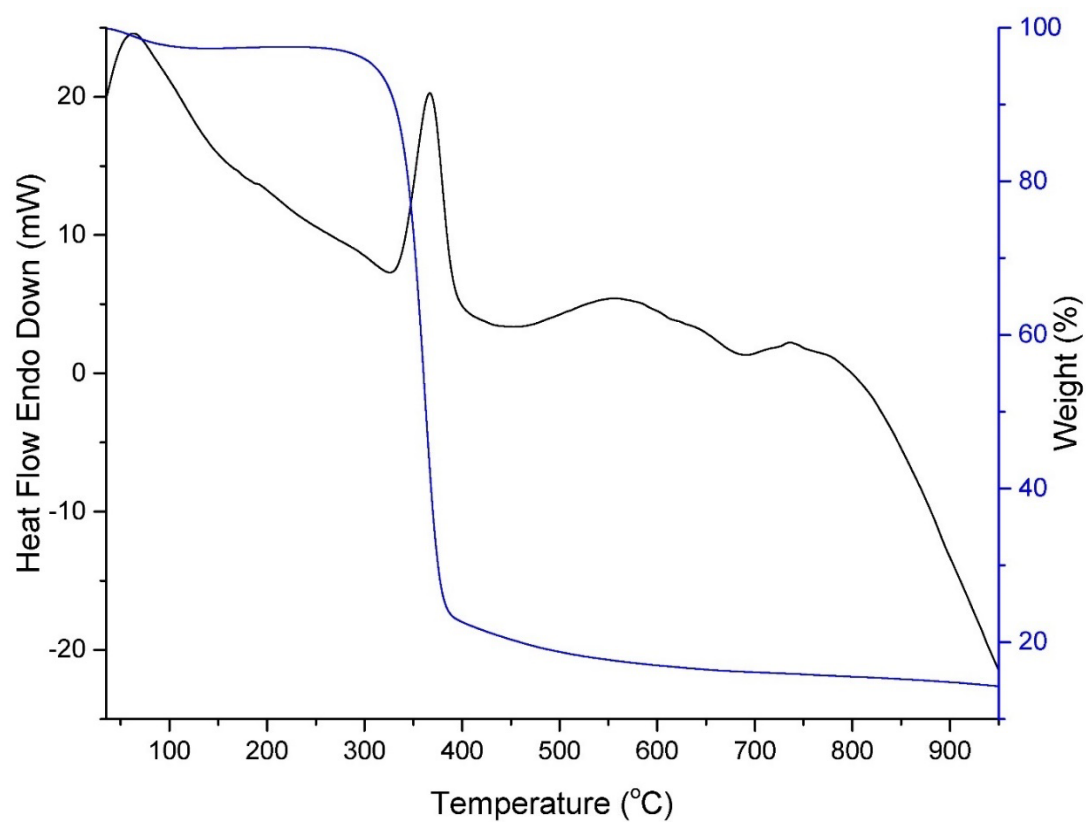




Figure D.1: Weight loss and Heat flow of defibrillated harakeke fibres (Hsep)

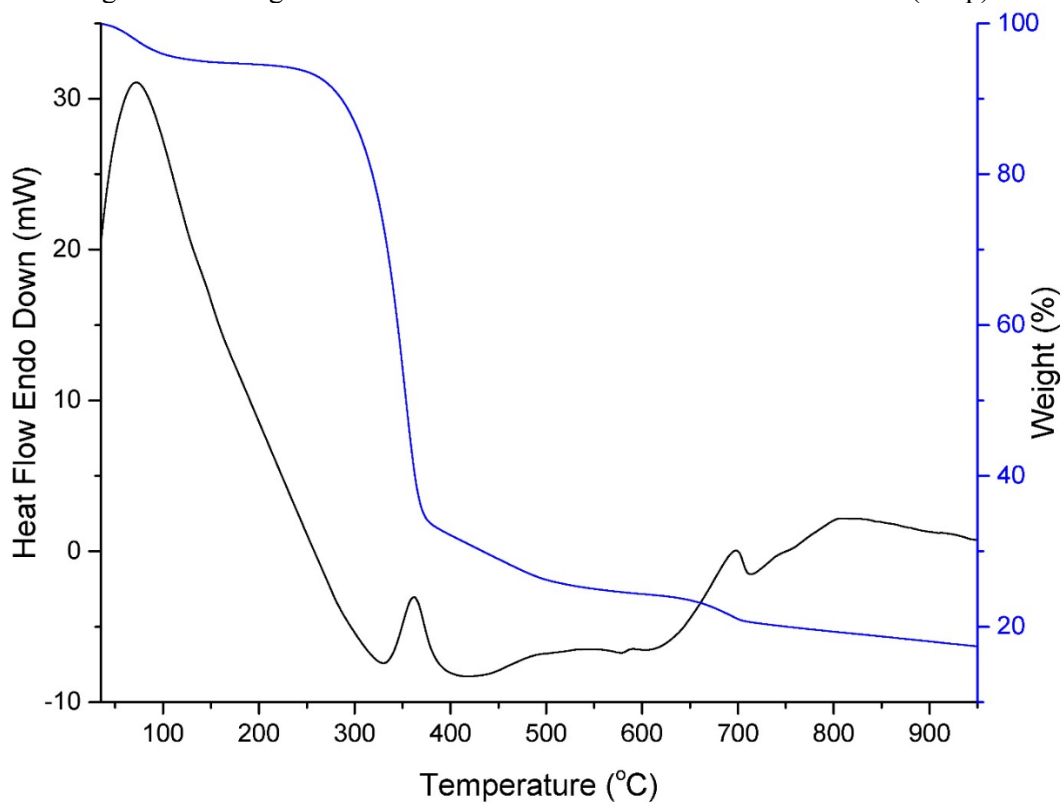


Figure D.2: Weight loss and Heat flow of defibrillated cabbage tree leaves fibres (Csep)

## APPENDIX E

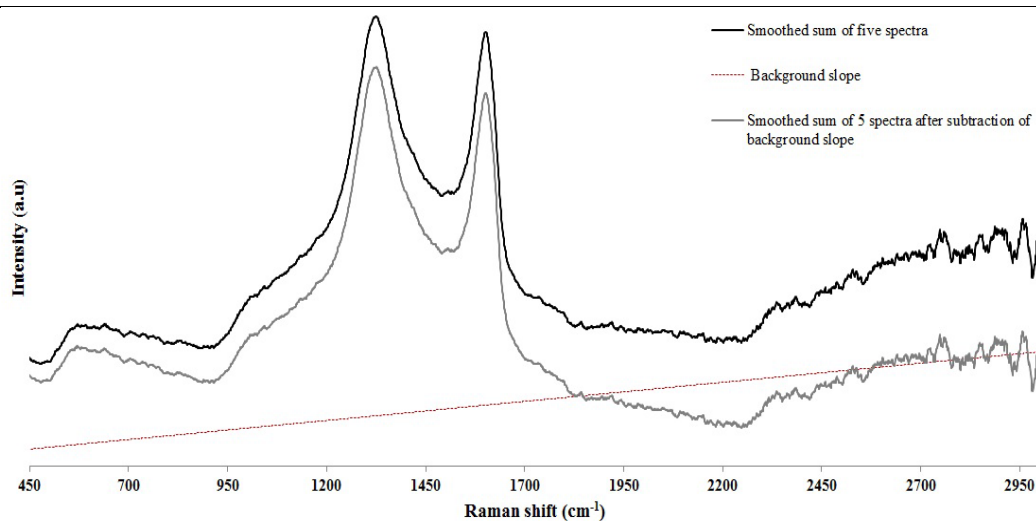


Figure E.1: A representation of the way Raman spectra were processed in this study

## APPENDIX F

---

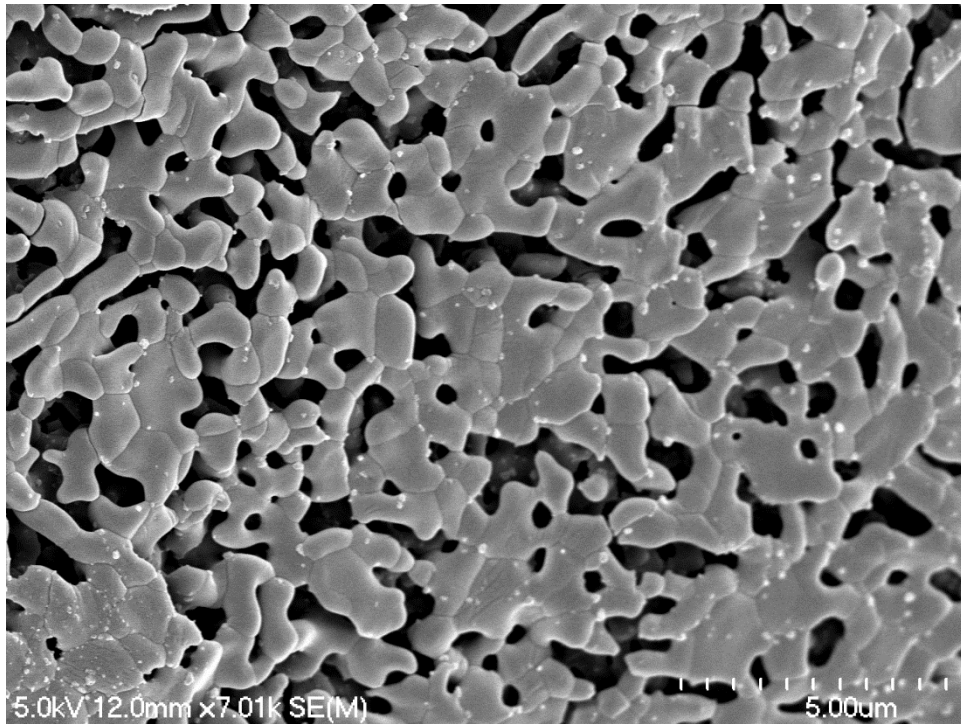


Figure F.1: SEM image of precipitated HAp ( $H_p$ )

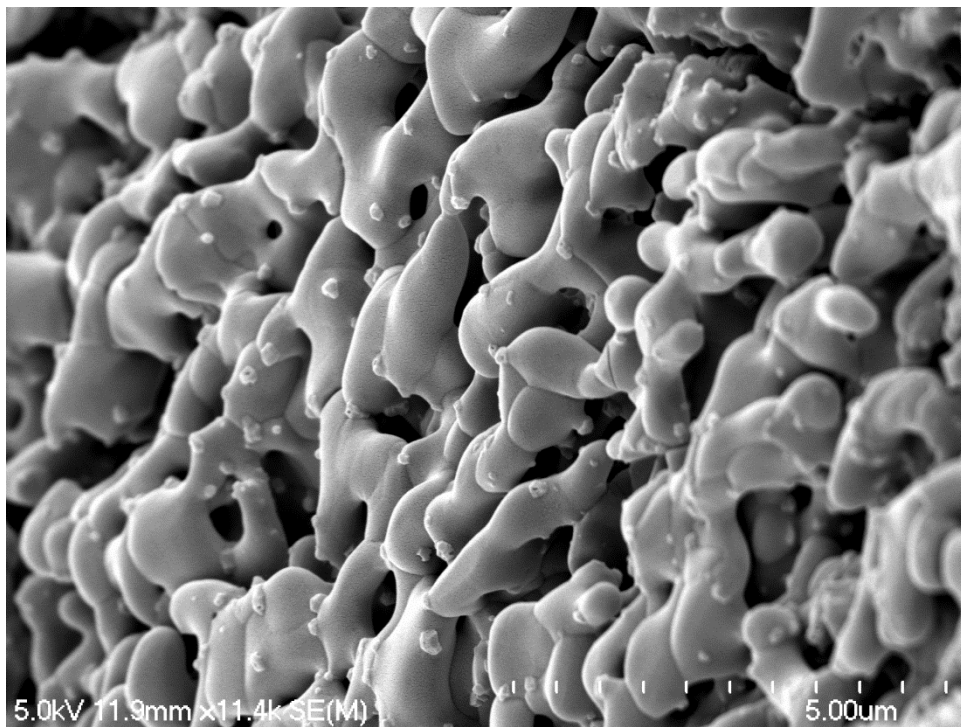


Figure F.2: SEM image of precipitated HAp ( $H_p$ )

Since, precipitated HAp was powdered and dissolved in acid for further processing hence, the SEM images of this material was not added in the chapter.

# APPENDIX G

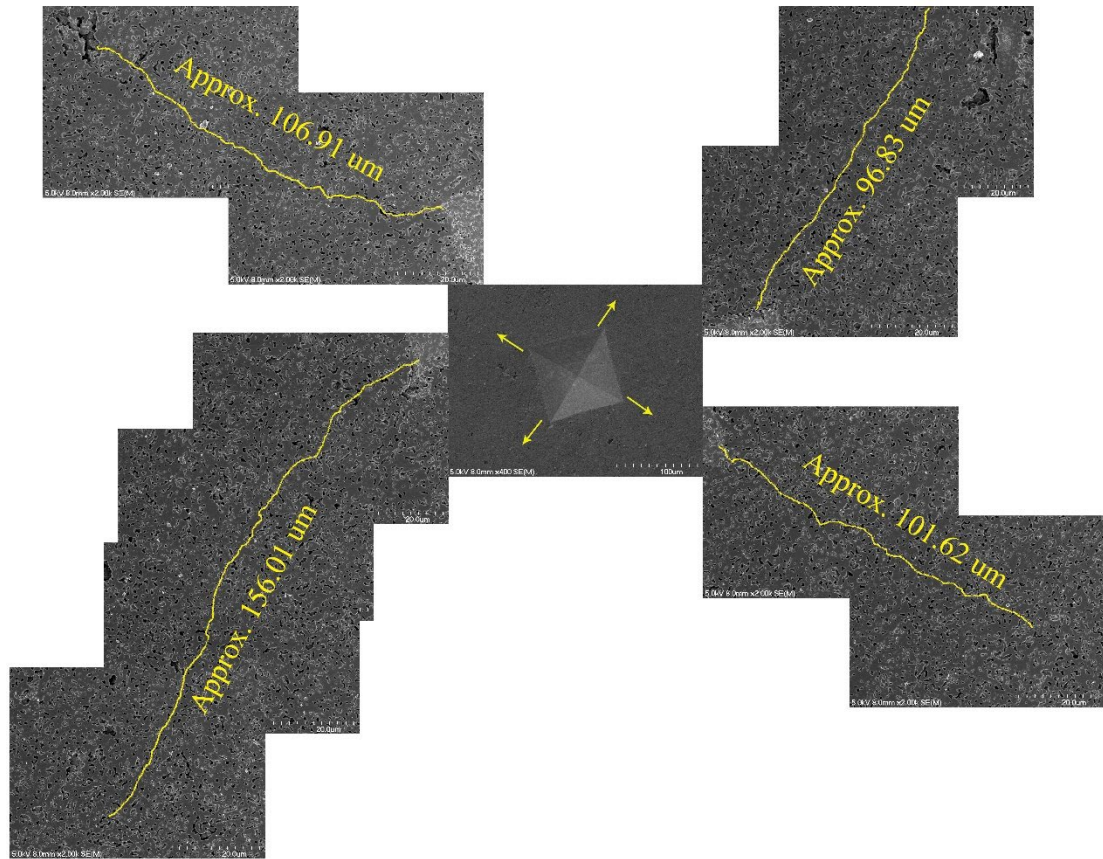


Figure G.1: The process of calculating crack lengths using SEM